Characterization of TiN-rich Particles in Thick Walled X70 Microalloyed Steels

by

Mehdi Arjomandpur

A thesis submitted in partial fulfillment of the requirements for the degree of

Master of Science

in

Materials Engineering

Department of Chemical and Materials Engineering

University of Alberta

Abstract

Microalloyed steels derive their superior properties from the introduction of microalloying elements (titanium (Ti), niobium (Nb), and vanadium (V)). These elements form various carbonitride particles at different stages of production. Titanium nitride (TiN) has the lowest solubility limit in the liquid and solid, resulting in the formation of coarse TiN-rich particles (micron size) in the liquid during solidification and fine TiN-rich particles (some tens of nanometers in size) in austenite. The coarse TiN-rich particles decrease the toughness of microalloyed steels by acting as initiation sites for cleavage cracks. Conversely, the fine TiN-rich particles increase the toughness of microalloyed steels by hindering austenite grain growth during homogenization and welding.

This study considers the effect of Ti and N concentrations on the sizes, compositions, and volume fractions of the coarse and fine TiN-rich particles in several as-rolled steels. Also, the type of precipitates in an as-cast steel was studied. Scanning electron microscopy (SEM) equipped with energy dispersive X-ray (EDX) analysis was used to measure the sizes and compositions of the coarse TiN-rich particles. Scanning transmission electron microscopy (STEM) equipped with EDX was employed to measure the sizes and compositions of the fine TiN-rich particles. Matrix dissolution was performed to extract the coarse and fine TiN-rich particles and measure the concentration of Ti in the matrix through inductively coupled plasma (ICP) analysis of the supernatant solutions. Quantitative X-ray diffraction (QXRD) analysis was conducted on the XRD patterns of the particles extracted via matrix dissolution to measure the volume fractions of the particles. The Scheil-Gulliver solidification model was employed to gain insight into the coarse TiN-rich particle characteristics.

The results showed that an increase in the product of the nominal Ti and N concentrations led to an increase in the size and volume fraction of the coarse TiN-rich particles. The compositional analysis indicated that the coarse TiN-rich particles were not pure TiN but contained Nb. The amounts of Ti and N bound in the coarse TiN-rich particles were subtracted from the nominal concentrations to obtain the adjusted Ti and N concentrations. An increase in the product of the adjusted Ti and N concentrations led to a decrease in the size and an increase in the volume fraction of the fine TiN-rich particles. The compositional analysis indicated that the fine TiN-rich particles contained a larger concentration of Nb in comparison with the coarse TiN-rich particles. The characteristics of the coarse or fine TiN-rich particles at the quarterline and centerline locations were compared, and no significant differences were observed. The study of the precipitates in the as-cast steel showed that the fine TiN-rich particles were absent in the as-cast steel, indicating that they form during the reheating (homogenization) stage. The measured volume fractions of the coarse TiN-rich particles were in good agreement with the predicted values obtained using the Scheil-Gulliver solidification model, except for the steel with the lowest nominal Ti and N concentration product.

Acknowledgment

I would like to first and foremost express my sincere gratitude to my supervisors Prof. H. Henein and Prof. D. G. Ivey, for their continuous support and guidance throughout this study. I would like to give special thanks to Dr. J. B. Wiskel for his patience and valuable suggestions and inputs in the course of the work. Thanks to all the members of the AMPL research group for their support: Aziz, Jonas, Lu, Vanda, Rishav, Mingzhang, and Tailin. I appreciate all your inputs.

I would also like to thank EVRAZ NA, TC Energy, and the Natural Sciences and Engineering Research Council (NSERC) of Canada for their financial sponsorship.

Finally, I would like to express my thanks and great appreciation to my family and friends for their endless love, support, and encouragement over the years.

Contents

List of Figures

List of Tables

1 Introduction

1-1 Statement of the problem

Micro-additions of transition metals, such as titanium (Ti), niobium (Nb), and vanadium (V), are made to low carbon steels to contribute to a combination of high strength, good toughness, and weldability. Low to limited solubility of the (microalloying) elements in the presence of nitrogen (N) and carbon (C) leads to the formation of their carbonitride particles at different stages of microalloyed steel production. Generally, the production process of microalloyed steels comprises two essential stages: continuous casting and thermomechanical controlled processing (TMCP). During continuous casting, partitioning of alloying elements into the liquid and their limited diffusion rates in the solid result in microsegregation and macrosegregation of the alloying element. Segregation causes the concentrations of the alloying elements in the liquid to exceed their solubility limits, leading to the formation of coarse secondary phases, such as TiN-rich particles. The coarse TiN-rich particles can be as large as several microns in size. The remainder of microalloying elements that are not consumed by the stable coarse TiN-rich particles will precipitate as finer particles, such as fine TiN-rich particles with sizes in the range of tens of nanometers, during post-solidification cooling or subsequent thermomechanical controlled processing.

The coarse and fine TiN-rich particles affect the processing parameters and properties of microalloyed steels. The coarse TiN-rich particles are ineffective at retarding austenite grain growth and promoting fine microstructure. Also, the presence of the coarse TiN-rich particles in the matrix can adversely affect the mechanical properties of the products. Since these particles are large and brittle in nature, they cleave and cause microcracks initiation at the onset of significant deformation [1]. The particles have been found to act as cleavage nucleation sites during Charpy V notch (CVN) tests, hence reducing the toughness of the steels [1].

Conversely, fine TiN-rich particles improve heat-affected zone (HAZ) toughness in weld samples by retarding austenite grain growth during welding and promoting finer post-welding microstructures. This mechanism provides an effective method for toughness improvement over a

wide range of heat inputs [2]–[5]. Additionally, their high-temperature stability ensures that austenite grain boundaries are pinned during reheating (homogenization) performed prior to hot rough rolling, thereby limiting austenite grain growth. Fine austenite grains provide a larger number of nucleation sites for ferritic phases, which in turn improves the strength and toughness of the product [6], [7]. However, fine TiN-rich particles can also influence the formation kinetics of NbC-rich particles by becoming their preferred nucleation sites during hot rolling. Comparable lattice parameter values and the same crystal structure for TiN-rich and NbC-rich phases promote epitaxial nucleation of NbC-rich particles on the fine TiN-rich particles by reducing the energy barrier for nucleation [8]. In addition, the presence of Nb in the fine TiN-rich particles affects the available Nb for precipitation during hot rolling of Ti-containing Nb steels, which in turn further complicates the kinetics of NbC-rich precipitation.

To exploit the beneficial effects of fine TiN-rich particles and minimize the detrimental effect of coarse TiN-rich particles, it is necessary to be able to quantify the effect of Ti and N concentration on their sizes, compositions, and volume fractions. The small amount of Ti added to microalloyed steels leads to the formation of particles of varying sizes and small volume fractions. Normally, the sizes and compositions are measured using scanning electron microscopy (SEM) and transmission electron microscopy (TEM) equipped with energy dispersive X-ray (EDX) analysis. Several techniques have been used to quantify the volume fractions of the particles, including using equilibrium calculations based on the solubility limits [9]–[12], evaluating the particles area per measured sample area [13], estimating the volume fraction through the number density of particles on replicas [14]. However, these techniques offer limited reliability due to the limited volume of the material analyzed. Additionally, some studies have used matrix dissolution methods to analyze larger volumes of materials. These studies rely on inductively coupled plasma (ICP) analysis of the dissolved matrix [15] or the extracted particles [16]–[19] to measure the amount of alloying elements in the precipitates. However, this technique cannot distinguish between different types of particles (fine or coarse), rendering it less practical. Recently, a number of studies have applied quantitative X-ray diffraction (QXRD) analysis to measure the volume fraction of the particles extracted with the matrix dissolution method. The technique enables researchers to distinguish different types of particles and to analyze a relatively large volume of the microalloyed steel.

1-2 Objectives

The study is conducted to realize the following objectives:

1- To study the effect of varying Ti and N concentrations on the size, composition, and volume fraction of fine and coarse TiN-rich particles.

2- To measure the volume fraction of fine and coarse TiN-rich particles using the matrix dissolution and QXRD analyses.

3- To compare the characteristics of fine and coarse TiN-rich particles at the quarterline and centerline locations of the thickness of steel strip.

4- To compare the findings with the available commercial modeling software (ThermoCalc).

1-3 Outline of the thesis

Chapter 2 provides a literature review of microalloyed steels, fine and coarse TiN-rich particles, and the characterization methods commonly used to analyze such particles. Chapter 3 presents the experimental methods used to characterize the particles from the commercial steels studies in this work. Chapter 4 presents and discusses the results obtained. The conclusions and recommended future work are provided in Chapter 5.

2 Literature review

This chapter starts with an introduction to microalloyed steels and their production process. It follows with a review of the studies investigating the effect of coarse and fine TiN particles on microalloyed steels. This is followed with a review of the characterization methods used to study the carbonitrides of microalloying elements. The chapter concludes with a summary.

2-1 Microalloyed steels

Microalloyed steels account for over 10% of global steel production [20], [21]. Microalloyed steels are extensively used in pipelines [21], shipbuilding [22], automotive parts [23], and structural applications [24]. They are attractive for their high strength, with yield strengths in the range of 350-800 MPa compared to mild steels with yield strengths of 150-200 MPa in the as-rolled condition [20]. Due to their higher strength to weight ratio, substituting microalloyed steels for mild steels results in more efficient designs. A reduction in component weight leads to savings such as manufacturing savings in materials, transport, handling, and welding costs as well as operational savings due to increased pumping capacities for pipelines [25], [26].

The advantages of microalloyed steels originate from their chemical compositions. Although it is feasible to increase the strength of mild steels by adding carbon, maintaining the toughness and weldability of the alloy imposes certain restrictions. In microalloyed steels, the limitation in carbon content to amounts less than 0.1 wt.% is compensated by introducing alloying elements and by employing a variety of strengthening mechanisms. Table 2.1 lists the commonly used alloying elements and their roles [25]. Microalloying the steel with elements such as Nb, Ti, and V, either singly or in combination, in amounts less than 0.1 wt.%, is the characteristic chemical composition of microalloyed steels.

Table 2.1– Major alloying elements in microalloyed steels and their influence [25]

Element	Amount in HSLA (wt.%)	Influence
C	<0.25	Strengthener
N	<0.012	Forms TiN, VN and AlN
Mn	0.5-2	Delays austenite decomposition during accelerated cooling / mild solid solution strengthener
Si	0.1-0.5	Deoxidizer in molten steel / solid solution strengthener
Nb	0.02-0.06	Very strong ferrite strengthener / grain size control / delays γ to α transformation
Ti	0-0.06	Grain size control (TiN formation)
V	0-0.1	Strong ferrite strengthener
Ni	0-0.5	Increases fracture toughness
Cr	0-1.25	Improves atmospheric corrosion resistance

Existing studies on microalloyed steels demonstrate that the significance of the microalloying elements is, to a large degree, related to their potential to precipitate at desired temperatures [20], [25], [27], [28]. The precipitation occurs due to their limited solubility in the steel matrix in the presence of C or N. Figure 2.1 compares solubility limits of the carbides and nitrides of microalloying elements. These carbides and nitrides can be categorized into three types [29]. Type I precipitates are the highly stable ones; they exhibit limited solubility even in liquid. Coarse TiN particles (in the range of microns) belong to this type. They form in the liquid steel and persist throughout the steel production process. As the temperature drops and the steel becomes austenitic, the opportunity arises for Type II carbonitrides to form (fine particles). They are typically finer, a few tens of nanometer in size. Their ability to retard grain growth or recrystallization of deformed grains plays a significant role in achieving high-strength and high-toughness. Type III carbides of V and Nb precipitate during the austenite to ferrite phase transformation, nucleating on the advancing γ/α interface, or after the transformation, nucleating preferentially on dislocations in ferrite. Precipitate strengthening in microalloyed steels is mainly due to these small precipitates with diameters of about 1-5 nm [25], [30], [31].

The following section provides a brief description of the production process of microalloyed steels.

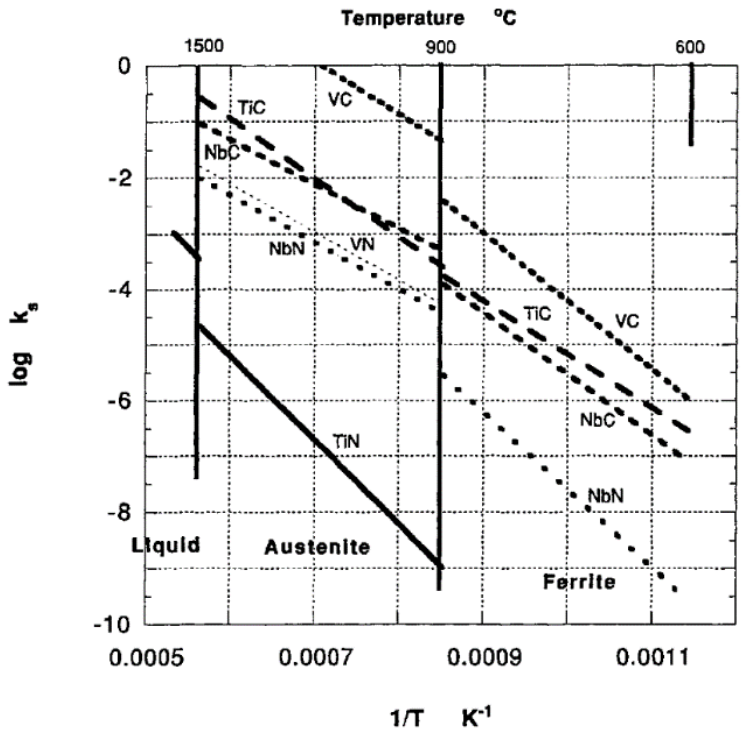

Figure 2.1–Solubility products for the carbides and nitrides of microalloying elements in the liquid, austenite, and ferrite [32].

2-2 Steel processing

This section presents a review of the main production stages of microalloyed steels.

2-2-1 Continuous casting

The majority of the steel produced in today's steel industry is cast via continuous casting technology [33]. Figure 2.2 shows a schematic of a continuous caster. During casting, molten steel with desirable composition and temperature is poured into a ladle from which it flows down into a tundish and then into a water-cooled copper mold. In the mold, enough heat is extracted to form a thin solid shell of steel next to the mold walls. While the solid shell enveloping the molten metal moves downward, more heat is extracted, and the shell grows inward in thickness. As solidification progresses, due to the lower solubility of alloying elements in the solid than that in the liquid, partitioning of the elements occurs, and the liquid increasingly becomes enriched in the elements. Typically, a significant portion of solidification advances in the form of columnar dendrites. The elements segregated to the front of the primary dendrites result in centerline segregation or macrosegregation, and the elements segregated to the side of the primary dendrites result in

microsegregation. When segregation is severe enough, the concentration of the dissolved elements in the liquid may exceed their solubility limits, and other phases, such as TiN particles, may form during solidification [34], [35]. A common practice is that the slabs are left to cool to ambient temperature, and then additional processing steps are carried out. Continuously cast slabs are usually semifinished products and subsequently undergo further processing, including reheating and hot rolling to the desired thickness and shape.

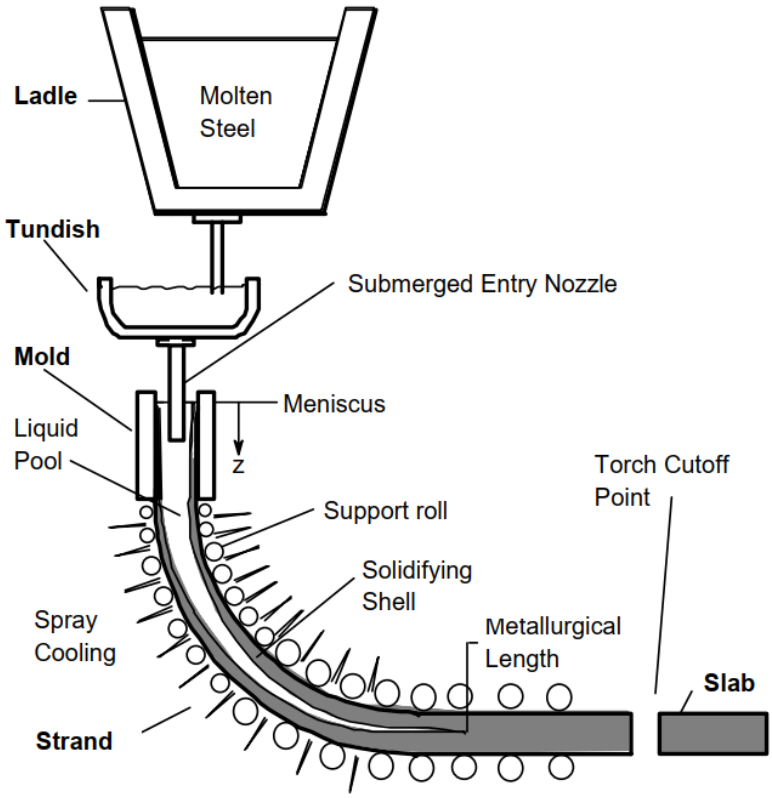

Figure 2.2– Schematic of continuous casting of steel [36].

2-2-2 Thermomechanical control processing (TMCP)

Modern pipeline steel manufacturers employ a combination of controlled hot rolling and accelerated cooling to tailor the steel's properties to customer specifications. Figure 2.3 shows the main production stages and microstructural evolution occurring in a production process known as TMCP [37]. The utilization of microalloying, along with TMCP, is a cost-effective way to produce skelp that satisfies mechanical requirements while keeping carbon content at low levels to preserve its weldability.

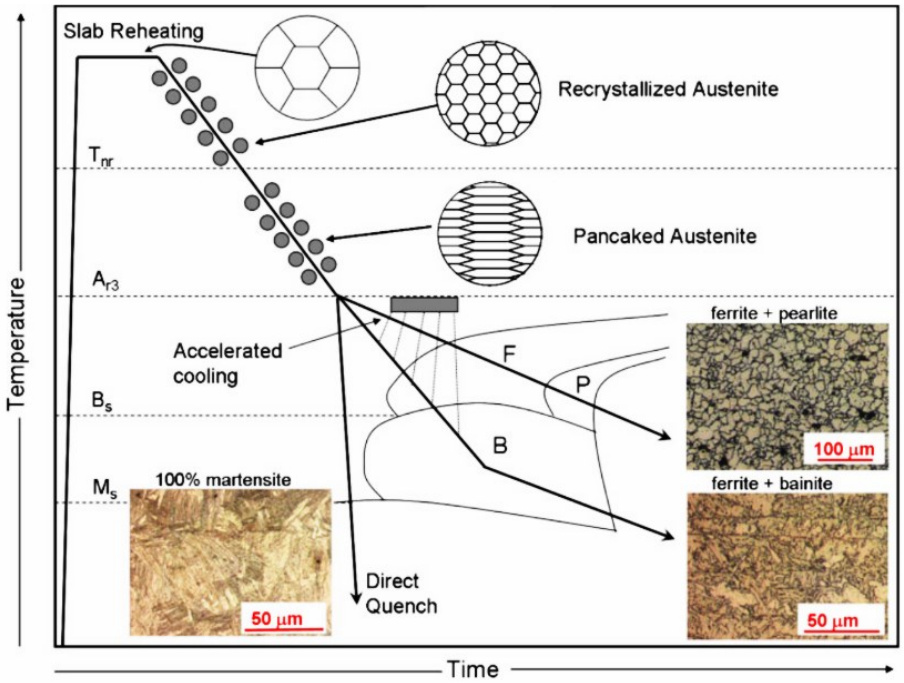

Figure 2.3– Schematic of TMCP [25].

TMCP begins with reheating the slabs. To make the forming process more accessible, the slabs are placed into a furnace and heated to the austenitization region, usually in the range of 1200 ˚C to 1300 ˚C. During soaking, some transition metal carbides and nitrides are dissolved, and the opportunity for homogenization of segregated alloying elements is provided. The high temperature accelerates the dissolution of carbides and nitrides as dissolution is a diffusion-controlled process. However, TiN particles are stable in austenite within these temperature ranges and limit the deleterious austenite grain growth.

Following homogenization, the slab undergoes several rolling passes, during which repeated recrystallization modifies the microstructure and results in substantial refinement of austenite grains. Depending on the degree of the deformation, static or dynamic recrystallization could take place. Subsequently, finish rolling takes place at temperatures below the non-recrystallization temperature. During finish rolling, the strain-induced precipitation of carbides, nitrides, or carbonitrides delays recrystallization of deformed austenite grains, resulting in accumulation of retained strain and formation of pancaked grains and deformation bands. The conditioned austenitic microstructure provides additional nucleation sites for austenite decomposition to ferrite in the following steps. Further nucleation sites and finer microstructures can be achieved by suppressing γ/α transformation start temperatures via employing fast cooling rates after finish

rolling. The cooling rate affects the final microstructure. Slower cooling rates favor the occurrence of reconstructive phase changes (ferrite and pearlite), while faster cooling rates favor more displacive transformations (bainite and martensite). Depending on the process design, the cooling process stops at a specific temperature and the warm strip is coiled. The relatively high temperature and slow cooling rate of the coils promote the formation of nano-precipitates (<10 nm) from the microalloying elements, which did not precipitate in the austenite region [20], [25], [37]. Since the nano-precipitates nucleate on dislocations, the plastic strain (increased dislocation density) resulted from the coiling process could promote their formation. However, it is possible that the recovery of dislocations may take place before the precipitation begins [38].

The final product contains several types of carbides, nitrides, or carbonitrides of transition metals, including coarse TiN and fine TiN particles. The importance of coarse and fine TiN particles on the processing and properties of the steel products is reviewed next.

2-3 Coarse TiN particles

This section presents a review of the role of coarse TiN-rich particles in microalloyed steels and the effect of Ti and N concentrations on the coarse TiN particles.

2-3-1 The role of coarse TiN particles

TiN particles forming during solidification are large. Due to their brittle nature, they adversely affect the product toughness and fatigue performance by acting as initiation sites for cleavage fracture in toughness tests [39]–[44]. A study on the effect of Ti and N concentrations on the fracture toughness of microalloyed steels has been conducted by Yan et al. [41]. They examined two steels with similar compositions (except for Ti and N concentrations) and similar production processes. The Charpy V-notch (CVN) tests showed that the steel with higher Ti and N concentrations exhibited lower toughness even at room temperature. For all tests carried out on the steel with higher Ti and N, the initiation sites for cleavage fracture were traced back to a coarse TiN particle. The initiation site for cleavage fracture in the other steel at -196 °C was determined to be the notch itself. In their earlier work [42], they studied three steels with different Ti and N concentrations and conducted CVN tests on the reheated and thermomechanically processed plates. The highest absorbed energies at room temperature and -20 °C were obtained for the steel with the lowest Ti and N levels. The observation was attributed to the absence of coarse TiN

particles in the steel with the best performance. Their equilibrium calculations of maximum solubility of Ti and N in austenite showed that the TiN phase started to form at temperatures below solidus in the steel which showed the highest toughness values. On the other hand, the coarse TiN particles acted as nucleation sites for cleavage cracks and significantly reduced the absorbed energy for the steels where the product of Ti and N concentrations (Ti·N value) was larger than the TiN solubility limit in austenite.

The detrimental effect of coarse TiN particles on the toughness of heat-affected zones (HAZ) of welds is also well established [1], [45], [46]. Fairchild et al.'s investigation [1] of the toughness of two steels containing 0.011 and 0.048 wt.% Ti showed that the steel with higher Ti concentration exhibited lower cleavage resistance over a wide range of microstructure resulting from simulated HAZ experiments. Their SEM studies of the fracture surfaces revealed that coarse TiN particles (larger than 0.5 μm) acted as cleavage initiators, while no specific feature could be detected at cleavage crack initiation sites in the steel with lower Ti concentration. Additionally, Fairchild et al. [1] found crack initiating TiN particles were broken in half (Figure 2.4), and the complementary TiN particle halves were detected on the mating faces of the fractured surfaces. It was suggested that instead of debonding the particle-matrix interface, applied stresses cleave coarse TiN particles, which in turn transfers the crack into the matrix. A similar mechanism of cleavage crack nucleation and propagation has been reported by [43].

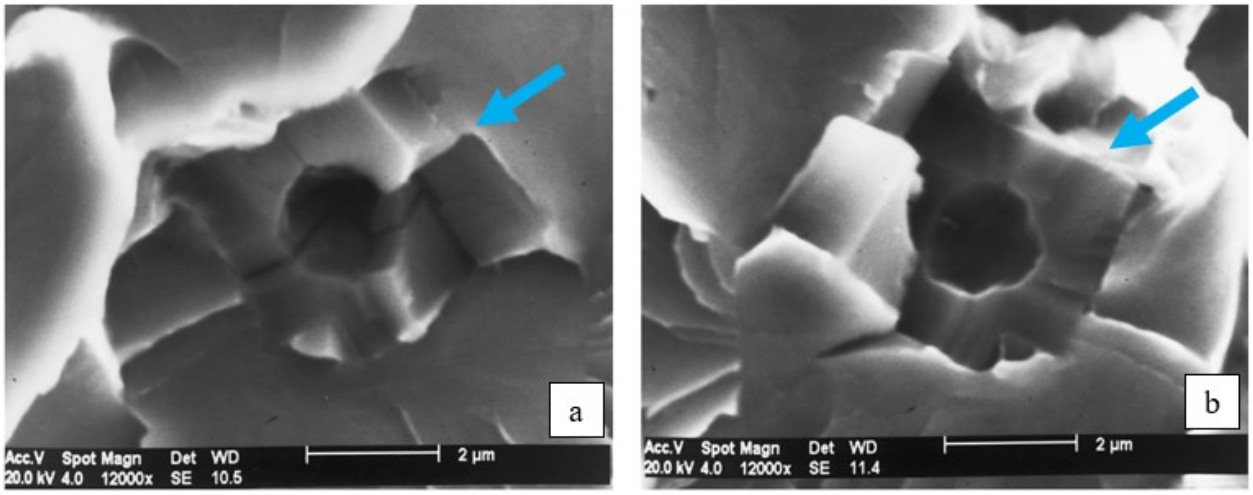

Figure 2.4a) Fractured coarse TiN particles at cleavage origin. b) The second half of the particle in (a) [1].

2-3-2 The effect of composition on coarse TiN particles

The characteristics of coarse TiN particles are affected by the composition of the steel, namely Ti and N concentrations. The size of coarse TiN particles decreases as the Ti and N concentrations of the steel decreases [44], [47]–[49]. A decrease in N concentration that is absorbed from the atmosphere or introduced by ferrotitanium alloys has been shown to decrease the amount and size of coarse TiN particles in microalloyed steels [49]. Linaza et al.'s investigation [44] of Ti-containing forging steels showed that an increase in Ti concentration (and Ti·N value) resulted in the formation of larger coarse TiN particles. A similar analysis was conducted by Zhang et al. [45] on steels microalloyed with Ti. Their optical microscope analysis of coarse TiN particles showed that an increase in the Ti concentration led to an increase in the average size as well as an increase in the maximum observed size of coarse TiN particles. When the Ti concentration was low enough (0.006 wt.% Ti and 0.0061 wt.% N), no coarse TiN particles were detected, and the steel showed the best fracture toughness.

In addition to size, the concentration of Ti and N can affect the volume fraction of coarse TiN particles [13], [44]. Shen et al. [13] measured the volume fraction of coarse TiN-rich particles in several medium-carbon Mn-B steels with compositions of 0.17 C-1.2 Mn-0.002 B-(0.009-0.039) Ti-(0.0058-0.0107) N (all in wt.%) using optical microscopy. Their findings, shown in Figure 2.5, demonstrated an increase in the volume fraction of coarse TiN particles as the Ti·N values increased.

2-4 Fine TiN-rich particles

This section provides a review of the role of fine TiN-rich particles (few tens of nanometers in size) in microalloyed steels and the effect of Ti and N concentrations on the characteristics of the fine TiN-rich particles.

2-4-1 The role of fine TiN-rich particles

Fine TiN particles restrict austenite grain growth during the reheating of slabs. Figure 2.6 shows the effect of several alloying elements on the grain coarsening temperature (the temperature at which grain coarsening becomes significant) in low carbon steels (<0.1 C-1.4 Mn-0.25 Si all in wt.%). Alloying with Ti and subsequent formation of TiN has been shown to be more effective

than alloying with Al, V, or Nb in retarding grain growth during soaking at temperatures between 900 and 1300 ˚C [50].

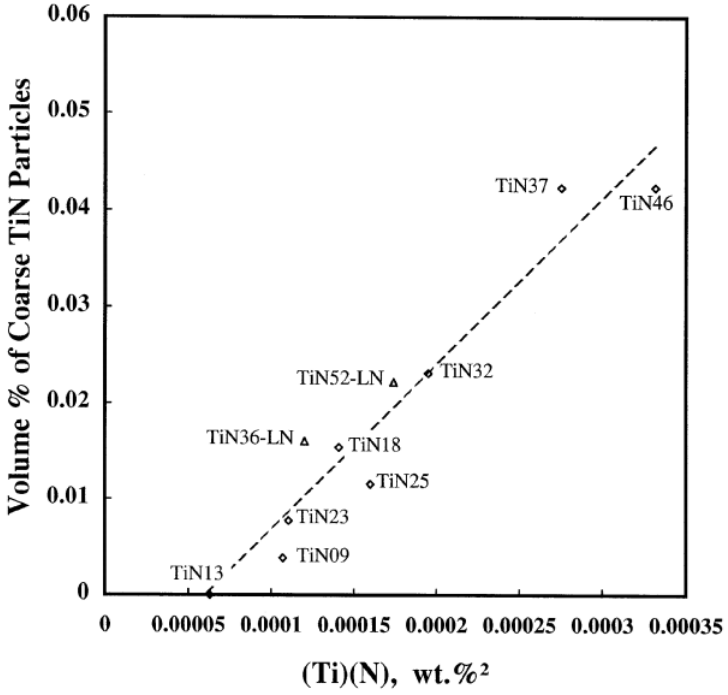

Figure 2.5– Volume fractions of coarse TiN particles as a function of Ti·N values determined using optical microscopy [13].

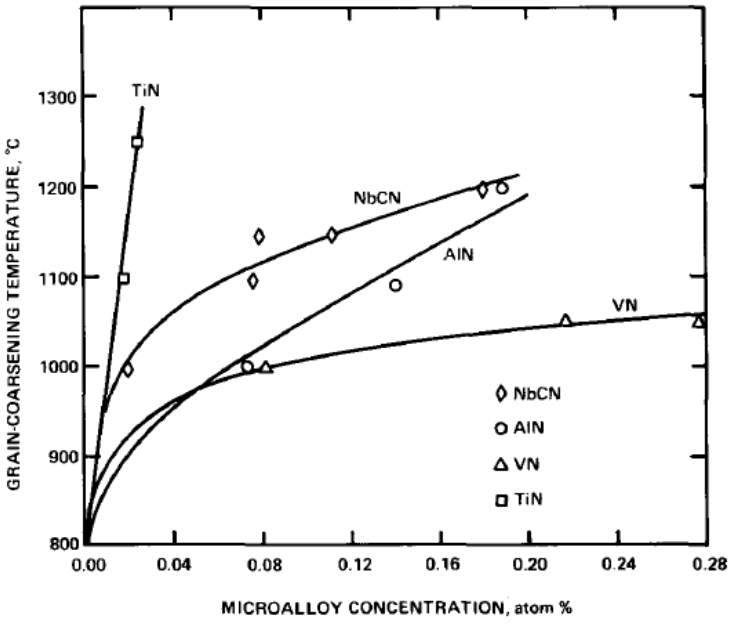

Figure 2.6– Effect of the concentration of microalloying elements on the grain coarsening temperature of austenite [50].

Studies on the effect of fine TiN particles on austenite grain size in simulated coarse grain heat-affected zones (CGHAZ) have shown smaller austenite grain sizes in Ti-containing steels. The addition of 0.012 wt.% Ti to low carbon steel has been shown to delay austenite grain growth by means of TiN pinning effects [51]. Similar improvement in the control of austenite grain size in simulated CGHAZ has been reported by Hamada et al. [52]. The simulated HAZ experiments were conducted on a series of steels with a composition of 0.06 C-1.6 Mn-0.045 V-0.5 Nb-0.011 Ti-(0.0012 to 0.0084) N (all in wt.%). Figure 2.7 shows the measured austenite grain size as a function of N concentrations after undergoing thermal cycles at two peak temperatures of 1350 ˚C and 1400 ˚C. The figure shows that austenite grain size decreases as N concentration increases. The TEM analysis of carbon replicas showed that the increase in the N concentration from 12 ppm to 84 ppm resulted in a decrease in the size of the fine TiN particles from about 0.1 μm to about 0.01 μm.

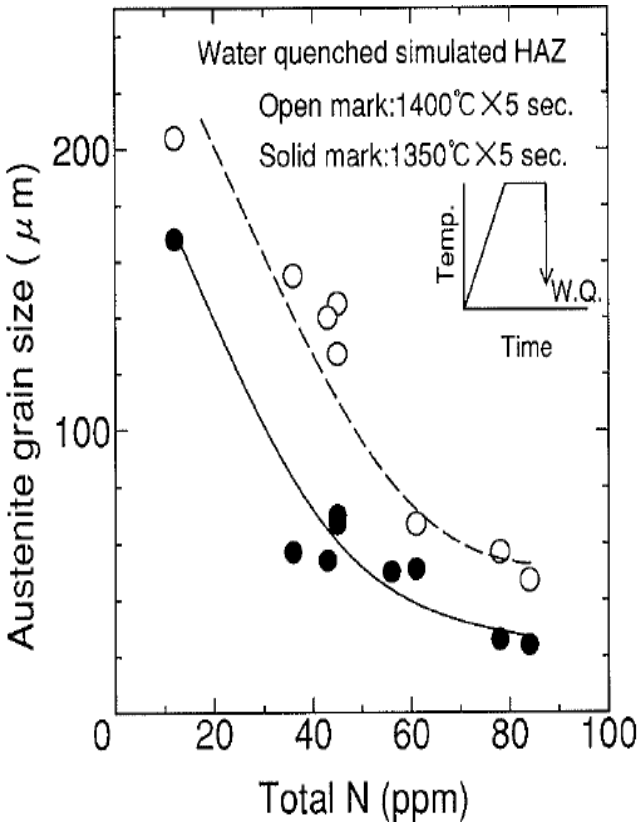

Figure 2.7– Influence of N concentration on austenite grain size after simulated HAZ experiments and water quenching [52].

2-4-2 The effect of composition on fine TiN particles

The Ti and N concentrations in steels affect the size of fine TiN particles. Kasamatsu et al. [53] measured the size of fine TiN-rich particles in several steels with a base composition of 0.13 C-0.35 Si-1.45 Mn (all in wt.%) and a variety of Ti and N concentrations. Their findings showed that an increase in the concentration of Ti or a decrease in the concentration of N increases the average size of the fine TiN-rich particles. An increase in Ti concentration from 0.009 to 0.018 wt.% (0.006 wt.% N) resulted in an increase in the average size of the fine TiN-rich particles from approximately 30 nm to 45 nm. It has been suggested that the coarsening rate of precipitates could be lowered by introducing excess nitrogen beyond the stoichiometric ratio [54]. Under equilibrium conditions, the concentration of Ti left in the solution can be determined by the solubility product of TiN at the temperature of interest. Figure 2.8 shows the solubility product curve for TiN in austenite at 1300 °C. The figure also shows that an increase in the N concentration causes a lower amount of Ti to remain in the solid solution. Using the Wanger equation [55], the coarsening rate can be related to solute concentrations:

$$r_t^3 - r_0^3 = \frac{8\sigma D[M]V}{9GT}.t \qquad Eq.\,2.1$$

where r_t is the precipitate radius at time t, r_0 is the precipitate size at time zero, σ is the interfacial energy at the matrix/precipitate interface, D is the diffusion coefficient of solute M, V is the molar volume of the precipitate, G is gas constant, T is the temperature in Kelvin, and [M] is the concentration of the solute (Ti in this case) in the matrix. Thus, increasing N concentrations beyond the stoichiometric value can lead to lower coarsening rates and smaller fine TiN particles.

2-5 Characterization of carbonitride particles

Several characterization methods could be used to quantify, directly or indirectly, features of the carbonitride particles found in microalloyed steels. The following subsections summarize the commonly used methods.

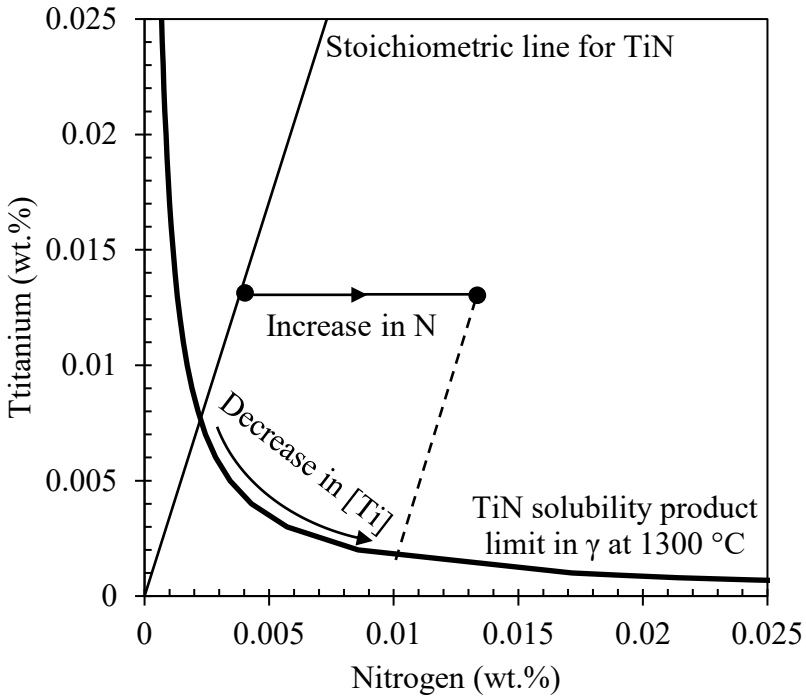

Figure 2.8– Effect of an increase in N concentration on the amount of precipitated Ti as TiN [54].

2-5-1 Transmission Electron Microscopy (TEM)

In modern research facilities, several types of microscopes are available for analyzing the samples at different magnifications. Optical microscopes are the easiest to use and can be used to observe features as small as 2000 Å. However, for practical purposes, they are not suitable for analyzing particles smaller than 1μm. Better resolution can be achieved using scanning electron microscopy (SEM). SEM can be used to analyze particles as small as 50 nm. When employing field emission type SEMs, finer particles (<10 nm) can be detected [56]. When studying the size, composition, morphology, and crystal structure of nano-sized particles, TEM is the technique of choice. However, there is some limitation to this method. The high resolution of TEM inevitably means that only a small region of the sample is studied at any one time, making the collection of statistically significant data a demanding task. Subsequently, the volume fraction information obtained with this method becomes less reliable as well, even when complex techniques are used to measure the volume of thin foil samples. Another limitation of imaging in transmission mode is that the particles of interest may overlap. Also, the region of interest in the TEM sample should be inevitably electron transparent. This requirement results in having to use specific sample

preparation techniques. Generally, there are two methods of sample preparation for metallic systems, thin foils and carbon replica extraction [57].

For ductile materials such as metals, the preparation process of thin foils involves several stages. First, a thin slice (<200 μm) of the bulk material is carefully prepared using mechanical polishing, a wafering saw, a chemical wire saw, or spark erosion. Then, using a mechanical punch, a 3 mm disk is cut from the slice. This is followed by mechanically or chemically pre-thining or dimpling the center of the disk down to about 10 μm thickness. Eventually, the final thinning process is done through electropolishing or ion milling to achieve electron transparency [57].

The other specimen preparation technique is carbon replica extraction. A schematic of the steps is shown in Figure 2.9. First, the surface of the sample is polished and etched to expose the particles. Then, a thin carbon film is evaporated onto the surface. The carbon film floats off when the underlying matrix is etched and is collected on a support grid [57].

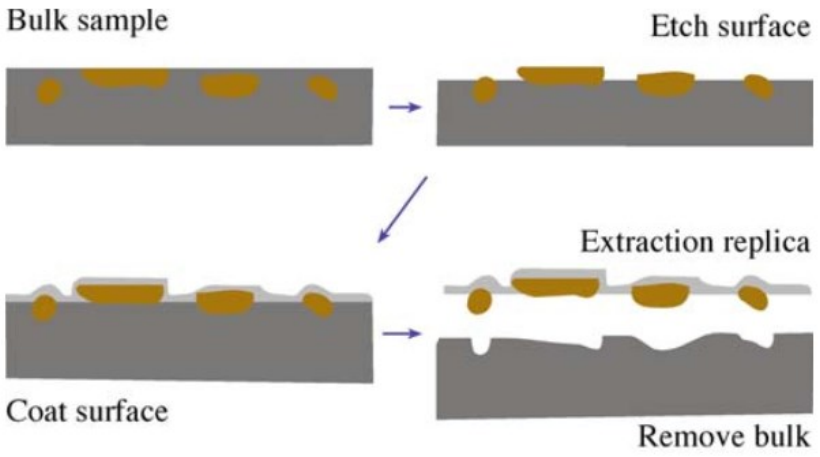

Figure 2.9– Steps of sample preparation in carbon replica extraction method [57].

2-5-2 Atom probe tomography (APT)

In this technique, atoms are removed from the tip of a sharp needle-shaped sample under intense electric fields. The evaporated atoms (technically, now ions) subsequently strike a detector recording the timing and position of the impact. The type of atom is identified by calculating the mass-to-charge ratio of the ions using the applied voltage, the distance between the detector and the tip, and the ion's time of flight. As the process continues, each atom and atomic-layer are evaporated and detected [58]. This makes it possible to resolve the atoms in the sample and,

therefore, the accurate composition of the matrix and particles. APT also provides the number density and size distribution of precipitates. However, the volume of the needle analyzed is small; e.g., 80 nm × 80 nm × 200 nm [59].

APT has been employed in several studies on microalloyed steels. Webel et al. [59] used APT to measure the concentration of remaining Nb in the matrix along with NbC-rich particles during deformation-induced precipitation. Zhang et al. [60] employed APT to measure size, number density, and volume fraction of interphase precipitates and studied the effect of microalloying element concentration on the characteristics of the precipitates. The technique has also been carried out to investigate the precipitation sequence in Mo-Ti microalloyed steels [61] and the evolution of interphase precipitates in Nb-Ti high strength low alloy (HSLA) steels [62].

2-5-3 Small angle neutron scattering (SANS)

The spatial and temporal resolution of SANS makes it a powerful characterization tool in the study of the precipitation and dissolution kinetics of particles in metallic systems. Bulk samples several mm in thickness can be analyzed, and statistically reliable particle size distributions can be obtained in a single measurement from a typical analyzed volume of ~200 mm^3. Since the majority of materials demonstrate low levels of absorption, it is possible to enclose the sample in an appropriate heating set-up and conduct in-situ analysis; for instance, in the study of the dissolution of precipitates. Additionally, sample preparation is usually quite simple. The samples can be prepared through mechanical polishing and a final wash to remove grease [63]. However, the technique has some disadvantages. The size of the particles that can be analyzed is limited to 1 to 100 nm. The monodispersity of particle sizes cannot be confirmed solely based on SANS data, and additional analysis of the sizes is required, for example, by using TEM [64].

Several researchers have employed SANS to take advantage of its characterization potential. SANS has been used to measure the size and volume fraction of precipitates in maraging steels, model IF steels, Fe-Cu steels, ultrahigh strength AF1410 steels, and microalloyed steels [56], [65]–[68]. Wiskel et al. [56] employed SANS to study the average size, size distribution, and number of carbonitride precipitates in several types of microalloyed steels, including X70 and X80. Van Dijk et al. [69] have carried out in-situ SANS analysis of high strength low alloy steels at 910 °C to 1200 °C and studied the evolution of niobium carbonitride particles.

2-5-4 Matrix dissolution

The small quantity of microalloying elements in microalloyed steels leads to the formation of a small volume fraction of carbonitride particles scattered throughout the matrix. Localized characterization techniques provide high-quality information on the morphology, size, structural relationship of the precipitates with respect to the matrix, and composition of individual particles. However, obtaining such data for a statistically adequate number of particles requires employing or adding a different technique. Statistically reliable data can be achieved by extracting the particles by selectively dissolving the matrix. The dissolution of the matrix can be realized chemically or electrochemically.

For chemical matrix dissolution, several acids or halogen-based solutions have been utilized. Typical acidic solutions used for matrix dissolution are HCl and H_2SO_4. Bruncková et al. [70] reported extraction of Ti/Nb carbides precipitated in IF steels through dissolution of the matrix in H_2SO_4. Hegetschweiler et al. [71] used HCl and H_2SO_4 to extract Ti/Nb carbonitrides from microalloyed steels. Successful HCl acid extraction of Ti/Nb carbonitrides from microalloyed steels has also been demonstrated by Lu [72] and Chatelier [73]. Moreover, solutions of I_2 in methanol or ethanol have been shown to be capable of dissolving the iron matrix while leaving Ti/Nb carbonitrides behind [72].

Alternatively, one can take advantage of the difference in the anodic potentials at which the matrix and particles of interest are dissolved in an electrolytic cell. The primary electrolyte used in this type of matrix dissolution experiment is 10% AA solution (10% acetylacetone - 1% tetramethylammonium chloride in methanol). Several researchers have employed the technique to extract Nb(C,N) [74], TiC and TiN [75], and Ti/Nb carbonitrides [72] from different grades of steels. However, the method can be time-consuming compared to the HCl acid solution method [72].

2-5-5 Quantitative X-ray diffraction (QXRD)

In recent studies, QXRD analysis has been employed to quantify the size, composition, and volume fraction of the particles extracted by matrix dissolution [72], [73]. The method involves obtaining an X-ray diffraction (XRD) pattern of the particles and carrying out Rietveld analysis [76] on the

collected XRD data. The average particle size is calculated based on the Scherrer equation [77] given below:

$$L_{Vol} = \frac{K'\lambda}{\beta_{hkl}\cos\theta_{hkl}} \quad Eq.2.2$$

where L_{Vol} is volume-weighted domain size, K' is a constant, λ is the wavelength of the incident X-ray, and β is the integral breadth of the peak located at 2θ [78]–[80]. The relationship between L_{Vol} and the average size (R) of a size distribution of crystallites can be expressed by the following equation:

$$L_{Vol} = \frac{3R(1+c)^3}{2} \quad and\ c = \frac{\sigma^2}{R^2} \quad Eq.2.3$$

where σ is the standard deviation of the size distribution and c is equal to 0.2 when the particles show a lognormal size distribution. The relative abundance of the phases present in the XRD data is calculated using the following equation:

$$w_i = \frac{SF_i M_i Z_i V_i}{\sum_j SF_j M_j Z_j V_j} \quad Eq.2.4$$

where w_i is the relative weight fraction of phase i in a mixture of j phases, SF is the scale factor obtained from the Rietveld refinement, M is the mass of the formula unit, Z is the number of formula units per unit cell, and V is the volume of the unit cell [81].

A number of recent studies have used this technique to study the size, composition, and volume fraction of precipitates extracted with the matrix dissolution method. Lu et al. [31] extracted the carbonitrides of microalloying elements using electrolytic and chemical matrix dissolution methods and evaluated the characteristics of the collected particles via QXRD analysis. The technique has also been employed by Chatelier [73] to study the precipitates forming in X70 and heat treated L80 and T95 steels.

2-5-6 ThermoCalc

ThermoCalc software [82] uses CALPHAD methodology to provide a computational tool to predict the characteristics of phases of specific materials systems in the equilibrium state. In the development stages of the software, the available information in the form of binary and ternary

systems has been used to generate thermodynamic data that makes it possible to extrapolate the characteristics of phases in higher order systems (over ten alloying elements) as a function of composition, pressure, and temperature [83].

This model has been employed by several researchers to study solidification and the effect of Ti and N concentrations on the formation of TiN [45], [48], [49], [84]. Huang et al. [84] used the Scheil-Gulliver solidification model in ThermoCalc to study the solidification path and the solid fractions at which coarse TiN particles form. Schneider et al. [48] compared the results of the Scheil-Gulliver and DICTRA (DIffusion Controlled TRAnsformation) modules of the software with their experimental findings and concluded that the Scheil-Gulliver model is a better representative of coarse TiN formation. Zhang et al. [45] used the software to verify the absence of coarse TiN particles in the steels with superior toughness properties.

2-6 Volume fraction measurements

Understanding the effect of TiN particles on steel properties requires the characterization of the fine and coarse TiN particles. The size and composition of the particles can be evaluated using TEM/EDX and SEM/EDX. However, studies have employed different methods to determine the volume fraction of the particles. A commonly used method is estimating the volume fraction of the coarse TiN particles based on the evaluation of the area fraction of the particles. A number of studies evaluated the volume fractions of coarse TiN particles using the point counting method on the micrographs obtained by optical microscopes [13], [85], [86]. Li et al. [87] evaluated the area fraction of coarse TiN particles and reported the results as the volume fraction of the particles. Fairchild et al.[1] obtained the number per volume of coarse TiN particles via measuring the number per area of the particles using an optical microscope. Then, the amounts of Ti in the coarse particles were estimated using the measured average size of the particles. A similar method has been used to convert the number density and the average size of the fine TiN particles on carbon replicas to the volume fraction of the particles [14]. Apart from the limited material analyzed in these studies, these methods rely on several assumptions, including the spherical shape of the particles with the same size and uniformity of particle dispersion.

Additionally, the solubility product limit of TiN has been used to determine the volume fraction of the coarse and fine particles [11], [12], [88]–[90]. Gao et al. [12] used the solubility product limits of TiN to determine the volume fraction of coarse and fine TiN particles. A similar approach

has been taken by Vega et al. [88]. Medina et al. [11] used equilibrium calculation to relate the volume fraction of the fine TiN particles to the observed austenite grain sizes during a 10 min heat treatment at 1100 and 1300 °C. These studies either neglect to consider the presence of coarse TiN particles in calculating the volume fraction of the fine TiN particles or use the solubility product to determine the volume fraction of the coarse particles as well. Since solidification is not an equilibrium process, the predicted values for the volume fraction of the coarse TiN particles will not be reliable.

Several studies have used the matrix dissolution method to analyze a statistically significant volume of materials to determine the volume fraction of the TiN particles. Hamada et al. [52] evaluated the quantity of fine TiN precipitates by chemical analysis of extracted residues and reported the amount of Ti present in the residues. A similar method has been employed by Okaguchi et al. [91] to study the influence of homogenization temperature on the tensile strength of Ti-containing HSLA steels. Doi et al. [17] also determined the quantity of Ti in the fine TiN particles by dissolving the extracted residues obtained using electrolytic matrix dissolution. Combining the matrix dissolution method and the subsequent dissolution of the extracted particles is a useful technique to determine the volume fraction of the fine TiN particles when the nominal Ti concentration is low enough so that only the fine TiN particles are present. When the coarse TiN particles are present, the evaluation becomes complicated. Zhang et al. [15] used ICP analysis of the supernatant solutions obtained from the matrix dissolution experiment to determine the volume fractions of coarse Ti(C,N) and fine (Ti,V)(C,N) particles in a Ti-V HSLA steel. Their calculation used the fact that V was virtually only present in the fine (Ti,V)(C,N) particles and the Ti/(Ti+V) ratio of the fine (Ti,V)(C,N) particles were know. Such an analysis can have very limited applicability in Nb-Ti microalloyed steels since Nb is present in the coarse and fine TiN-rich particles [92] and also forms NbC-rich particles at higher temperatures than V. In the present study, the measurement of the volume fraction of the coarse and fine TiN-rich particles using QXRD analysis is evaluated as an alternative technique.

2-7 Summary and objectives

The addition of Ti as a microalloying element results in the formation of coarse TiN particles during solidification and fine TiN particles in subsequent steps. Coarse TiN particles cleave under stress applied during toughness tests and act as an initiation site for cleavage crack. Therefore, they

should be avoided. On the other hand, fine TiN particles impede austenite grain growth during reheating and welding and improve the toughness of the product. Several characterization methods can be employed to study the particles. Each method has its unique advantages and corresponding drawbacks. SEM/EDX and TEM/EDX have often been used to determine the size and composition of the coarse and fine TiN particles, respectively. However, the methods employed for volume fraction measurements of the coarse and fine TiN particles rely on the measurements conducted on a small area of the material or are based on the equilibrium calculations. Other methods that make use of the relatively large volume of the material (that is analyzed with matrix dissolution methods combined with ICP analysis of the extracted particles) cannot be used for Nb-Ti containing microalloyed steels. In the present study, the implementation of QXRD analysis is considered as an alternative method for measuring the volume fractions of the coarse and fine TiN particles.

This work studies the effect of the Ti and N concentrations on the characteristics of the coarse and fine TiN-rich particles using SEM, STEM (scanning transmission electron microscopy) equipped with EDX, matrix dissolution, ICP, and QXRD analysis. Additionally, the thesis compares the characteristics of the particles at the quarterline and centerline locations and compares the experimental results with ThermoCalc software predictions.

3 Experimental procedures

Eight thick wall X70 microalloyed steels were selected for the study. The chemical composition and conditions of the steels are discussed in Section 3-1. The preparation sequence and equipment used for microstructural analysis of the samples are detailed in Section 3-2. Section 3-3 describes the carbon replica extraction method to prepare samples for SEM/EDX and STEM/EDX analysis. Details of SEM/EDX and STEM/EDX analysis are provided in Sections 3-4 and 3-5, respectively. Sections 3-6 presents the steps taken in the matrix dissolution experiments used to extract TiN-rich particles. Specifications of the equipment used in inductively coupled plasma-mass spectrometry (ICP-MS) and XRD analysis conducted on the matrix dissolution products are provided in Sections 3-7 and 3-8, respectively. Section 3-9 details the quantitative XRD analysis of the collected XRD data. Section 3-10 presents the configuration of ThermoCalc software applied to simulate solidification and post-solidification treatments.

3-1 Materials analyzed

The steels analyzed in this study were provided by EVRAZ Inc. NA. The chemical composition of the steels is presented in Table 3.1. The steels show the typical composition of a microalloyed steel including the composition range for Ti and N. The Ti concentration varies from 0.014 to 0.023 wt.%, and the N concentration varies from 42 to 93 ppm, so the steels cover a wide variety of Ti/N ratio and Ti·N values. Except for 3F-565, the steels were all cast and TMCP processed at an industrial processing facility. The reheat, rolling, and laminar cooling of 3F-565 was conducted using a pilot-scale rolling mill.

Table 3.1– Chemical composition of studied steels (wt.%)

Steel	C	Mn	Si	Cr + Ni + Cu	Nb	Mo	Ti	N ppm	Ti/N*	Ti·N (10^4)**	Thickness (mm)
T36-1	0.039	1.59	0.27	0.85	0.075	0.16	0.023	70	3.3	1.6	19
T36-2	0.046	1.62	0.25	0.85	0.078	0.12	0.015	42	3.6	0.6	19
T36-3	0.04	1.56	0.24	0.82	0.076	0.12	0.015	63	2.4	0.9	19
D-1	0.054	1.73	0.29	0.86	0.036	0.01	0.014	47	3.0	0.7	19
B60	0.049	1.71	0.32	0.58	0.089	0.32	0.018	74	2.4	1.3	19
3F-565	0.039	1.59	0.24	0.73	0.075	0.11	0.014	72	1.9	1.0	15
3F-as cast	0.039	1.59	0.24	0.73	0.075	0.11	0.014	72	1.9	1.0	-
TWX70	0.043	1.67	0.26	0.45	0.067	0.19	0.016	93	1.7	1.5	17

* wt.% / wt.%

** $wt.\%^2$

3-2 SEM study of microstructures

Samples from each steel were obtained from quarterline (QL) and centerline (CL) locations parallel to the surface and at the middle location along the width direction of skelps, as shown in Figure 3.1. The samples were mechanically ground with 80, 320, 600, and 800 grit SiC papers and then polished with 9, 3, and 1 μm diamond suspensions. Nital 2% was used to etch the polished surfaces and reveal the microstructures.

The X70 microstructure was analyzed using optical microscopy and field emission scanning electron microscopy (FESEM). The main advantage of FESEM is its better resolution compared with an optical microscope. Thus, a FESEM (Zeiss Sigma) operating at 5 kV was used to observe and record the microstructure of the samples. Images captured with a secondary electron (SE) detector were used to estimate the average grain size.

A typical example of the observed microstructures is shown in Figure 3.2a. A common feature of the microstructures is ferrite grains with irregular shapes. When grains are irregular in shape, the preferred method to measure grain size is the mean linear intercept method. In this study, the approach taken by Lu et al. [31] was employed to measure ferrite grain sizes. The grain sizes were

estimated by counting the number of intersections a line (or several parallel lines) makes with grain boundaries, and then dividing the length of the line by the number of intersections. Figure 3.2b shows the configuration of the lines used to evaluate grain sizes; three parallel lines in four orientations with a 45° orientation difference were used in the measurements. For each steel, three SEM micrographs were analyzed with a minimum of 144 measurements made on each micrograph.

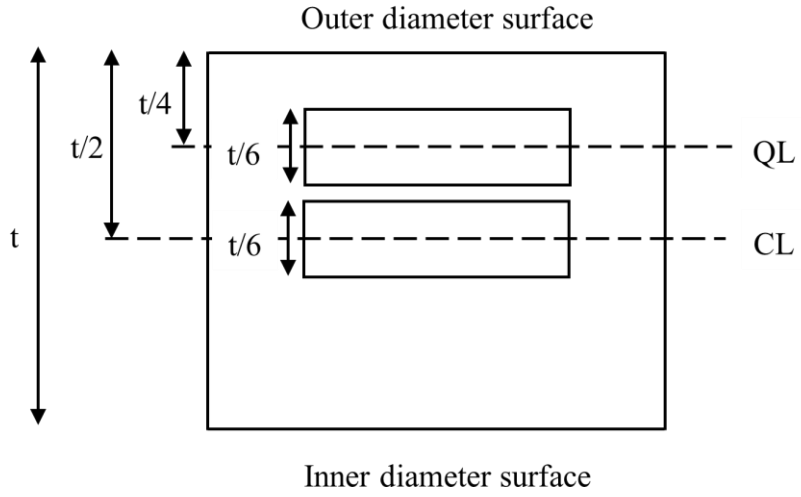

Figure 3.1– Schematic of the positions for quarterline (QL) and centerline (CL) samples from the cross section of a typical strip.

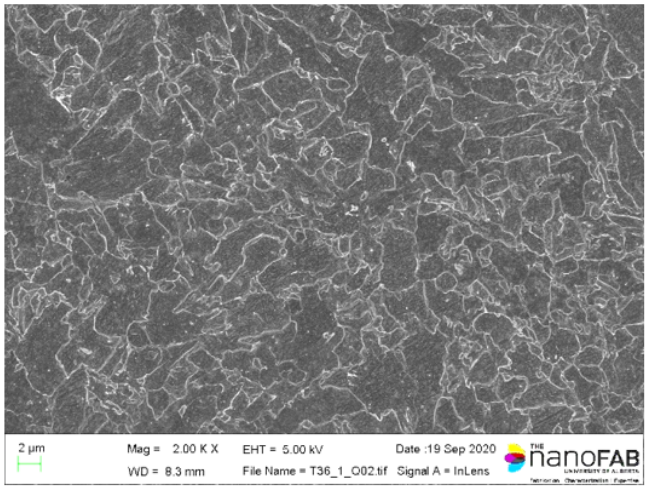

(a)

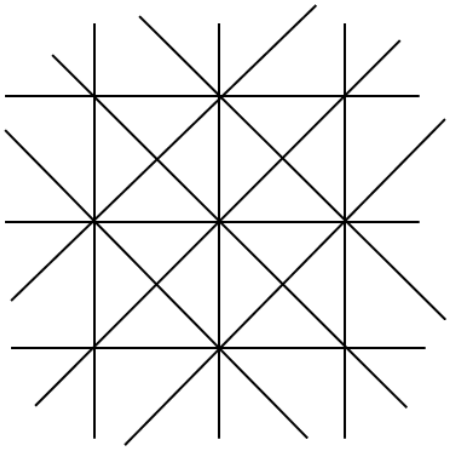

(b)

Figure 3.2a) SEM SE micrograph of T36-1 QL. b) Configuration of parallel lines used in the mean linear intercept method for grain size determination [31].

3-3 Carbon replica preparation

Carbon replica samples were obtained from all steels, both QL and CL locations. Following polishing and etching, described in Section 3-2, a Leica ACE600 Carbon/Metal coater was used to deposit an 8 nm carbon film onto the samples. The carbon film was manually scribed with a sharp blade into ~3x3 mm^2 pieces. Subsequently, the samples were immersed in 2% Nital solution to strip the carbon film off the surface of the samples. When carbon pieces separated, they were transferred into another dish containing ethanol and deionized water (1:1 mixture by volume). The solution allows for removal of contamination from the previous step and helps with unfolding of the carbon pieces. Finally, the pieces were collected using a 75-mesh copper grid and dried. For the as-cast sample, 4% Nital was used to release the carbon film from the sample surface, as a higher concentration of Nital can expedite the process. The carbon replicas were used to examine coarse (in the range of μm) and fine (in the range of nm) TiN-rich particles using SEM/EDX and STEM/EDX, respectively.

3-4 SEM/EDX analysis of carbon replicas

A Zeiss Sigma FESEM, operating at 10 kV and equipped with an Oxford EDX detector, was employed to measure the size and composition of coarse TiN-rich particles. Internal standards of the EDX software were used in the elemental composition analysis of particles. A minimum of 28 particles was evaluated to collect data for the size distribution and composition of coarse TiN-rich particles in every steel sample. Figure 3.3 shows an example of a coarse TiN-rich particle extracted via the carbon replica method and its EDX spectrum. Size measurements were performed using ImageJ software (version 1.52p). For conducting size measurement, a line was drawn around the particle of interest, and the area enclosed by the drawn line was measured by ImageJ, which converted the number of pixels in the area to conventional units of area. Subsequently, the square root of the measured area was recorded as the size of the particle. Additional SEM micrographs and EDX spectra of the coarse TiN-rich particles are provided in Appendix A.

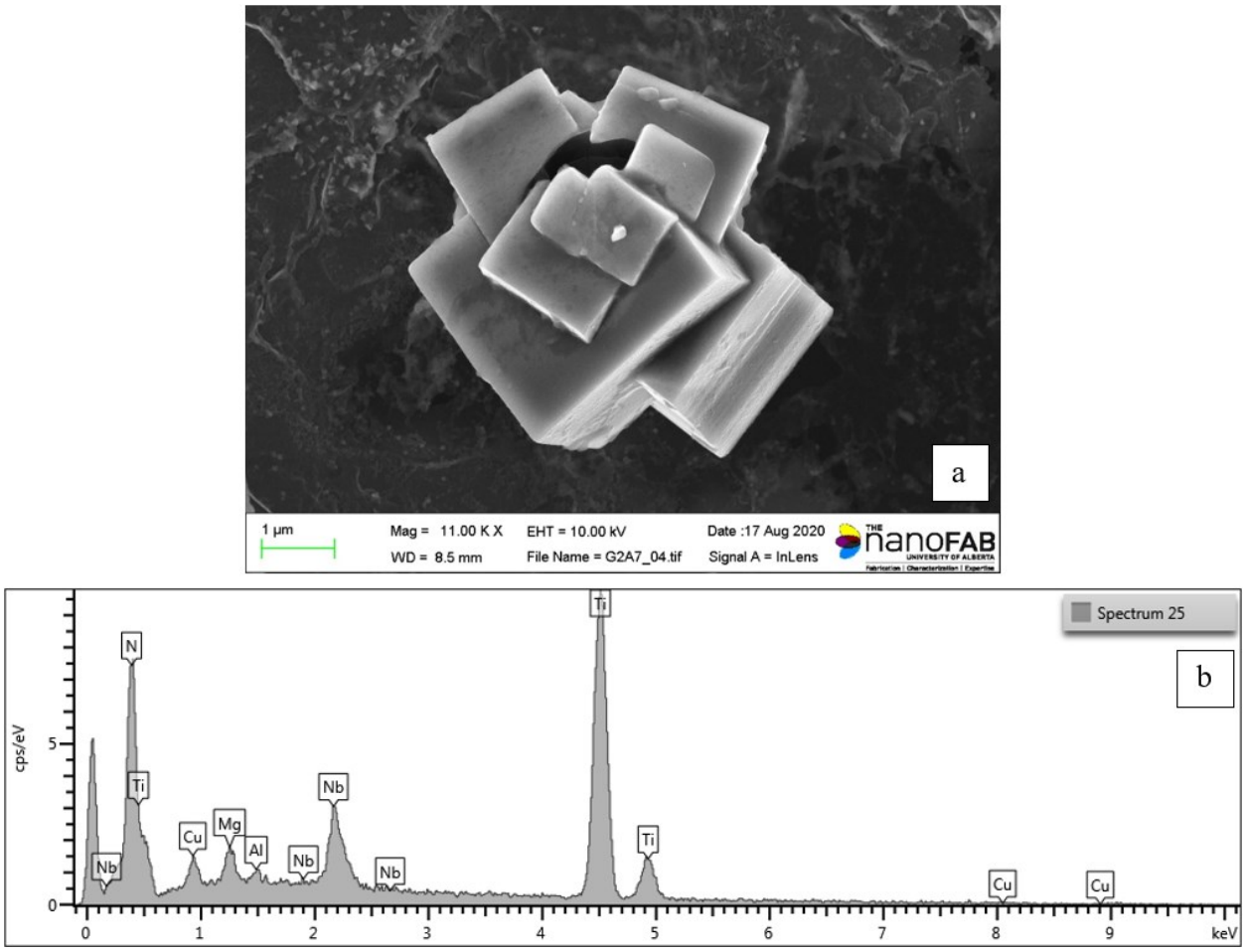

Figure 3.3a) SEM SE micrograph of a carbon replica extracted from T36-1 QL and b) EDX spectrum of the particle in (a).

3-5 STEM/EDX analysis of carbon replicas

A JEOL JEM-ARM200CF STEM operating at 200 kV was employed to conduct size and composition analysis on fine TiN-rich particles observed in the carbon replicas. Figure 3.4a shows several fine TiN-rich particles along with NbC-rich particles epitaxially nucleated on TiN-rich particles. An example of the EDX map and spectra obtained from the particles are shown in Figure 3.4b, Figure 3.4c, and Figure 3.4d. A minimum of 140 particles from two different replicas was evaluated to obtain the size distribution of fine TiN-rich particles for every steel sample. A similar procedure was used to measure fine particle sizes. For the composition of fine particles, at least fifteen particles were analyzed. Additional STEM micrographs and EDX spectra of the fine TiN-rich particles are provided in Appendix B.

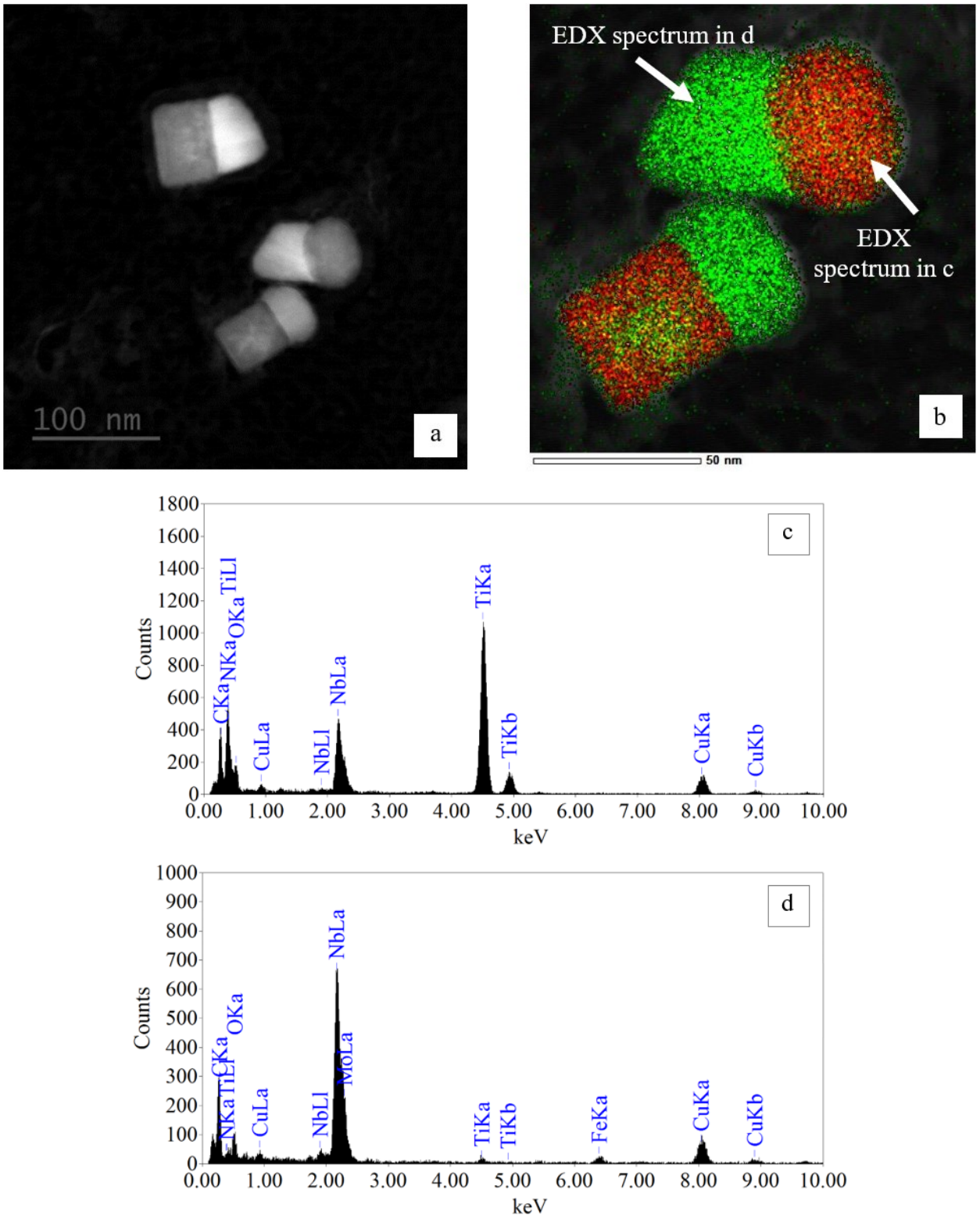

Figure 3.4– Fine TiN-rich and NbC-rich particles extracted with a carbon replica from T36-1 QL. a) STEM annular dark field (ADF) image; b) EDX map (red: Ti, green: Nb); c) EDX spectrum of top TiN-rich particle in (b); d) EDX spectrum of top NbC-rich particle in (b).

3-6 Matrix dissolution

An alternative method that can be used to separate particles from the Fe-rich matrix is to dissolve the matrix in a solution that does not attack the particles of interest. In this study, hydrochloric acid was used to dissolve the matrix and collect TiN-rich particles. A high-speed centrifuge (to be described in detail below) was employed to separate residues from the solution. The collected residues were analyzed using an X-ray diffractometer (Section 3-8), and the collected solution was analyzed using ICP-MS (Section 3-7).

Figure 3.5 shows a schematic of the dissolution set-up used in this study. A 1 L 3-neck Pyrex flask was used as the reactor for dissolution. A condenser was used to maintain the volume of the solution constant during the experiment. In order to provide an inert atmosphere in the flask, N_2 gas was bubbled through the solution throughout the experiment. The inert gas was also used to purge dissolved oxygen from the solution prior to the start of dissolution. The deoxygenation process was performed for 1 h.

For each dissolution experiment, approximately 10 g sample of steel was cut from the region of interest (quarterline or centerline). Any surface contamination occurring in the preparation process was removed by grinding the sample faces with SiC paper. Subsequently, samples were sonicated for 15 min, dried, and weighed on a high precision scale with an accuracy of 0.1 mg.

Based on the work of Chatelier [73], a 500 ml mixture of 12-M HCl acid and deionized water (1:4 by volume) was used as the solvent. The solution temperature was raised to 90 °C to accelerate dissolution. When dissolution was complete, the solution was transferred into 50 mL high-speed polypropylene copolymer (PPCO) centrifuge tubes. The tubes were centrifuged using a Sorvall RC-6 superspeed centrifuge at 40,000 RCF (relative centrifugal force) for 30 min. Subsequently, the supernatant solution was carefully removed using 2 mL pipettes and stored for ICP-MS analysis. Then, the tubes were refilled with deionized water and centrifuged for at least four more cycles to clean the residues. After the cleaning process, the residues were collected by filling the tubes with ethanol, sonicating the tube for several minutes, transferring the resulting suspension into a dish with known mass, and drying the residues over a hotplate at about 40 °C. The transferring process of residues from the tubes into the dish was repeated several times to ensure all residues were collected. Finally, the residues were weighed, and a sample for XRD analysis was prepared.

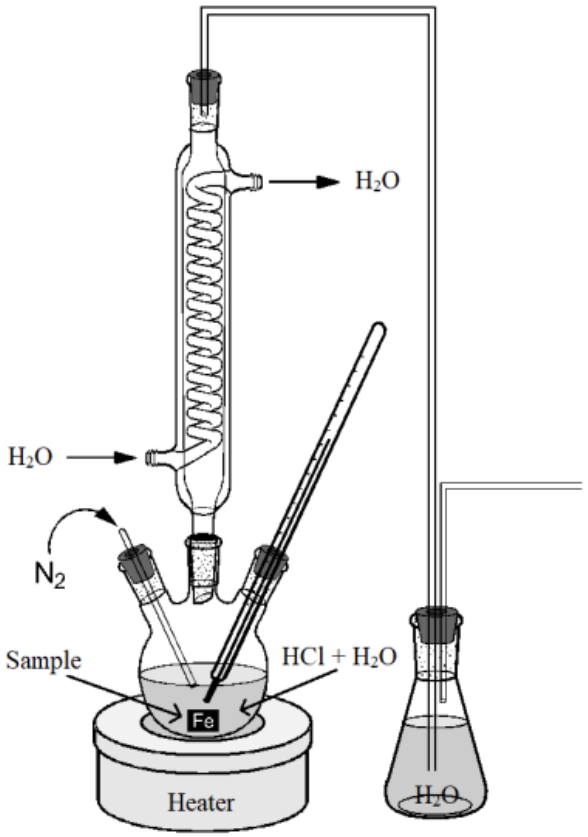

Figure 3.5– A schematic of the matrix dissolution set-up [73].

3-7 ICP-MS analysis

One product of matrix dissolution is the supernatant solution. The solution mainly contains chlorides of iron as well as other alloying elements that have been dissolved. The collected supernatant solutions were analyzed using ICP-MS (Perkin Elmer Elan 6000 quadrupole ICPMS) to obtain information regarding the concentration of alloying elements in the supernatant solutions. The ICP-MS instrument can provide concentration data in the resolution range of parts per billion (ppb). Table 3.2 shows the concentration of Ti in the supernatant solutions obtained from the centerline (CL) samples. ICP analysis was conducted three times for the centerline samples listed in Table 3.2. For the rest of the samples, the analysis was conducted once since only slight variations were observed in the results for the centerline samples. For the quarterline samples, the results are presented in Table 4.2.

Table 3.2– ICP-MS results of Ti for CL samples

Steel	Volume of solution	Mass of steel sample	Concentration in supernatant solution	Concentration in supernatant solution*	Nominal concentration of Ti in steel	Ti in collected residue
	(L)	(mg)	(mg/L)	(10^{-4} wt.%)	(wt.%)	(%)
T36-1 CL	0.5	10077.6	0.158	7.8	0.023	96.6
			0.168	8.3		96.4
			0.155	7.7		96.7
T36-2 CL	0.5	9441.9	0.105	5.6	0.015	96.2
			0.111	5.9		96.1
			0.0854	4.5		97.0
T36-3 CL	0.5	9942.7	0.0761	3.8	0.015	97.5
			0.0833	4.2		97.2
			0.0661	3.3		97.8
D-1 CL	0.5	10107.0	0.0590	2.9	0.014	97.9
			0.124	6.1		95.6
			0.111	5.5		96.1

* Measured by dividing the mass of Ti in the supernatant solution by the mass of the dissolved steel sample

3-8 XRD analysis

The extracted residues from matrix dissolution experiments were analyzed with a Rigaku Ultima IV diffractometer to measure their XRD data. The scan specifications are included in Table 3.3. The collected data can be used to identify the phases present in the samples. Phase identification was carried out using Jade software (version 9.0). Figure 3.6 shows an example of the observed XRD pattern for T36-1 QL and the identified phases. The data used in the identification of the oxide phase are presented in Appendix C. The possibility of forming the oxide phase when the residues are exposed to the air is evaluated using ThermoCalc in Appendix D.

In addition to phase identification, XRD data can be used to obtain further information, such as average domain size. However, for such an analysis, instrument contribution to XRD data needs to be determined. A LaB_6 standard sample was analyzed with every residue sample collected from matrix dissolution experiments. For a more detailed study, the collected information from the residues and the standard samples were subsequently analyzed with Rietveld refinement [76] (Section 3-9).

Table 3.3– XRD parameters

Radiation source	Cobalt tube at 38 kV and 38 mA
Kα1	1.78900 Å
Kα2	1.79283 Å
K-beta filter	D/Tex Ultra with Fe Filter
Geometry	Bragg Brentano
Range (2θ)	5 to 100°
Step size (2θ)	0.0200°
Scan speed	2.00 deg/min
Sample holder	Zero background plate

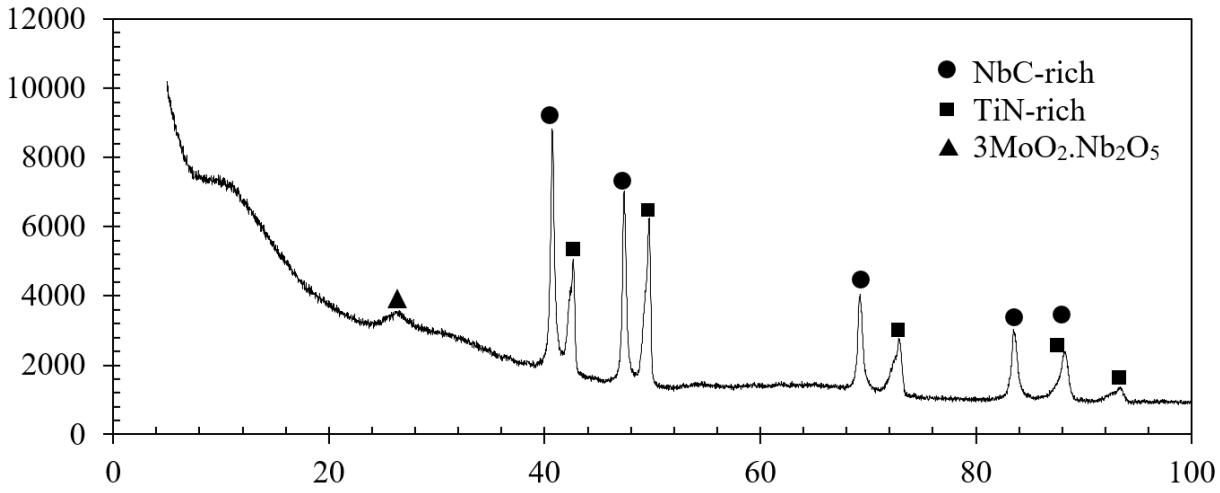

Figure 3.6– Observed XRD pattern for T36-1 QL[1].

[1] $3MoO_2.Nb_2O_5$ has been suggested by Dr. Douglas Ivey based on SAED and STEM/EDX analysis conducted by him on residue extracted form T36-1 QL.

3-9 Quantitative XRD analysis

The information that XRD patterns carry is not limited to the type of constituent phases; it can be used to quantify additional characteristics of the phases, such as average domain size, composition, and relative abundance. Such information can be acquired by characterizing the measured XRD data with Rietveld refinement. The method uses a least-squares approach to find a calculated diffraction pattern that best fits the observed data [93]. In this study, TOPAS Academic software V5 [94] was used to analyze the XRD data of LaB_6 standard samples to obtain necessary information about the diffractometer and, subsequently, to analyze the XRD data of the residues extracted via matrix dissolution experiments.

3-9-1 LaB_6 standard sample analysis

The XRD data measured from the LaB_6 standard sample were used to incorporate the instrument aberrations in the analysis of XRD data of the residues. This was achieved by performing Rietveld refinement on the data and refining the parameters of the Caglioti function [95], axial divergence model, and zero error. A screenshot of the script used to obtain the parameters from the LaB_6 standard is provided in Appendix E.

3-9-2 QXRD analysis of residue extracted with matrix dissolution

After obtaining the parameters describing the instrument contribution, additional information can be extracted from the residue XRD data using TOPAS Academic software. A screenshot of the script used in analyzing the XRD data of the extracted residue is shown in Appendix E. Figure 3.7 shows the observed XRD pattern (blue line) and calculated XRD pattern (red line) for the residue extracted from T36-1 QL. The Rietveld refinement and XRD patterns for all samples are provided in Appendix E. Although the software is capable of handling refinement of several parameters simultaneously [93], a step-by-step approach was adopted to facilitate the refinement process. The following steps were taken in the analysis of the XRD pattern of the residues extracted from the matrix dissolution experiments:

1- The XRD pattern of interest was input.
2- The instrument parameters (Caglioti) were included.
3- The background was fit with 11^{th}-order Chebyshev polynomials of the first kind.

4- The first phase was added by importing its crystal information file (CIF)[1]. Its lattice parameters and scale factor, along with sample displacement, were refined.

5- Size and strain parameters were refined.

6- To correct the composition of the phase, atomic positions and occupation were refined.

7- Steps 4 to 6 were repeated for every phase.

8- Due to the non-spherical shape of particles, spherical harmonics were added to account for the anisotropically sized domains [93].

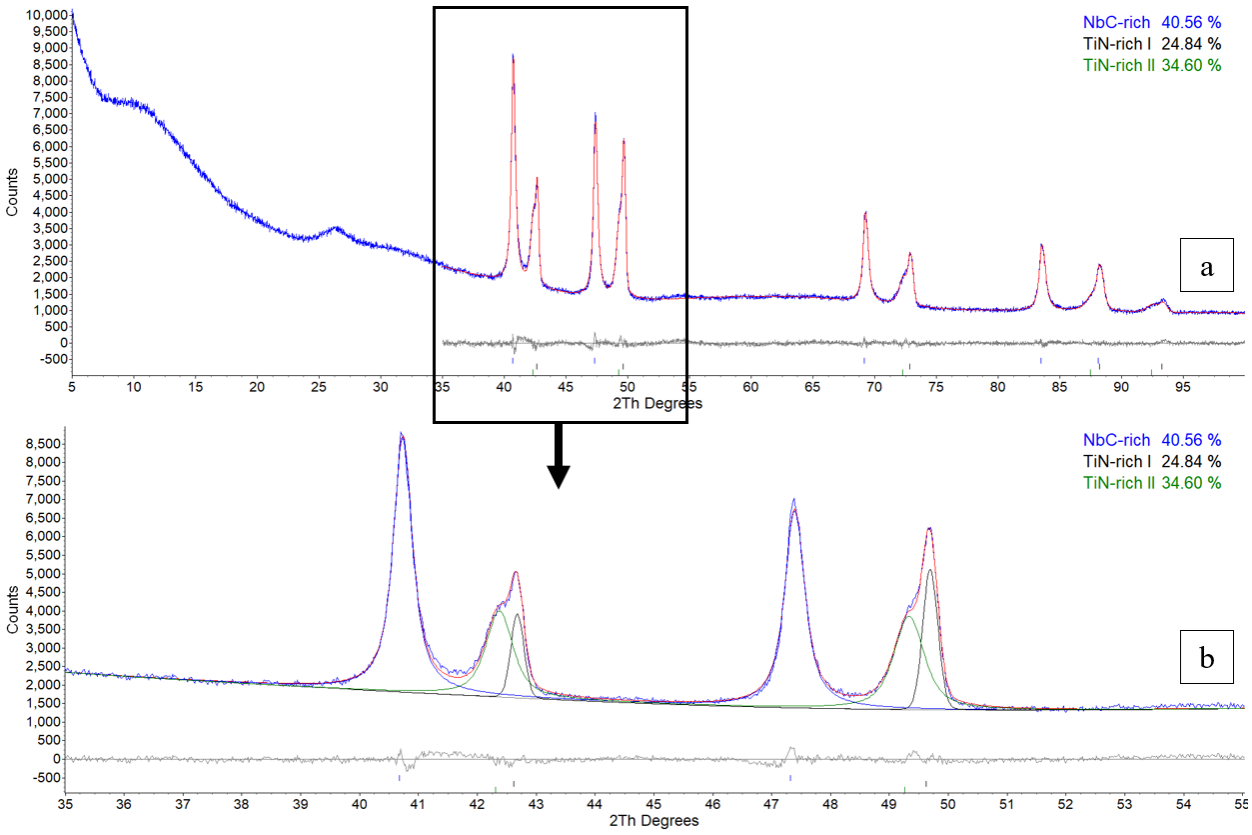

Figure 3.7a) Observed and calculated XRD patterns for residues extracted from T36-1 QL via matrix dissolution; b) enclosed part in (a) showing peaks of individual phases.

Following the approach taken by Lu [72], the compositions of NbC-rich (Table C.1), coarse TiN-rich (Table 4.1), and fine TiN-rich particles (Table 4.4) measured with SEM-STEM/EDX analysis were used as the compositions of the phases detected in the XRD data. Although EDX analysis of TiN-rich particles provides Ti/(Ti+Nb) ratios, it cannot measure a reliable N/(N+C) ratio for the

[1] Available at www.materialsproject.org

particles. In order to make a reasonable estimation of the concentration of N in the particles, the Ti/(Ti+Nb) ratios and the lattice parameters were compared with $(Ti_x,Nb_{1-x})C$ and $(Ti_x,Nb_{1-x})N$ ($0 \leq x \leq 1$). The comparison is presented in Figure 3.8 and Figure 3.9, showing the Ti/(Ti+Nb) ratios from the EDX analysis along with the lattice parameters obtained from the QXRD analysis. In most cases, the particles are not fully nitrides. The N/(N+C) ratio of fine TiN-rich particles in D-1 QL (Figure 3.8) was estimated as 0.5. For the rest, four QXRD analyses were carried out for each sample while assuming that the N/(N+C) ratio of fine and coarse TiN-rich particles could be either 1 or 0.75. Table 3.4 shows the maximum and minimum volume fraction values obtained from the analysis. The variation in the results is very low, probably because C and N are light elements with similar atomic numbers.

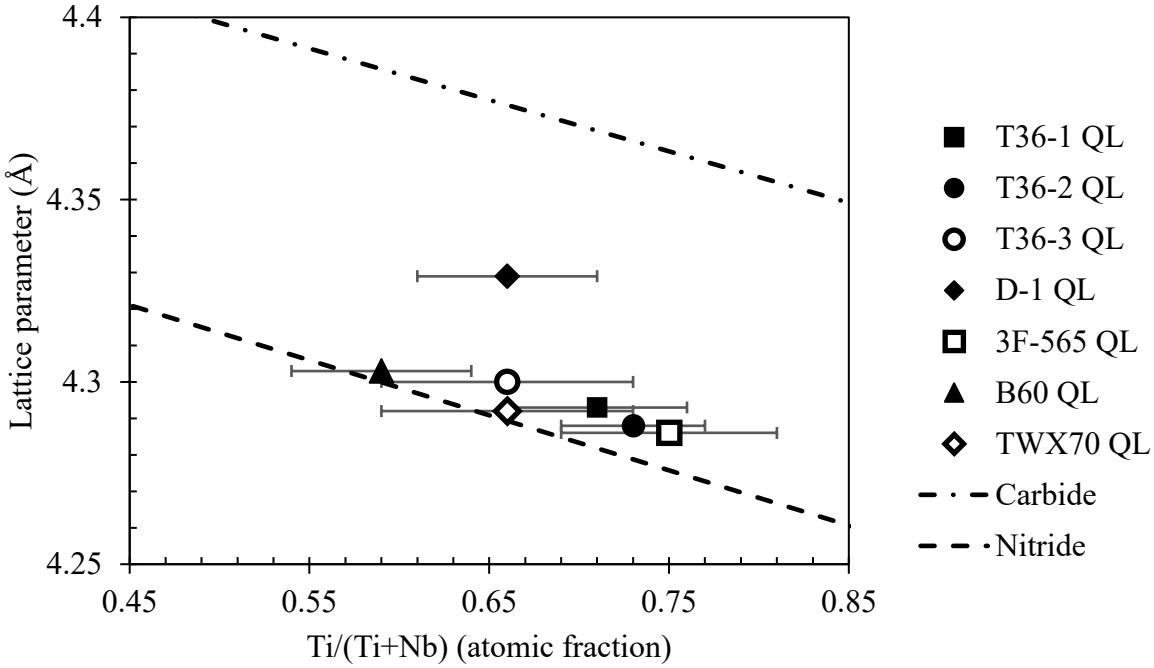

Figure 3.8– Ti/(Ti+Nb) ratio of fine TiN-rich particles measured with STEM/EDX versus their lattice parameters obtained from QXRD analysis.

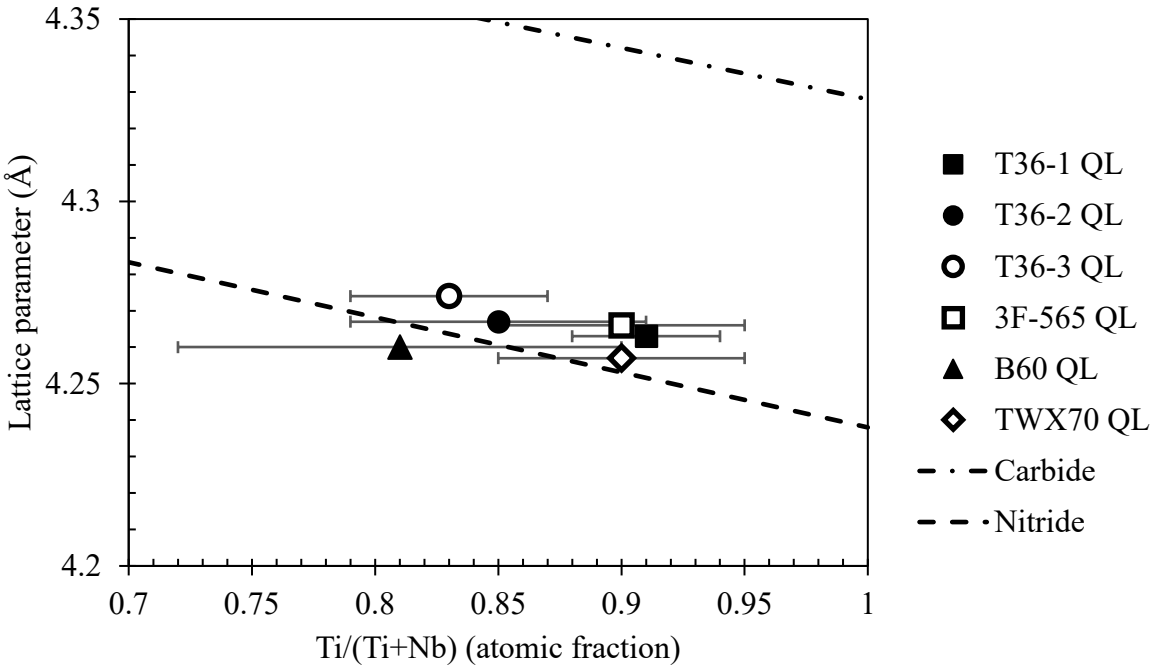

Figure 3.9– Ti/(Ti+Nb) ratio of coarse TiN-rich particles measured with SEM/EDX versus their lattice parameters obtained from QXRD analysis.

Table 3.4– Minimum and maximum volume fraction (V_f) of fine and coarse TiN-rich particles extracted from the QL when N/(N+C) varies from 0.75 to 1 in QXRD analysis

Steel	Fine TiN-rich		Coarse TiN-rich	
	Min V_f (%)	Max V_f (%)	Min V_f (%)	Max V_f (%)
T36-1 QL	0.029	0.030	0.023	0.024
T36-2 QL	0.031	0.032	0.005	0.005
T36-3 QL	0.029	0.029	0.011	0.011
3F-565 QL	0.018	0.018	0.014	0.014
B60 QL	0.048	0.048	0.007	0.007
TWX70 QL	0.024	0.025	0.015	0.015

In the analysis shown in Figure 3.8 and Figure 3.9, a linear relationship was assumed between $(Ti_x,Nb_{1-x})C$ or $(Ti_x,Nb_{1-x})N$ and the lattice parameters. Such a relationship between the composition of $(Ti_x,Nb_{1-x})C$ and its lattice parameter has been reported elsewhere, [96]. The relationship is known as Vegard's Law. Figure 3.10 shows the lattice parameter of $(Ti_x,Nb_{1-x})C$ as a function of composition.

The TOPAS software provides several agreement factors to evaluate the quality of the refinement. A commonly used agreement factor is the weighted profile R-factor (Rwp). Low values of Rwp indicate better refinement qualities since Rwp evaluates the difference between the observed and the calculated profile. Although the statistical agreement factors provide useful tools to assess the progress of the refinement, it has been suggested that a more reliable approach is evaluating the quality of the fit by visually comparing the calculated pattern with the measured pattern and validating whether the constituents are chemically sensible [97].

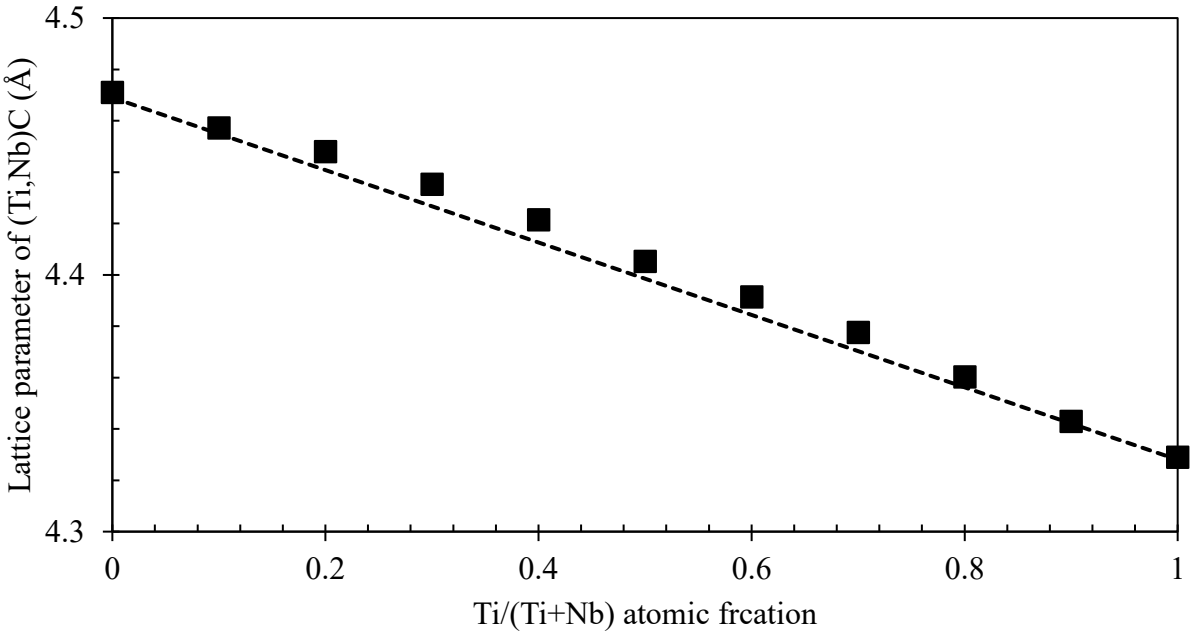

Figure 3.10– Relationship between $(Ti_x,Nb_{1-x})C$ lattice parameter and composition [96].

3-9-3 Calculation of volume fractions of TiN-rich phases

The volume fractions of the phases detected in the XRD patterns were calculated using the notion of mass conservation of Ti. A similar concept has been employed by Lu [72] to calculate the

amount of (Nb,Mo)C nanoprecipitates extracted with HCl acid matrix dissolution from X70 and X80 microalloyed steels.

When the nominal composition of Ti in the steel samples and the concentration of Ti in the supernatant solutions are known, the amount of Ti in the particles extracted via matrix dissolution can be calculated from the following

$$Ti_{ppt} = Ti_{total} - Ti_{super} \quad Eq.3.1$$

where Ti_{ppt}, Ti_{total}, and Ti_{super} are the masses of Ti in the collected particles, in the dissolved steel sample, and in the supernatant solution, respectively. Assuming three phases with the compositions of (I) $Nb_xMo_yTi_{1-x-y}C$, (II) $Ti_zNb_{1-z}N$, and (III) $Ti_uNb_{1-u}N$ as identified in QXRD analysis, their molar masses can be written as:

$$M_I = xA_{Nb} + yA_{Mo} + (1-x-y)A_{Ti} + A_C \qquad Eq.3.2$$

$$M_{II} = zA_{Ti} + (1-z)A_{Nb} + A_N \qquad Eq.3.3$$

$$M_{III} = uA_{Ti} + (1-u)A_{Nb} + A_N \qquad Eq.3.4$$

where M_I and A_i are the molar masses of phase I and element i, respectively. Taking m_I, m_{II} and m_{III} as the actual masses of the phases in the residue extracted with matrix dissolution method, the amount of Ti in each phase can be written as:

$$Ti_I = \frac{m_I}{M_I}(1-x-y)A_{Ti} \qquad Eq.3.5$$

$$Ti_{II} = \frac{m_{II}}{M_{II}}zA_{Ti} \qquad Eq.3.6$$

$$Ti_{III} = \frac{m_{III}}{M_{III}}uA_{Ti} \qquad Eq.3.7$$

where Ti_I, Ti_{II}, Ti_{III} are the masses of Ti in the respective phases. Since

$$Ti_{ppt} = Ti_I + Ti_{II} + Ti_{III} \quad Eq.3.8$$

substituting Equation 3.1 and Equations 3.5 to 3.7 into Equation 3.8 gives:

$$Ti_{total} - Ti_{super} = \frac{m_I}{M_I}(1-x-y)A_{Ti} + \frac{m_{II}}{M_{II}}zA_{Ti} + \frac{m_{III}}{M_{III}}uA_{Ti} \quad Eq.3.9$$

From QXRD analysis, the relative weight percentages of the phases are known. Therefore, the following ratios can be expressed

$$\frac{wt.\%_{II}}{wt.\%_{I}} = \frac{m_{II}}{m_{I}} = K_1, \qquad \frac{wt.\%_{III}}{wt.\%_{I}} = \frac{m_{III}}{m_{I}} = K_2 \qquad Eq.3.10$$

where $wt.\%_{I}$, $wt.\%_{II}$, and $wt.\%_{III}$ are relative weight percentages of the phases obtained from QXRD. Substituting Equation 3.10 into Equation 3.9 results in:

$$Ti_{total} - Ti_{super} = m_I \left\{ \frac{1}{M_I}(1-x-y)A_{Ti} + \frac{K_1}{M_{II}} z A_{Ti} + \frac{K_2}{M_{III}} u A_{Ti} \right\} \quad Eq.3.11$$

The only unknown parameter in Equation 3.11 is m_I. The values of m_{II} and m_{III} can be obtained using Equation 3.10. Then, the following equation can be used to calculate the volume fraction of the phases.

$$V_{fI} = \frac{m_I}{\frac{4M_I}{a_I^3 * N_A}} * \frac{1}{V_{Fe}} \qquad Eq.3.12$$

where V_{fI} is the volume fraction of phase I, a_I is the lattice parameter of phase I, N_A is Avogadro's number, and V_{Fe} is the volume of the dissolved steel sample.

3-10 ThermoCalc modeling

ThermoCalc V10.1 with the TCFE10 database was used to model the formation of coarse and fine TiN-rich particles during solidification and subsequent processing steps. The same version and database were used to obtain thermodynamic information on the steels. In the models, ten elements (Table 3.1) were included in the chemistry since they were the only elements provided by the supplier for the steels. In the study of coarse TiN-rich particles, the Scheil-Gulliver module was employed. The Scheil-Gulliver module is commonly used to predict the type, composition, and fraction of phases solidifying from a liquid alloy. It is based on the assumptions that no diffusion occurs in solid phases, complete homogeneity is achieved in the liquid, and thermodynamic equilibrium is held at the solidification front. However, some light elements with high diffusion rates could diffuse considerable distances in solidified phases during solidification. To consider the high diffusion rate of the light elements, a modified Scheil-Gulliver model was used in which carbon and nitrogen were indicated as fast diffusing species. In addition to the Scheil-Gulliver

module, the software provides the one-axis-equilibrium module that can be used to obtain the equilibrium composition of phases over a wide range of temperatures. The composition of fine TiN-rich particles was calculated by applying the module.

3-11 Summary

Seven as-rolled and one as-cast X70 microalloyed steels with a wide variety of Ti and N concentrations have been selected. The microstructure of the steels was analyzed using SEM. For the size and composition analysis of the coarse and fine TiN-rich particles, carbon replica samples were prepared. The size and Ti/(Ti+Nb) ratios of the coarse particles were analyzed using SEM/EDX. The size and Ti/(Ti+Nb) ratios of the fine particles were analyzed using STEM/EDX. The matrix dissolution analysis was performed to extract the particles from the steel samples. The concentration of Ti in the matrix was determined using ICP-MS analysis of the supernatant solutions. The volume fraction of the coarse and fine particles was determined with QXRD analysis of the residues obtained using the matrix dissolution method. The chemical analysis of the coarse and fine TiN-rich particles was determined using SEM/EDX, STEM/EDX, and the lattice parameters obtained from QXRD analysis. The next chapter presents and discusses the results obtained.

4 Results and discussion

The results of the characterization conducted on the microstructure, coarse TiN-rich particles, and fine TiN-rich particles in the eight studied steels are presented in this chapter. First, the type of microstructure for the as-received steels and the measured grain sizes are presented. Subsequently, data on the size, composition, and volume fraction of the coarse TiN-rich particles are provided and discussed. Then, the results of the fine TiN-rich particle characterization are presented. Finally, the coarse and fine particles in the as-cast sample are studied and discussed.

4-1 Microstructural analysis

In this section, SEM micrographs from each steel and the measured grain sizes are presented and discussed.

4-1-1 SEM microstructures

SEM micrographs of the polished and etched surfaces of the steels are shown in Figure 4.1. The microstructures are primarily composed of somewhat irregular polygonal ferrite grains. A few irregular grains are shown in the micrograph of T36-2 QL. In some cases, the steels exhibit small pearlite islands. In general, the micrographs exhibit similar features. Additional SEM microstructures of the steels are provided in Appendix F.

4-1-2 Mean linear intercept measurements (MLI)

The measured grain sizes for each steel using the MLI are shown in Figure 4.2. The values vary from 2.1 to 4 μm. The error bars indicate the standard deviation of the MLI values obtained for the lines in Figure 3.2b. The smallest grain size is observed for B60 QL and the largest is observed for 3F-565 QL. In microalloyed steels produced through TMCP, the final grain size depends on the chemistry of the steel and the TMCP parameters [32], [72], [98]. As shown in Table 3.1, B60 contains the highest nominal concentration of Mo. Introducing 0.16 wt.% Mo is known to increase the hardenability of microalloyed steels by delaying the formation of ferrite and bainite. Additionally, TMCP parameters could play a significant role in achieving a fine microstructure; however, these parameters were not provided.

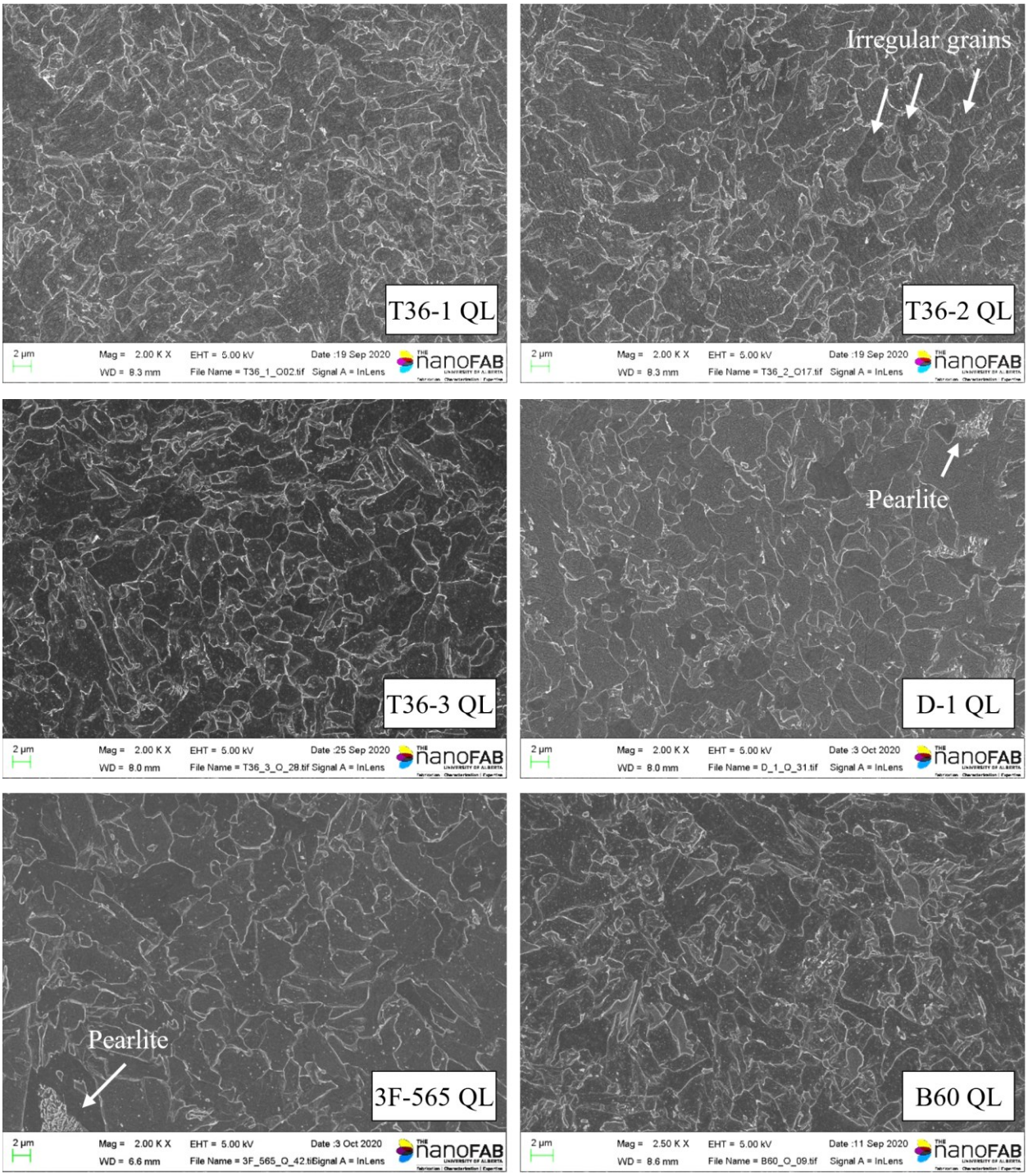

Figure 4.1– SEM SE micrographs of the studied steels (part 1 of 2).

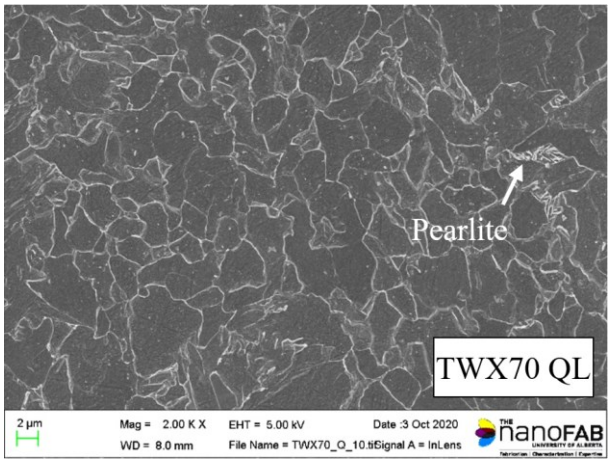

Figure 4.1– SEM SE micrographs of the studied steels (part 2 of 2).

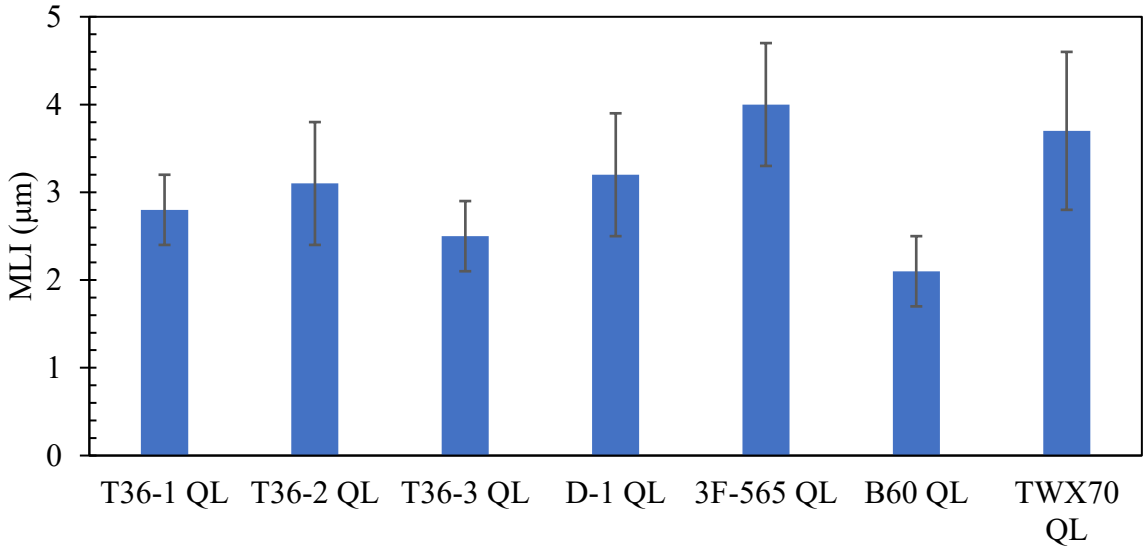

Figure 4.2– Mean linear intercept measurements for the studied steels.

4-2 Coarse TiN-rich particles

In this section, the measured size, composition, and volume fraction of the coarse TiN-rich particles are presented. The similarities and differences in these measured values are discussed.

4-2-1 Size of coarse TiN-rich particles

SEM was deemed suitable for analyzing the size and composition of coarse TiN-rich particles due to their relatively large sizes. Figure 4.3 shows the average size of coarse TiN-rich particles (extracted with the carbon replica method) plotted versus the product of the nominal composition of Ti and N in each steel. D-1 QL has the smallest average size of coarse TiN-rich particles. This steel also has the lowest nominal Ti and N concentration product (Ti·N value). Conversely, T36-

1 QL has the highest Ti·N value and exhibits the largest average size. Generally, an increase in the average size is seen as the Ti·N value increases. In addition, as the Ti·N value increases, the standard deviation increases. The larger standard deviations are a result of larger size distributions. The broader size distribution observed in T36-1 QL in comparison to D-1 QL is shown in Figure 4.4. The size distribution for T36-1 QL seems to be bimodal. A possible reason for observing bimodal distribution could be partial coarsening of the particles that had formed earlier during solidification, while those forming near the end of solidification might not find the time and opportunity to coarsen.

To report the size of the coarse TiN-rich particles, the average size was selected. The surveyed literature did not indicate any particular importance to the value of the mode or median (50% distribution) of the size distribution of coarse TiN-rich particles and reported their average sizes [1], [13], [19], [45], [47]. Since the purpose of the analysis was to investigate the effect of composition on the size of the particles, using the average size and standard deviation seemed the appropriate parameters for describing their sizes. The conclusions of this analysis are unlikely to be different if other particle size methods are used to report the differences between the size distributions.

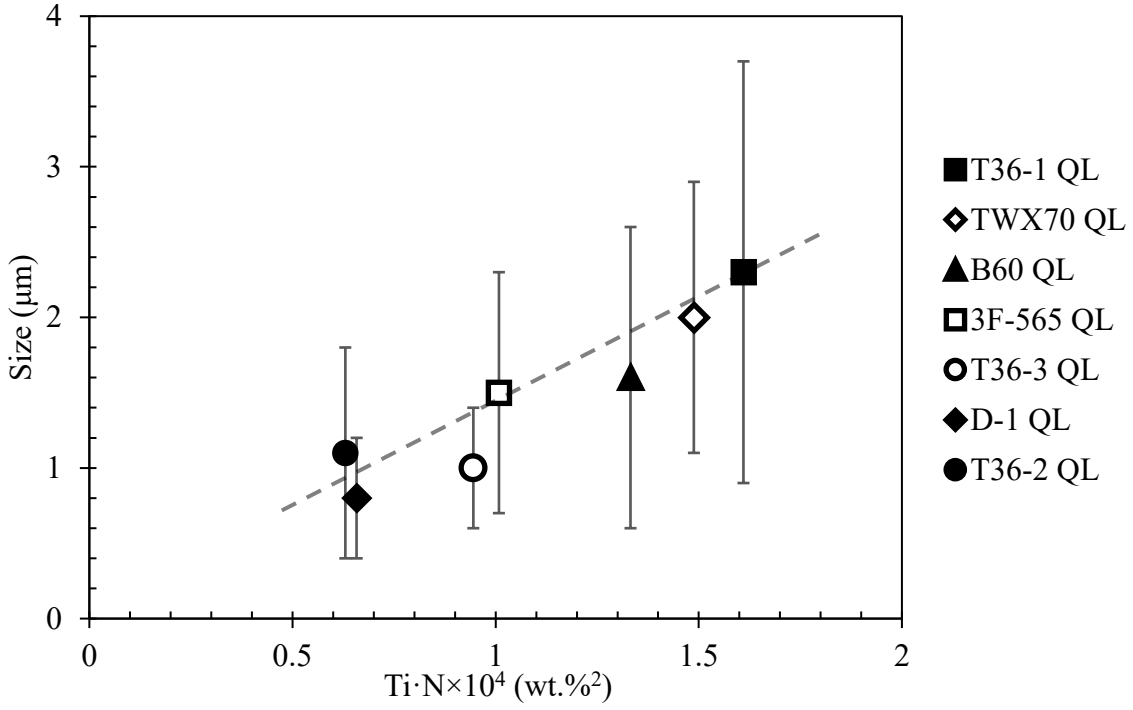

Figure 4.3– Average size of coarse TiN-rich particles as a function of the product of the nominal composition of Ti and N in each steel.

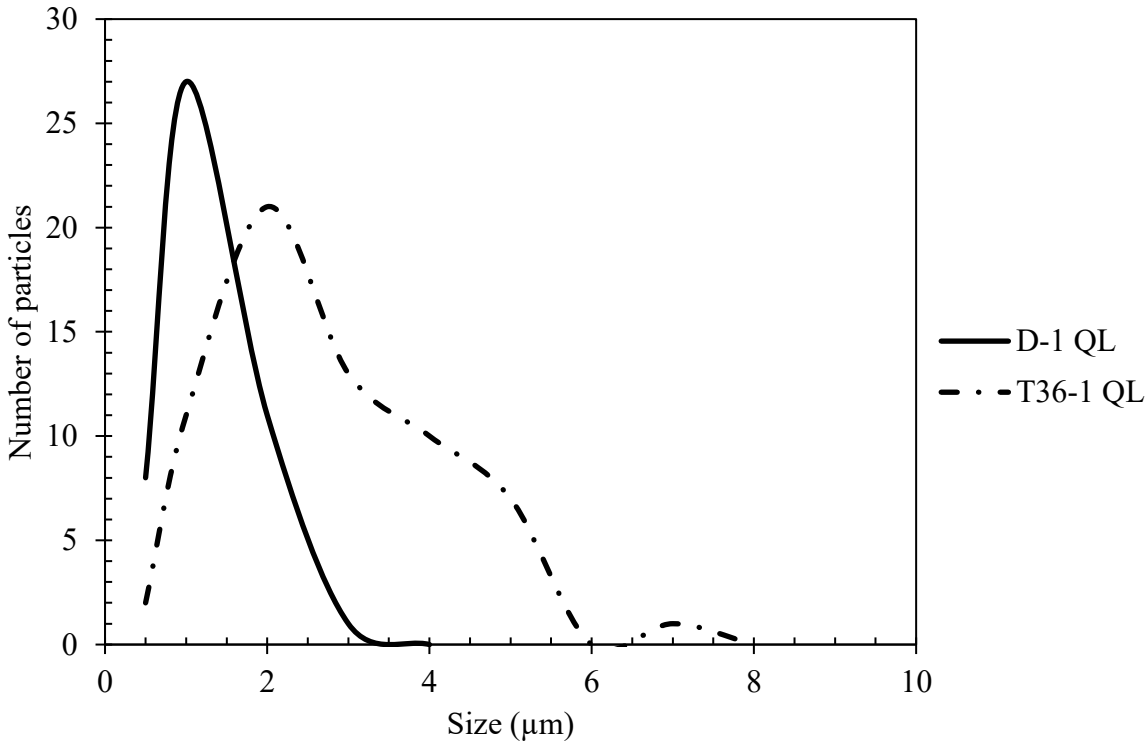

Figure 4.4– Size distribution of coarse TiN-rich particles in D-1 QL and T36-1 QL.

To demonstrate the change in the size of coarse TiN-rich particles more clearly, size measurements are also presented in a cumulative diagram in Figure 4.5. The legend is ordered so that the steel with the highest Ti·N value is at the top and the one with the lowest Ti·N value is located at the bottom. The figure shows that steels with lower Ti·N values (D-1 QL, T36-2 QL, and T36-3 QL) mainly contain particles with sizes in the range of ~0.5 to 2 μm, whereas the samples with higher Ti·N values (e.g., T36-1 QL) contain much larger particles in addition to ~0.5-μm particles, which results in a higher standard deviation for these steels. In any case, larger coarse TiN-rich particles are more frequently observed in steels with greater Ti·N values.

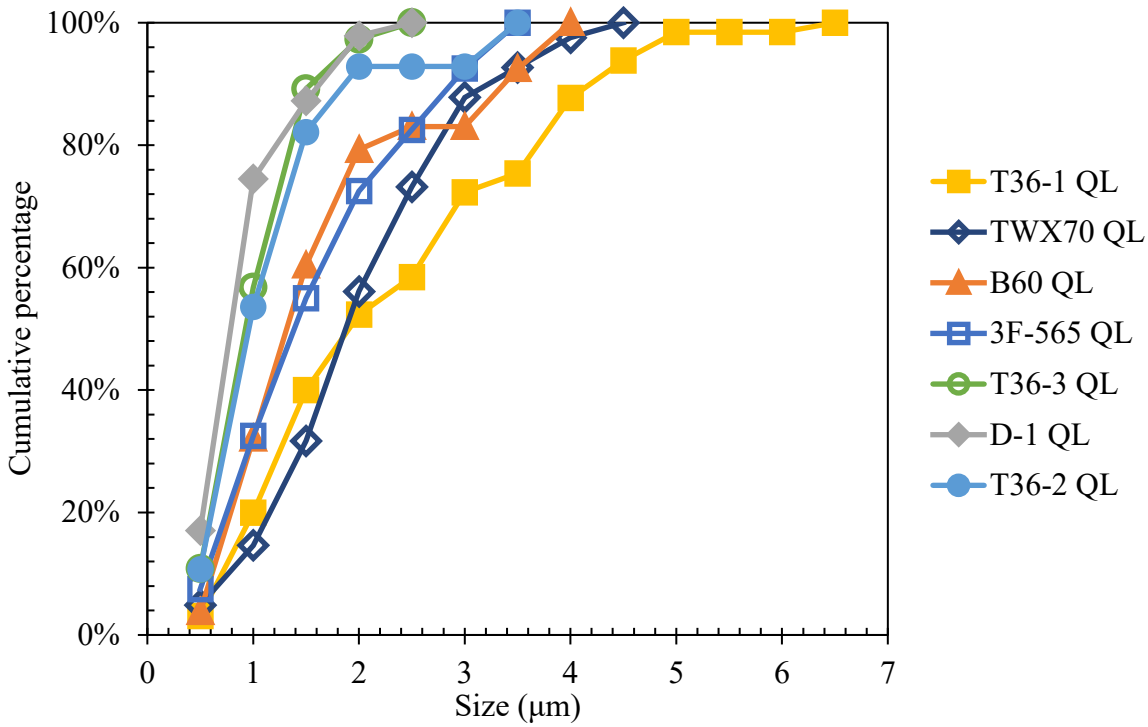

Figure 4.5– Cumulative distribution of coarse TiN-rich particles in the studied steels.

The size of coarse TiN particles is affected by the composition of steels, namely the Ti and N concentrations. The literature indicates that the size of coarse TiN particles decreases as Ti and N contents decrease [44], [47]–[49]. Coarse TiN particles are known to form in the liquid phase [99]. During solidification, segregation of alloying elements to the interdendritic regions occurs and results in a local increase in the concentration of Ti and N in the liquid. When the concentration of Ti and N solutes exceeds the solubility limit, precipitation of TiN-rich particles becomes thermodynamically feasible. The product of Ti and N is commonly used to describe the solubility limit of Ti and N in a phase.

The effect of steel composition on the onset of coarse TiN-rich particle formation during solidification was assessed using a modified Scheil-Gulliver model, where C and N were assumed to be fast diffusing species. Figure 4.6 shows the solid fraction at which the TiN-rich phase starts to form during solidification. The lowest solid fraction is 0.76, meaning that there is no sign of the TiN-rich phase at the start of solidification, indicating that at the nominal concentrations used in this study, Ti and N are initially entirely soluble in the melt. However, as the solidification progresses, segregation of alloying elements to interdendritic zones increases the concentration of Ti and N in the liquid beyond the solubility limit, leading to the formation of the TiN-rich phase

before the solidification is complete. The figure shows the solid fraction for initiation of TiN formation is inversely proportional to the Ti·N value; i.e., when larger nominal concentrations of Ti and N exist in the steel (higher Ti·N values), the liquid in the interdendritic region becomes saturated more rapidly. As such, this leads to earlier nucleation of coarse TiN-rich particles in the liquid and provides more time for particle growth, resulting in larger particle.

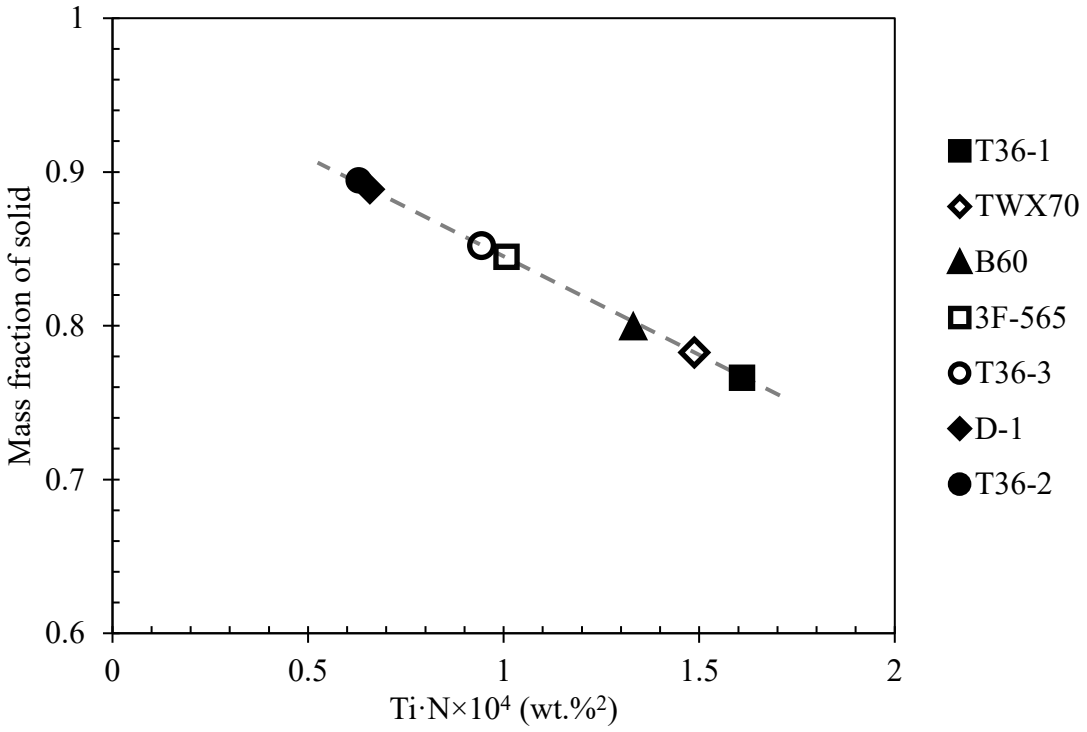

Figure 4.6– Effect of Ti·N values on mass fraction of solid at which TiN-rich particles start to form in modified Scheil-Gulliver solidification model.

4-2-2 Composition of coarse TiN-rich particles

The composition of the coarse TiN-rich particles was measured using SEM/EDX analysis of particles extracted with carbon replicas (Figure 3.3). Table 4.1 shows the Ti/(Ti+Nb) ratio of the particles, which indicates that the particles are not pure TiN. The presence of Nb in coarse TiN-rich particles has also been reported by [92], [100], [101]. The formation of compounds with complex chemical compositions is a result of the same crystal structures and similar lattice parameters for Nb and Ti carbonitrides [4]. The table also shows the nominal Ti/(Ti+Nb) ratios. The ratios are less than 0.5, indicating a higher Nb nominal concentration. However, the Ti/(Ti+Nb) ratios for the coarse TiN-rich particles are close to 1 due to the higher concentration

of Ti in the particles resulting from the significantly lower solubility of TiN than that of NbN or NbC in the liquid. The composition of the particles showed no dependence on the thickness of the skelp (Table 3.1).

Table 4.1– Measured Ti/(Ti+Nb) ratio for coarse TiN-rich particles using SEM/EDX and nominal composition of the studied steels

Sample	Measured Ti/(Ti+Nb) (atomic fraction)		Nominal composition (wt.%)			Nominal Ti/(Ti+Nb) (atomic fraction)
	Average	SD	Nb	Ti	N	
T36-1 QL	0.91	0.03	0.075	0.023	0.007	0.37
T36-2 QL	0.85	0.06	0.078	0.015	0.0042	0.27
T36-3 QL	0.83	0.04	0.076	0.015	0.0063	0.28
D-1 QL	0.92	0.04	0.036	0.014	0.0047	0.43
3F-565 QL	0.9	0.05	0.075	0.014	0.0072	0.27
B60 QL	0.81	0.09	0.089	0.018	0.0074	0.28
TWX70 QL	0.9	0.05	0.067	0.016	0.0093	0.32

* SD: Standard deviation

As Table 4.1 shows, the Ti/(Ti+Nb) ratio varies from 0.81 to 0.92. The highest and lowest ratios occur for B60 QL and D-1 QL, respectively. These steels also contain the highest and lowest nominal concentrations of Nb. However, the composition of coarse TiN-rich in D-1 QL is not significantly different from those in the other steels even though its nominal Nb concentration is less than half the value in the other steels. One possible reason could be that the composition of the liquid changes as solidification progresses and the amount of Nb in coarse TiN-rich particles may be influenced by the liquid composition while TiN-rich particles are forming during solidification. The Ti/(Ti+Nb) ratio in the liquid depends on the nominal Nb concentration as well as the solid fraction at which TiN-rich particles start to form during solidification. Since Nb has a higher segregation ratio (the ratio of the concentration in the liquid to the nominal concentration) than Ti [102], as solidification progresses the liquid becomes richer in Nb (in comparison to Ti) [103]. By the time the TiN-rich particles are beginning to form, the Ti/(Ti+Nb) ratio in the liquid

has decreased noticeably. When TiN-rich particles form near the end of solidification, the concentration of Nb in the liquid will be higher and, as a result, the concentration of Nb in TiN-rich particles is higher.

The effect can be seen when comparing T36-1, T36-2, and D-1 steels, which have similar nominal Ti/N ratios, but their nominal Ti and/or Nb concentrations are different. Figure 4.7 shows the composition of the coarse TiN-rich particles obtained using SEM/EDX as a function of the Ti/(Ti+Nb) ratio in the liquid just before the TiN-rich phase starts to form in the modified Scheil-Gulliver model for T36-1, T36-2, and D-1. D-1 and T36-2 have similar nominal concentrations of Ti and N (Table 3.1), while D-1 contains less nominal Nb than T36-2. The lower Ti/(Ti+Nb) ratio in the particles from T36-2 QL coincides with the lower Ti/(Ti+Nb) ratio in its liquid. T36-1 has larger nominal amounts of Ti and Nb than D-1, but their Ti/(Ti+Nb) ratios in particles obtained using SEM/EDX are very close. As the figure shows, their Ti/(Ti+Nb) ratios in the liquid are also similar. Although D-1 contains less nominal Nb, the lower Ti·N value in D-1 results in the formation of coarse TiN-rich particles later in the solidification process (Figure 4.6), leading to a similar Ti/(Ti+Nb) ratio in the liquid when the coarse TiN-rich particles are forming.

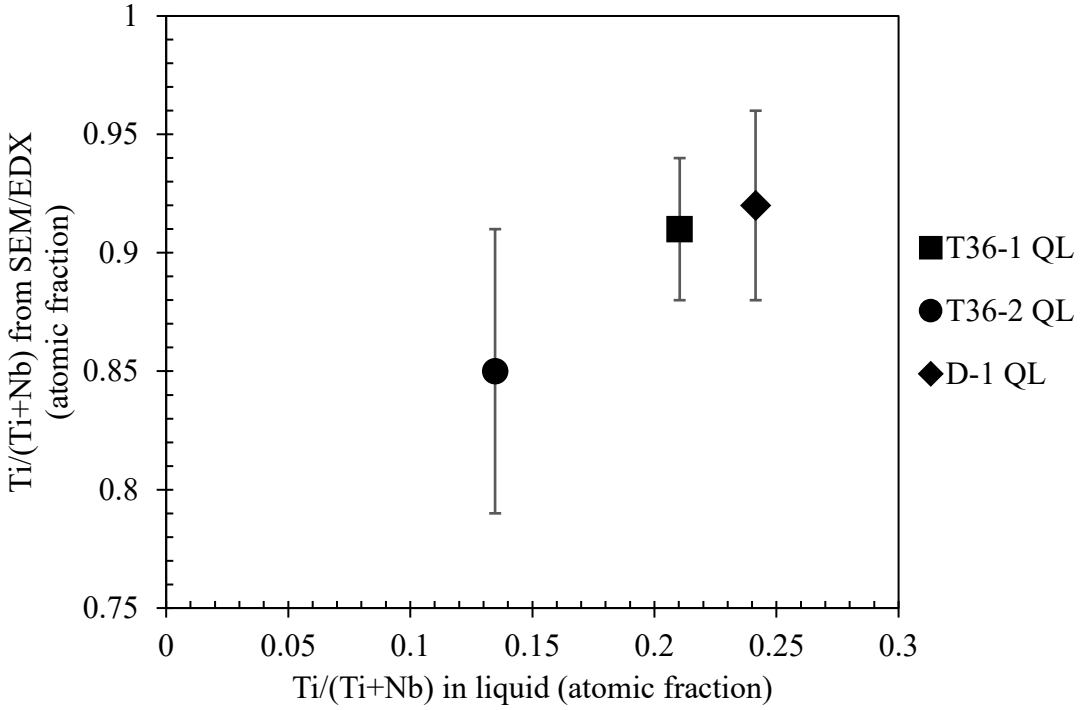

Figure 4.7– Ti/(Ti+Nb) ratio of coarse TiN-rich particles measured via SEM/EDX at QL versus Ti/(Ti+Nb) ratio in the liquid just before TiN-rich particles begin to form, based on the modified Scheil-Gulliver model.

Figure 4.8 compares Ti/(Ti+Nb) ratios obtained using SEM/EDX with those obtained through the modified Scheil-Gulliver model. The modified Scheil-Gulliver model for the entire solidification course was used since it was assumed the dendritic structure of the solidified portion entraps the liquid between the secondary dendrites and impedes its mixing with the bulk of the liquid. In the analysis, all elements presented in Table 3.1 were included. SEM/EDX results show a higher concentration of Nb in the particles than that predicted by the model. No relationship can be drawn between the measured and calculated Ti/(Ti+Nb) ratios. The thermodynamic potentials from ThermoCalc used to model the interaction between Nb, Ti, C, and N in the TiN-rich phase may not be representative of reality. The software predictions are based on the chemical potential of elements and the thermodynamic functions stored in the software database, which have been obtained by adjusting a series of model coefficients to reproduce the existing experimental data in the literature (such as phase diagrams). It appears that the coefficients are not optimized well to predict the amount of Nb in TiN-rich particles properly. Also, the model assumes a planar interface, while the dendritic interface could affect the chemical potential of the elements in the solid (Gibbs-Thomson effect), altering the composition of the solid and the liquid.

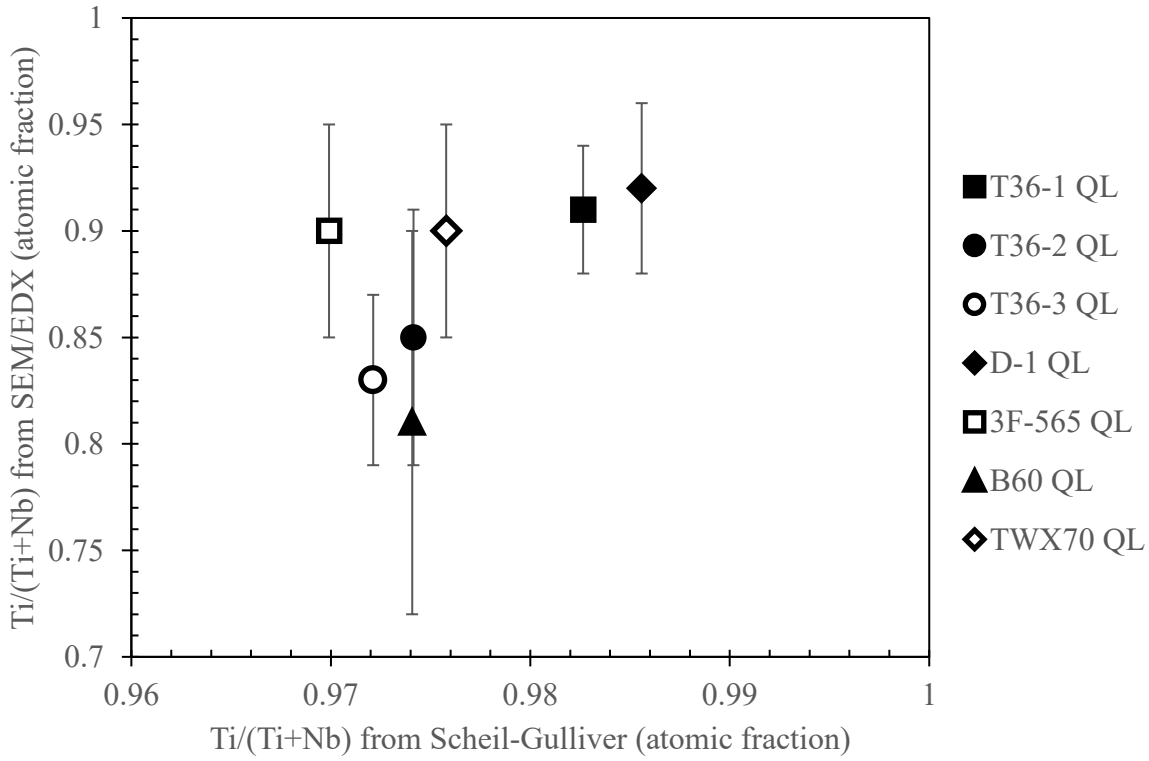

Figure 4.8– Ti/(Ti+Nb) ratio of coarse TiN-rich particles measured via SEM/EDX at QL versus Ti/(Ti+Nb) ratio TiN-rich phases modelled using the modified Scheil-Gulliver model.

4-2-3 Volume fraction of coarse TiN-rich particles

The volume fractions of the coarse TiN-rich particles were measured using QXRD analysis. Table 4.2 shows the mass balance of Ti in the studied steels, the supernatant solutions (ICP analysis), and the particles collected using the matrix dissolution method (QXRD analysis). A good agreement exists when comparing the nominal concentrations of Ti with the measured values using ICP and QXRD.

Table 4.2– Mass balance of Ti in steels, supernatant solutions (ICP results), and particles (QXRD analysis)

Sample	T36-1 QL	T36-2 QL	T36-3 QL	D-1 QL	3F-565 QL	B60 QL	TWX70 QL
Nominal (wt.%)	0.023	0.015	0.015	0.014	0.014	0.018	0.016
ICP (10^{-4} wt.%)	8.4	5.3	3.2	3.7	2.6	2.1	2.6
QXRD (wt.%)	0.022	0.014	0.015	0.014	0.014	0.018	0.016

Figure 4.9 shows the volume fraction of coarse TiN-rich particles obtained using QXRD analysis as a function of the Ti·N values. The figure does not include D-1 QL. Attempts to include a phase representing the coarse TiN-rich particles in the QXRD analysis of D-1 QL were not successful. This is an indication that the volume fraction of coarse TiN-rich particles in the D-1 QL sample is small. Generally, an increase in the volume fraction of the particles occurs as the Ti·N value increases. A similar observation has been reported by Shen et al. [13]. In their study, the volume fraction of coarse TiN-rich particles in several medium-carbon Mn-B steels was measured by optical microscopy of polished specimens. Figure 4.9 also shows the data from [13], which were obtained using an optical microscope. The results are comparable. However, there is a deviation at the lower Ti·N values. Optical microscopes have relatively low resolutions, and the size of the coarse TiN-rich particles becomes smaller at the lower Ti·N values, resulting in an underestimation of the volume fraction of the particles.

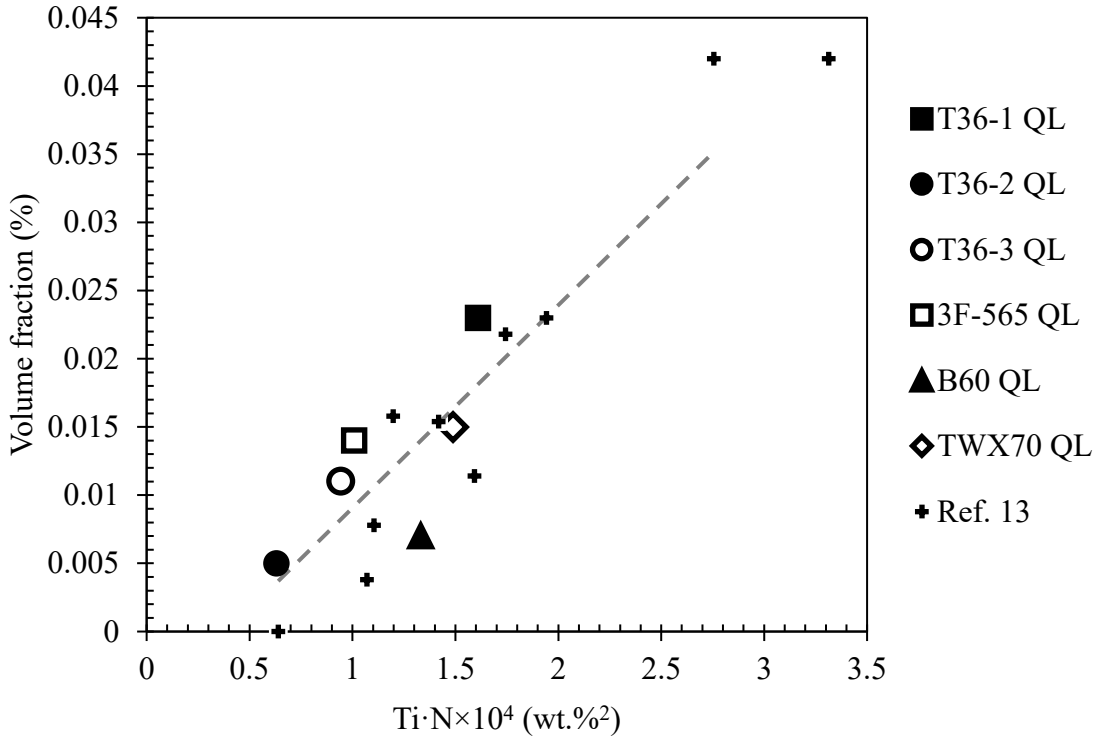

Figure 4.9– Volume fraction of coarse TiN-rich particles, measured using QXRD, as a function of Ti·N value.

An increase in the Ti·N value enhances the potential for the formation of coarse TiN-rich particles during casting. A steel with a higher Ti·N value experiences greater supersaturation at a given temperature and, consequently, the driving force for precipitation of the TiN-rich phase will be greater. The solubility limit of Ti and N in the liquid depends on temperature. When the solubility product of Ti and N in the liquid exceeds this limit at any temperature, it is expected, based on thermodynamic considerations, that the Ti-N rich phase will begin to form. The approximate equilibrium amount of TiN-rich phase precipitating during solidification can be shown using Figure 4.10. The figure shows the nominal Ti and N concentrations for the studied steels. The dashed lines represent the solubility limits of TiN in the liquid and austenite at the average liquidus and solidus temperatures, respectively. The liquidus and solidus temperatures were obtained using the one axis equilibrium module of ThermoCalc. The approximate equilibrium amount of TiN-rich phase precipitating during solidification can be demonstrated by drawing a line parallel to the stoichiometric line that connects the nominal composition to the line representing the solubility limit in austenite at solidus temperature. This practice shows that as the content of Ti and N in the steels increases, the position from the austenite solubility limit line also increases. Therefore, a

larger Ti·N value could result in the formation of a greater amount (and volume) of TiN-rich particles during solidification.

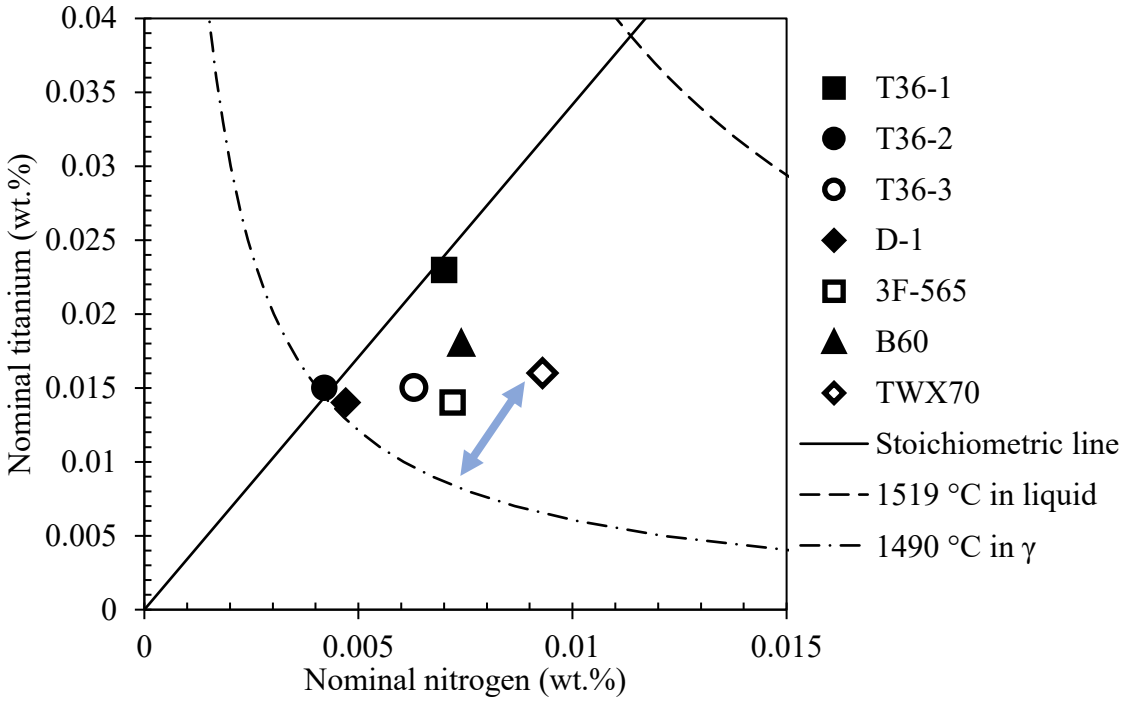

Figure 4.10– Solubility limits for titanium and nitrogen in austenite [104] and the liquid [105], respectively, at the average liquidus and solidus temperatures and the chemistry of the steels.

The amount of TiN-rich particles precipitated during solidification will be different from the equilibrium quantities. During solidification, the first solidified phase usually contains a lower concentration of alloying elements than the nominal concentration since the partition coefficient values are usually less than one. The negligible diffusion rates in the solid intensify the segregation of alloying elements at the solidification front. This results in an ever-increasing concentration of Ti and N in liquid and lower concentrations of Ti and N in solid than that expected for equilibrium solidification. Consequently, the final microstructure of the as-cast steel could contain more coarse TiN-rich particles than equilibrium calculations would predict. Indeed, the calculations performed for 3F-565 using ThermoCalc showed the volume fraction of the TiN-rich phase forming during equilibrium solidification is half that forming in the modified Scheil-Gulliver model.

A comparison between the volume fractions of coarse TiN-rich particles measured using QXRD for the quarterline samples and those obtained with the modified Scheil-Gulliver model is shown in Figure 4.11. The results seem to be comparable, except for B60 and T36-2. The calculated

volume fractions for B60 and T36-2 are larger than the measured values. In addition to nominal Ti and N concentrations, casting superheat and cooling intensity can influence the formation of coarse TiN-rich particles during casting [106]. However, such parameters were not provided. ThermoCalc does not consider the supersaturation required for the formation of the TiN-rich phase. The necessary level of supersaturation of Ti and N in the liquid becomes important when the Ti·N values are low enough that the saturation of the interdendritic liquid occurs near the end of solidification. Additionally, ThermoCalc carries out modeling using CALPHAD methodology. Although the software allows including several alloying elements in the analysis, its thermodynamic databases for Ti consist of some of those alloying elements, and only a few of them are based on Fe-rich phases. The full composition of the steels was not provided and it appears there is a lack of studies on the effect of those elements on TiN formation. More investigation is required to establish an understanding of the observed deviations.

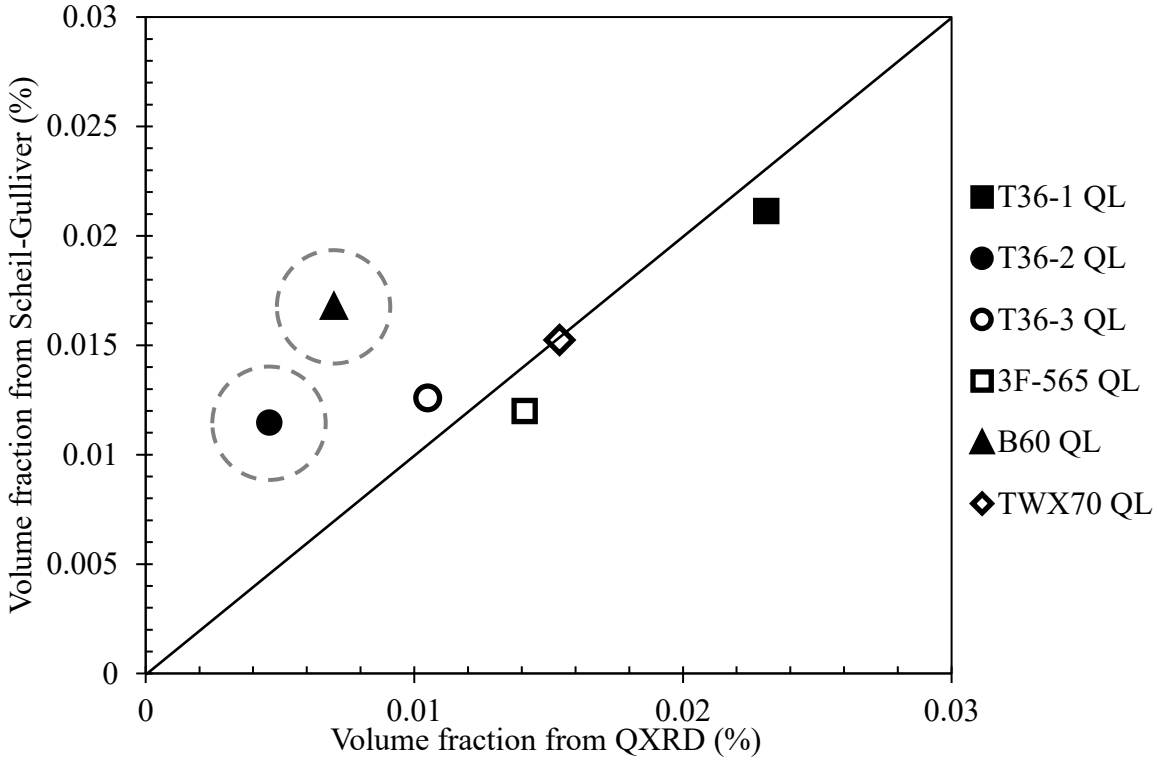

Figure 4.11– Volume fraction of coarse TiN-rich particles measured using QXRD analysis of QL samples versus those obtained using the modified Scheil-Gulliver solidification model.

The amount of Ti and N tied up in the coarse TiN-rich particles can be calculated using their volume fractions and compositions. Considering coarse TiN-rich particles with a composition of

$(Ti_xNb_{1-x})N$ and volume fraction of V_f (%), the amount of Ti in coarse TiN-rich particles can be calculated using the following Equation:

$$Ti\ (wt.\%) = \frac{V_f}{\rho_{Fe}} \frac{1}{{a_P}^3} 4x \frac{1}{N_A} A_{Ti} \qquad Eq.4.1$$

where ρ_{Fe} is the density of iron, a_p is the lattice parameter of the particles (obtained from QXRD analysis), N_A is Avogadro's number, and A_{Ti} is the molar mass of Ti. A similar equation can be used to determine the amount of N in the particles.

Figure 4.12 and Figure 4.13 show a comparison between the amount of Ti and N tied up in the coarse TiN-rich particles measured using QXRD for the quarterline samples and those obtained with the modified Scheil-Gulliver model. The results are similar to those observed in Figure 4.11 since the coarse TiN-rich particles are mainly composed of Ti and N.

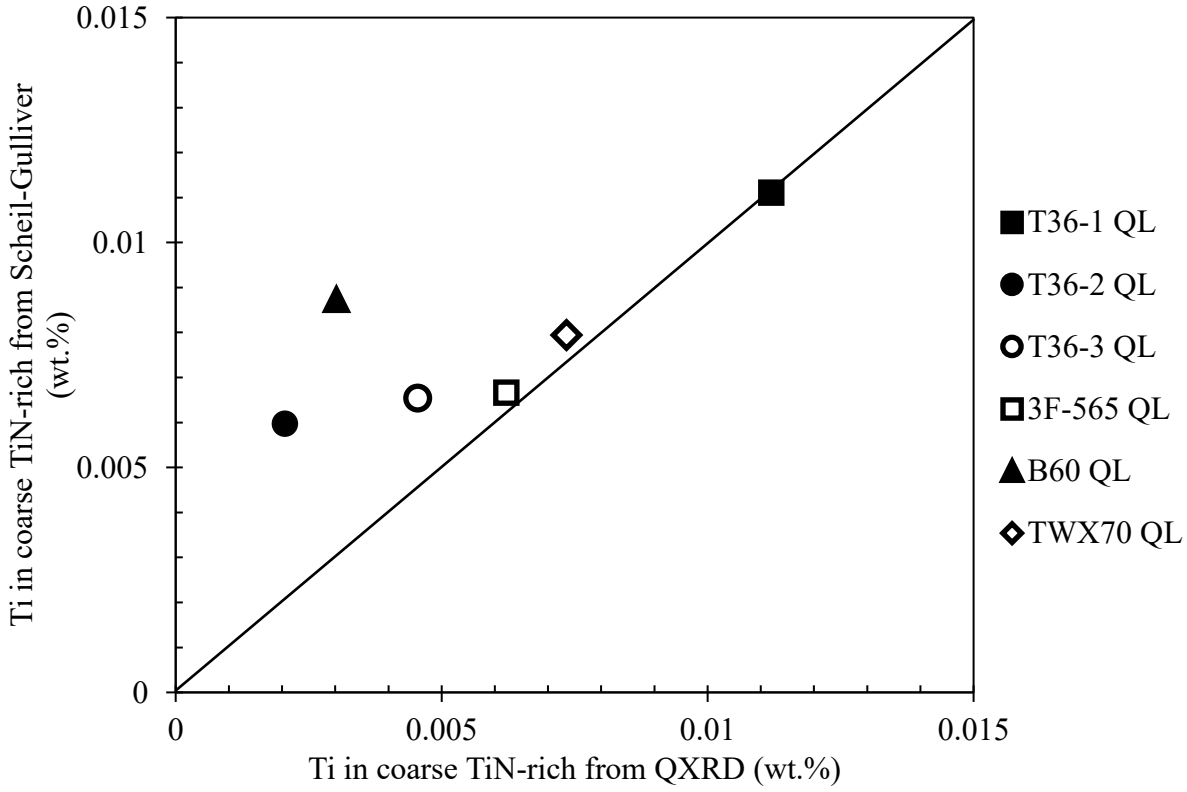

Figure 4.12– The amount of Ti in coarse TiN-rich particles measured using QXRD analysis of quarterline samples versus those obtained using the modified Scheil-Gulliver solidification model.

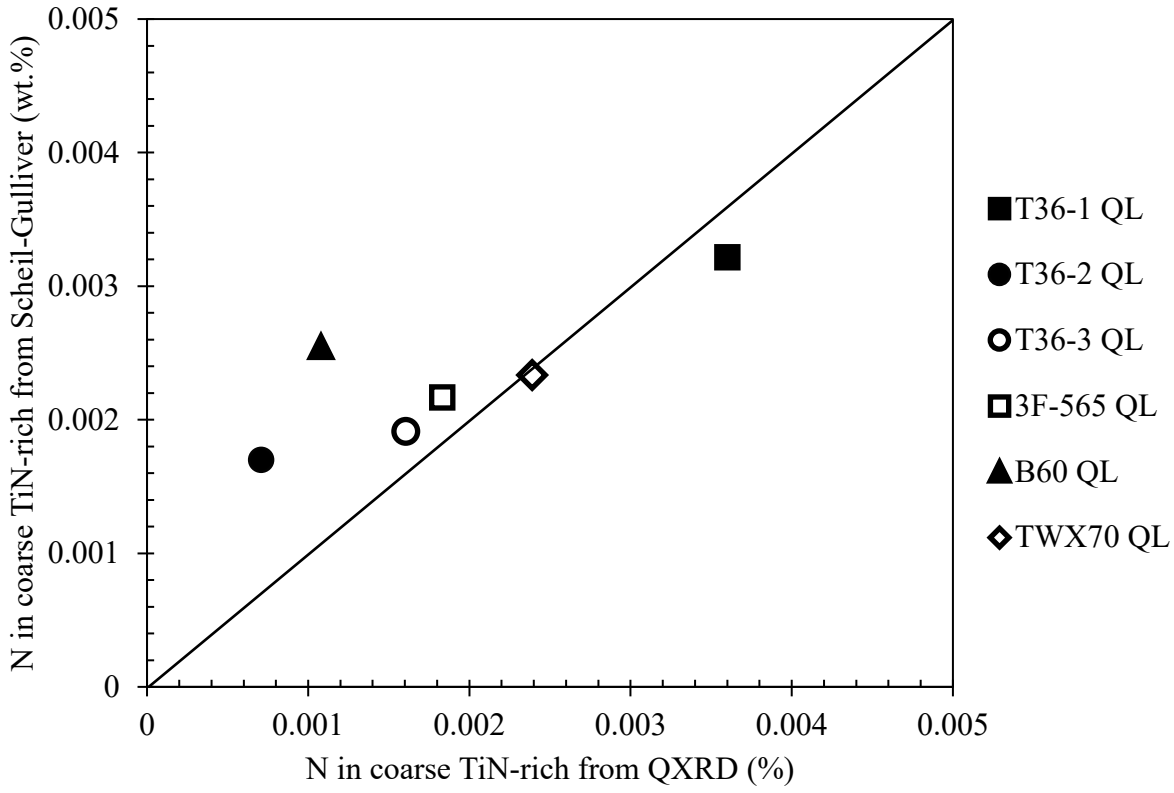

Figure 4.13– The amount of N in coarse TiN-rich particles measured using QXRD analysis of quarterline samples versus those obtained using the modified Scheil-Gulliver solidification model.

Table 4.3 shows the percentage of the nominal Ti tied up in the coarse TiN-rich particles for the studied steels. Over 40% of Ti added to T36-1, 3F-565, and TWX70 were ended up as coarse particles, suggesting a revision of alloy design toward a lower concentration of Ti or N can be beneficial. The table does not include D-1 QL. Attempts to include a phase representing the coarse TiN-rich particles in the QXRD analysis of D-1 QL were not successful.

Table 4.3– Percentage of nominal Ti in coarse TiN-rich particles

Sample	T36-1 QL	T36-2 QL	T36-3 QL	3F-565 QL	B60 QL	TWX70 QL
Ti in coarse TiN-rich particles (%)	49	14	30	47	17	46

4-2-4 Comparison between quarterline and centerline samples

The average size, composition, and volume fraction of the coarse TiN-rich particles at the quarterline and centerline locations of four of the studied steels are presented in Figure 4.14 to Figure 4.16, respectively. Since the incorporation of a coarse TiN-rich phase to the QXRD analysis of D-1 QL was not possible, the volume fraction information for D-1 QL and CL are not presented. Generally, the particle sizes are similar, and they show similar volume fractions and concentrations of Ti and Nb. The average size of the particles in D-1 is slightly larger at the centerline. Regarding the composition, the particles from T36-3 CL were slightly more enriched in Nb than the ones from T36-3 QL.

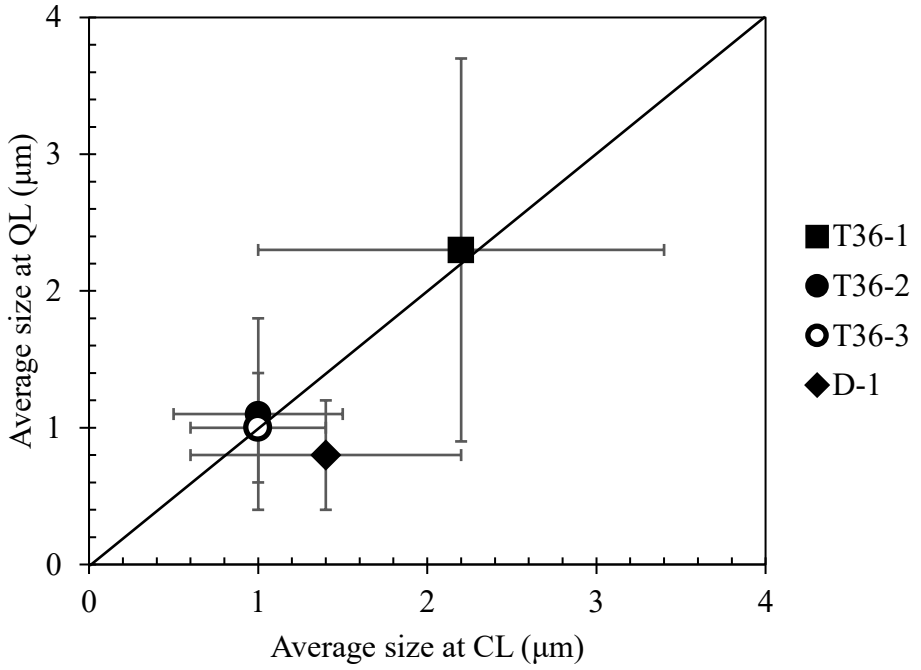

Figure 4.14– Average size of coarse TiN-rich particles at QL and CL, measured using SEM.

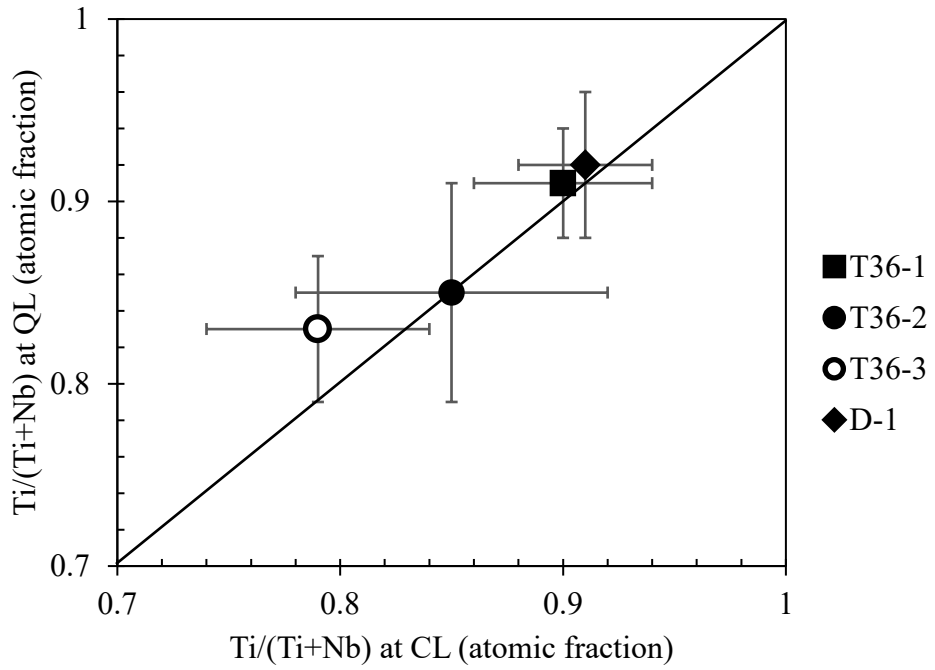

Figure 4.15– Ti/(Ti+Nb) ratio of coarse TiN-rich particles at QL and CL, measured using SEM/EDX.

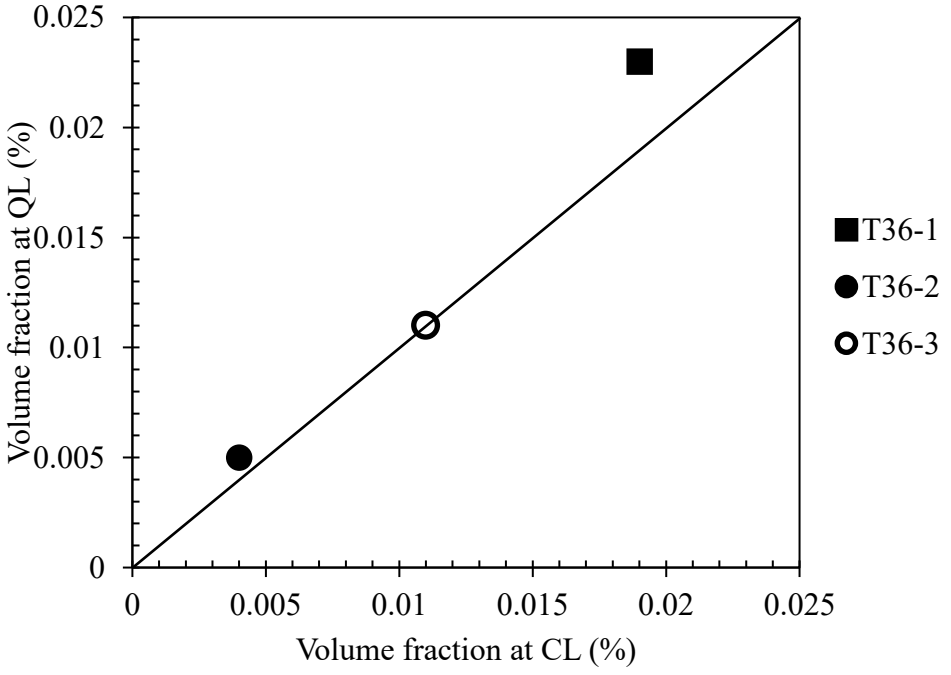

Figure 4.16– Volume fraction of coarse TiN-rich particles at QL and CL, measured using QXRD.

The size, composition, and volume fraction of particles at centerline locations might be expected to be different from those located away from the centerline. As solidification progresses during slab casting, the combination of microsegregation at the tip of primary dendrites and transport phenomena in the melt leads to the occurrence of macrosegregation near the centerline location [48]. Macrosegregation to the centerline of the slab enriches the region with alloying elements. Lower cooling rates and higher alloying concentrations are expected to result in the formation of larger secondary particles [44], [47]–[49], [107], [108]. Depending on the partition coefficient values of the alloying elements, the relative concentration of the alloying elements at the centerline could differ from those at the quarterline, resulting in possible changes in the composition of the particles as well. Schneider et al. [48] studied the segregation of Ti in steel with the composition of 0.04 C-0.036 Nb-0.01 Ti-0.0028 N (all in wt.%). Their observations did not show any significant segregation of Ti in EMPA analysis. However, using a high-resolution EMPA (0.5 μm spot size), they qualitatively reported a larger number of coarse TiN particles in macrosegregation zones than in other regions. However, such behavior was not observed in this study.

The lack of a significant difference in the characteristics of the coarse TiN-rich particles extracted from the quarterline and centerline locations may have resulted from the soft reduction during casting. In a soft reduction process, the slab undergoes limited compressive deformation exerted by a series of rolls on the solidification end of the strand, reducing segregation levels [109], [110]. ICP analysis conducted on the supernatant solutions provided the concentrations of additional alloying elements (such as Si, Cr, Mn) in the quarterline and centerline samples. The results for T36-1 QL and T36-1 CL are shown in Figure 4.17. Three ICP analyses were conducted on the solution obtained from T36-1 CL and one ICP analysis was conducted on the solution obtained from T36-1 QL. The concentration of Mn in one of the three analyses was significantly lower than expected and caused its standard deviation to increase, possibly due to an inaccurate calibration for this element at the time. Figure 4.18 shows the same results when the inaccurate data point for Mn is not included. The concentration of alloying elements in the centerline and quarterline are similar, suggesting that the concentration of Ti could be similar in both the quarterline and centerline samples as well. The ICP data for other samples are presented in Appendix G. Additionally, it is possible that the metallurgical centerline was not located exactly at the geometrical centerline of the slab [111] from which the centerline samples were prepared.

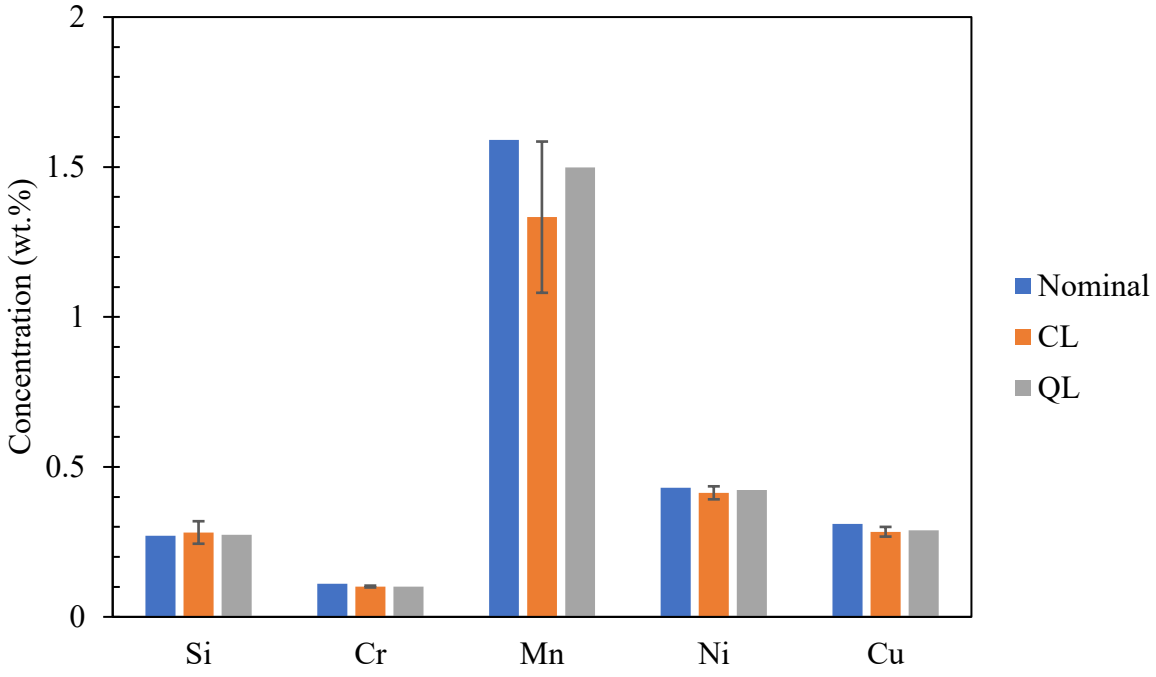

Figure 4.17– Concentration of alloying elements in supernatant solutions of T36-1 QL and T36-1 CL.

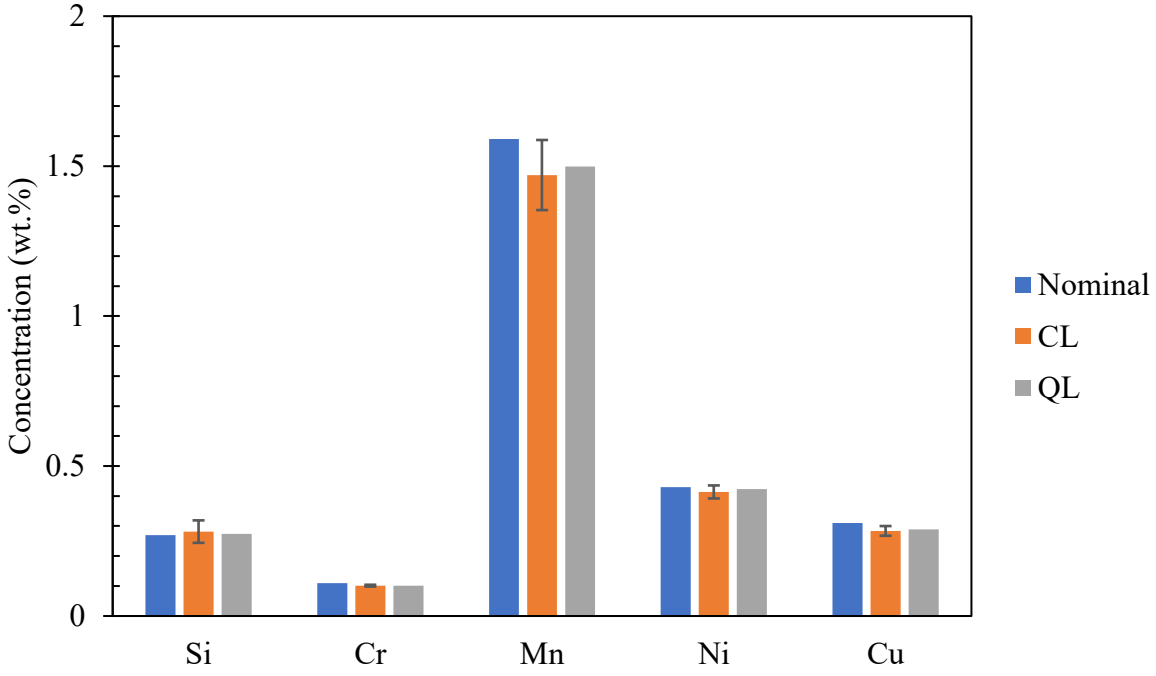

Figure 4.18– Concentration of alloying elements in supernatant solutions of T36-1 QL and T36-1 CL with a removed data point for Mn from the CL sample.

4-2-5 Summary

Based on the size and composition of coarse TiN-rich particles, it appears they are formed in the liquid. Therefore, the segregation of alloying elements during solidification can significantly affect their characteristics. Since Ti in the presence of N has limited solubility in the liquid, the product of the nominal concentrations of Ti and N plays an essential role in the formation of the particles. The size and volume fraction of the particles increase as the product of the Ti and N nominal concentrations increases. Also, SEM/EDX analysis of the particles showed that they are not pure TiN, but contain some Nb. The size, composition, and volume fraction of coarse TiN-rich particles do not show significant differences at the quarterline and centerline locations. The soft reduction process performed on the samples may have reduced the expected compositional differences between quarterline and centerline samples. Also, the metallurgical centerline may not have been located at the geometrical centerline from which centerline samples were prepared.

4-3 Fine TiN-rich particles

This section presents the measured size, composition, and volume fraction of the fine TiN-rich particles. The similarities and differences in the measured values are discussed.

4-3-1 Size of fine TiN-rich particles

Figure 4.19 shows the average size of fine TiN-rich particles as a function of the product of the adjusted Ti and N concentrations in the studied steels. The adjusted concentrations were obtained by subtracting the amount of Ti and N in coarse TiN-rich particles (Equation 4.1) from the nominal concentrations. Apart from D-1 QL, as the adjusted Ti·N values increase, an asymptotic decrease in the average size is observed.

The concentration of Ti and N in the steels could affect the size of fine TiN-rich particles. Larger adjusted Ti·N values result in a larger driving force for nucleation of fine TiN-rich particles. The nucleation rate can be defined by Equation 4.2 [112]:

$$\frac{dN}{dt} = N_0 Z \beta^* exp\left(-\frac{\Delta G}{kT}\right)\left(1 - exp\left(-\frac{t}{\tau}\right)\right) \qquad Eq.4.2$$

where N_0 is the number of available nucleation sites per volume, Z is the Zeldovich factor, β* is the condensation rate, ΔG is the nucleation barrier energy, k is the Boltzmann constant, and τ is

the incubation time. Assuming TiN as the nuclei composition [62], based on a similar equation used for NbC [113], the relationship between the energy barrier for nucleation (ΔG) and the product of Ti and N concentrations at a given temperature (T) can be expressed as:

$$\Delta G = \frac{16}{3}\pi \frac{{V_{TiN}}^2 \gamma^3}{\left(kT \ln\left(\frac{X_N X_{Ti}}{K_s}\right)\right)^2} \qquad Eq.\ 4.3$$

where X_i is the atomic concentration of element i, K_s is the solubility limit of TiN at temperature T, V_{TiN} is the atomic volume of TiN, and γ is the interfacial energy between TiN and matrix. Assuming that the other parameters (such as γ, N_0, Z, β*, and K_s) are similar for the steels, an increase in adjusted Ti·N values could lead to a higher nucleation rate and finer TiN-rich particles. Equation 4.4 [73] shows the relationship between the critical radius of the nuclei and adjusted Ti·N values at 1250 °C. An increase in the adjusted Ti·N value results in a similar decrease in the critical radius of the nuclei (Figure 4.20).

$$R^* = \frac{2\gamma V_{TiN}}{KT \ln\left(\frac{X_N X_{Ti}}{K_s}\right)} \qquad Eq.\ 4.4$$

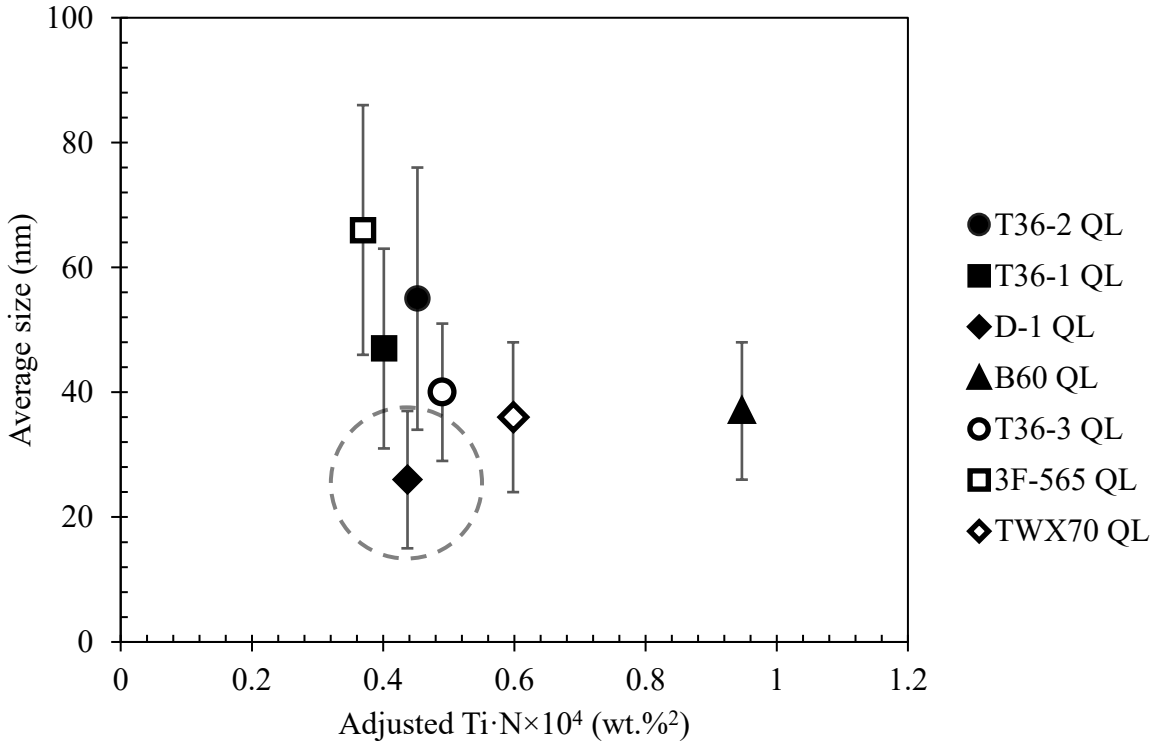

Figure 4.19– Average size of fine TiN-rich particles as a function of adjusted Ti·N values.

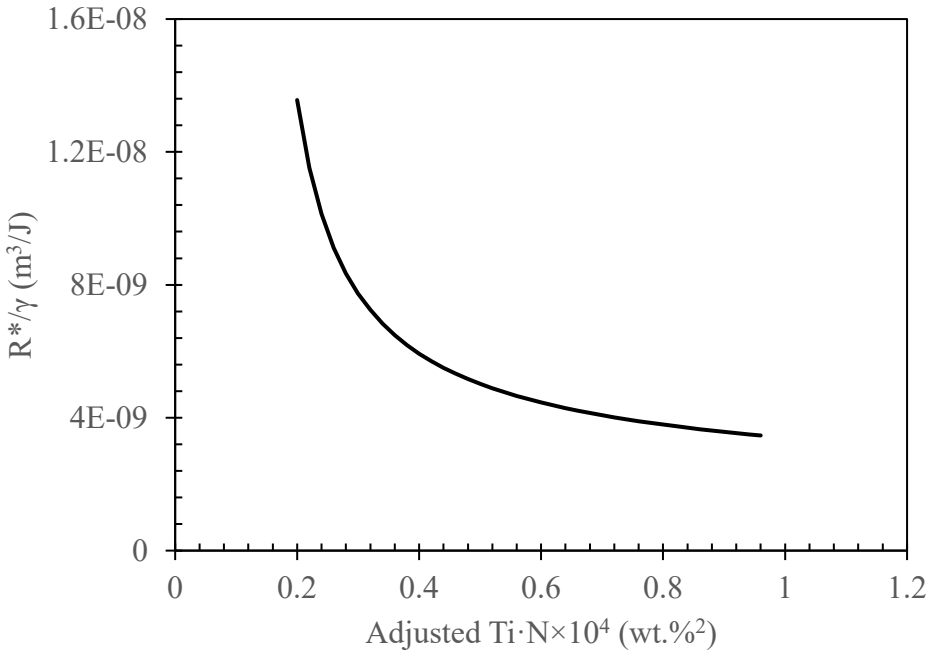

Figure 4.20– Critical radius of nuclei (R*) as a function of the product of the adjusted Ti and N concentrations.

As seen in Figure 4.19, D-1 QL had the smallest average size of fine TiN-rich particles. One possible reason is its lower nominal Nb concentration. The presence of nitride forming elements in microalloyed steels has been identified as a factor influencing the coarsening rate of TiN particles [114]. Loberg et al. investigated the effect of nitride forming elements, such as Al and V, on the stability of TiN and reported that the presence of nitride forming elements decreases the stability of TiN and increases its coarsening rate. It was suggested the presence of strong nitride formers in the matrix reduces the available N for Ti by pairing up with N atoms, which in turn reduces the stability of TiN particles. Additionally, there is a possibility that the reheating condition for D-1 was different from that for the other steels. It has been reported that increasing the reheating temperature from 1150 to 1200 °C increases the average size of fine TiN-rich particles from 20 to 40 nm in a steel containing 0.066 C-1.32 Mn-0.014 Nb-0.017 Ti-0.0063 N (all in wt.%) [29].

It seems Figure 4.19 suggests that the size of fine TiN-rich particles cannot be smaller than ~30 nm. However, several studies have reported that fine TiN-rich particles as small as 10 nm have been detected in microalloyed steels [10], [89], [99]. The size of the particles is a function of the

nucleation and growth kinetics which in turn is affected by the composition of the steel and processing parameters. A lower concentration of Nb and lower reheating temperature could decrease the size of the particles [10], [115].

The average size of fine TiN-rich particles was also measured using QXRD analysis. The results are shown in Figure 4.21. There is a reasonable agreement between the QXRD and STEM analysis results.

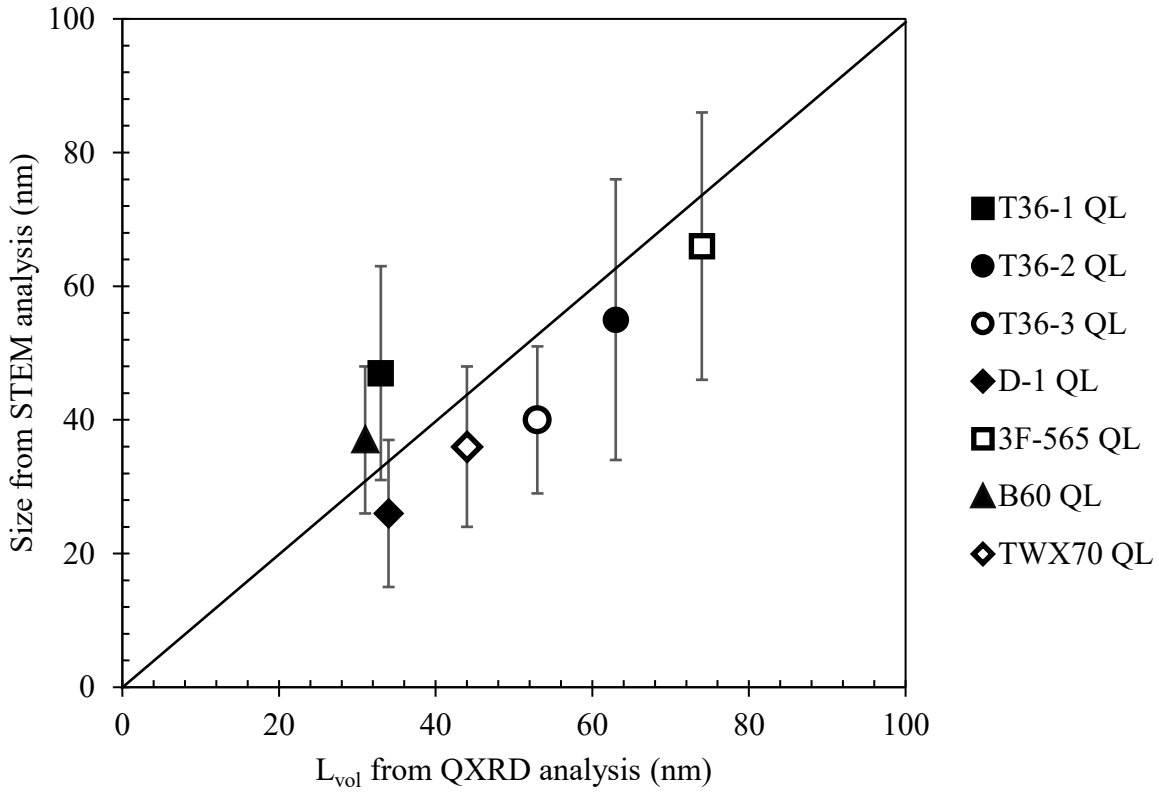

Figure 4.21– Size of fine TiN-rich particles measured using STEM analysis and QXRD analysis.

4-3-2 Composition of fine TiN-rich particles

The composition of fine TiN-rich particles was measured using STEM/EDX analysis conducted on the particles extracted with carbon replicas. Table 4.4 shows the Ti/(Ti+Nb) ratio of the particles. The lowest ratio occurred for B60 QL, which has the highest Nb concentration, while the Ti/(Ti+Nb) ratio in D-1 QL (with the lowest Nb concentration) is not significantly different from that in the other steels. No particular relationship between the composition of steels and the composition of their fine TiN-rich particles could be found. Additional parameters, such as

reheating conditions (temperature and time), may be involved, or the particles have not reached the equilibrium conditions. Subsequent processing stages following reheating may have additionally affected the composition of the fine TiN-rich particles since they were extracted from the fully processed samples.

Table 4.4– Measured Ti/(Ti+Nb) ratio of fine TiN-rich particles at quarterline using STEM/EDX and the adjusted composition of studied steels

Sample	Ti/(Ti+Nb) (atomic fraction)		Adjusted composition (wt.%)			Adjusted Ti/(Ti+Nb) (atomic fraction)
	Average	SD*	Nb	Ti	N	
T36-1 QL	0.71	0.05	0.073	0.012	0.0034	0.24
T36-2 QL	0.73	0.04	0.077	0.013	0.0035	0.25
T36-3 QL	0.66	0.07	0.074	0.010	0.0047	0.21
D-1 QL	0.66	0.05	0.036	0.014	0.0047	0.43
3F-565 QL	0.75	0.06	0.074	0.007	0.0050	0.16
B60 QL	0.59	0.05	0.088	0.015	0.0063	0.25
TWX70 QL	0.66	0.07	0.065	0.009	0.0069	0.21

* SD: Standard deviation

The presence of Nb in fine TiN-rich particles and the effect of the heating cycle on TiN particle composition have been reported by [116]. Their TEM/EDX analysis resulted in a Ti/(Ti+Nb) ratio of 0.75 in a steel with a composition of 0.07 C-0.014 Nb-0.017 Ti-0.0063 N (all in wt.%) reheated at 1200 °C for 2 h prior to hot-rolling. However, the ratio increased to more than 0.8 after undergoing simulated HAZ experiments with a maximum peak temperature of 1350 °C. A similar dependence of fine TiN-rich compositions to high-temperature treatments is also demonstrated by Hong et al. [117]. They reheated as-cast samples with a composition of 0.06C-0.039Nb-0.018Ti-0.004 wt.% N, and showed an increase in reheating temperature results in the formation of fine TiN-rich particles that are more enriched in Ti. Their findings are presented in Figure 4.22. The Ti/(Ti+Nb) ratio decreased from approximately 0.9 to 0.6 when the reheating temperature was decreased from 1400 °C to 1050 °C.

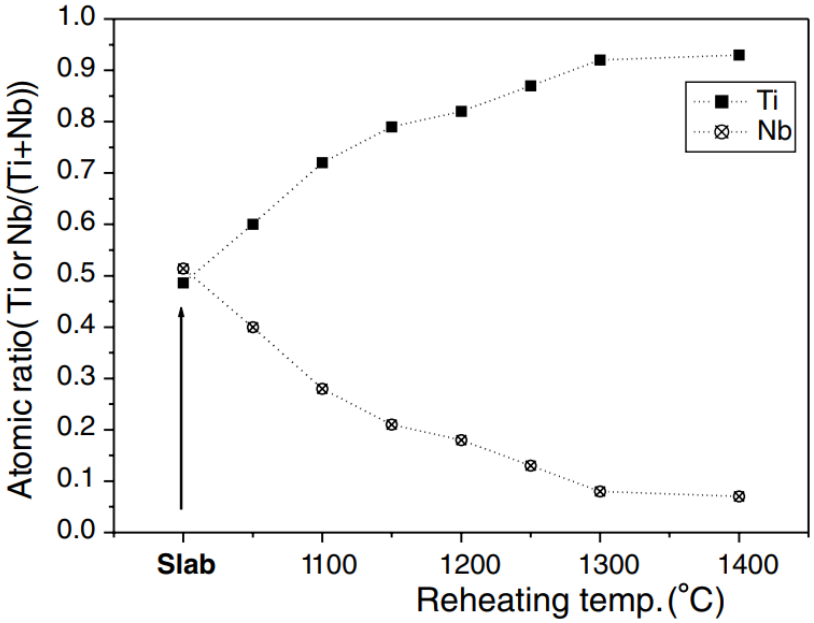

Figure 4.22– Composition of fine particles in slab reheated at different temperatures [117].

Figure 4.23 shows the variation in Ti/(Ti+Nb) ratio for the TiN-rich phase in equilibrium with austenite in the studied steels, as a function of temperature, calculated using ThermoCalc. The calculations were conducted using the one axis equilibrium module, which determines the equilibrium compositions of phases as a function of temperature. The adjusted concentrations of Ti, Nb, and N along with the concentrations of the elements shown in Table 3.1 were used as the composition of the system. As the temperature decreases, the Ti/(Ti+Nb) ratio of the TiN-rich phase decreases until it reaches a minimum. The minimum corresponds with the start of NbC-rich phase formation, which limits the available Nb. The typical temperature range for reheating in industry is 1200 °C to 1300 °C. The calculated Ti/(Ti+Nb) values are greater than the measured ones shown in Table 4.4. The discrepancy between the measured and calculated Ti/(Ti+Nb) ratios for fine TiN-rich particles persists even when the lowest calculated Ti/(Ti+Nb) values at lower temperatures are considered. The lowest calculated Ti/(Ti+Nb) ratio belongs to TWX70, while the lowest measured ratio was observed for B60. The discrepancy between the measured and calculated Ti/(Ti+Nb) ratios for fine TiN-rich particles suggests that interaction values for the involved species used in the ThermoCalc thermodynamic database may not be explained using thermodynamic principles. The software is programmed to predict a system with the lowest free energy, i.e., equilibrium conditions, while the reheating conditions that the steels underwent may not have achieved the equilibrium composition for fine TiN-rich particles.

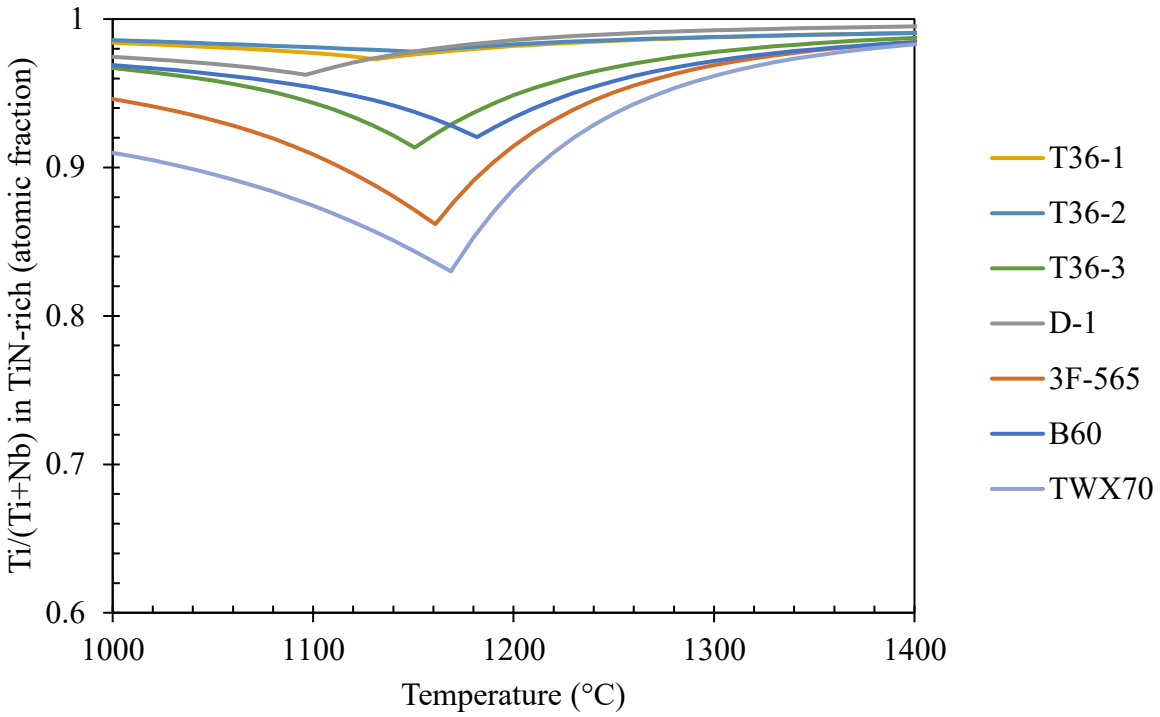

Figure 4.23– Calculated Ti/(Ti+Nb) ratio of TiN-rich phase versus temperature using ThermoCalc with the adjusted composition.

4-3-3 Volume fraction of fine TiN-rich particles

Figure 4.24 shows the volume fraction of fine TiN-rich particles as a function of adjusted Ti·N values. The volume fraction increases with an increase in the adjusted Ti·N values. It is necessary to mention that attempts to include a phase representing the coarse TiN-rich particles in the QXRD analysis of D-1 QL were not successful. However, coarse TiN-rich particles were observed in the SEM/EDX analysis of the carbon replicas extracted from D-1 QL. This is an indication that the volume fraction of coarse TiN-rich particles in the D-1 QL sample is small. The actual volume fraction of fine TiN-rich particles in D-1 QL (Figure 4.24) is, therefore, slightly less than the presented value.

The ICP results (Table 4.5) showed that the concentration of Ti in solid solution is quite low. Thus, virtually all the Ti that is not tied up in coarse TiN-rich particles exists in fine TiN-rich particles. Therefore, as the Ti and N amounts available for the formation of fine TiN-rich particles increases, the volume fraction will increase.

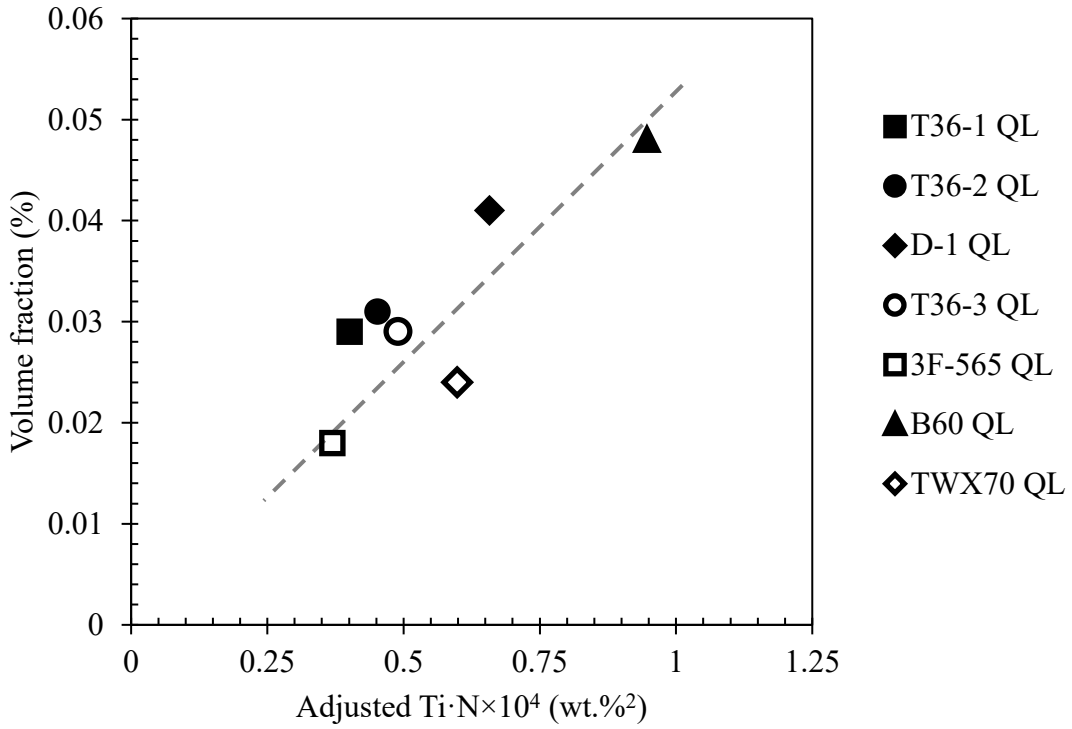

Figure 4.24– Volume fraction of fine TiN-rich particles measured using QXRD as a function of adjusted Ti·N values.

Table 4.5– ICP-MS results of Ti for QL samples

Sample	T36-1 QL	T36-2 QL	T36-3 QL	D-1 QL	3F-565 QL	B60 QL	TWX70 QL
Ti in collected residue (%)	96.3	96.5	97.9	97.4	98.1	98.8	98.4

4-3-4 Comparison between quarterline and centerline samples

The average size, composition, and volume fraction of the fine TiN-rich particles at the quarterline and centerline of four of the studied steels are presented in Figure 4.25 to Figure 4.27, respectively. Similar to the coarse particles, the fine TiN-rich particles did not show a significant difference at the quarterline and centerline locations. The apparent higher volume fraction of fine TiN-rich particles for D-1 QL in comparison with those for D-1 CL is because QXRD for D-1 QL did not include the coarse TiN-rich phase. However, coarse TiN-rich particles were observed in both samples.

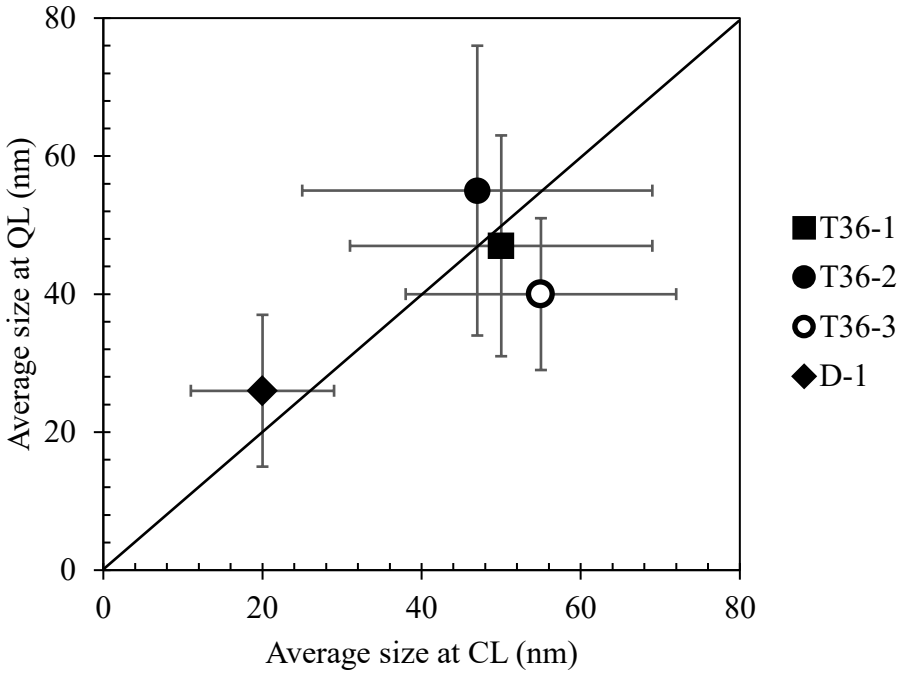

Figure 4.25– Average size of fine TiN-rich particles at the QL and CL measured using STEM.

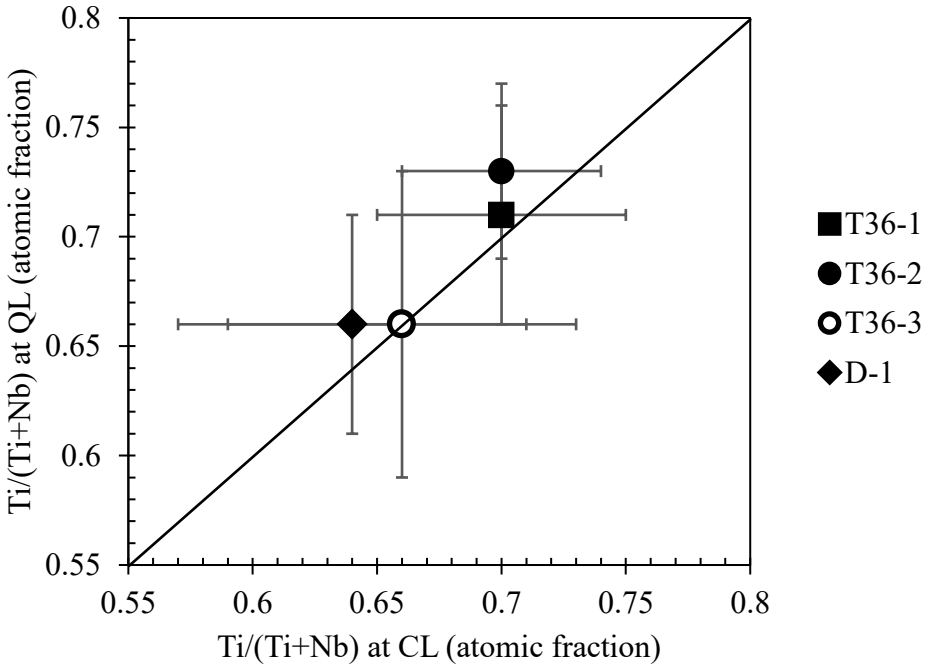

Figure 4.26– Ti/(Ti+Nb) ratio of fine TiN-rich particles at the QL and CL measured using STEM/EDX.

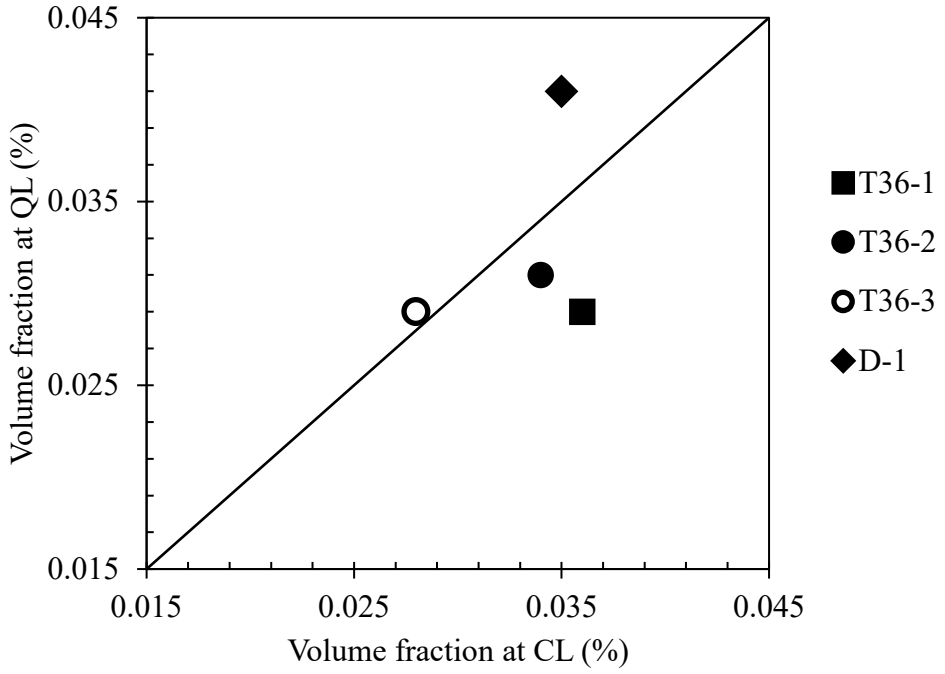

Figure 4.27– Volume fraction of fine TiN-rich particles at the QL and CL measured using QXRD.

In addition to possible compositional differences between quarterline and centerline locations discussed in Section 4-2-4, the difference in their cooling rates during post-solidification cooling may affect the characteristics of particles forming at these locations [118]. Lower post-solidification cooling rates at centerline locations have been associated with larger fine TiN particles [119]. However, the observations carried out in the current study do not show significant differences between the fine TiN-rich particles at quarterline and centerline locations. The formation of the fine TiN-rich particles in the studied steels may not have been affected by post-solidification cooling rates. As will be discussed in Section 4-4, the steels likely did not contain fine TiN-rich particles in the as-cast condition. Therefore, the particles were formed during the reheating process usually carried out from 1200 °C to 1300 °C. As discussed in Section 4-3, the reheating process influences the size and composition of fine TiN-rich particles. A similar reheating cycle at the quarterline and centerline locations could be the reason for the observed lack of a considerable difference in the characteristics of the fine TiN-rich particles at these locations.

4-3-5 Summary

A decrease in the size of fine TiN-rich particles was observed as the adjusted Ti·N value increased. A larger adjusted Ti·N value provides a larger driving force for nucleation and leads to finer particles. The composition of the fine TiN-rich particles in the studied steels did not show significant differences, which could be due to the complicating effect of the heat treatment history (reheating process) in addition to the composition of the steels. The volume fraction of the fine particles is affected by the nominal composition and solidification process, which eventually determine the amount of Ti and N available for the formation of fine TiN-rich particles. The differences in characteristics of fine TiN-rich particles at the quarterline and centerline locations were not significant. In addition to the lack of a significant compositional dissimilarity between these locations, the formation of fine TiN-rich particles during reheating (and not post-solidification cooling) may have contributed to the observed behavior.

4-4 Precipitates in the as-cast steel

Microalloying elements that are present in the melt at the beginning of the casting form various types of precipitates with different sizes, morphology and compositions as the steel is cast into a slab. The characteristics of the precipitates affect the production process schedule and the final product properties. This section focuses on the coarse and fine particles observed in 3F-as-cast.

4-4-1 Coarse particles

The carbon replica extraction method was used to extract particles from the quarterline and centerline of 3F-as-cast. The purpose of analyzing 3F-as-cast was to obtain information on the condition of fine TiN-rich particles in the steels before reheating. SEM/EDX analysis of the replicas showed coarse dendritic Nb-rich precipitates in addition to coarse TiN-rich particles. Figure 4.28 and Figure 4.29 show examples of the coarse Nb-rich particles at the quarterline and centerline locations. Additional SEM micrographs and EDX spectra and maps of the coarse TiN-rich and Nb-rich particles in as-cast slabs are provided in Appendix H. Such particles were absent in the fully processed steels. A similar precipitate type has been observed in continuously cast microalloyed steels. Chen et al. [92] used the replica method to extract particles from the edge and centerline of a 0.02 C-0.098 Nb-0.013 Ti-0.003 N (all in wt.%) steel and observed micron-sized dendritic precipitates with Ti/(Ti+Nb) ratio of 0.20 (atomic fraction). Based on the morphology

and size of the particles, it was suggested that the particles were formed in interdendritic regions before solidification was complete, and microsegregation in the interdendritic regions provided a high concentration of microalloying elements eliminating the need for long distance diffusion.

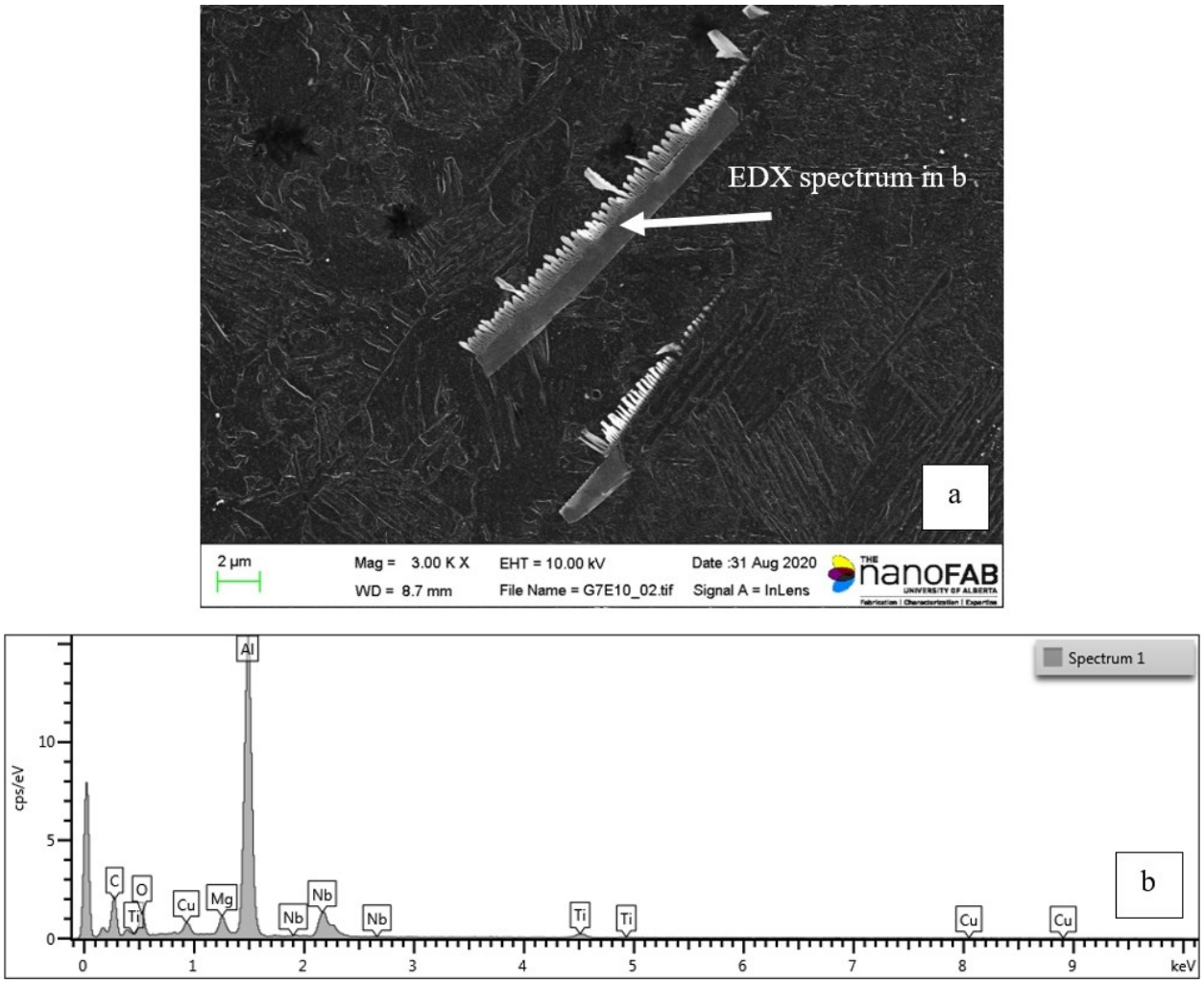

Figure 4.28a) SEM SE micrograph of carbon replica extracted from the quarterline sample of 3F-as-cast; b) EDX spectrum of the top particle in (a) (Ti/(Ti+Nb) = 0.32 atomic fraction). The Al and Mg peaks are from the Al alloy SEM stub used to hold the grids. The Cu peak is from the Cu grid.

Figure 4.29a) SEM SE micrograph of carbon replica extracted from the centerline sample of 3F-as-cast; b) EDX spectrum of the particle in the middle of (a) which is indicated by an arrow (Ti/(Ti+Nb) = 0.28 atomic fraction). The Al and Mg peaks are from the Al alloy SEM stub used to hold the grids. The Cu peak is from the Cu grid.

Figure 4.30 shows the composition of the precipitate phase forming during the solidification of 3F-as-cast using the modified Scheil-Gulliver model. As the solid fraction approaches 0.84, the secondary phase (precipitate) starts to form with a composition enriched in Ti and N. When the solid fraction is just over 0.99, the composition of the phase changes from TiN-rich to Nb-rich (Figure 4.30b), although the calculated concentration of Ti is less than measured values (Figure 4.28 and Figure 4.29).

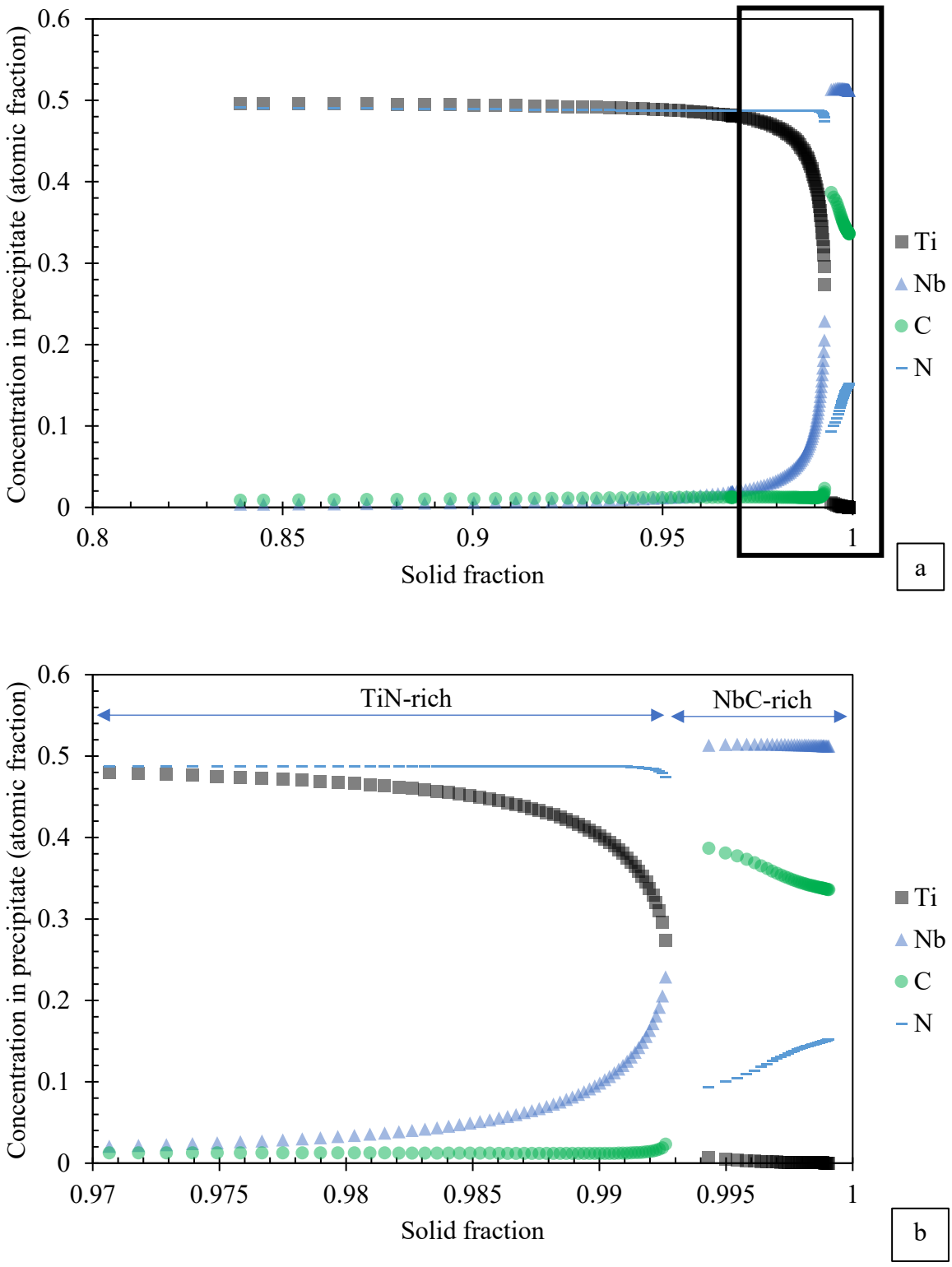

Figure 4.30a) Concentration of Ti, Nb, C, and N in a precipitate forming during solidification of 3F-as-cast using the modified Scheil-Gulliver model; b) the enclosed zone in (a) magnified.

During solidification, alloying elements segregate into the liquid. The partition coefficients (the ratio of the concentration of the element in solid to that in liquid at the solidification front) for Nb and Ti are not equal. The modified Scheil-Gulliver model shows that the Nb and Ti partition coefficients are 0.18 and 0.29, respectively. Additionally, the higher nominal concentration of Nb and consumption of Ti when coarse TiN-rich particles form may lead to larger Nb segregation ratios (the concentration of the element in liquid to its nominal concentration) compared with that of Ti (~57 to 1 just before Nb-rich particles start to form). This is likely the reason coarse Nb-rich particles were observed in the as-cast samples [102].

4-4-2 Fine particles

Fine particles were also observed at both quarterline and centerline locations. In the as-cast sample, the fine particles were mostly faceted Nb-rich particles. Occasionally, star-like, rod-like, and dendritic Nb-rich particles were detected with decreasing frequency. Their morphology indicates the early stage of dendritic growth. Since they form at the last stage of solidification, some of the particles may not have access to the necessary Nb enriched liquid to develop dendritic structures fully. Additional STEM ADF micrographs and EDX maps of the fine Nb-rich particles in as-cast slabs are provided in Appendix I.

Again, the purpose of analyzing 3F-as-cast was to obtain information on the condition of fine TiN-rich particles in the steels before reheating. However, no fine TiN-rich particles were detected in 3F-as-cast. STEM/EDX was employed to measure the composition of more than 40 fine particles at the quarterline location of 3F-as-cast, which were suspected to be fine TiN-rich particles based on their faceted shapes. However, all the particles were Nb-rich with an average Ti/(Ti+Nb) fraction of 0.13 (standard deviation: 0.01). These types of particle are shown in Figure 4.31. The morphology of the particles may suggest that they formed in the last stages of solidification.

Another type of detected particles was dendritic or star-like in shape. Figure 4.32 shows examples of particles at the quarterline and centerline locations. The average size and composition of the particles are given in Table 4.6. They had similar sizes and compositions and were Nb-rich as well. Other studies conducted on as-cast slabs have reported similar particles in as-cast Nb-containing microalloyed steels [117], [120]. Jun et al [120] reported that star-like particles in as-cast slabs containing 0.063 C-0.056 Nb-0.017 Ti-0.006 N (all in wt.%) were Nb-rich (Ti/(Ti+Nb) ~ 0.3) with sizes ranging from 50 to 200 nm. The presence of star-like Nb-rich precipitates with an average

size of 153 nm has been reported by Wang et al. [101] in a steel with a composition of 0.06 C-0.063 Nb-0.044 Ti-0.008 N (all in wt.%) produced via compact strip processing (CSP). Their TEM/EDX analysis showed that the particles were Nb-rich with a Ti/(Ti+Nb) ratio of about 0.3. The particles observed by Wang et al. were not limited to star-like shapes. Smaller Nb-rich particles with spherical shapes and sizes in the range of 10 to 70 nm were also detected. Their compositions were in the same range as that of the star-like particles. Wang et al. also detected 40 to 80 nm cuboidal Ti-rich particles. The difference between the type of particles observed by Wang et al. and those observed in this study can be attributed to different processing routes. In CSP, the cast strip is directly fed to a furnace at around 1100 °C for a short time (~ 20 min). However, in cold charge rolling (CCR) (the production route for the studied steels in this work), the room-temperature slabs are reheated at 1200-1300 °C for 2-3 h. The limited heating process in CSP could lead to the presence of a combination of particles in the final product.

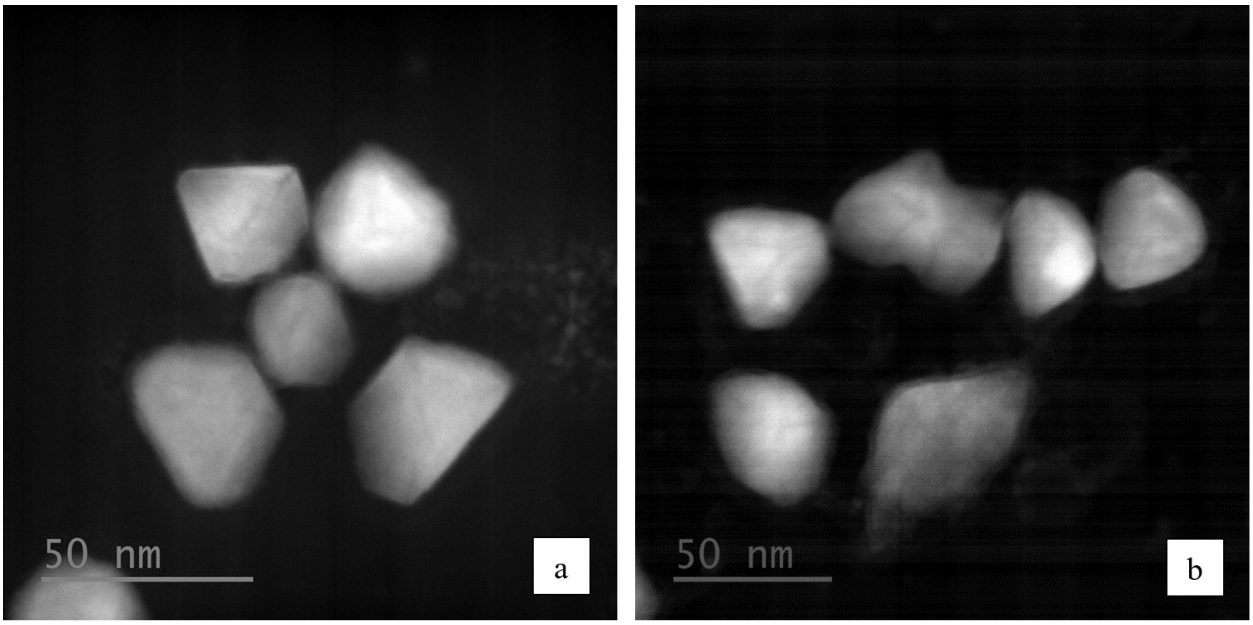

Figure 4.31– Faceted particles observed in carbon replicas extracted from the a) quarterline and b) centerline of 3F-as-cast.

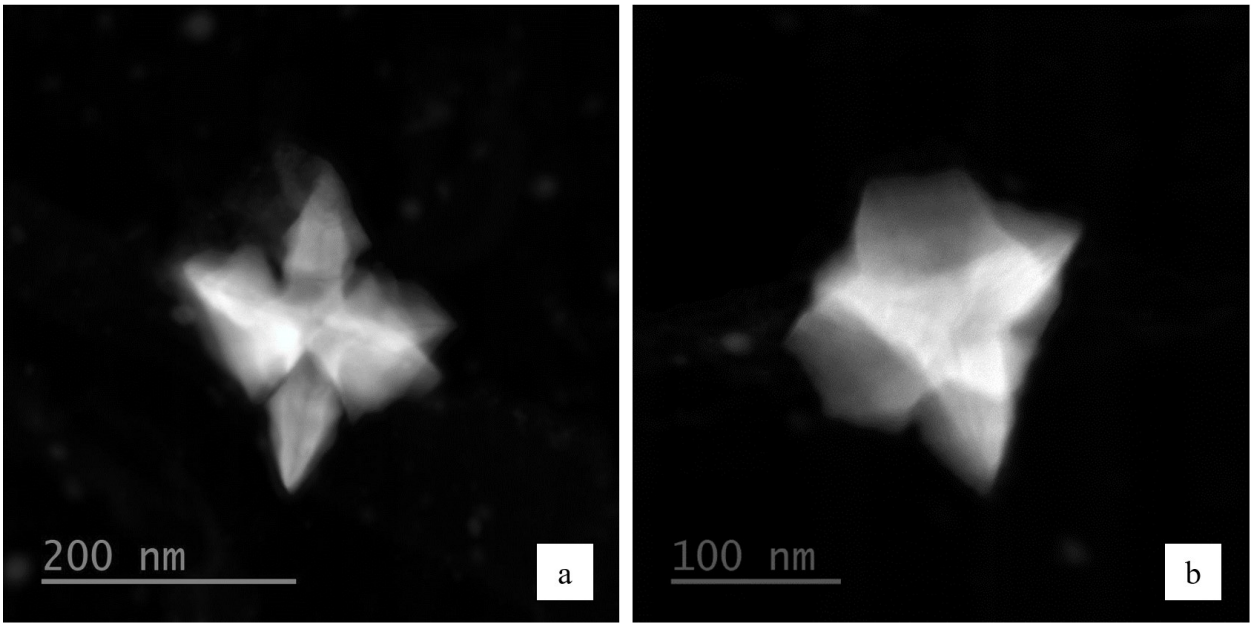

Figure 4.32– Star-like particles observed in carbon replicas extracted from the a) quarterline and b) centerline of 3F-as-cast.

Table 4.6– Average size and composition of faceted and star-like particles in 3F-as-cast

Type	Location	Size (nm)		Composition Ti/(Ti+Nb) (atomic fraction)	
		Average	SD*	Average	SD
Faceted	Quarterline	35	7	0.13	0.01
	Centerline	34	11	0.16	0.02
Star-like	Quarterline	138	34	0.15	0.02
	Centerline	117	24	0.17	0.03

* SD: standard deviation

Several studies have reported the presence of fine TiN-rich particles in post-solidification conditions. Kunze et al. [99] observed 10 nm TiN particles, in addition to coarse TiN particles, after solidification of a steel containing 0.051 Ti-0.77 Mn-0.08 C-0.016 N (all in wt.%) with a post-solidification cooling rate of 25 K/s. The presence of fine TiN particles in as-cast samples containing 0.089 C-1.24 Mn-0.015 Ti-0.006 N-0.018 V (all in wt.%) has been reported by Nagata

et al. [119]. The average sizes of TiN particles at locations near the surface and centerline of a continuously cast slab were reported to be approximately 30 nm and 45 nm, respectively. The chemistry of the steels in the above-mentioned studies did not include Nb. A study on several microalloyed steels with a composition of 0.05 C-0.027 Nb-(0.005-0.038) Ti-(0.005-0.011) N (all in wt.%) showed only fine Ti-rich particles in as-cast samples in which the concentration of Ti was 0.038 wt.% or when N content was increased from 50 to 110 ppm [102]. It seems that when Nb is present in the chemistry of the steel, fine TiN-rich particles only form under certain conditions.

The absence of fine TiN-rich particles in the as-cast sample could be related to the formation of coarse Nb-rich particles near the end of solidification. ThermoCalc software was used to determine the phases that are present in 3F-as-cast under equilibrium conditions. The result is shown in Figure 4.33. The amount of the TiN-rich phase continues to increase as the temperature is decreased after solidification is complete, indicating that fine TiN-rich particles form during post-solidification cooling. Also, the NbC-rich phase only exists below 1160 °C. However, in the as-cast sample, only coarse TiN-rich and coarse Nb-rich particles, which formed in the liquid, and finer Nb-rich particles were observed without any trace of fine TiN-rich particles. The deviation from equilibrium predictions could be because the solidification path is not an equilibrium one. During solidification, the segregation of Nb into interdendritic regions leads to the formation of coarse Nb-rich particles with a significant concentration of Ti. This, in turn, leaves the high-temperature austenite undersaturated with respect to Ti or leads to Ti supersaturation levels that are not adequate to provide a sufficient driving force for fine TiN-rich particle nucleation, thereby impeding the formation of fine TiN-rich particles during subsequent post-solidification cooling. Eventually, when the as-cast steel is reheated, the Ti-containing Nb-rich particles will dissolve and pave the way for the precipitation of fine TiN-rich particles [117].

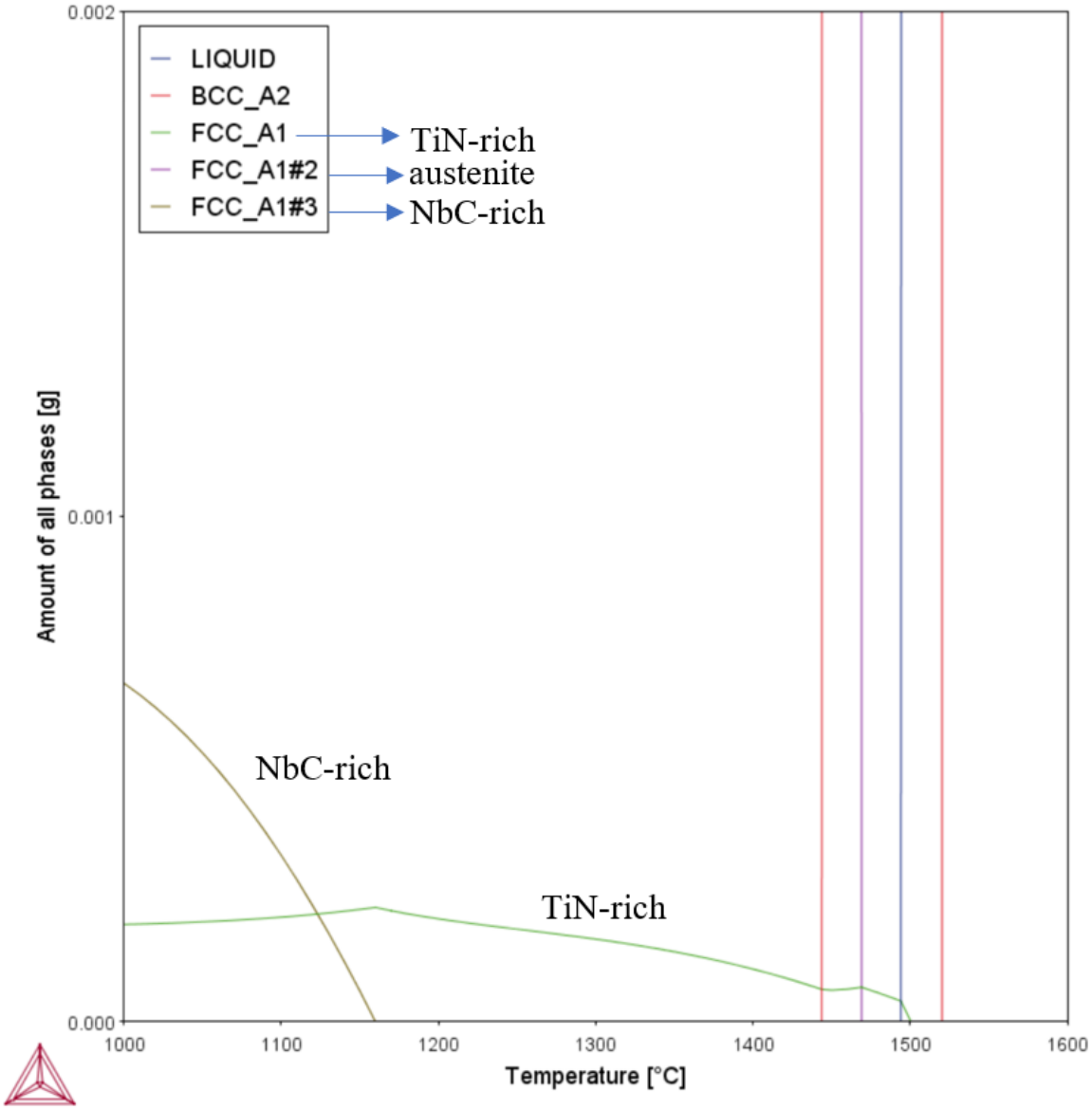

Figure 4.33– Equilibrium phases present in 3F-as-cast between 1000 °C and 1600 °C, calculated using ThermoCalc. The size of the system is 1 g.

4-4-3 Summary

The SEM-STEM/EDX analysis conducted on the carbon replicas of 3F-as-cast revealed coarse and fine Nb-rich particles in addition to coarse TiN-rich particles. Fine TiN-rich particles were not detected in the samples. The coarse Nb-rich particles exhibited a dendritic morphology and these precipitated during the last stage of solidification. Since the Nb-rich particles consume the Ti left in the liquid, the nucleation of fine TiN-rich particles during post-solidification cooling was

impeded. Fine TiN-rich particles were formed during the reheating process (carried out prior to hot rolling) while the Ti-containing coarse and fine Nb-rich particles were dissolved. In this study, steels in as-cast condition and fully processed condition were studied, and various Ti and Nb carbonitride particles were detected. Solidification of steel involves segregating alloying elements into the liquid (for the elements with the partition coefficients of less than 1, including Ti, Nb, N, and C). As solidification progresses, Ti and N segregate into the liquid. When the liquid becomes saturated with Ti and N, the continued segregation of Ti and N results in the formation of the coarse TiN-rich particles. Similarly, segregation of Nb results in the formation of dendritic and faceted Nb-rich carbonitride particles at the last stage of solidification since Nb carbonitrides have greater solubility in the liquid than TiN does [32]. The study of the as-cast steel showed that coarse cuboidal TiN-rich particles, coarse dendritic Ti-containing Nb-rich particles, and fine faceted Ti-containing Nb-rich particles were the primary detected particles after casting. However, in the fully processed steels, in addition to the coarse cuboidal TiN-rich particles, fine TiN-rich particles and NbC-rich particles epitaxially grown on the fine TiN-rich particles were observed. Thus, the coarse dendritic Ti-containing Nb-rich particles and fine faceted Ti-containing Nb-rich particles disappeared during the TMCP process. It has been suggested that the Nb-rich particles dissolve and reprecipitate as fine TiN-rich particles during reheating stage [117]. Alternatively, the dissolution of Nb-rich particles could have involved the partial dissolution of Nb into the austenitic matrix followed by the growth of the remaining TiN-rich core. However, the obtained results in this study cannot clarify which one is the main mechanism for the formation of fine TiN-rich particles from the Nb-rich particles. Further investigation is required to understand the kinetics of fine TiN-rich particle formation. After reheating, when the temperature of the steel is lowered to perform rough and finish rolling, NbC-rich particles become more stable, and they can preferentially form on the existing fine TiN-rich particles. While Nb-rich particles forming during solidification are usually dendritic or faceted, the epitaxially grown NbC-rich particles take the form of a cap. Further decrease in temperature during coiling can lead to the formation of spherical NbC-rich nano-precipitates (<10 nm) in the ferrite phase [73].

5 Conclusions and future work

SEM/EDX, STEM/EDX, matrix dissolution, ICP, and QXRD analysis were employed to measure sizes, compositions, and volume fractions of the coarse and fine TiN-rich particles in several as-rolled thick walled X70 microalloyed steels containing 0.014-0.023 wt.% Ti and 42-93 ppm N. Additionally, the types of the particles present in an as-cast steel were studied using SEM/EDX and STEM/EDX. The following presents the conclusions and recommended future work.

5-1 Conclusions

- The size of the coarse TiN-rich particles increased with increasing nominal Ti and N concentration product. The coarse TiN-rich particles formed during solidification, and the nominal Ti and N concentration product affected the solubility of TiN in the liquid during solidification. As solidification progressed, the alloying elements, including Ti and N, partitioned to the solidification front and, due to the lack of significant diffusion in the solid, segregated into the interdendritic regions. The segregation was more significant in the steels with the higher products, and larger coarse TiN-rich particles were more frequently observed in those steels. The volume fractions of the coarse TiN-rich particles also increased with increasing nominal Ti and N concentration product. The limited solubility of Ti and N in the solid led to the precipitation of larger volumes of the coarse TiN-rich particles in the steels with larger Ti and N concentrations (i.e., larger nominal Ti and N concentration products) during solidification. The compositional analysis of the coarse TiN-rich particles showed that they were not pure TiN and contained Nb. The similar crystal structure and lattice parameters of Nb and Ti carbonitrides promoted the formation of particles with complex chemical compositions. For steels with similar Ti/N ratios, lower Ti/(Ti+Nb) ratios in the coarse TiN-rich particles were related to the lower Ti/(Ti+Nb) ratios of the liquid as the particles formed.
- The size of the fine TiN-rich particles decreased as the product of the adjusted Ti and N concentrations increased. The adjusted Ti and N concentrations were obtained by subtracting the Ti and N bound in the coarse TiN-rich particles from the nominal concentrations. The effect of a larger adjusted product was related to the reduction in the

energy barrier for the nucleation of the particles, which led to higher nucleation rates and smaller fine TiN-rich particles. Since nearly all the adjusted Ti concentrations were precipitated as fine TiN-rich particles, the volume fraction of the fine TiN-rich particles increased with increasing product of the adjusted Ti and N concentrations. The Ti/(Ti+Nb) ratios of the fine TiN-rich particles were lower than that of the coarse TiN-rich particles, indicating a greater concentration of Nb in the fine particles.

- No significant differences were observed in sizes, compositions, and volume fractions of the coarse TiN-rich particles at the quarterline and centerline locations for T36-1, T36-2, T36-3, and D-1. The concentrations of several alloying elements (such as Cr, Si, Mn, and Ni) at both locations were similar, suggesting that the soft reduction process performed during casting had reduced segregation levels at the centerline. Also, the metallurgical centerline may not have been located in the region from which the centerline samples were prepared. A similar observation was made for the fine TiN-rich particles. The observation was related to the formation of the fine TiN-rich particles during the reheating (homogenization) stage and the possibility that the centerline and quarterline locations experience similar heating cycles during the stage.
- In addition to coarse TiN-rich particles, coarse and fine Ti-containing Nb-rich particles were detected in the as-cast steel. The formation of the Nb-rich phase in the last stages of solidification was verified by the Scheil-Gulliver solidification model. Fine TiN-rich particles were absent in the as-cast steel. It is suggested the formation of Ti-containing Nb-rich particles during solidification hindered the formation of the fine TiN-rich particles during post-solidification cooling.
- The Scheil-Gulliver solidification model showed that the TiN-rich phase started to form at lower solid fractions for the steels with the larger products of the nominal Ti and N concentrations. The earlier nucleation of the TiN-rich phase during solidification led to larger coarse TiN-rich particles. The volume fractions of the TiN-rich phases obtained from the model were in good agreement with the measured values for the coarse TiN-rich particles, except at the lowest products of the nominal Ti and N concentrations. The issue was attributed to the supersaturation required for the nucleation of the particles. Also, the composition of the TiN-rich phases showed lower Nb levels than the measured values for the coarse TiN-rich particles. A similar difference in the predicted and measured

compositions of the fine TiN-rich particles was also observed when modeling using one axis equilibrium module of ThermoCalc.

5-2 Proposed future work

- The majority of the studied steels had Ti concentrations varying from 0.014 wt.% to 0.016 wt.%. For a given Ti concentration (e.g., 0.015 wt.%), excess N leads to the formation of large coarse TiN-rich particles and fine TiN-rich particles, as observed for TWX70. On the other hand, when N concentrations are near the stoichiometric ratio, smaller coarse TiN-rich particles with relatively larger fine TiN-rich particles are expected, as observed for T36-2. Since large coarse TiN-rich particles and fine TiN-rich particles in the range between 30 and 60 nm are not desirable, a compromise could be N concentrations in between these two conditions, similar to T36-3. Another strategy could be reducing the nominal Ti concentration; for example, a Ti concentration of 0.012 wt.% along with a N concentration of 50 ppm. Such a steel will have $Ti \cdot N \times 10^4 = 0.6$, which is less than that of T36-2 (Figure 4.3). Alternatively, reducing the nominal concentration of Nb and reducing the reheating temperature (the likely condition for D-1) should be explored.
- The results of STEM/EDX analysis done on the as-cast steel indicated that fine TiN-rich particles do not form during post-solidification cooling. The absence of the particles was attributed to the formation of Ti-containing Nb-rich particles in the last stages of solidification. It is proposed that the as-cast microstructure of a series of microalloyed steels without Nb and with a range of Nb concentrations should be analyzed to determine the role of Nb in suppressing the formation of fine TiN-rich particles during post-solidification cooling. The samples need to be quenched at different temperatures following the casting process to determine the concentration of Ti in the matrix prior to the formation of the fine TiN-rich particles.
- Fine TiN-rich particles are important for exerting pinning forces on austenite grain boundaries during the reheating stage. However, the particles appear to form during the reheating stage in the steels studied. A study should be conducted to investigate the kinetics of fine TiN-rich particle formation and the effect on austenite grain growth during the reheating stage.

- A more accurate compositional analysis of the fine TiN-rich particles should be performed using atom probe tomography.
- A comparison can be made with the area fraction of the coarse TiN-rich particles obtained using SEM/EDX equipped with an automatic inclusion analysis system. It is claimed that the technique can analyze large areas of steel samples over relatively short periods.
- To reduce the size of coarse TiN-rich particles, it is suggested to maintain the product of nominal Ti and N below 0.6×10^{-4} wt.%^{2} (Figure 4.3). Since reducing the concentration of nitrogen via vacuum degasser to the below 50 PPM level could be practically challenging, reducing the concentration of Ti is suggested to limit the product of Ti and N concentrations. To decrease the size of fine TiN-rich particles, it is suggested that the reheating temperature be lowered. Reducing the reheating temperature will affect the dissolution kinetics of Nb-rich particles, which must be compensated by reducing the Nb concentration in the steel.

References

[1] D. P. Fairchild, D. G. Howden, and W. A. T. Clark, "Mechanism of brittle fracture in a microalloyed steel: Part I. Inclusion-induced cleavage," *Metallurgical and Materials Transactions A*, 2000, vol. 31, pp. 641–652, doi: 10.1007/s11661-000-0007-4.

[2] Y. Tomita, N. Saito, T. Tsuzuki, Y. Tokunaga, and K. Okamoto, "Improvement in HAZ toughness of steel by TiN-MnS addition," *ISIJ International*, 1994, vol. 34, pp. 829–835, doi: 10.2355/isijinternational.34.829.

[3] G. R. Wang, T. W. Lau, G. C. Weatherly, and T. H. North, "Weld thermal cycles and precipitation effects in Ti-V-containing HSLA steels," *Metallurgical Transactions A*, 1989, vol. 20, pp. 2093–2100, doi: 10.1007/BF02650295.

[4] J. Strid and K. E. Easterling, "On the chemistry and stability of complex carbides and nitrides in microalloyed steels," *Acta Metallurgica*, 1985, vol. 33, pp. 2057–2074, doi: 10.1016/0001-6160(85)90129-4.

[5] S. Kanazawa, A. Nakashima, K. Okamoto, and K. Kanaya, "Improved toughness of weld fussion zone by fine TiN particles and development of a steel for large heat input welding," *Tetsu-to-Hagané*, 1975, vol. 61, pp. 2589–2603.

[6] M. Militzer and E. B. Hawbolt, "Austenite grain growth in microalloyed low carbon steels," in *Grain Growth in Polycrystalline Materials III, TMS*, 1998, pp. 639–644.

[7] C. Stallybrass, F. Grimpe, H. Meuser, and H. G. Hillenbrand, "Development of high strength heavy plate optimised for low-temperature toughness for pipeline applications," in *Pipeline Technology Conference*, 2009, pp. 12–14.

[8] S. G. Hong, K. B. Kang, and C. G. Park, "Strain-induced precipitation of NbC in Nb and Nb-Ti microalloyed HSLA steels," *Scripta Materialia*, 2002, vol. 46, pp. 163–168, doi: 10.1016/S1359-6462(01)01214-3.

[9] S. C. Wang, "The effect of titanium and nitrogen contents on the microstructure and mechanical properties of plain carbon steels," *Materials Science and Engineering A*, 1991,

vol. 145, pp. 87–94, doi: 10.1016/0921-5093(91)90298-2.

[10] M. I. Vega, S. F. Medina, A. Quispe, M. Gomez, and P. P. Gomez, “Influence of TiN particle precipitation state on static recrystallisation in structural steels,” *ISIJ International*, 2005, vol. 45, pp. 1878–1886, doi: 10.2355/isijinternational.45.1878.

[11] S. F. Medina, M. Chapa, P. Valles, A. Quispe, and M. I. Vega, “Influence of Ti and N contents on austenite grain control and precipitate size in structural steels,” *ISIJ International*, 1999, vol. 39, pp. 930–936, doi: 10.2355/isijinternational.39.930.

[12] N. Gao and T. N. Baker, “Austenite grain growth behaviour of microalloyed Al-V-N and Al-V-Ti-N steels.,” *ISIJ International*, 1998, vol. 38, pp. 744–751, doi: 10.2355/isijinternational.38.744.

[13] Y. Shen and S. S. Hansen, “Effect of the Ti/N ratio on the hardenability and mechanical properties of a quenched-and-tempered C-Mn-B steel,” *Metallurgical and Materials Transactions A*, 1997, vol. 28, pp. 2027–2035, doi: 10.1007/s11661-997-0159-6.

[14] M. Chen, C. Wu, J. Gao, and Y. Tang, “Kinetic model of TiN particle dissolution and coarsening during welding thermal cycle,” *Journal of Materials Science and Technology*, 2002, vol. 18, pp. 439–442.

[15] X. Zhang, C. Loannidou, G. H. ten Brink, A. Navarro-López, J. Wormann, and B. J. Kooi, “Microstructure, precipitate and property evolution in cold-rolled Ti-V high strength low alloy steel,” *Materials and Design*, 2020, vol. 192, p. 108720, doi: 10.1016/j.matdes.2020.108720.

[16] A. L. Rivas, E. Vidal, D. K. Matlock, and J. G. Speer, “Electrochemical extraction of microalloy carbides in Nb-steel,” *Revista de Metalurgia*, 2008, vol. 44, pp. 447–456, doi: 10.3989/revmetalm.0771.

[17] M. Doi, S. Endo, and K. Osawa, “Effect of Ti content on TiN morphology, microstructure and toughness in coarse-grained heat affected zone of Ti-containing steels,” *Welding International*, 2000, vol. 14, pp. 281–287, doi: 10.1080/09507110009549180.

[18] J. C. Herman, B. Donnay, and V. Leroy, “Precipitation kinetics of microalloying additions during hot-rolling of HSLA steels,” *ISIJ International*, 1992 vol. 32, pp. 779–785, , doi:

10.2355/isijinternational.32.779.

[19] J. Stock, “NbC and TiN precipitation in continuously cast microalloyed steels,” MSc Thesis, Colorado School of Mines, 2013.

[20] T. N. Baker, “Microalloyed steels,” *Ironmaking & Steelmaking*, 2016, vol. 43, pp. 264–307, doi: 10.1179/1743281215Y.0000000063.

[21] W. B. Morrison, “Microalloy steels - The beginning,” *Materials Science and Technology*, 2009, vol. 25, pp. 1066–1073, doi: 10.1179/174328409X453299.

[22] Z. Shi, R. Wang, H. Su, F. Chai, Q. Wang, and C. Yang, “Effect of nitrogen content on the second phase particles in V-Ti microalloyed shipbuilding steel during weld thermal cycling,” *Materials and Design*, 2016, vol. 96, pp. 241–250, doi: 10.1016/j.matdes.2016.01.111.

[23] A. Graux, S. Cazottes, D. D. Castro, D. San-Martín, C. Capdevila, and J. M. Cabrera, “Design and development of complex phase steels with improved combination of strength and stretch-flangeability,” *Metals*, 2020, vol. 10, p. 824.

[24] C. L. Davis and M. Strangwood, “Segregation behaviour in Nb microalloyed steels,” *Materials Science and Technology*, 2009, vol. 25, pp. 1126–1133, doi: 10.1179/174328409X453262.

[25] S. Vervynckt, K. Verbeken, B. Lopez, and J. J. Jonas, “Modern HSLA steels and role of non-recrystallisation temperature,” *International Materials Reviews*, 2012, vol. 57, pp. 187–207, doi: 10.1179/1743280411Y.0000000013.

[26] W. B. Morrison, “Overview of microalloying in steel,” in *The Use of Vanadium in Steel - Proceedings of the Vanitec Symposium*, 2000, pp. 25–35.

[27] A. J. DeArdo, “Niobium in modern steels,” *International Materials Reviews*, 2003, vol. 48, pp. 371–402, doi: 10.1179/095066003225008833.

[28] T. N. Baker, “Processes, microstructure and properties of vanadium microalloyed steels,” *Materials Science and Technology*, 2009, vol. 25, pp. 1083–1107, doi: 10.1179/174328409X453253.

[29] S. Gündüz and R. C. Cochrane, “Influence of cooling rate and tempering on precipitation and hardness of vanadium microalloyed steel,” *Materials and Design*, 2005, vol. 26, pp. 486–492, doi: 10.1016/j.matdes.2004.07.022.

[30] R. D. K. Misra, K. K. Tenneti, G. C. Weatherly, and G. Tither, “Microstructure and texture of hot-rolled Cb-Ti and V-Cb microalloyed steels with differences in formability and toughness,” *Metallurgical and Materials Transactions A*, 2003, vol. 34 A, pp. 2341–2351, doi: 10.1007/s11661-003-0297-4.

[31] J. Lu, O. Omotoso, J. B. Wiskel, D. G. Ivey, and H. Henein, “Strengthening mechanisms and their relative contributions to the yield strength of microalloyed steels,” *Metallurgical and Materials Transactions A*, 2012, vol. 43, pp. 3043–3061, doi: 10.1007/s11661-012-1135-3.

[32] T. Gladman, *The Physical Metallurgy of Microalloyed Steels*. London, UK: The Institute of Materials, 1997.

[33] D. Mazumdar and J. W. Evans, *Modeling of Steelmaking Processes*. CRC Press, 2009.

[34] S. Louhenkilpi, “Continuous casting of steel,” in *Treatise on Process Metallurgy*, vol. 3, Elsevier Ltd., 2014, pp. 373–434.

[35] A. W. Cramb, “Solidification and steel casting,” in *Fundamentals of Metallurgy*, Elsevier Inc., 2005, pp. 399–452.

[36] B. G. Thomas, “Continuous casting of steel,” in *Modeling for Casting and Solidification Processing*, K.-O. Yu, Ed. New York, NY: CRC Press, 2001, pp. 499–540.

[37] M. Militzer, “Thermomechanical processed steels,” in *Comprehensive Materials Processing*, vol. 1, Elsevier Ltd, 2014, pp. 191–216.

[38] F. Perrard, A. Deschamps, and P. Maugis, “Modelling the precipitation of NbC on dislocations in α-Fe,” *Acta Materialia*, 2007, vol. 55, no. 4, pp. 1255–1266, doi: 10.1016/j.actamat.2006.10.003.

[39] A. Echeverría and J. M. Rodriguez-Ibabe, “The role of grain size in brittle particle induced fracture of steels,” *Materials Science and Engineering A*, 2003, vol. 346, pp. 149–158,

doi: 10.1016/S0921-5093(02)00538-5.

[40] J. Fu, J. Zhu, L. Di, F. S. Tong, D. L. Liu, and L. Y. Wang, “Study on the precipitation behavior of TiN in the microalloyed steels,” *Acta Metallurgical Sinica*, 2000, vol. 36, pp. 801–804.

[41] W. Yan, Y. Y. Shan, and K. Yang, “Influence of TiN inclusions on the cleavage fracture behavior of low-carbon microalloyed steels,” *Metallurgical and Materials Transactions A*, 2007, vol. 38, pp. 1211–1222, doi: 10.1007/s11661-007-9161-2.

[42] W. Yan, Y. Y. Shan, and K. Yang, “Effect of TiN inclusions on the impact toughness of low-carbon microalloyed steels,” *Metallurgical and Materials Transactions A*, 2006, vol. 37, pp. 2147–2158, doi: 10.1007/BF02586135.

[43] M. A. Linaza, J. M. Rodriguez-Ibabe, and J. J. Urcola, “Determination of the energetic parameters controlling cleavage fracture initiation in steels,” *Fatigue & Fracture of Engineering Materials & Structures*, 1997, vol. 20, pp. 619–632, doi: 10.1111/j.1460-2695.1997.tb00296.x.

[44] M. A. Linaza, J. L. Romero, J. M. Rodríguez-Ibabe, and J. J. Urcola, “Influence of the microstructure on the fracture toughness and fracture mechanisms of forging steels microalloyed with titanium with ferrite-pearlite structures,” *Scripta Metallurgica et Materiala*, 1993, vol. 29, pp. 451–456, doi: 10.1016/0956-716X(93)90146-J.

[45] L. P. Zhang, C. L. Davis, and M. Strangwood, “Effect of TiN particles and microstructure on fracture toughness in simulated heat-affected zones of a structural steel,” *Metallurgical and Materials Transactions A*, 1999, vol. 30, pp. 2089–2096, doi: 10.1007/s11661-999-0019-7.

[46] S. Mukae, K. Nishio, and M. Katoh, “Solution of TiN during synthetic weld thermal cycles and heat affected zone toughness in low carbon steels,” *Transactions of the Japan Welding Society*, 1987, vol. 18, pp. 148–158.

[47] W. J. Ma, Y. P. Bao, L. H. Zhao, and M. Wang, “Control of the precipitation of TiN inclusions in gear steels,” *International Journal of Minerals, Metallurgy and Materials*, 2014, vol. 21, pp. 234–239, doi: 10.1007/s12613-014-0900-2.

[48] A. Schneider, C. Stallybrass, J. Konrad, A. Kulgemeyer, H. Meuser, and S. Meimeth, "Formation of primary TiN precipitates during solidification of microalloyed steels – Scheil versus DICTRA simulations," *International Journal of Materials Research*, 2008, vol. 99, pp. 674–679, doi: 10.3139/146.101689.

[49] L. Xing, J. Guo, X. Li, Z. Zhang, M. Wang, and Y. Bao, "Control of TiN precipitation behavior in titanium-containing micro-alloyed steel," *Materials Today Communications*, 2020, vol. 25, p. 101292, doi: 10.1016/j.mtcomm.2020.101292.

[50] L. J. Cuddy and J. C. Raley, "Austenite grain coarsening in microalloyed steels," *Metallurgical Transactions A*, 1983, vol. 14, pp. 1989–1995, doi: 10.1007/BF02662366.

[51] N. Fujiyama, T. Nishibata, A. Seki, H. Hirata, K. Kojima, and K. Ogawa, "Austenite grain growth simulation considering the solute-drag effect and pinning effect," *Science and Technology of Advanced Materials*, 2017, vol. 18, pp. 88–95, doi: 10.1080/14686996.2016.1244473.

[52] M. Hamada, Y. Fukada, and Y. Komizo, "Microstructure and precipitation behavior in heat affected zone of C-Mn microalloyed steel containing Nb, V and Ti.," *ISIJ International*, 1995, vol. 35, pp. 1196–1202, doi: 10.2355/isijinternational.35.1196.

[53] Y. Kasamatsu, S. Takashima, and T. Hosoya, "Effect of titanium and nitrogen on toughness of heat-affected zone of steel plate with tensile strength of 50kg/mm2 in high heat input welding," *Tetsu-to-Hagane*, 1979, vol. 65, pp. 1232–1241.

[54] F. B. Pickering, "Overview of titanium microalloyed steels," in *Titanium Technology in Microalloyed Steels*, 1997, pp. 10–43.

[55] C. Wagner, "Theorie der alterung von niederschlagen durch umlosen (Ostwald-reifung)," *Z. Elektrochem*, 1961, vol. 65, pp. 581–591.

[56] J. B. Wiskel, D. G. Ivey, and H. Henein, "The effects of finish rolling temperature and cooling interrupt conditions on precipitation in microalloyed steels using small Angle neutron scattering," *Metallurgical and Materials Transactions B*, 2008, vol. 39, pp. 116–124, doi: 10.1007/s11663-007-9104-8.

[57] D. B. Williams and C. B. Carter, *Transmission Electron Microscopy: A Textbook for*

Materials Science. Springer, Boston, MA, 2009.

[58] B. Gault, M. P. Moody, J. M. Cairney, and S. P. Ringer, *Atom Probe Microscopy*, vol. 160. New York, NY: Springer New York, 2012.

[59] J. Webel, A. Herges, D. Britz, E. Detemple, V. Flaxa, and H. Mohrbacher, "Tracing microalloy precipitation in Nb-Ti HSLA steel during austenite conditioning during austenite conditioning," *Metals*, 2020, vol. 10, p. 243.

[60] Y. Zhang, G. Miyamoto, K. Shinbo, and T. Furuhara, "Comparative study of VC, NbC, and TiC interphase precipitation in microalloyed low-carbon steels," *Metallurgical and Materials Transactions A*, 2020, vol. 51, pp. 6149–6158, doi: 10.1007/s11661-020-06001-x.

[61] S. Mukherjee, I. Timokhina, C. Zhu, S. P. Ringer, and P. D. Hodgson, "Clustering and precipitation processes in a ferritic titanium-molybdenum microalloyed steel," *Journal of Alloys and Compounds*, 2017, vol. 690, pp. 621–632, doi: 10.1016/j.jallcom.2016.08.146.

[62] M. Kapoor, R. O'Malley, and G. B. Thompson, "Atom probe tomography study of multi-microalloyed carbide and carbo-nitride precipitates and the precipitation sequence in Nb-Ti HSLA steels," *Metallurgical and Materials Transactions A*, 2016, vol. 47, pp. 1984–1995, doi: 10.1007/s11661-016-3398-6.

[63] A. D. Sequeira, J. S. Pedersen, and G. Kostorz, "The anisotropy of metallic systems-analysis of small angle scattering data," in *Modem Aspects of Small-Angle Scattering*, H. Brumberger, Ed. Springer Netherlands, 1995, pp. 267–297.

[64] O. Glatter, "Modern methods of data analysis in small angle scattering and light scattering," in *Modem Aspects of Small-Angle Scattering*, H. Brumberger, Ed. Springer Netherlands, 1995, pp. 107–180.

[65] P. Staron, B. Jamnig, H. Leitner, R. Ebner, and H. Clemens, "Small-angle neutron scattering analysis of the precipitation behaviour in a maraging steel," *Journal of Applied Crystallography*, 2003, vol. 36, pp. 415–419, doi: 10.1107/S0021889803000293.

[66] F. Perrard, A. Deschamps, P. Donnadieum, and P. Maugis, "Characterization and modeling on NbC heterogeneous precipitation in model IF steels," in *MS&T Conference*

Proceedings, 2004, pp. 31–37.

[67] K. Osamura, H. Okuda, S. Ochiai, M. Takashima, K. Asano, and M. Furusaka, "Precipitation hardening in Fe-Cu binary and quaternary alloys," *ISIJ International*, 1994, vol. 34, pp. 359–365, doi: 10.2355/isijinternational.34.359.

[68] A. J. Allen, D. Gavillet, and J. R. Weertman, "SANS and TEM studies of isothermal M2C carbide precipitation in ultrahigh strength AF1410 steels," *Acta Metallurgica Et Materialia*, 1993, vol. 41, pp. 1869–1884, doi: 10.1016/0956-7151(93)90207-9.

[69] N. H. Van Dijk, S. E. Offerman, W. G. Bouwman, M. T. Rekveldt, J. Sietsma, and S. Van Der Zwaag, "High temperature SANS experiments on Nb(C, N) and MnS precipitates in HSLA steel," *Metallurgical and Materials Transactions A*, 2002, vol. 33, pp. 1883–1891, doi: 10.1007/s11661-002-0021-9.

[70] H. Bruncková and Š. Nižník, "Chemical isolation of precipitates in IF steels," *Chemical Papers*, 1993, vol. 47, pp. 346–350.

[71] A. Hegetschweiler, T. Kraus, and T. Staudt, "Colloidal analysis of particles extracted from microalloyed steel," *La Metallurgia Italiana*, 2017, pp. 23–28.

[72] J. Lu, "Quantitative microstructural characterization of microalloyed steels," PhD Thesis, University of Alberta, 2009.

[73] C. Chatelier, "Precipitation analysis in microalloyed X70 steels and heat treated L80 and T95 steels," MSc Thesis, University of Alberta, 2017.

[74] B. Soenen, S. Jacobs, and C. Klinkenberg, "Development of precipitation modeling tools for transfer of processing conditions to a CSP line," in *Microalloyed Steels 2000, Proceedings from Materials Solutions Conference*, 2002, pp. 16–24.

[75] Y. Ishiguro, T. Murayama, A. Chino, K. Sato, Y. Shima, and A. Kido, "A precise quantitative analysis of precipitates in Ti-bearing interstitial-free steel," *Tetsu-to-Hagane*, 1997, vol. 83, pp. 479–484, doi: 10.2355/tetsutohagane1955.83.8_479.

[76] H. M. Rietveld, "A profile refinement method for nuclear and magnetic structures," *Journal of Applied Crystallography*, 1969, vol. 2, pp. 65–71, doi:

10.1107/s0021889869006558.

[77] P. Scherrer, “Bestimmung der größe und der inneren struktur von kolloidteilchen mittels röntgenstrahlen,” *Nachrichten von der Gesellschaft der Wissenschaften zu Göttingen, Mathematisch-Physikalische Klasse*, 1918, vol. 1918, pp. 98–100.

[78] D. Balzar, N. Audebrand, M. R. Daymond, A. Fitch, A. Hewat, and J. I. Langford, “Size-strain line-broadening analysis of the ceria round-robin sample,” *Journal of Applied Crystallography*, 2004, vol. 37, pp. 911–924, doi: 10.1107/S0021889804022551.

[79] N. C. Popa and D. Balzar, “An analytical approximation for a size-broadened profile given by the lognormal and gamma distributions,” *Journal of Applied Crystallography*, 2002, vol. 35, pp. 338–346, doi: 10.1107/S0021889802004156.

[80] A. L. Patterson, “The scherrer formula for X-ray particle size determination,” *Physical Review*, 1939, vol. 56, pp. 978–982, doi: 10.1103/PhysRev.56.978.

[81] R. J. Hill and C. J. Howard, “Quantitative phase analysis from neutron powder diffraction data using the Rietveld method,” *Journal of Applied Crystallography*, 1987, vol. 20, pp. 467–474, doi: 10.1107/S0021889887086199.

[82] J. O. Andersson, T. Helander, L. Höglund, P. Shi, and B. Sundman, “Thermo-Calc & DICTRA, computational tools for materials science,” *Calphad: Computer Coupling of Phase Diagrams and Thermochemistry*, 2002, vol. 26, pp. 273–312, doi: 10.1016/S0364-5916(02)00037-8.

[83] “The CALPHAD Methodology | Thermo-Calc Software.” https://thermocalc.com/about-us/methodology/the-calphad-methodology/ (accessed Apr. 10, 2021).

[84] Y. Huang, G. G. Cheng, S. J. Li, W. X. Dai, and Y. Xie, “Effect of Ti(C, N) particle on the impact toughness of B-microalloyed steel,” *Metals*, 2018, vol. 8, no. 868.

[85] G. A. Miller and E. T. Stephenson, “The effect of the carbide phases on the crack grow of 0.5 pct Mo-B steels under impact, cyclic, and monotonically increasing loading,” *Metallurgical Transactions*, 1974, vol. 5, pp. 659–666, doi: 10.1007/bf02644662.

[86] R. L. Bodnar, Y. Shen, and W. Furdanowicz, “An assessment of the application of TiN

technology to controlled-rolled, low-carbon Nb - (V) steels," in *Mechanical Working Steel Processing Proceedings*, 1998, pp. 929–945.

[87] J.-Y. Li and W.-Y. Zhang, "Effect of TiN inclusion on fracture toughness in ultrahigh strength steel.," *ISIJ International*, 1989, vol. 29, pp. 158–164, doi: 10.2355/isijinternational.29.158.

[88] M. I. Vega, S. F. Medina, A. Quispe, M. Gómez, and P. P. Gómez, "Recrystallisation driving forces against pinning forces in hot rolling of Ti-microalloyed steels," *Materials Science and Engineering A*, 2006, vol. 423, pp. 253–261, doi: 10.1016/j.msea.2006.02.037.

[89] M. Arribas, B. López, and J. M. Rodriguez-Ibabe, "Influence of Ti on static recrystallization in near net shape steels," *Materials Science Forum*, 2005, vol. 500–501, pp. 131–138, doi: 10.4028/www.scientific.net/msf.500-501.131.

[90] S. C. Wang, "The effect of titanium and nitrogen contents on the austenite grain coarsening temperature," *Journal of Materials Science*, 1989, vol. 24, pp. 105–109, doi: 10.1007/BF00660940.

[91] S. Okaguchi and T. Hashimoto, "Characteristics of precipitates and mechanical properties in Ti bearing HSLA steels," *Transactions of the Iron and Steel Institute of Japan*, 1987, vol. 27, pp. 467–473, doi: 10.2355/isijinternational1966.27.467.

[92] Z. Chen, M. H. Loretto, and R. C. Cochrane, "Nature of large precipitates in titanium-containing HSLA steels," *Materials Science and Technology*, 1987, vol. 3, pp. 836–844, doi: 10.1179/mst.1987.3.10.836.

[93] R. E. Dinnebier, A. Leineweber, and J. S. O. Evans, *Rietveld Refinement Practical Powder Diffraction Pattern Analysis using TOPAS*. De Gruyter, 2019.

[94] A. A. Coelho, "TOPAS and TOPAS-Academic : an optimization program integrating computer algebra and crystallographic objects written in C++," *Journal of Applied Crystallography*, 2018, vol. 51, pp. 210–218, doi: 10.1107/S1600576718000183.

[95] G. Caglioti, A. Paoletti, and F. P. Ricci, "Choice of collimators for a crystal spectrometer for neutron diffraction," *Nuclear Instruments*, 1958, vol. 3, pp. 223–228.

[96] A. Mehdad, R. E. Jentoft, and F. C. Jentoft, “Single-phase mixed molybdenum-niobium carbides: Synthesis, characterization and multifunctional catalytic behavior in toluene conversion,” *Journal of Catalysis*, 2017, vol. 351, pp. 161–173, doi: 10.1016/j.jcat.2017.04.022.

[97] B. H. Toby, “R factors in Rietveld analysis: How good is good enough?,” *Powder Diffraction*, 2006, vol. 21, pp. 67–70, doi: 10.1154/1.2179804.

[98] D. A. Porter, K. E. Easterling, and K. E. Easterling, *Phase Transformations in Metals and Alloys*. CRC Press, 2009.

[99] J. Kunze, C. Mickel, M. Leonhardt, and S. Oswald, “Precipitation of titanium nitride in low-alloyed steel during solidification,” *Steel Research*, 1997, vol. 68, pp. 403–408, doi: 10.1002/srin.199700574.

[100] I. Rak, V. Gliha, and M. Kqçak, “Weldability and toughness assessment of Ti-microalloyed offshore steel,” *Metallurgical and Materials Transactions A*, 1997, vol. 28, pp. 199–206, doi: 10.1007/s11661-997-0096-4.

[101] R. Wang, C. I. Garcia, M. Hua, K. Cho, H. Zhang, and A. J. Deardo, “Microstructure and precipitation behavior of Nb, Ti complex microalloyed steel produced by compact strip processing,” *ISIJ International*, 2006, vol. 46, pp. 1345–1353, doi: 10.2355/isijinternational.46.1345.

[102] C. Zhou and R. Priestner, “The evolution of precipitates in Nb-Ti microalloyed steels during solidification and post-solidification cooling,” *ISIJ International*, 1996, vol. 36, pp. 1397–1405, doi: 10.2355/isijinternational.36.1397.

[103] G. Basanta, A. L. Rivas, and A. Ruiz, “SEM characterization of complex precipitates in an as-cast Nb-V-Ti microalloyed steel,” *Revista Latinoamericana de Metalurgia y Materiales*, 2011, vol. 31, pp. 138–144.

[104] S. Matsuda and N. Okumura, “Effect of distribution of TiN precipitate particles on the austenite grain size of low carbon low alloy steels,” *Transactions of the Iron and Steel Institute of Japan*, 1978, vol. 18, pp. 198–205, doi: 10.2355/isijinternational1966.18.198.

[105] K. Narita, “Physical chemistry of the groups IVa (Ti, Zr), Va (V, Nb, Ta) and the rare

earth elements in steel," *Transactions of the Iron and Steel Institute of Japan*, 1975, vol. 15, pp. 145–152, doi: 10.2355/isijinternational1966.15.145.

[106] Y. L. Jin and S. L. Du, "Precipitation behaviour and control of TiN inclusions in rail steels," *Ironmaking & Steelmaking*, 2016, vol. 45, pp. 224–229, doi: 10.1080/03019233.2016.1253448.

[107] J. Stock, C. Enloe, R. O'Malley, K. Findley, and J. Speer, "Cooling rate effects on the as-cast titanium nitride precipitation size distribution in a low-carbon steel," *AIST Transactions*, 2014, vol. 11, pp. 180–187.

[108] T. Liu, D. Chen, M. Long, P. Liu, H. Duan, and L. Gui, "Control of coarse precipitates of titanium nitride in high-strength low-alloy steel," *Metal Science and Heat Treatment*, 2020, vol. 61, pp. 534–542, doi: 10.1007/s11041-020-00477-5.

[109] A. N. Zavalishchin, M. I. Rumyantsev, D. N. Chikishev, M. V. Efremova, and E. V. Kozhevnikova, "Influence of 'soft' reduction on the structure of continuous cast ingot and the properties of rolled products of microalloyed steels," *Metallurgist*, 2019, vol. 63, pp. 238–248, doi: 10.1007/s11015-019-00817-8.

[110] Y. Chen, G. J. Li, S. B. Yang, and M. Y. Zhu, "Dynamic soft reduction for continuously cast rail bloom," *Journal of Iron and Steel Research International*, 2007, vol. 14, pp. 13–51, doi: 10.1016/S1006-706X(07)60066-1.

[111] R. Raj, "Segregation and homogenization of alloying elements in X70 steels," MSc Thesis, University of Alberta, 2020.

[112] R. Kampmann and R. Wagner, "Kinetics of precipitation in metastable binary alloys - theory and application to Cu-1.9 at.% Ti and Ni-14 at.% Al," in *Decomposition of alloys: the early stages*, P. Haasen, V. Gerold, and R. Wagner, Eds. Oxford: Pergamon Press, 1984.

[113] D. Gendt, "Cinétique de précipitation du carbure de niobium dans la ferrite," PhD Thesis, CEA Saclay - Usinor, 2001.

[114] B. Loberg, A. Nordgren, J. Strid, and K. E. Easterling, "Role of alloy composition on the stability of nitrides in Ti-microalloyed steels during weld thermal cycles," *Metallurgical*

and Materials Transactions A, 1984, vol. 15 A, pp. 33–41, doi: 10.1007/BF02644385.

[115] J. Moon, J. Lee, and C. Lee, "Prediction for the austenite grain size in the presence of growing particles in the weld HAZ of Ti-microalloyed steel," *Materials Science and Engineering A*, 2007, vol. 459, pp. 40–46, doi: 10.1016/j.msea.2006.12.073.

[116] H. R. Wang and W. Wang, "Precipitation of complex carbonitrides in a Nb-Ti microalloyed plate steel," *Journal of Materials Science*, 2009, vol. 44, pp. 591–600, doi: 10.1007/s10853-008-3069-0.

[117] S. G. Hong, H. J. Jun, K. B. Kang, and C. G. Park, "Evolution of precipitates in the Nb-Ti-V microalloyed HSLA steels during reheating," *Scripta Materialia*, 2003, vol. 48, pp. 1201–1206, doi: 10.1016/S1359-6462(02)00567-5.

[118] F. Ma, G. Wen, P. Tang, G. Xu, F. Mei, and W. Wang, "Effect of cooling rate on the precipitation behavior of carbonitride in microalloyed steel slab," *Metallurgical and Materials Transactions B*, 2011, vol. 42, pp. 81–86, doi: 10.1007/s11663-010-9454-5.

[119] M. T. Nagata, J. G. Speer, and D. K. Matlock, "Titanium nitride precipitation behavior in thin-slab cast high-strength low-alloy steels," *Metallurgical and Materials Transactions A*, 2002, vol. 33, pp. 3099–3110, doi: 10.1007/s11661-002-0294-z.

[120] H. J. Jun, K. B. B. Kang, and C. G. G. Park, "Effects of cooling rate and isothermal holding on the precipitation behavior during solidification of Nb-Ti bearing HSLA steels," in *The Thirteenth International Offshore and Polar Engineering Conference*, Dec. 2003, vol. 49, pp. 1081–1086, doi: 10.1016/j.scriptamat.2003.08.013.

Appendix A SEM/EDX analysis of coarse TiN-rich particles

The following presents the SEM SE micrographs and EDX spectra of the coarse TiN-rich particles extracted with the carbon replica method.

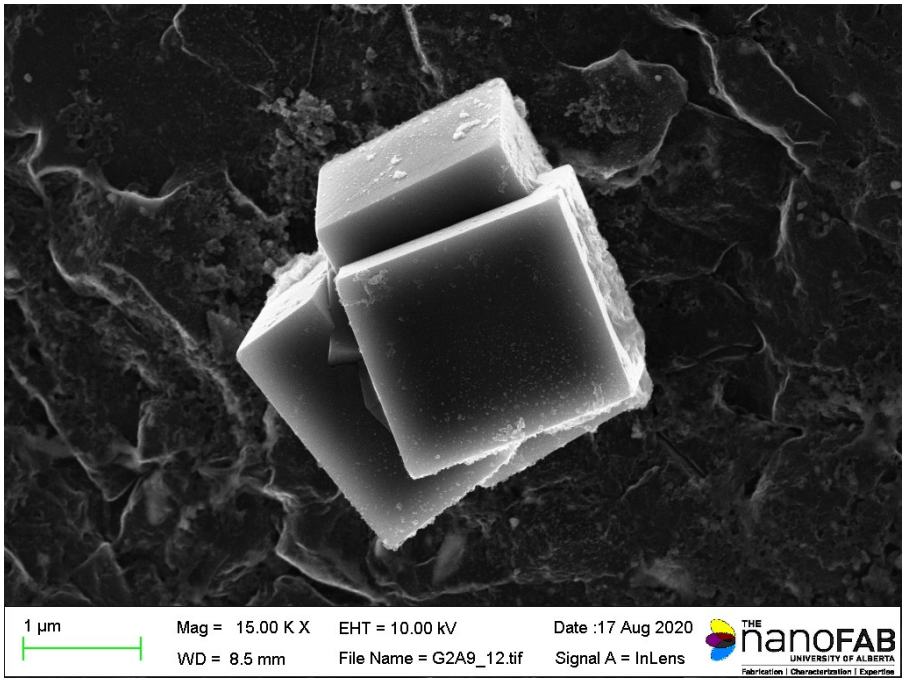

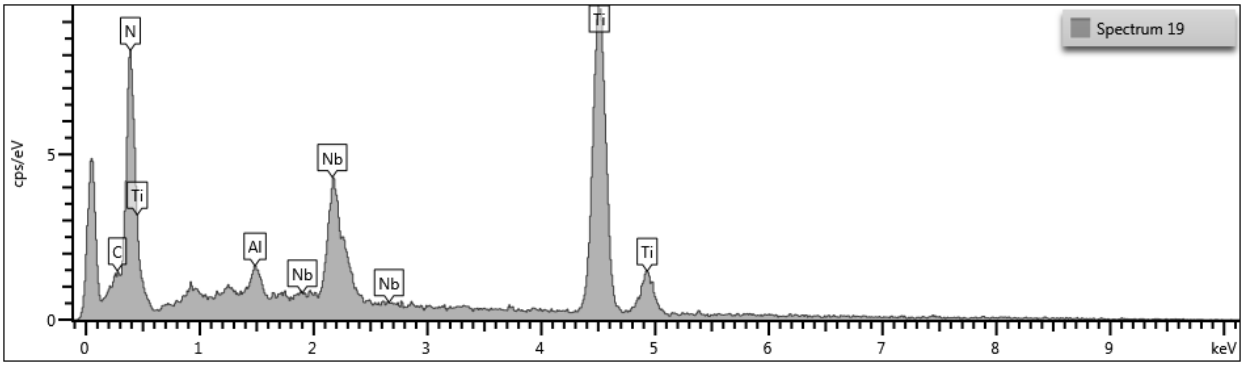

Figure A.1– SEM SE micrograph and EDX spectrum of the coarse TiN-rich particle extracted using carbon replica from T36-1 QL.

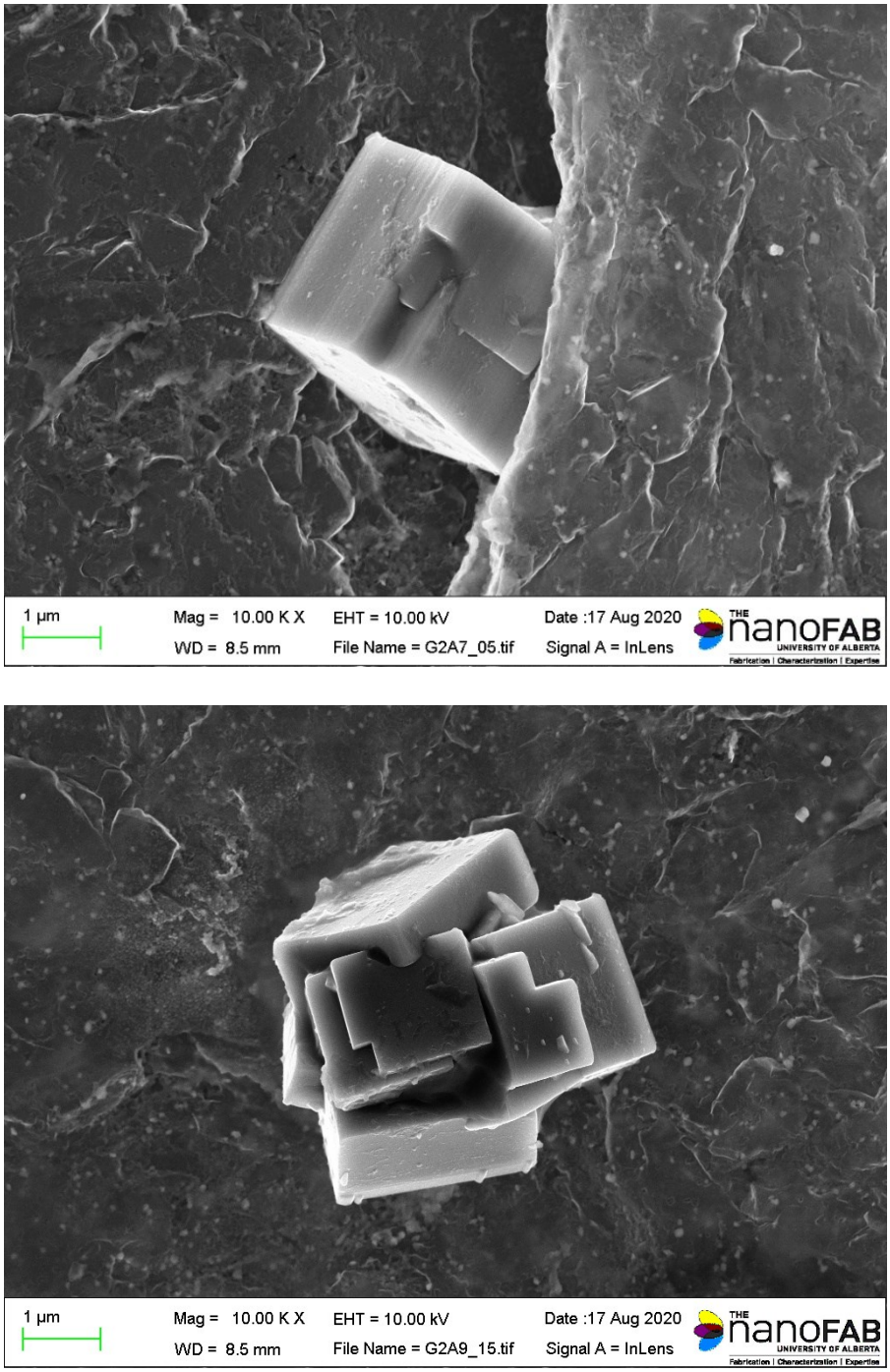

Figure A.2– SEM SE micrographs of the coarse TiN-rich particles extracted using carbon replica from T36-1 QL.

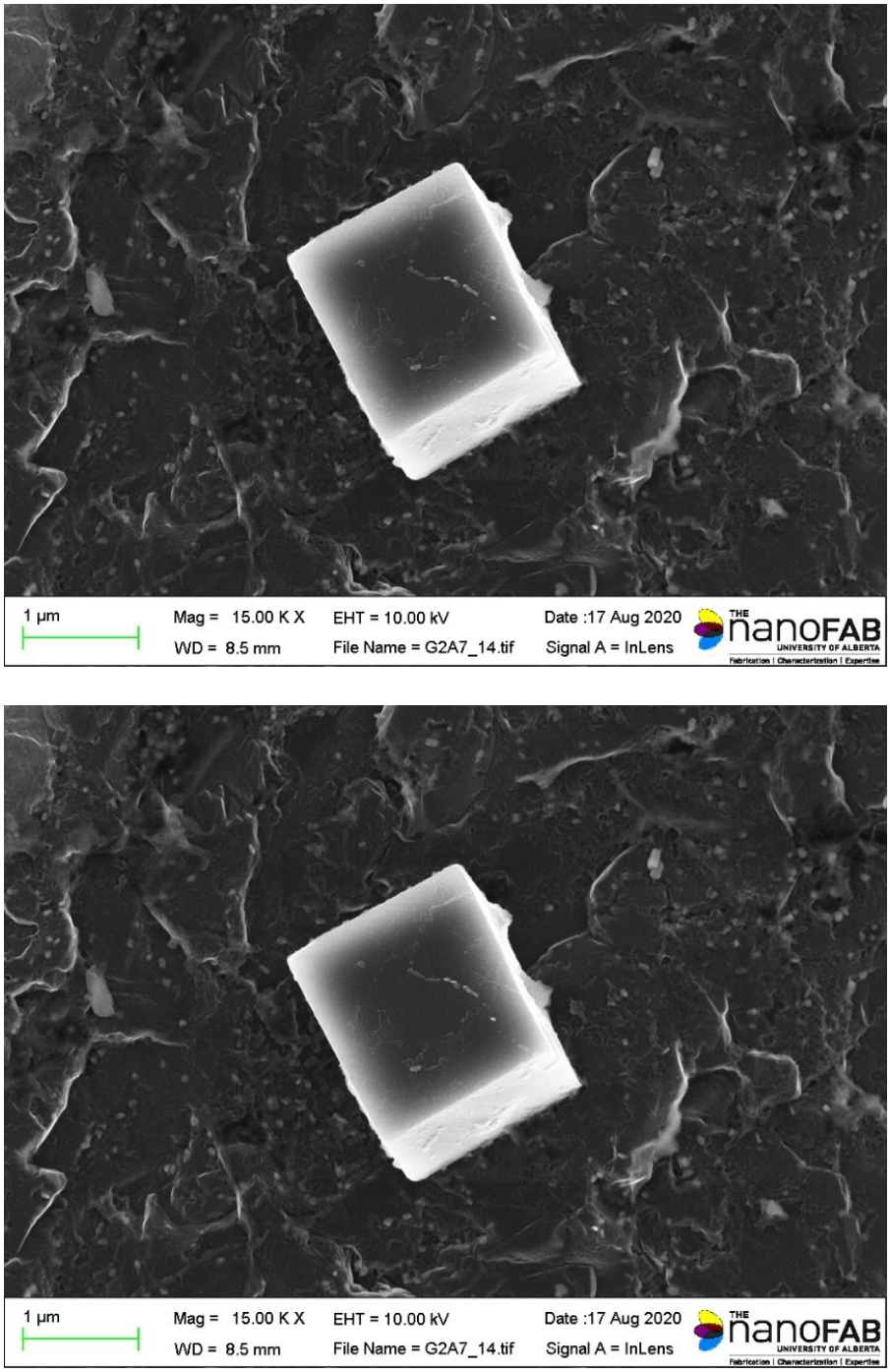

Figure A.3– SEM SE micrographs of the coarse TiN-rich particles extracted using carbon replica from T36-1 QL.

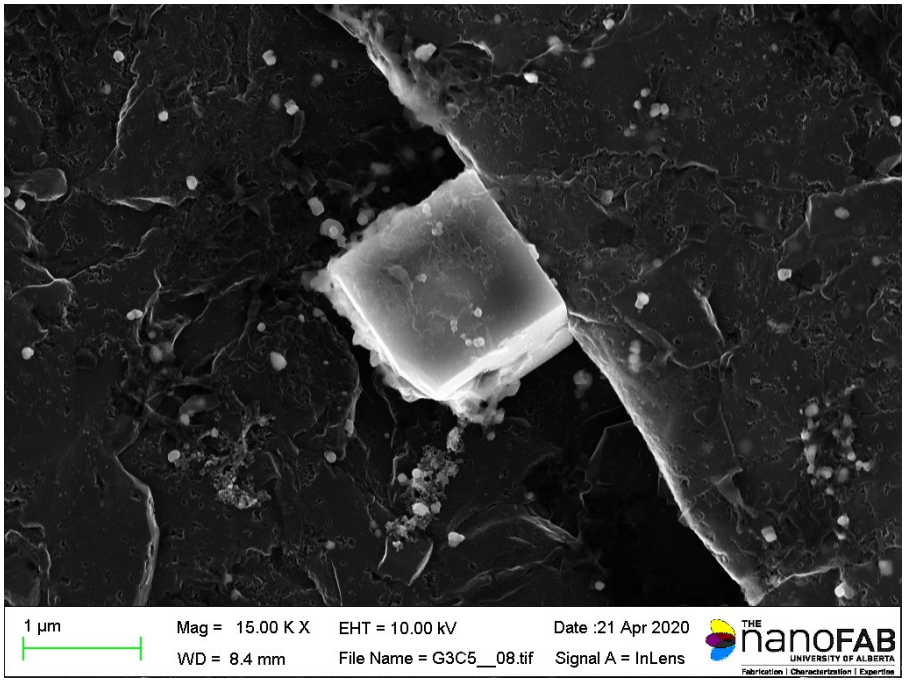

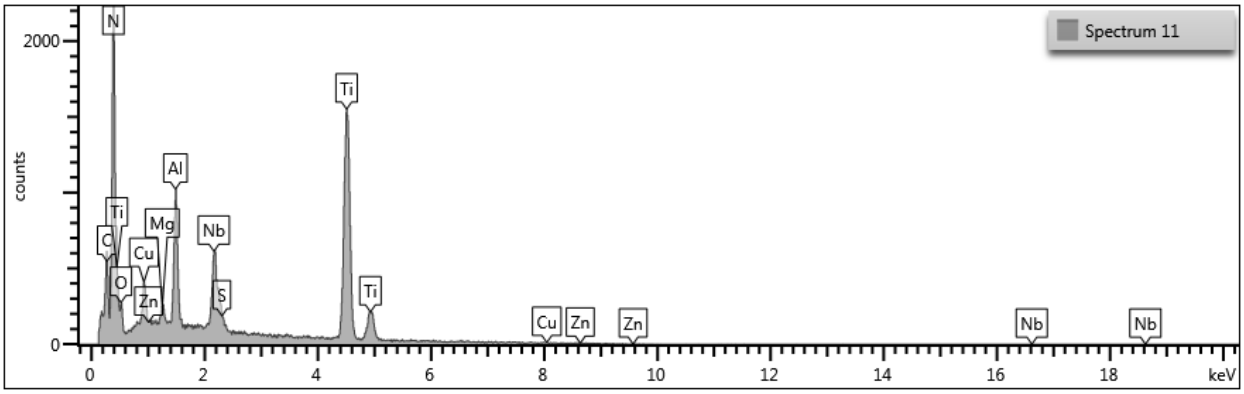

Figure A.4– SEM SE micrograph and EDX spectrum of the coarse TiN-rich particle extracted using carbon replica from T36-2 QL.

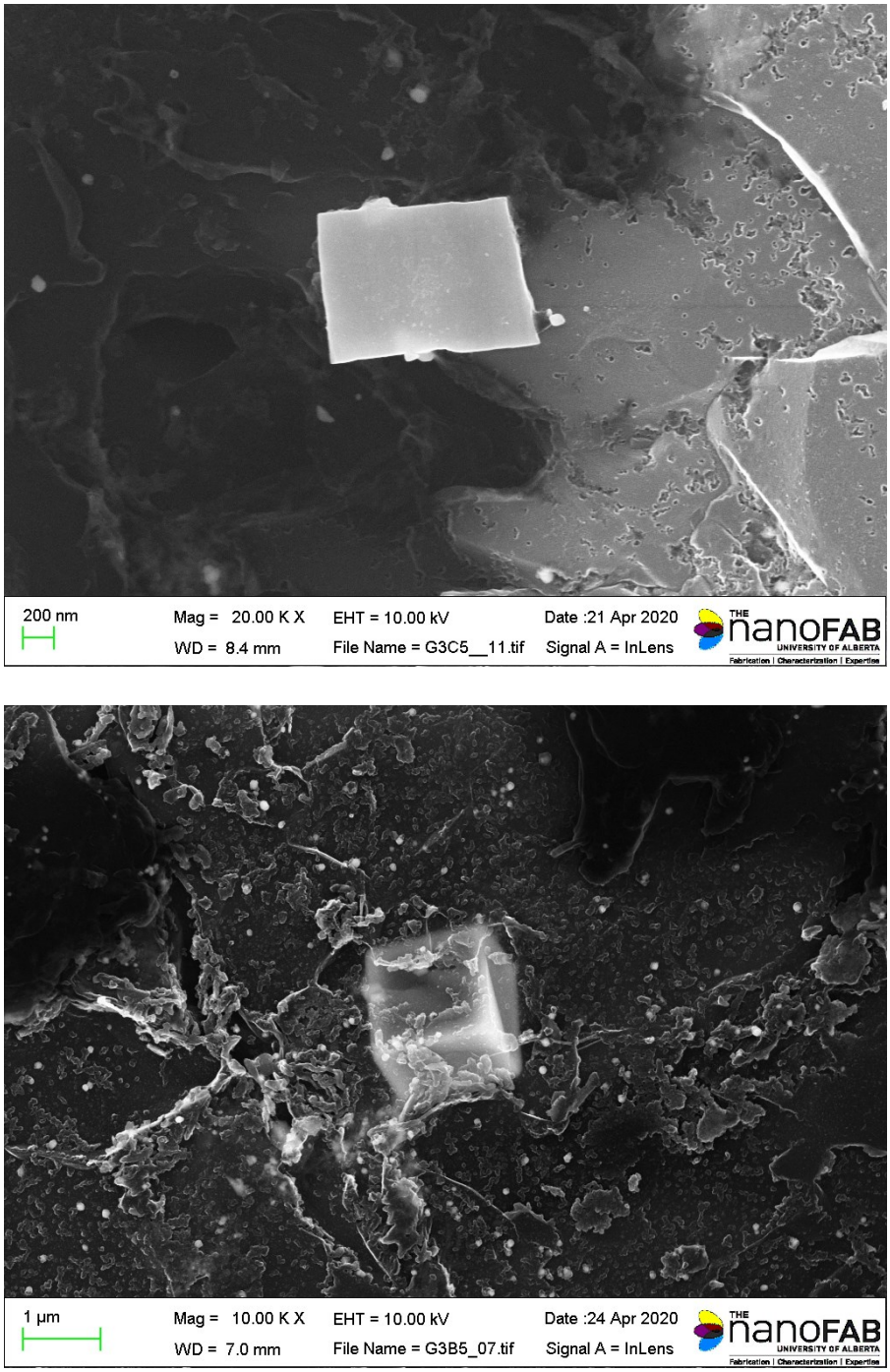

Figure A.5– SEM SE micrographs of the coarse TiN-rich particles extracted using carbon replica from T36-2 QL.

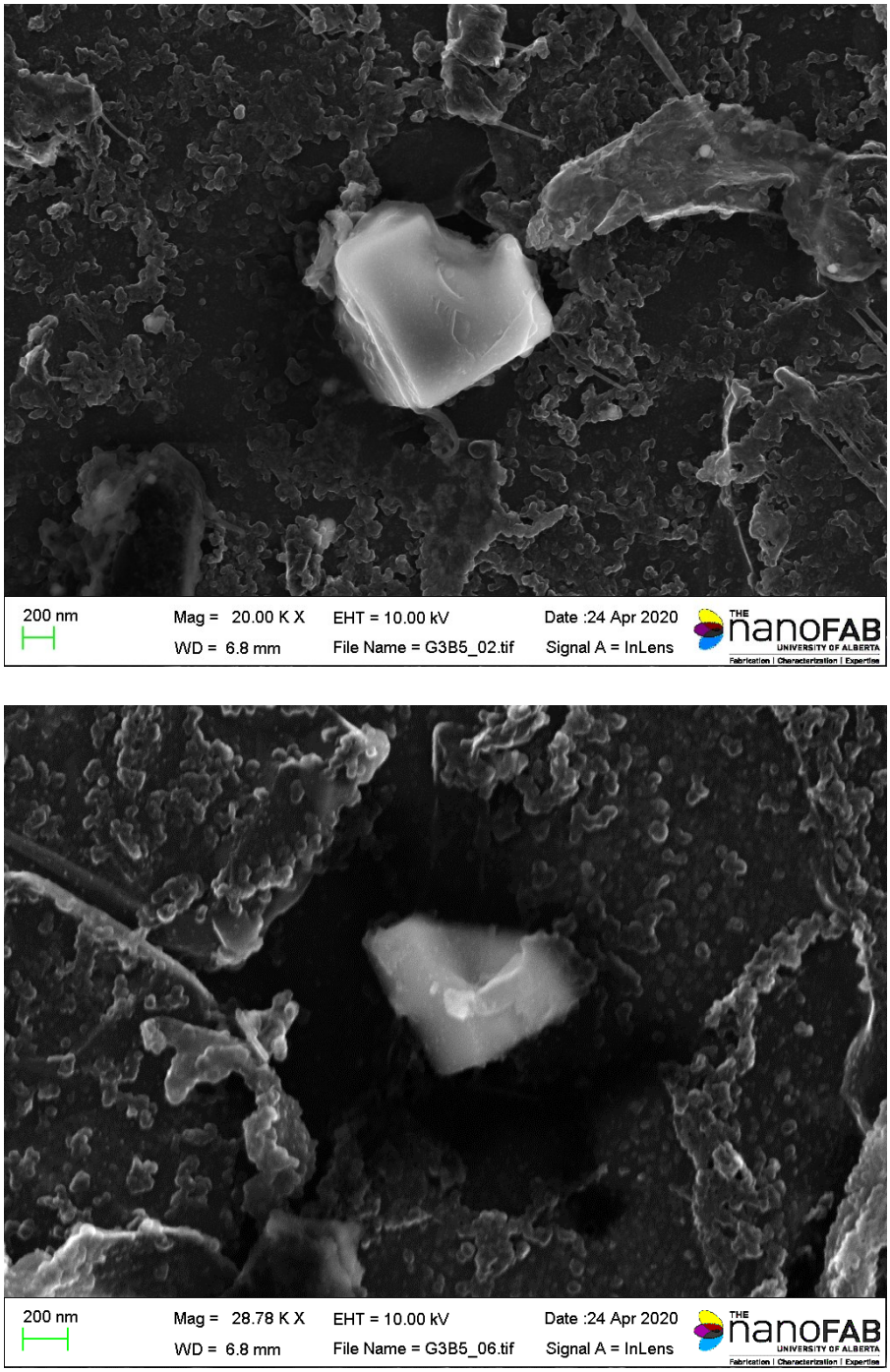

Figure A.6– SEM SE micrographs of the coarse TiN-rich particles extracted using carbon replica from T36-2 QL.

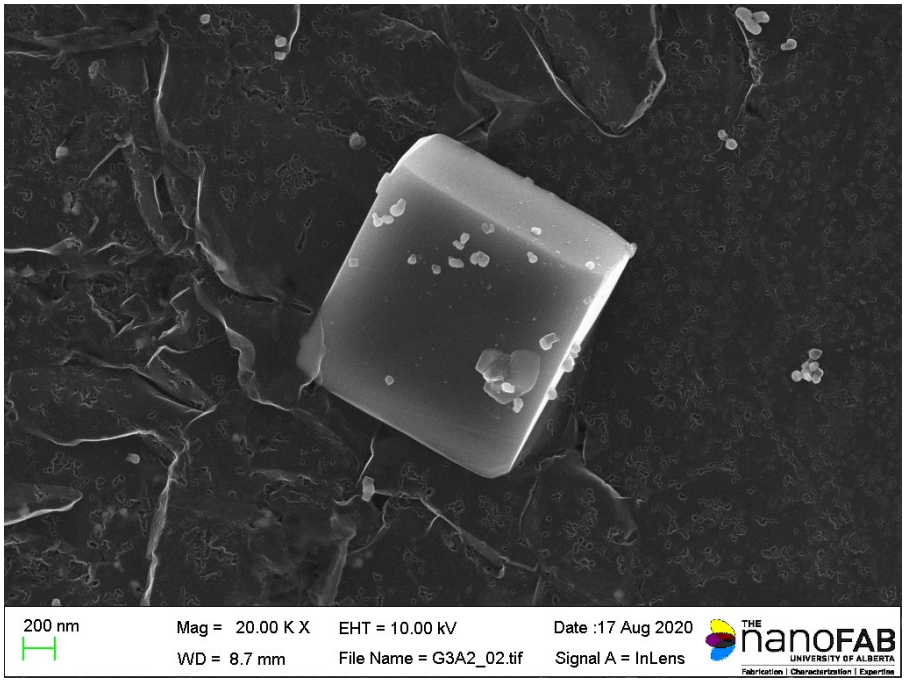

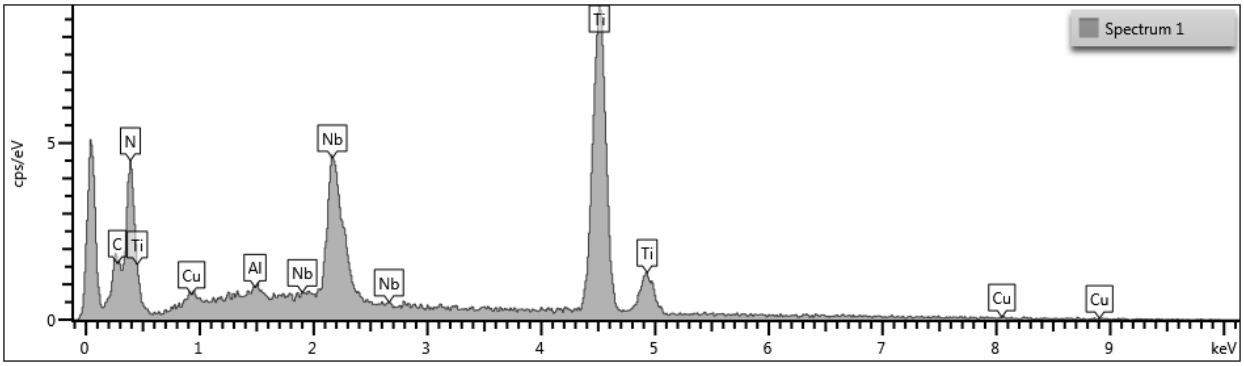

Figure A.7– SEM SE micrograph and EDX spectrum of the coarse TiN-rich particle extracted using carbon replica from T36-3 QL.

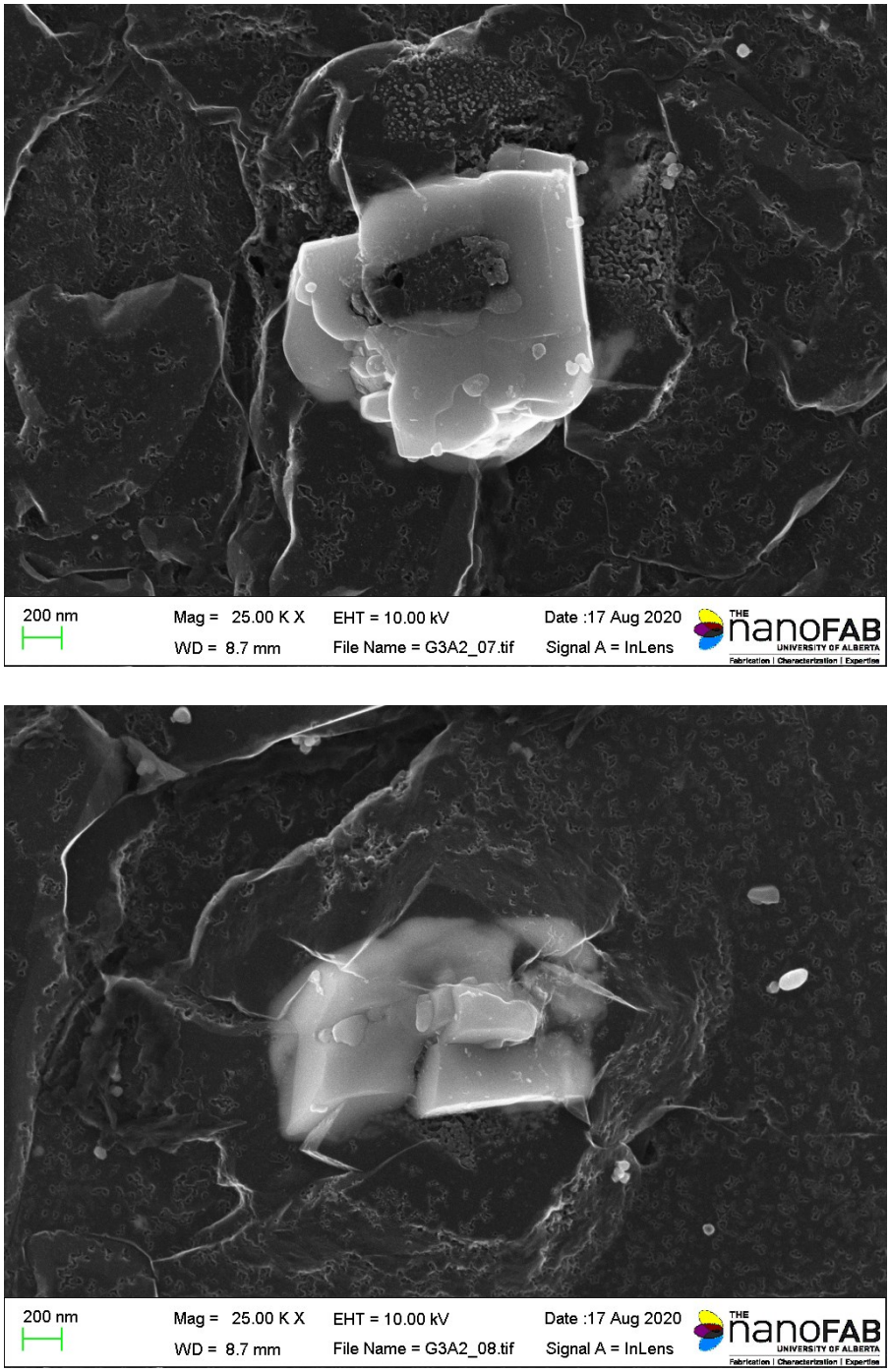

Figure A.8– SEM SE micrographs of the coarse TiN-rich particles extracted using carbon replica from T36-3 QL.

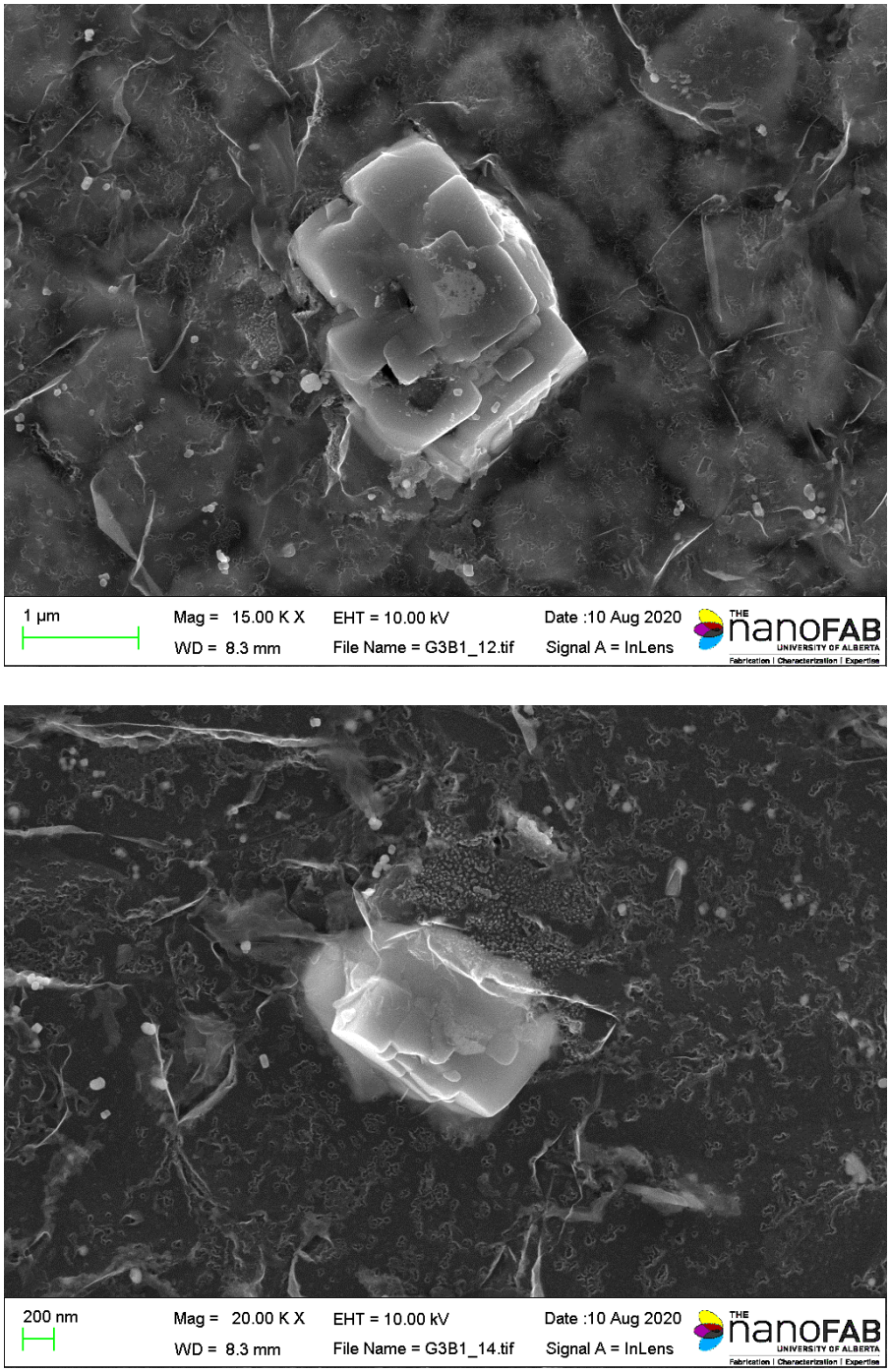

Figure A.9– SEM SE micrographs of the coarse TiN-rich particles extracted using carbon replica from T36-3 QL.

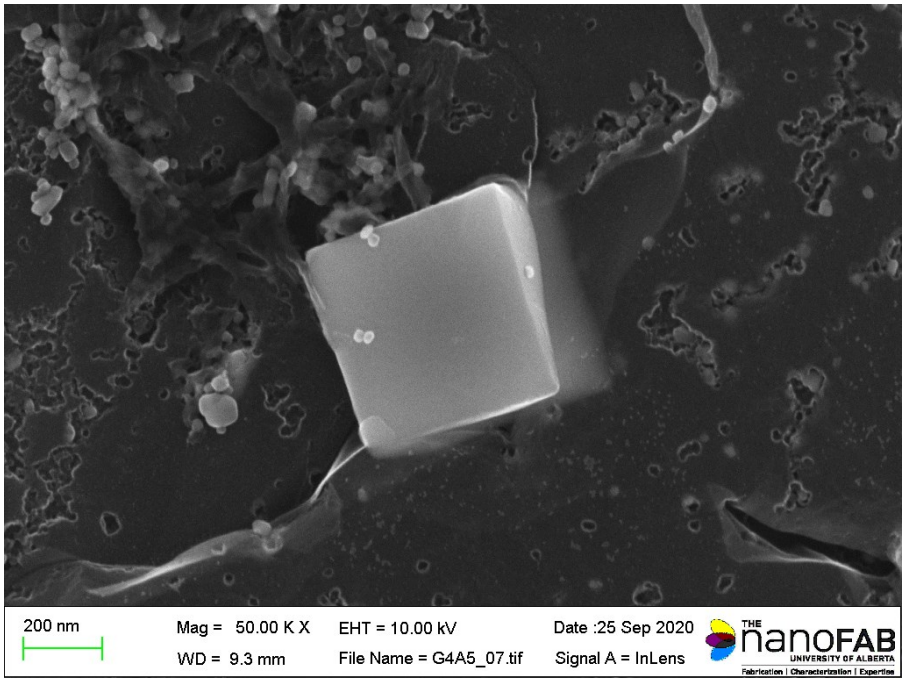

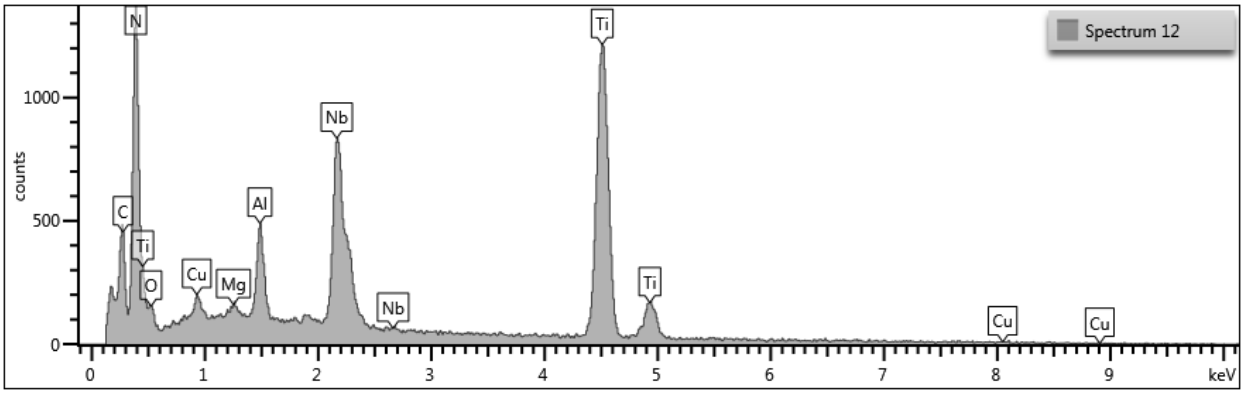

Figure A.10– SEM SE micrograph and EDX spectrum of the coarse TiN-rich particle extracted using carbon replica from D-1 QL.

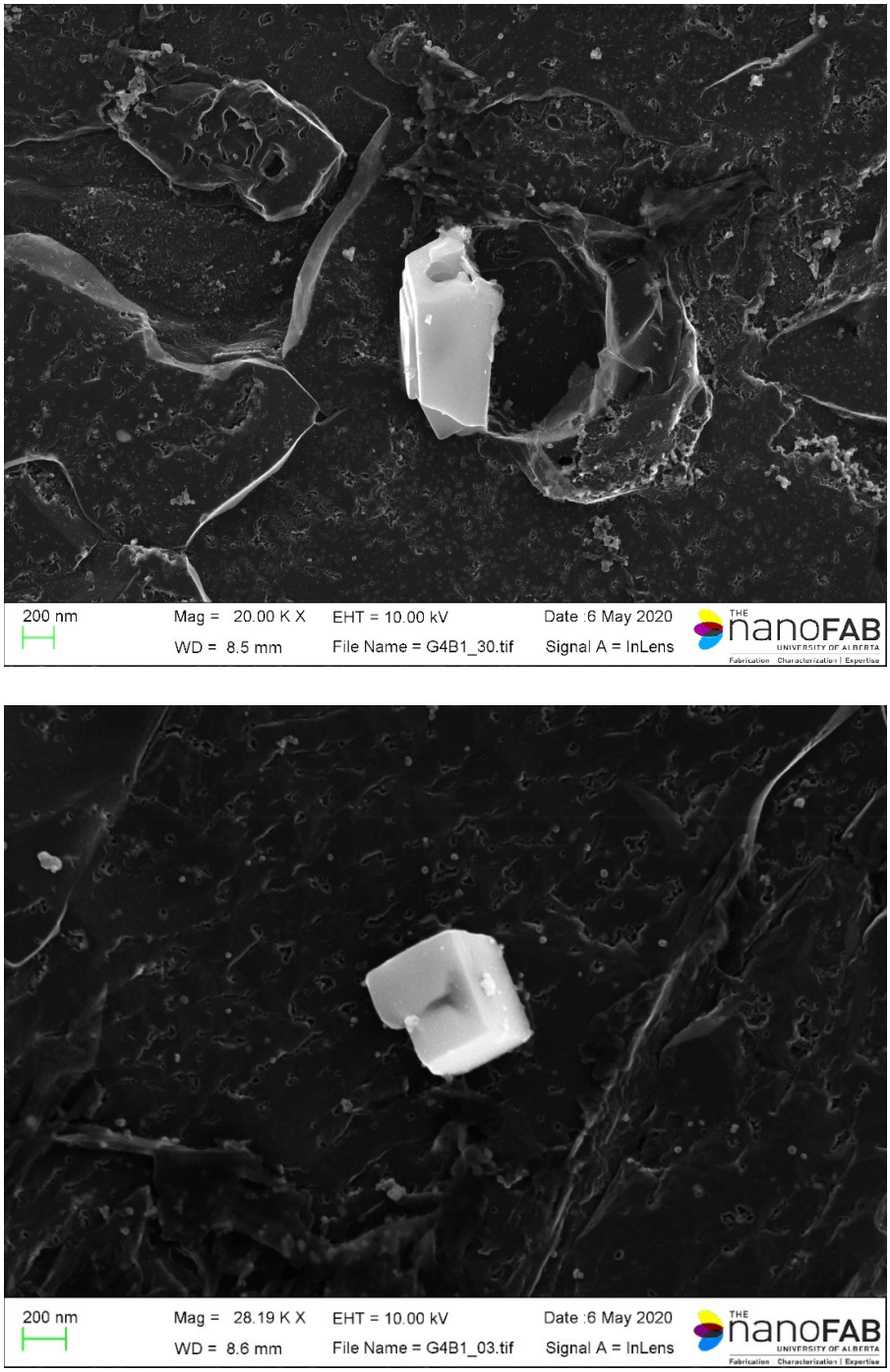

Figure A.11– SEM SE micrographs of the coarse TiN-rich particles extracted using carbon replica from D-1 QL.

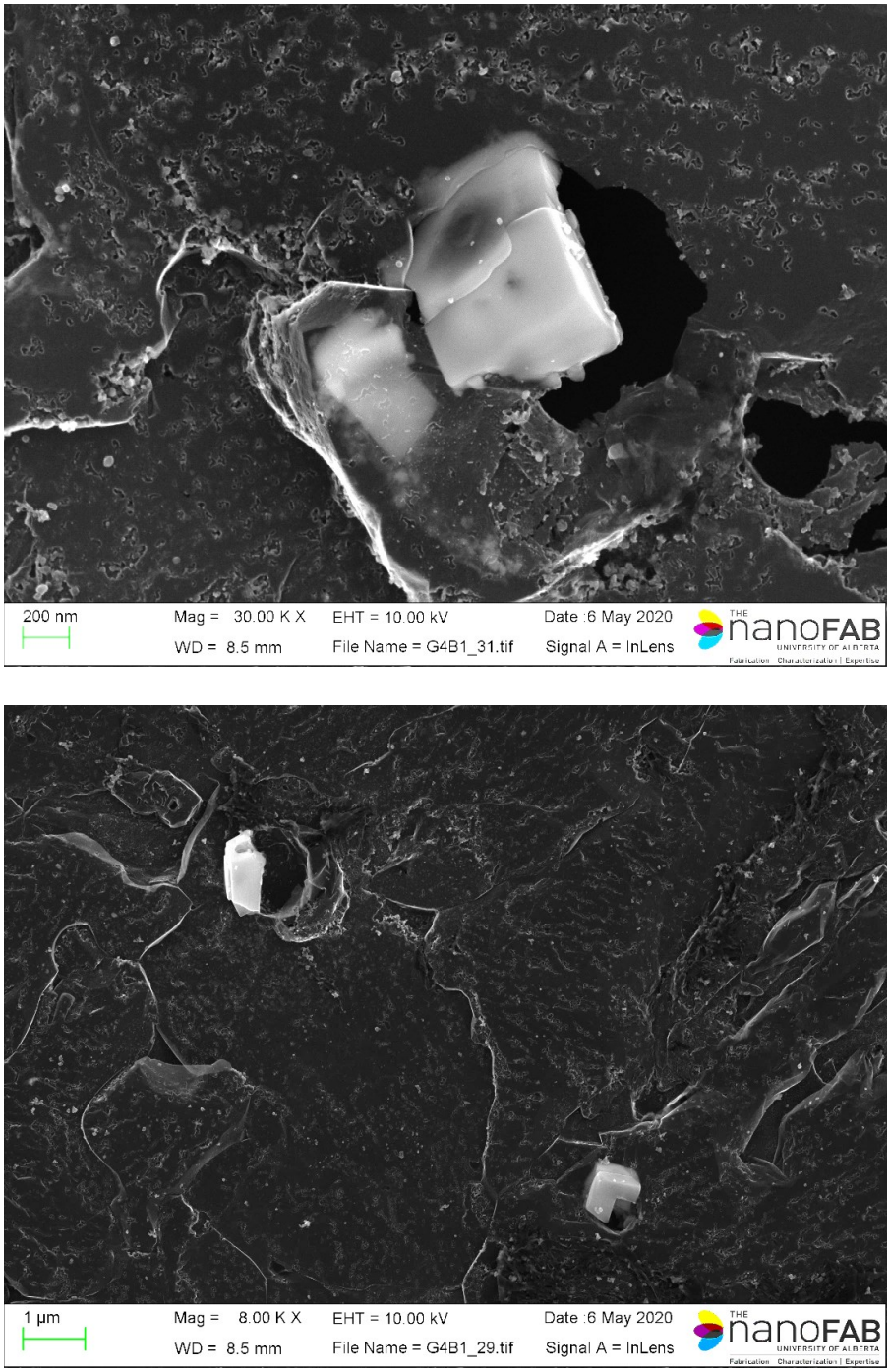

Figure A.12– SEM SE micrographs of the coarse TiN-rich particles extracted using carbon replica from D-1 QL.

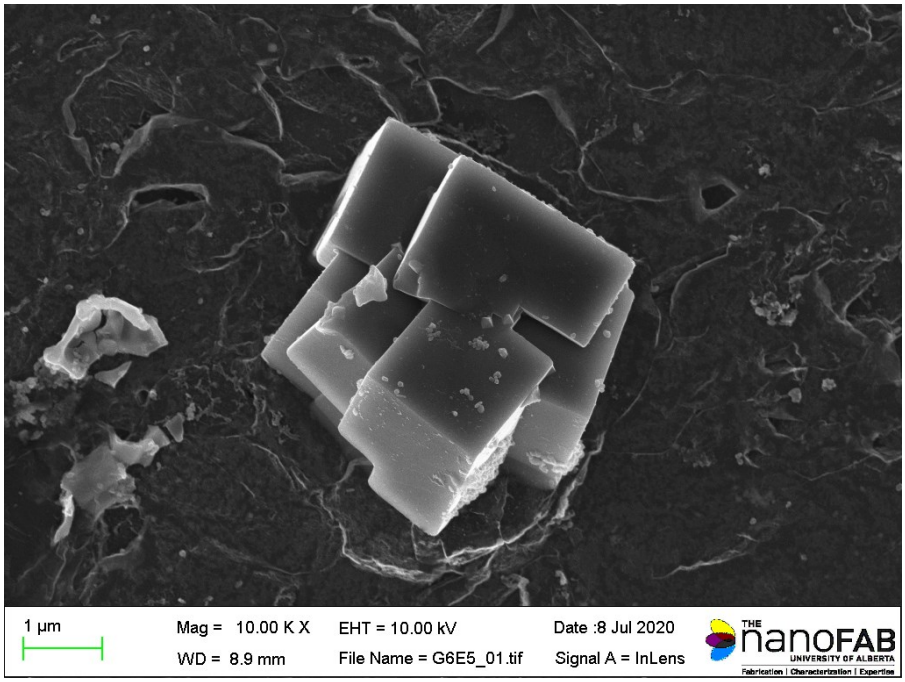

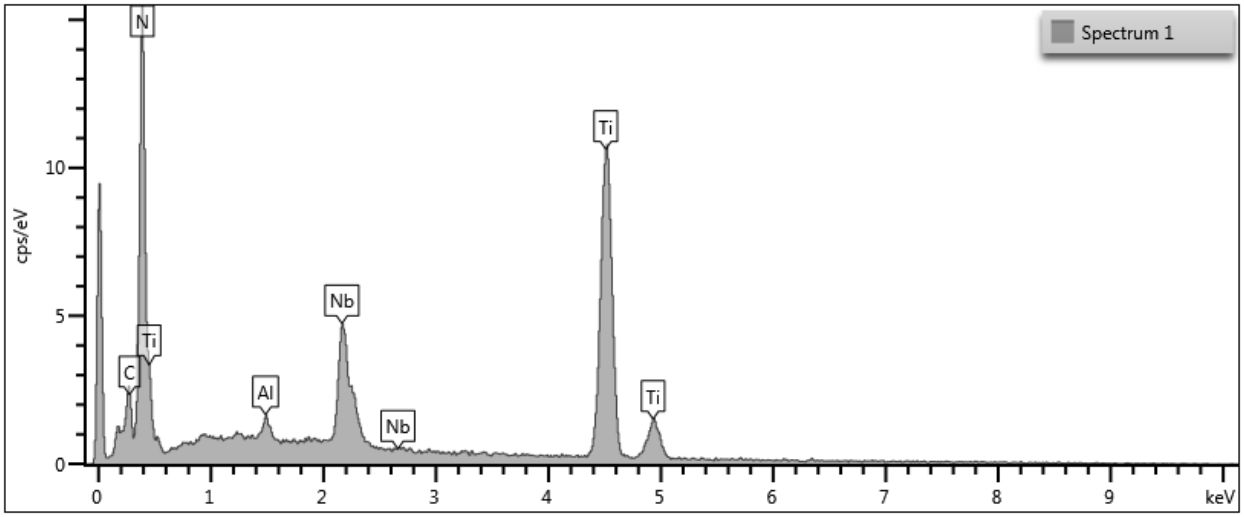

Figure A.13– SEM SE micrograph and EDX spectrum of the coarse TiN-rich particle extracted using carbon replica from B60 QL.

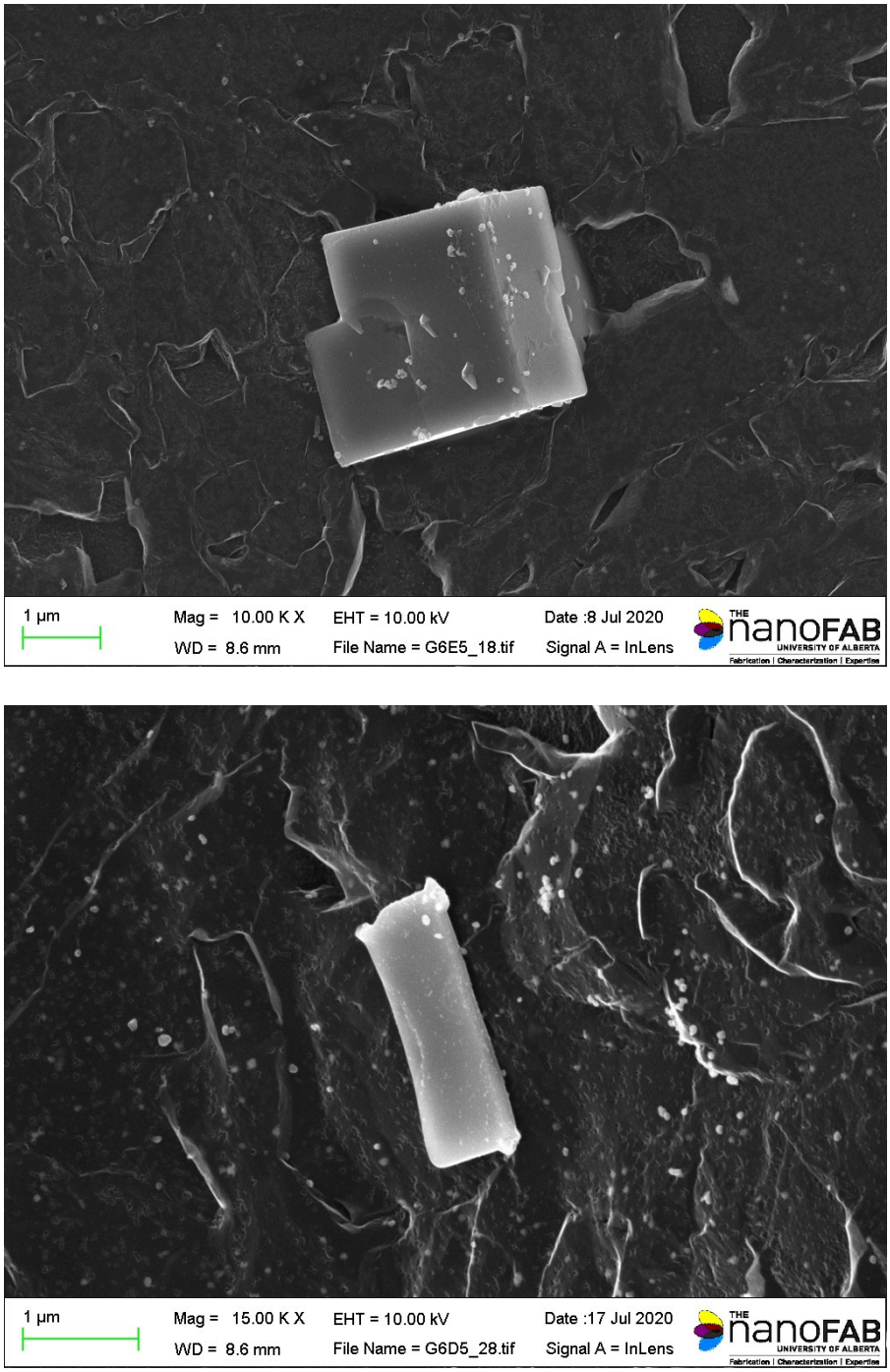

Figure A.14– SEM SE micrographs of the coarse TiN-rich particles extracted using carbon replica from B60 QL.

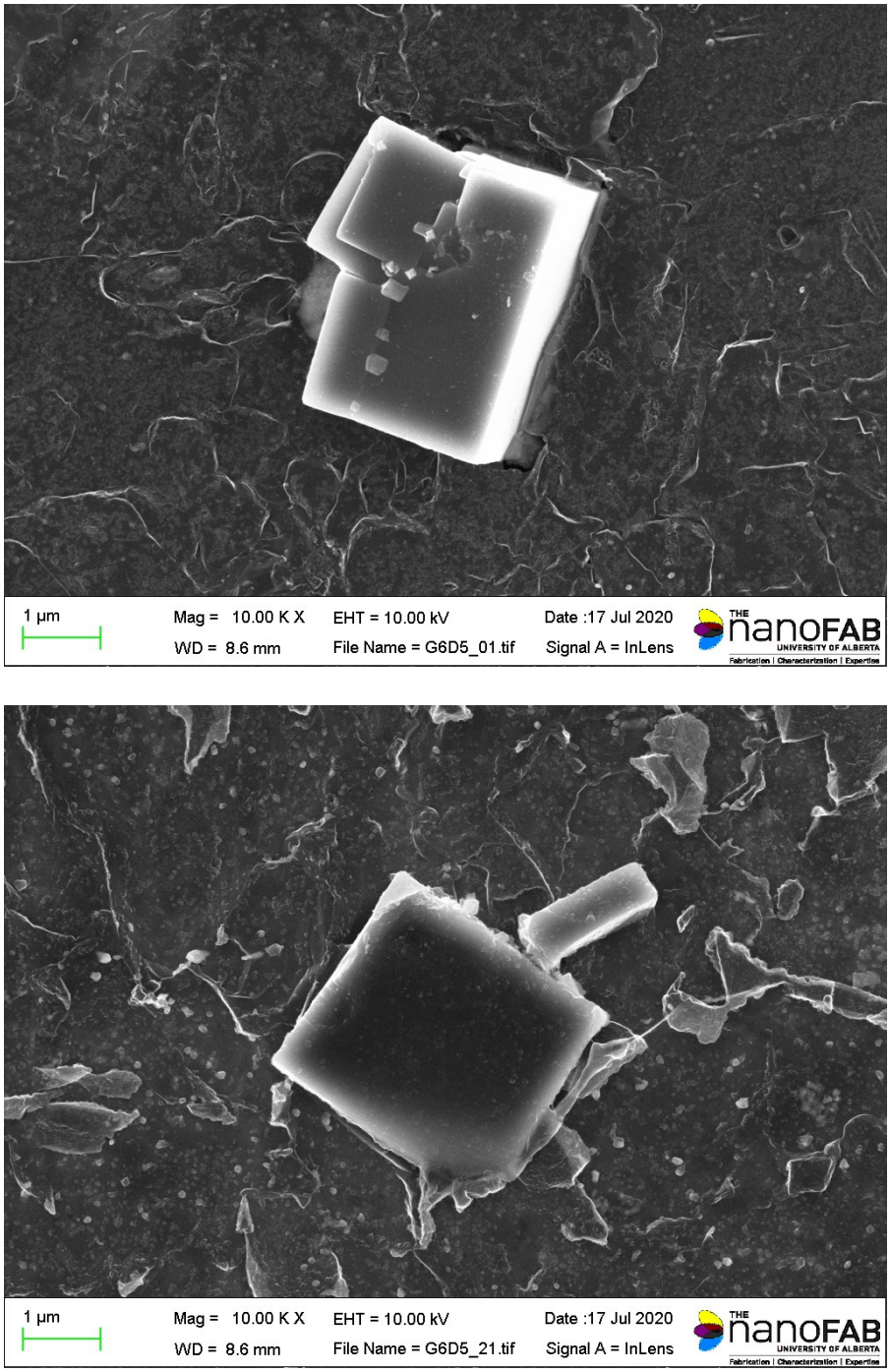

Figure A.15– SEM SE micrographs of the coarse TiN-rich particles extracted using carbon replica from B60 QL.

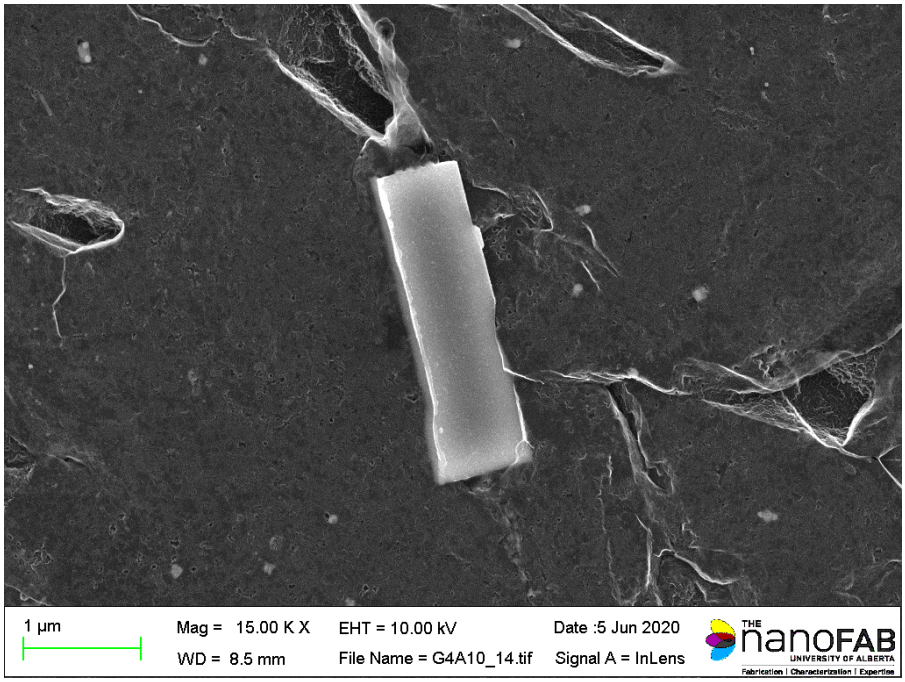

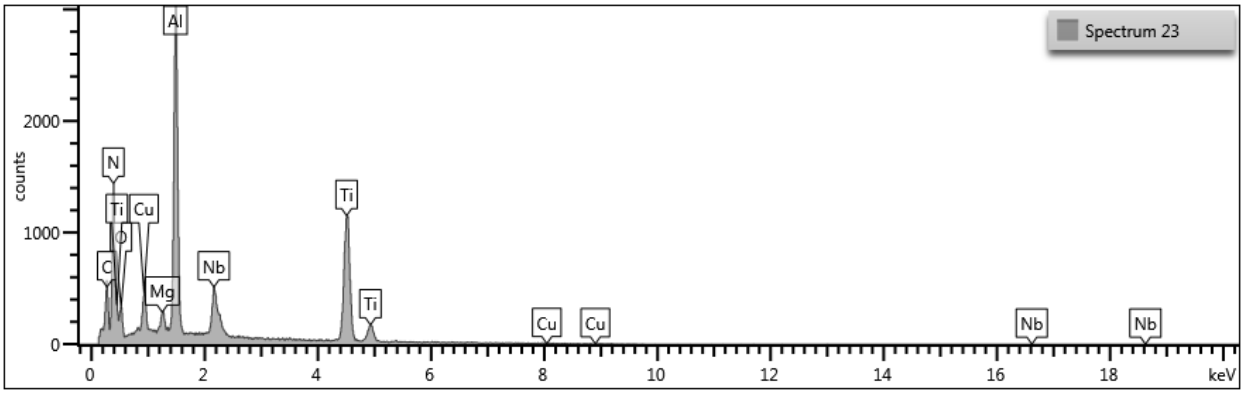

Figure A.16– SEM SE micrographs and EDX spectrum of the coarse TiN-rich particle extracted using carbon replica from 3F-565 QL.

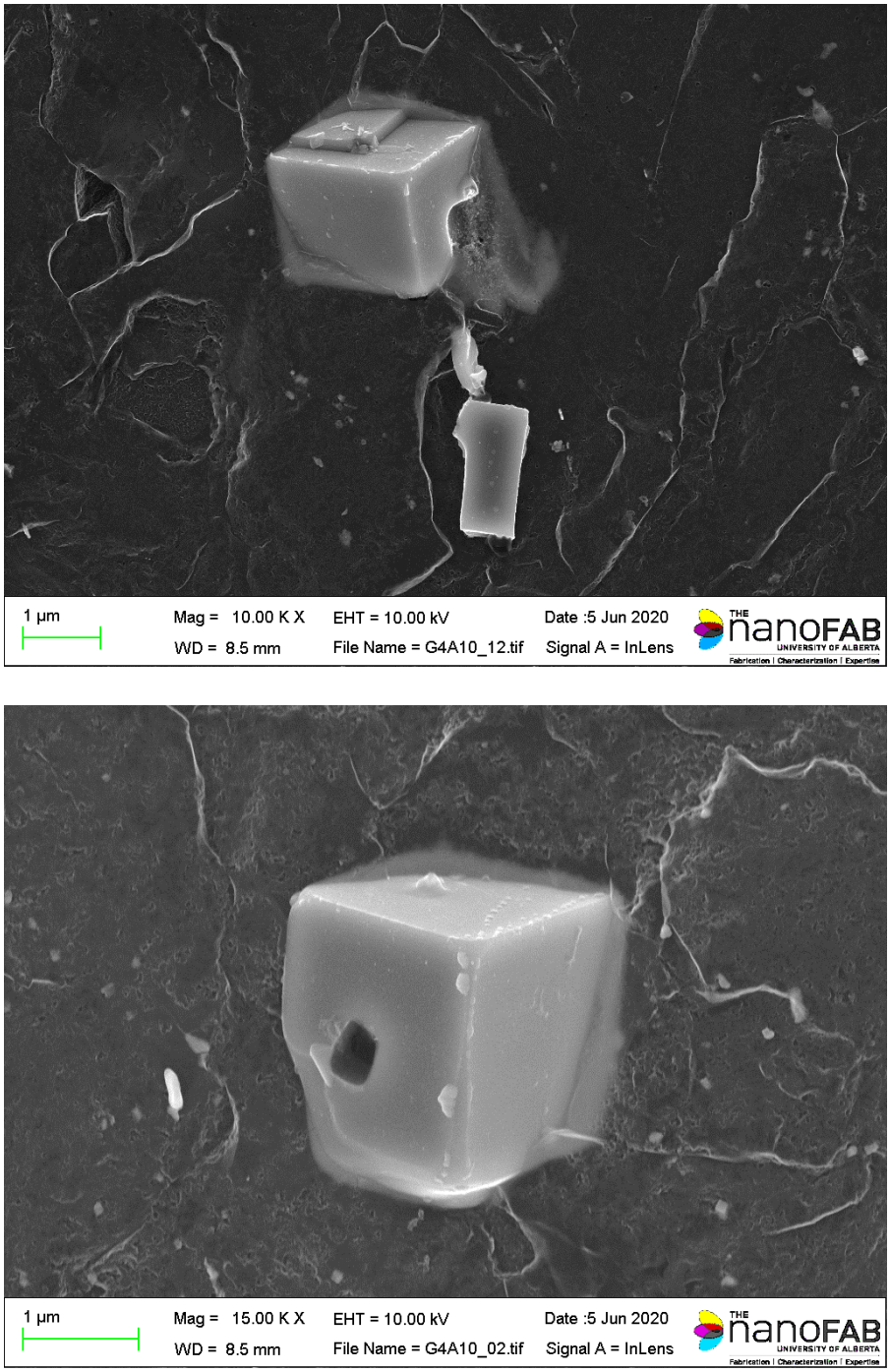

Figure A.17– SEM SE micrographs of the coarse TiN-rich particles extracted using carbon replica from 3F-565 QL.

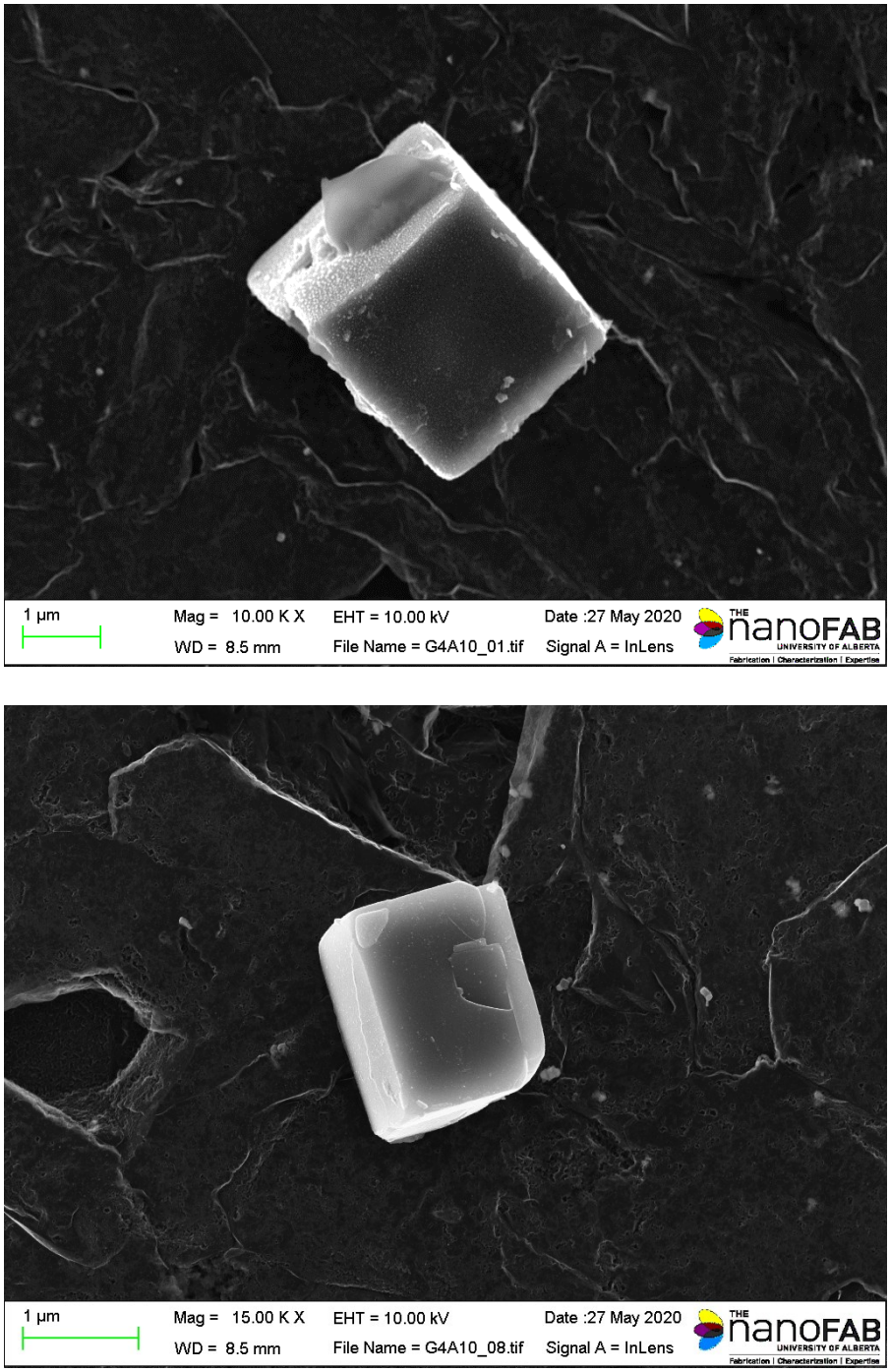

Figure A.18– SEM SE micrographs of the coarse TiN-rich particles extracted using carbon replica from 3F-565 QL.

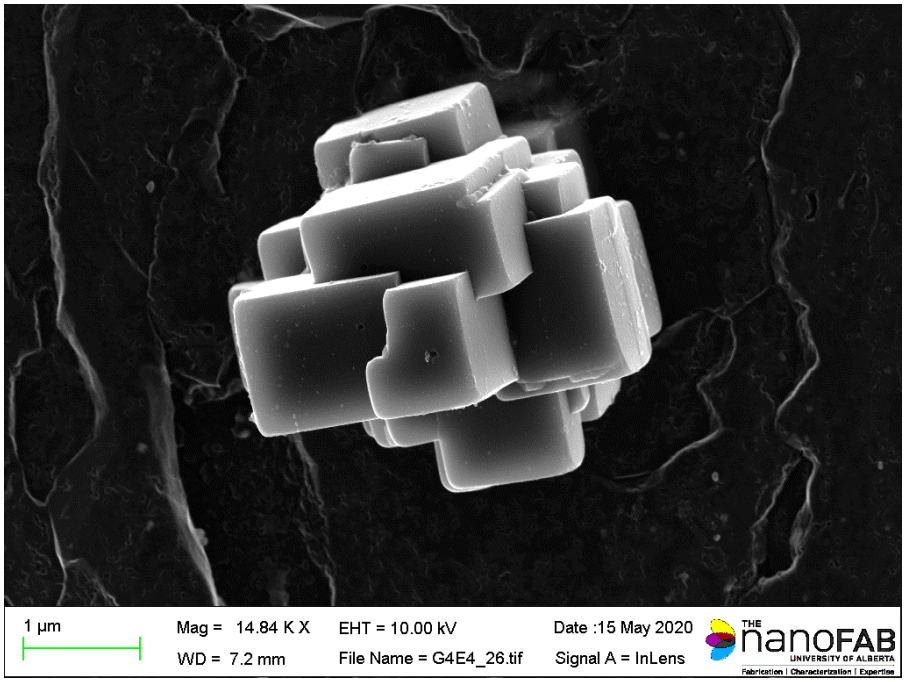

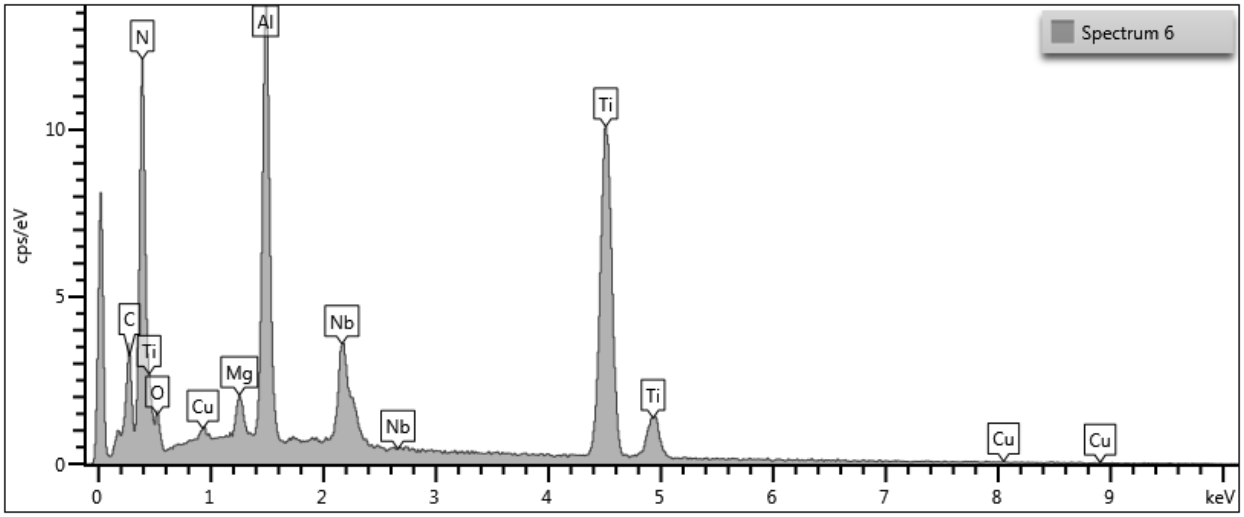

Figure A.19– SEM SE micrographs and EDX spectrum of the coarse TiN-rich particle extracted using carbon replica from TWX70 QL.

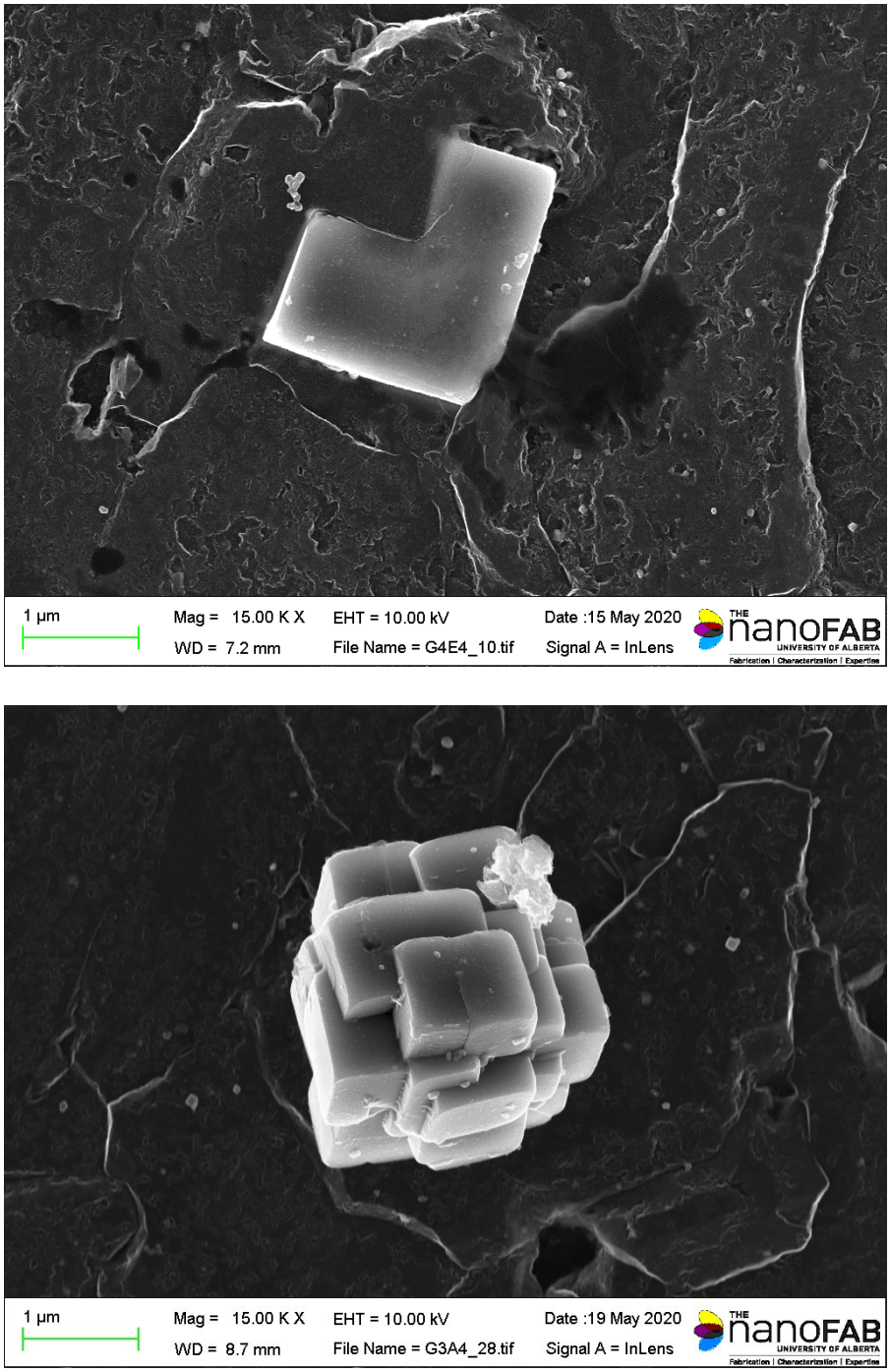

Figure A.20– SEM SE micrographs of the coarse TiN-rich particles extracted using carbon replica from TWX70 QL.

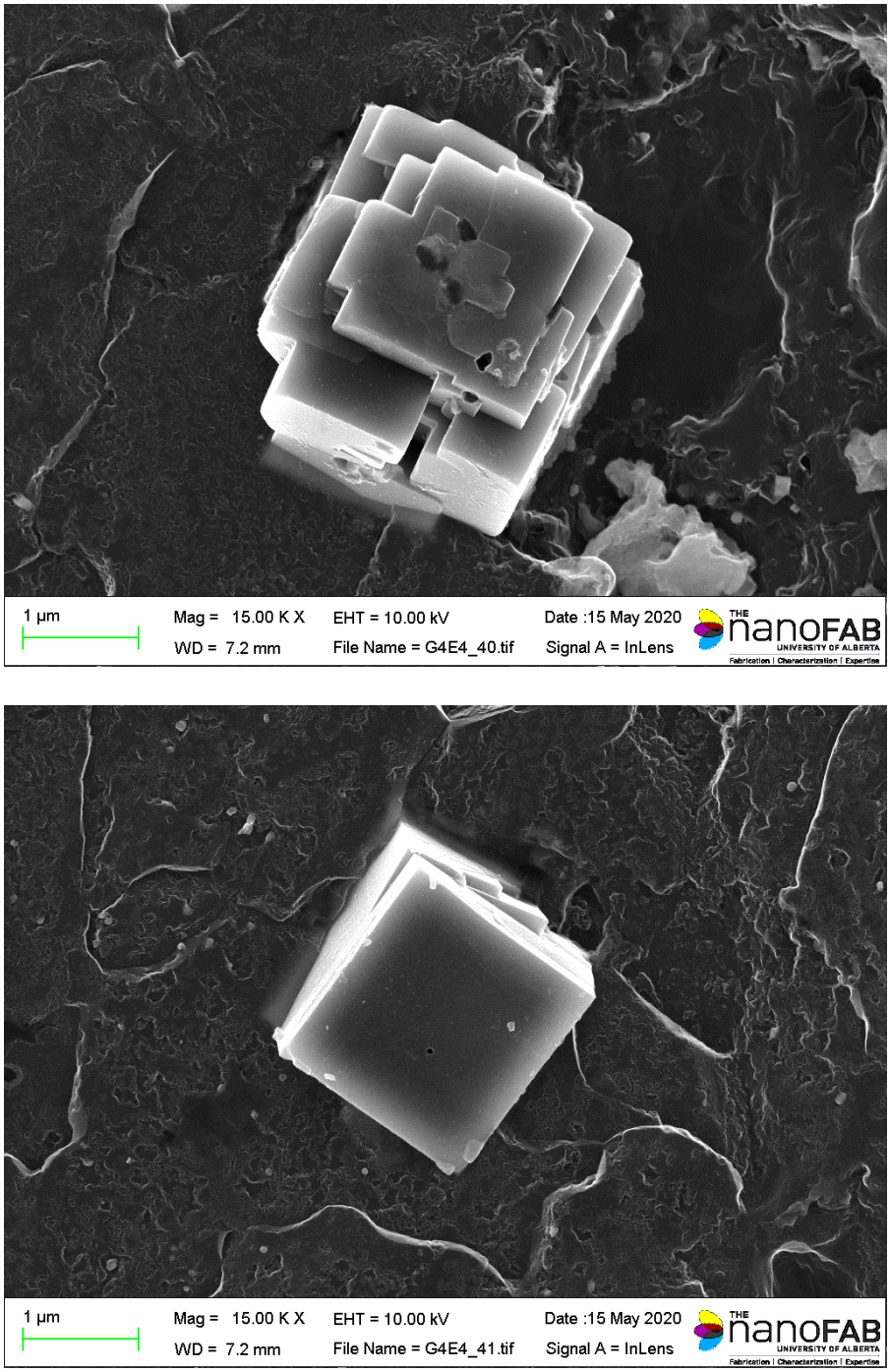

Figure A.21– SEM SE micrographs of the coarse TiN-rich particles extracted using carbon replica from TWX70 QL.

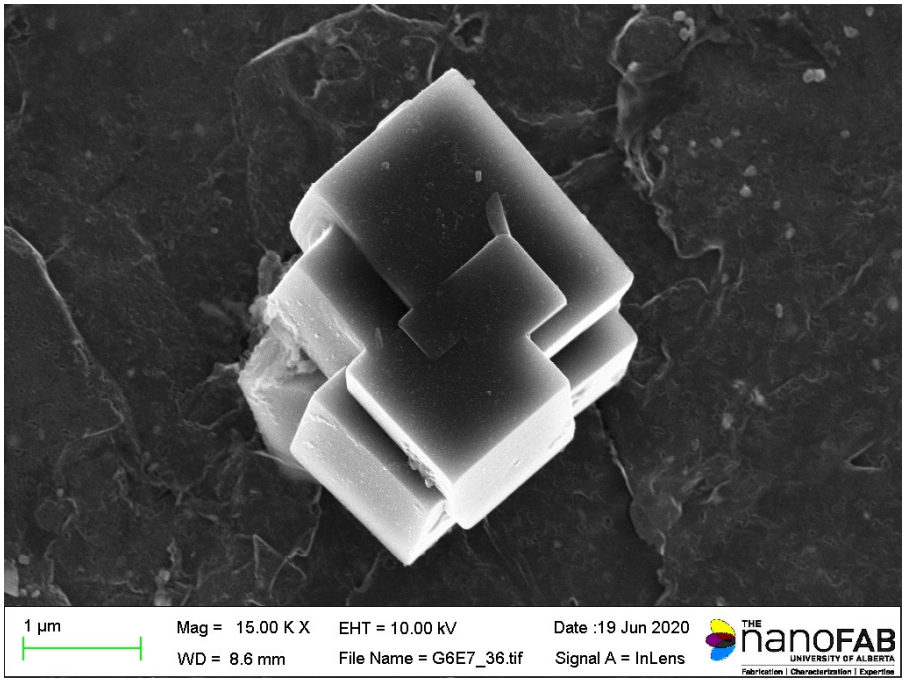

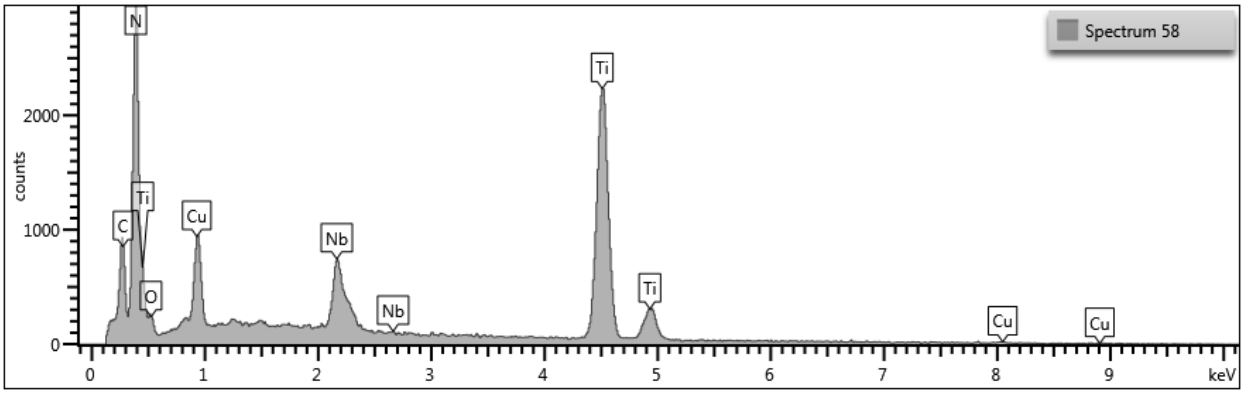

Figure A.22– SEM SE micrograph and EDX spectrum of the coarse TiN-rich particle extracted using carbon replica from T36-1 CL.

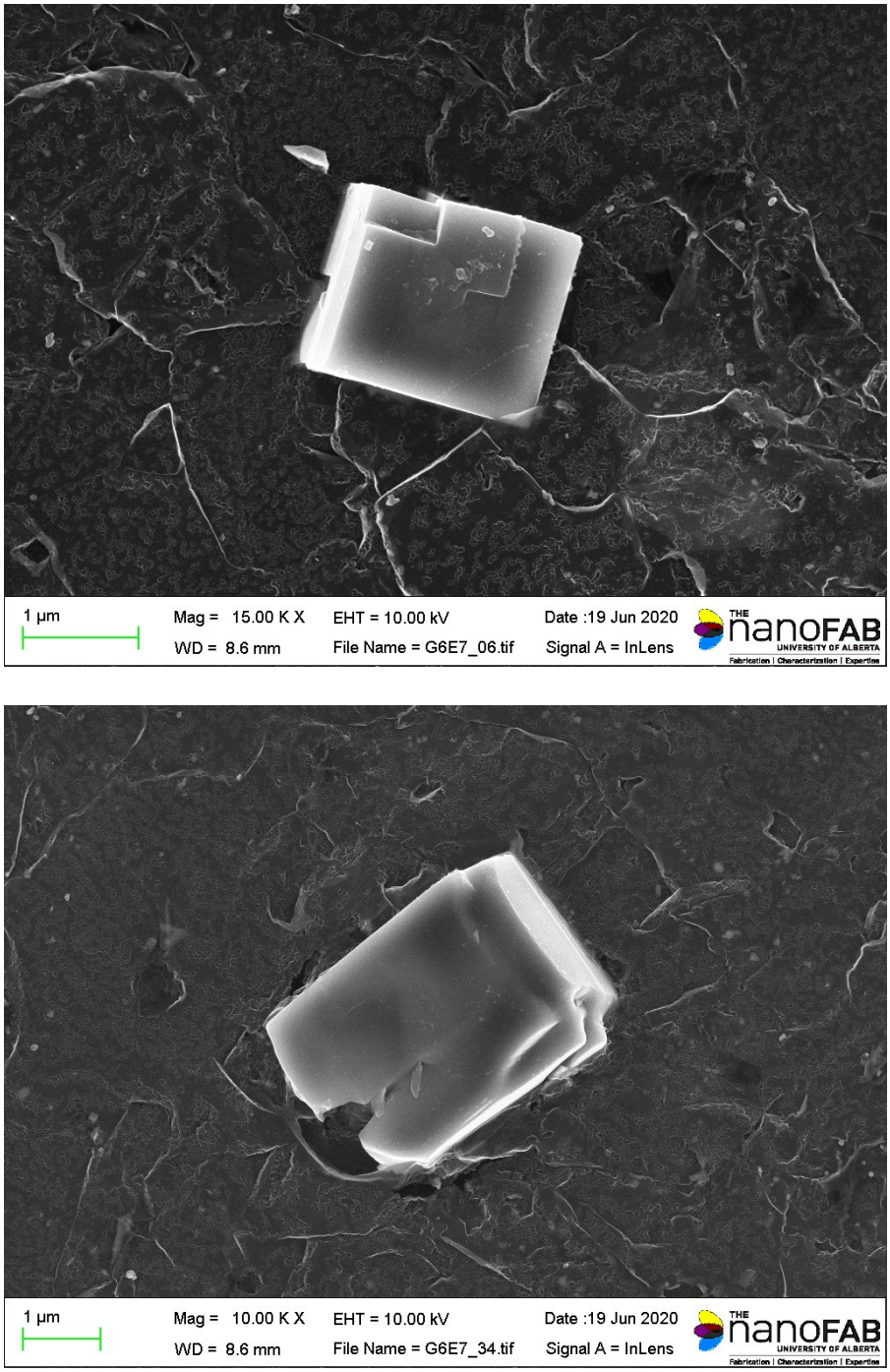

Figure A.23– SEM SE micrographs of the coarse TiN-rich particles extracted using carbon replica from T36-1 CL.

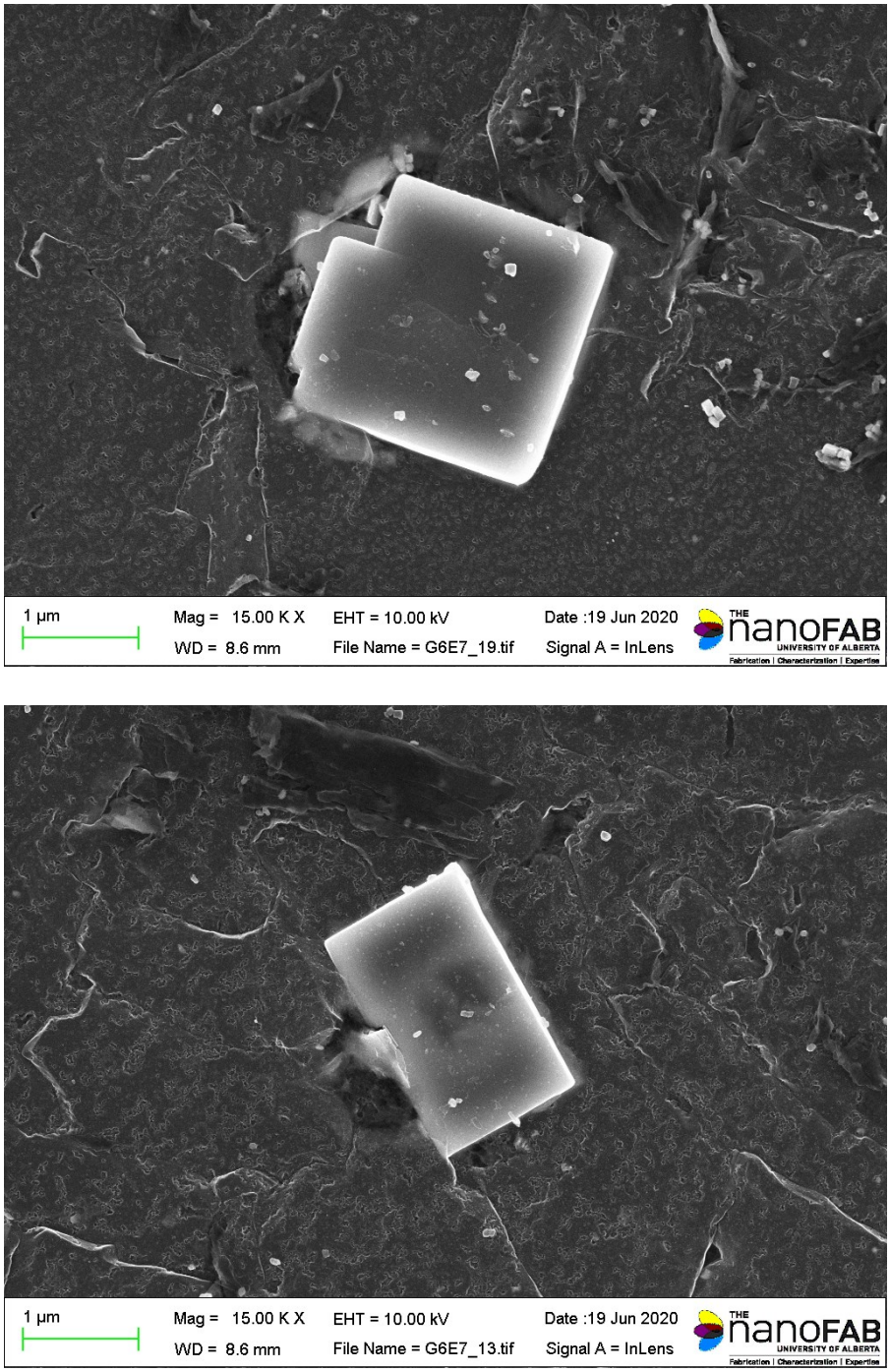

Figure A.24– SEM SE micrographs of the coarse TiN-rich particles extracted using carbon replica from T36-1 CL.

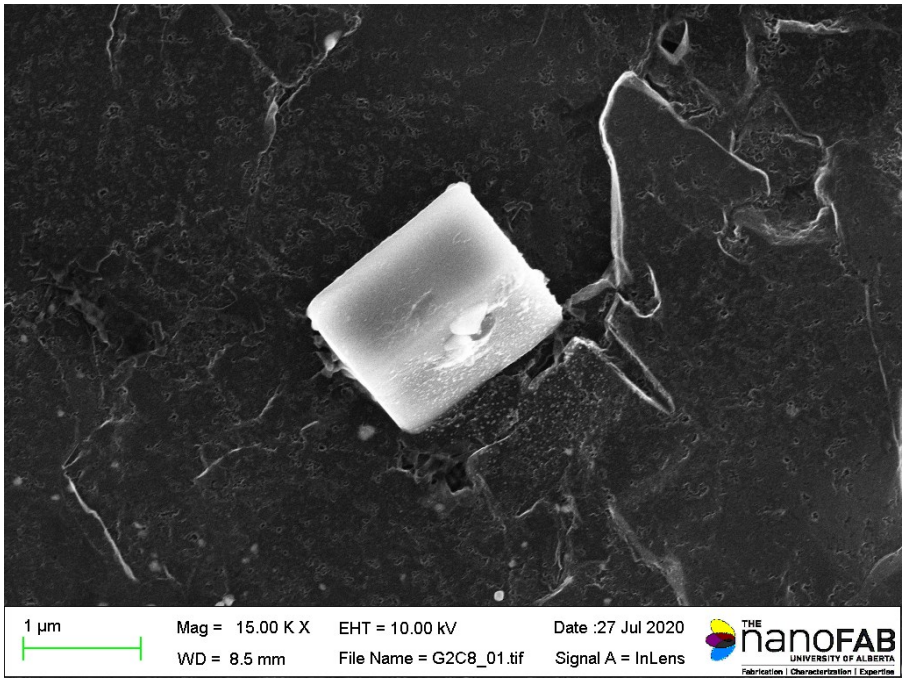

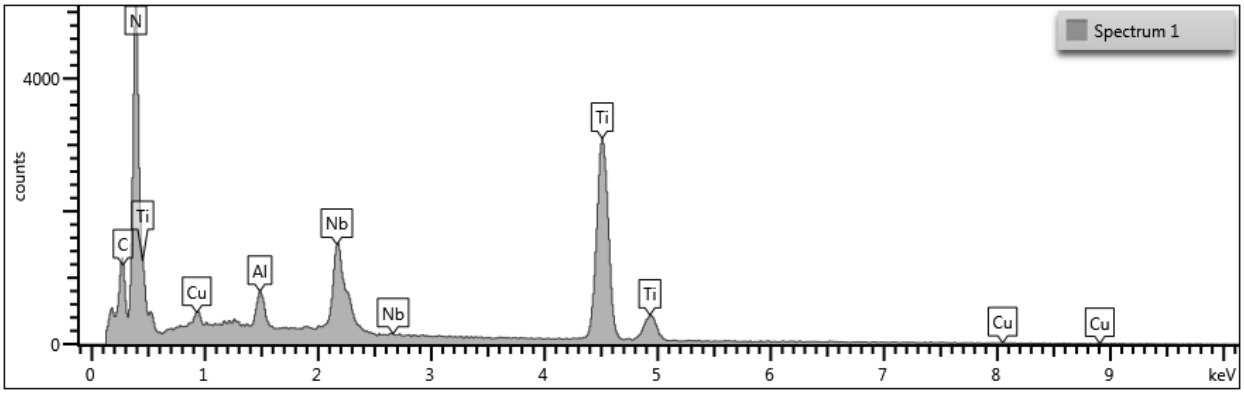

Figure A.25– SEM SE micrograph and EDX spectrum of the coarse TiN-rich particle extracted using carbon replica from T36-2 CL.

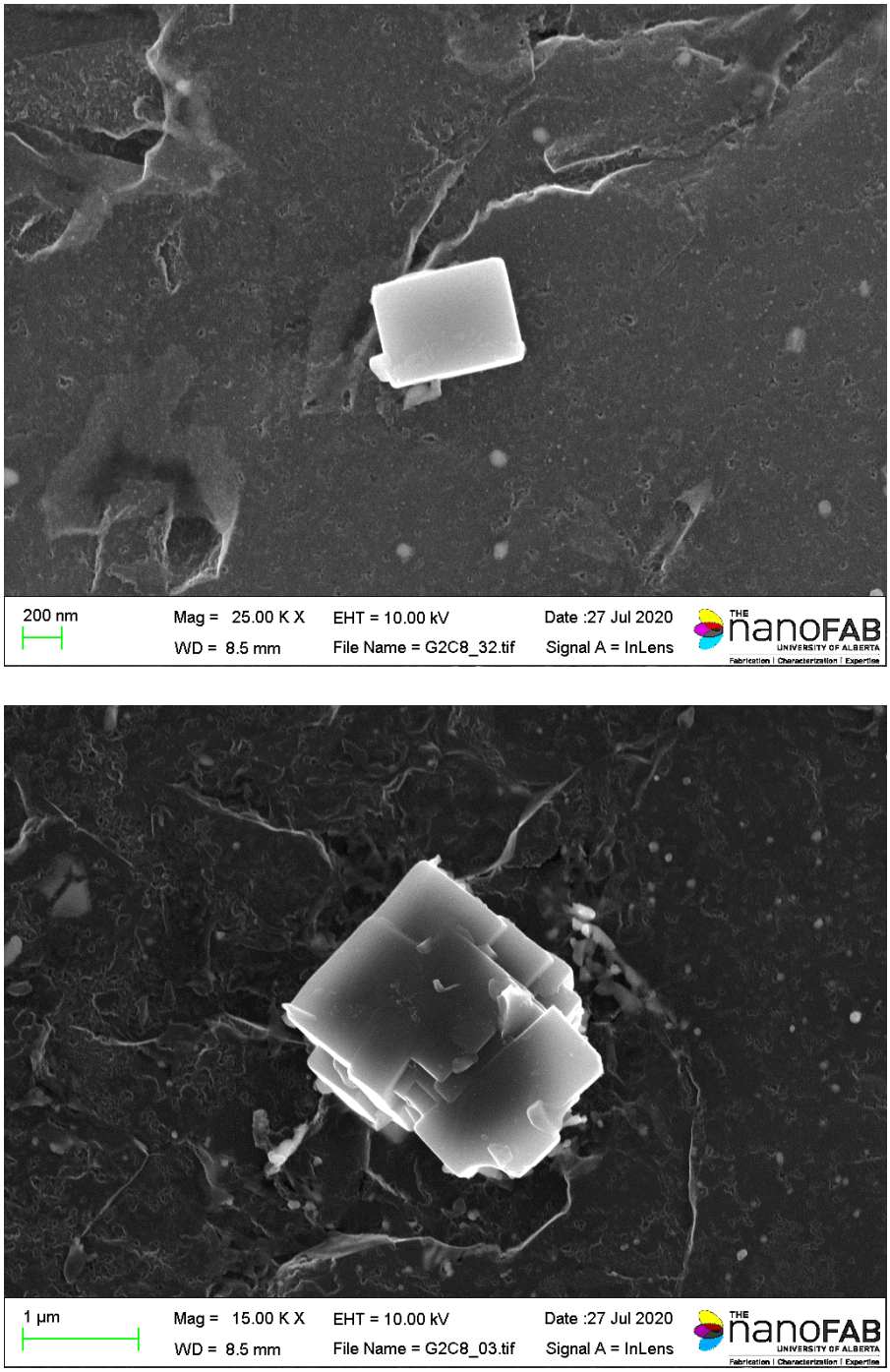

Figure A.26– SEM SE micrographs of the coarse TiN-rich particles extracted using carbon replica from T36-2 CL.

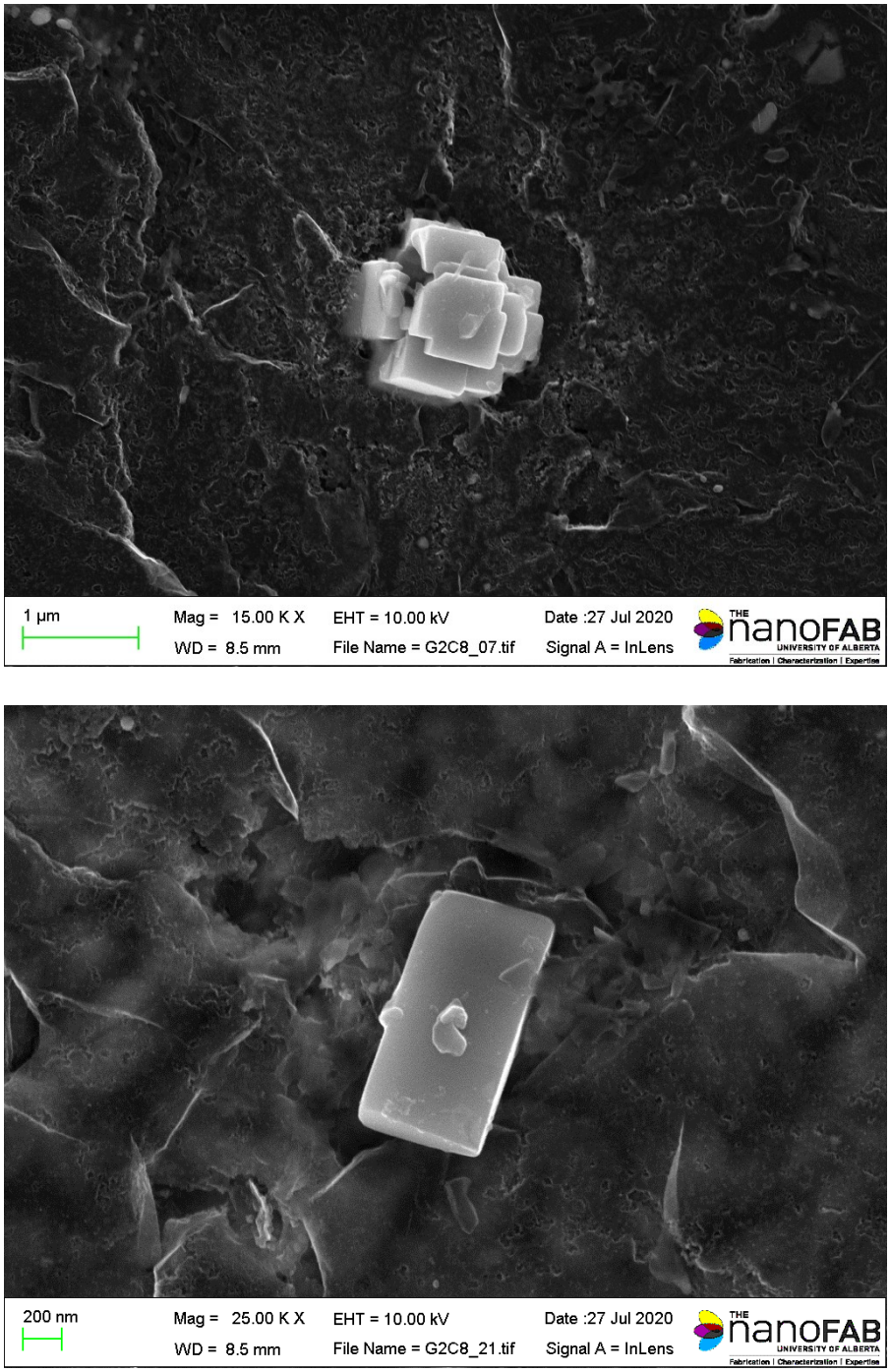

Figure A.27– SEM SE micrographs of the coarse TiN-rich particles extracted using carbon replica from T36-2 CL.

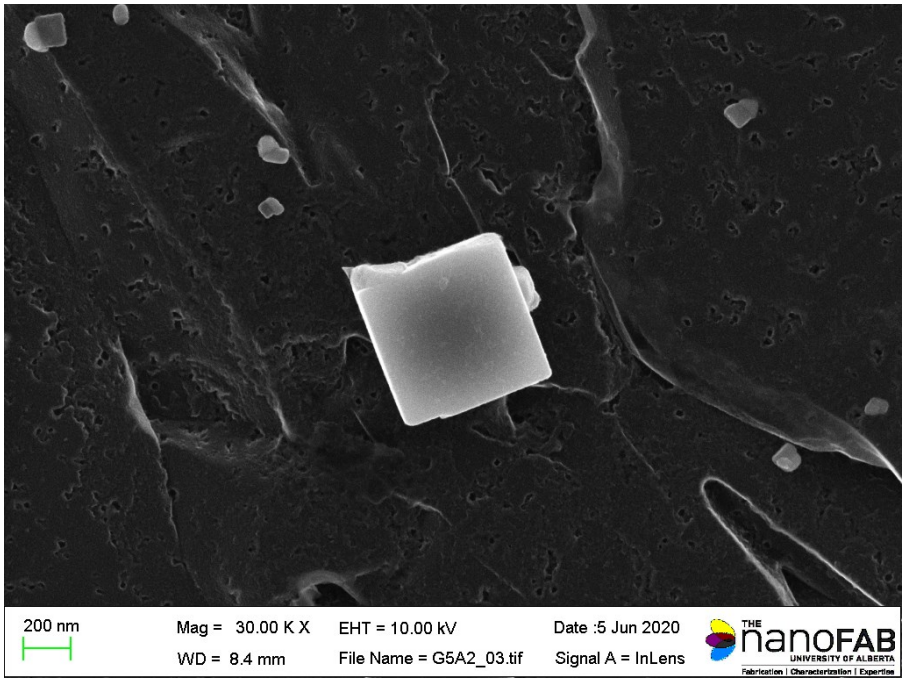

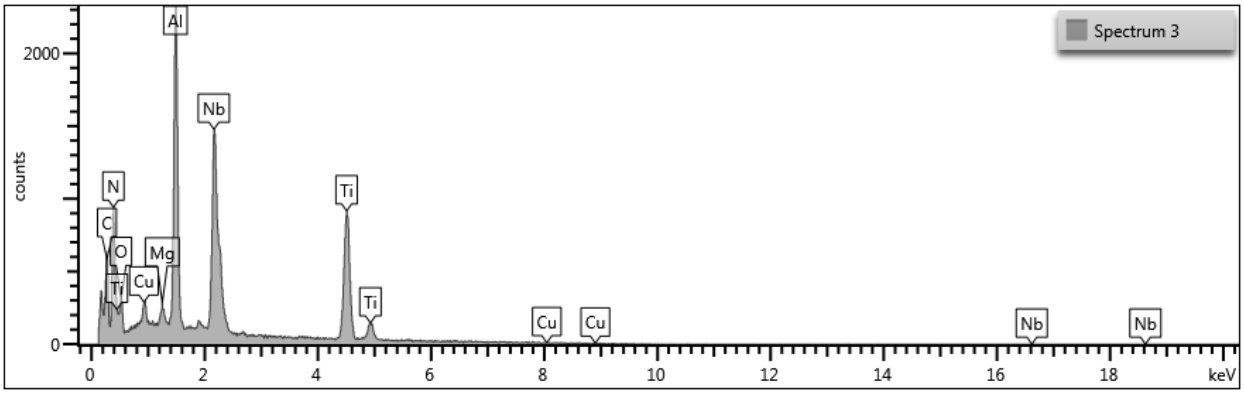

Figure A.28– SEM SE micrograph and EDX spectrum of the coarse TiN-rich particle extracted using carbon replica from T36-3 CL.

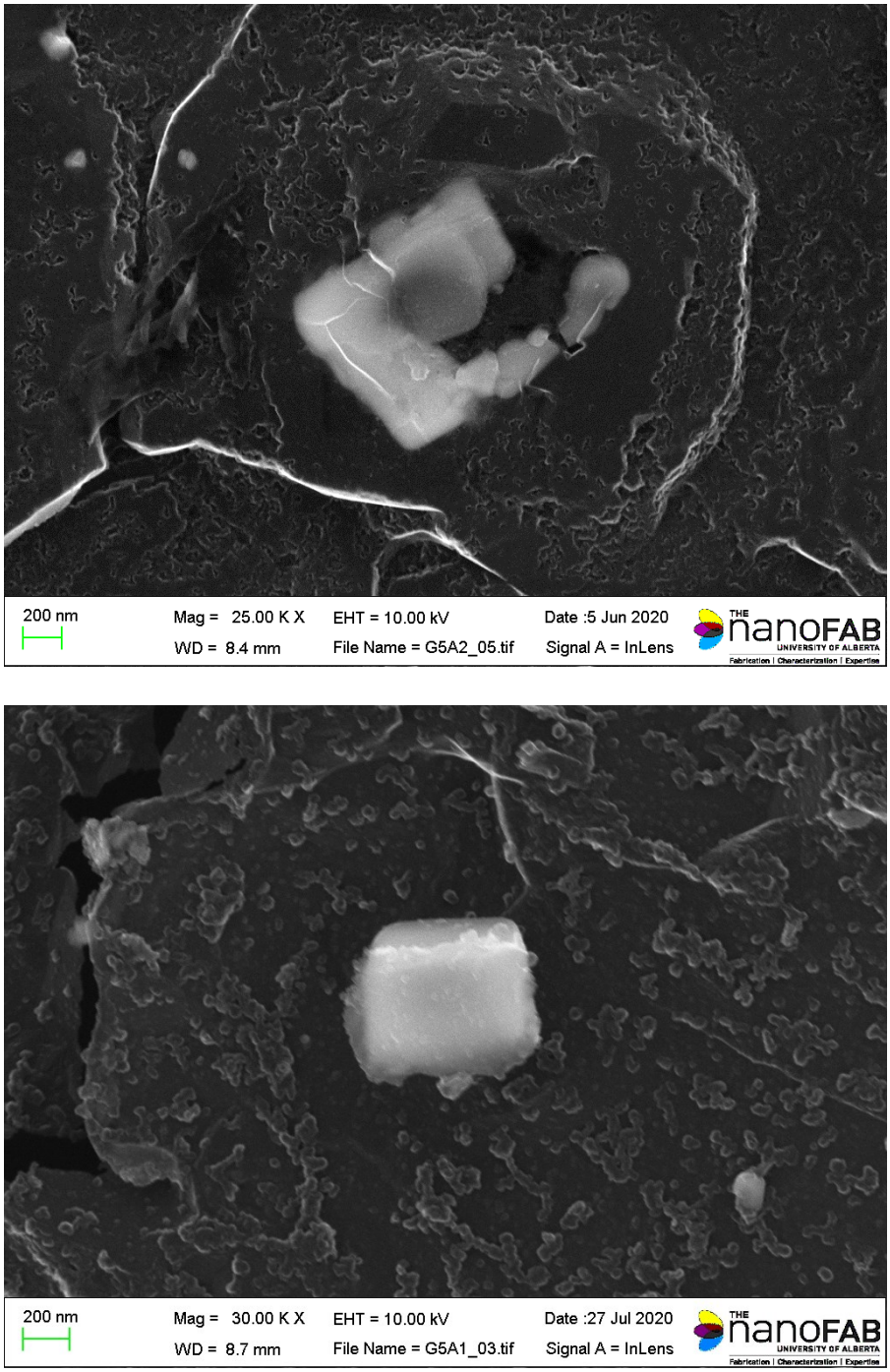

Figure A.29– SEM SE micrographs of the coarse TiN-rich particles extracted using carbon replica from T36-3 CL.

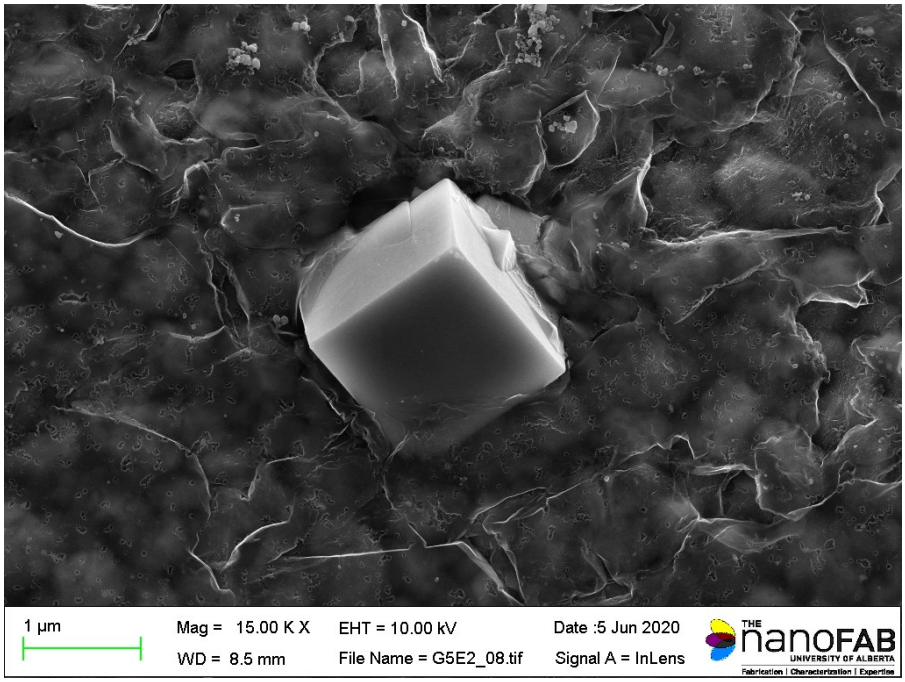

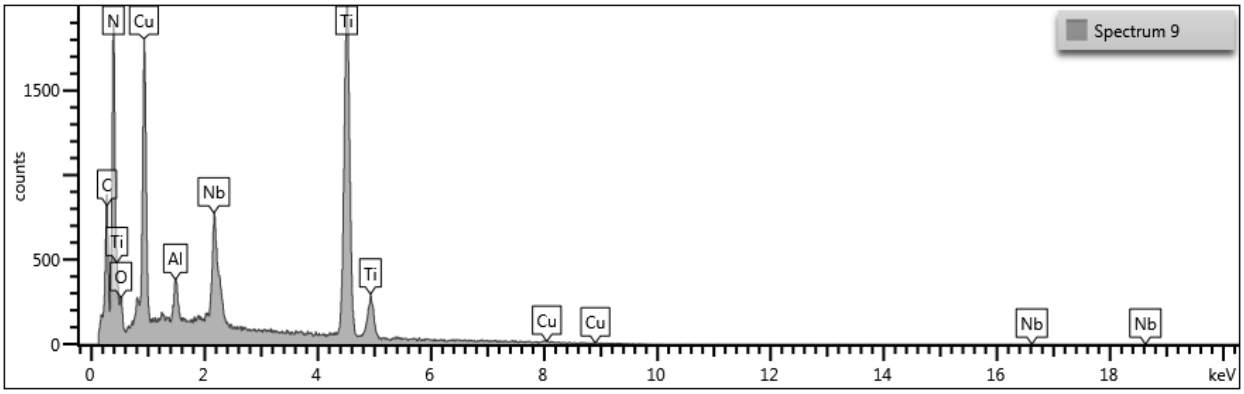

Figure A.30– SEM SE micrograph and EDX spectrum of the coarse TiN-rich particle extracted using carbon replica from D-1 CL.

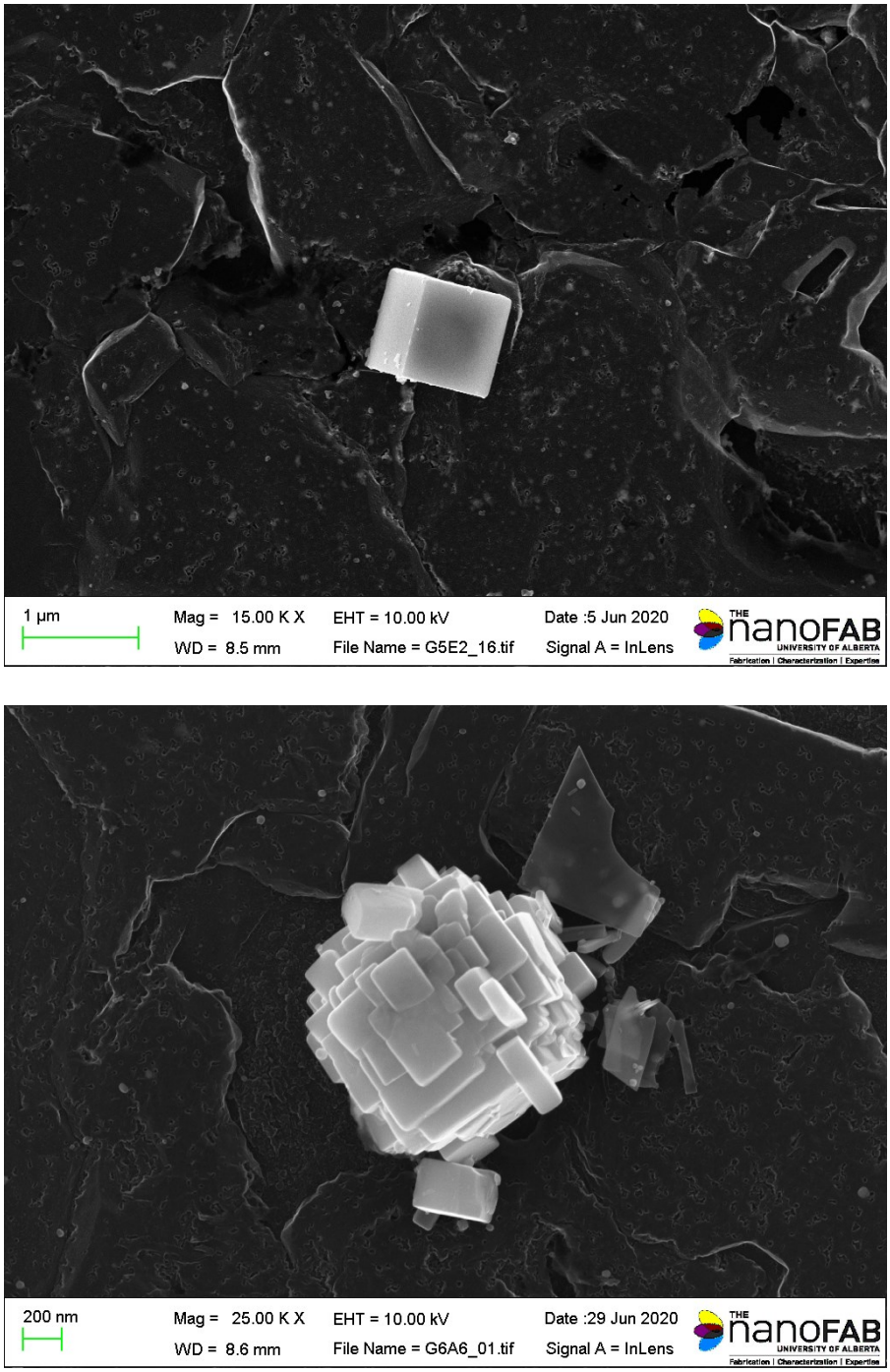

Figure A.31– SEM SE micrographs of the coarse TiN-rich particles extracted using carbon replica from D-1 CL.

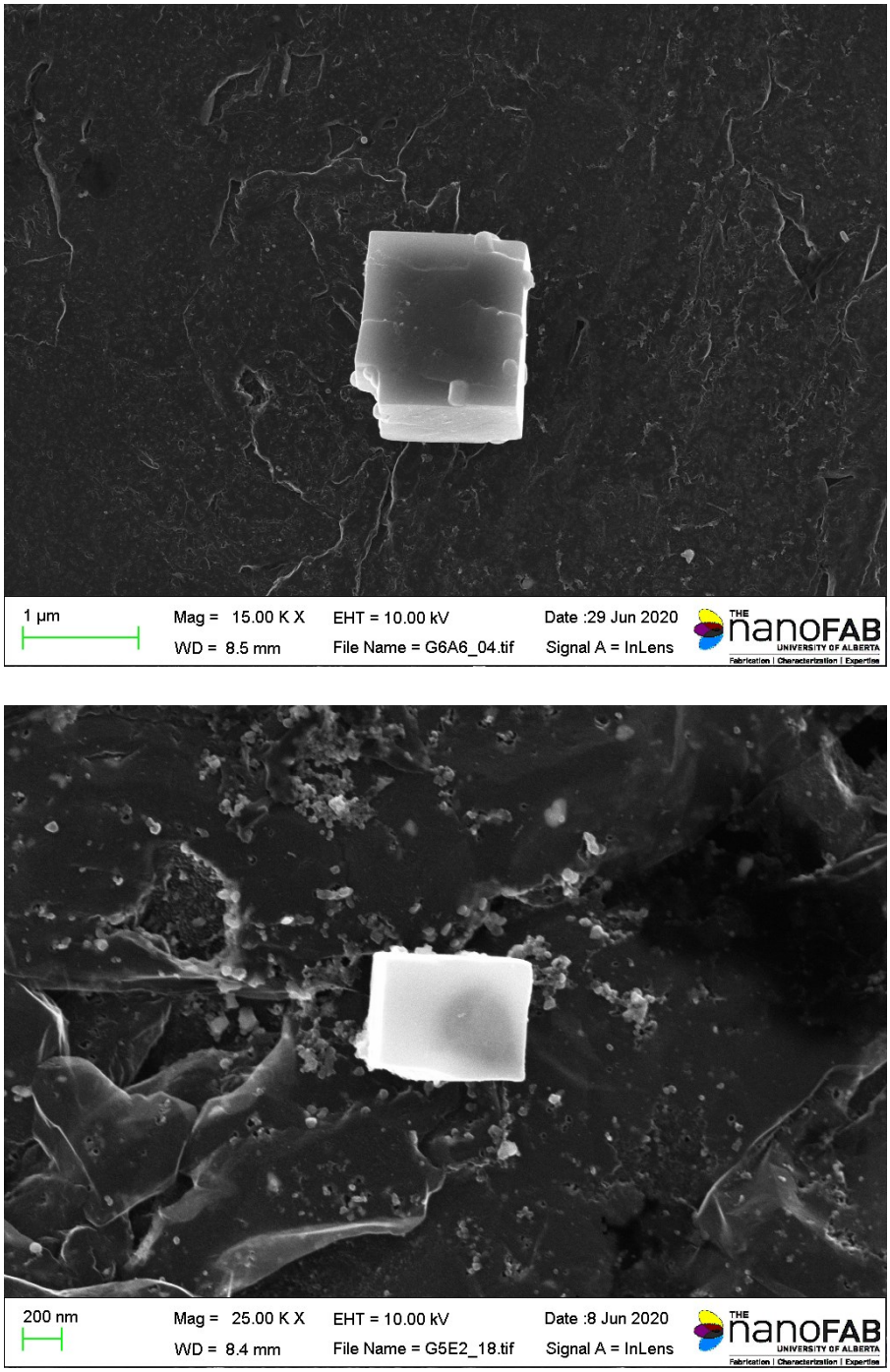

Figure A.32– SEM SE micrographs of the coarse TiN-rich particles extracted using carbon replica from D-1 CL.

Appendix B STEM/EDX analysis of fine TiN-rich particles

This Appendix presents STEM/EDX measurements conducted on epitaxial NbC-rich particles. Subsequently, the STEM DF micrographs and EDX spectra, and EDX maps of the fine TiN-rich particles extracted with the carbon replica method are shown. Then, the results of the analysis conducted on the residues extracted using the matrix dissolution method are presented.

B-1 STEM/EDX results for epitaxial NbC-rich particles

Table B.1 shows the results of STEM/EDX measurements conducted on epitaxial NbC-rich particles.

Table B.1– STEM/EDX measurements conducted on epitaxial NbC-rich particles in the steels

Steel	Precipitate chemistry	SD* of composition in atomic fraction		
		Nb	Mo	Ti
T36-1 QL	$Nb_{0.96}Mo_{0.02}Ti_{0.02}C$	0.01	0.01	0.01
T36-2 QL	$Nb_{0.97}Mo_{0.01}Ti_{0.02}C$	0.01	0.01	0.01
T36-3 QL	$Nb_{0.97}Mo_{0.02}Ti_{0.01}C$	0.01	0.01	0.01
D-1 QL	$Nb_{0.98}Ti_{0.02}C$	0.01	-	0.01
TWX70QL	$Nb_{0.96}Mo_{0.03}Ti_{0.01}C$	0.01	0.01	0.01
3F-565 QL	$Nb_{0.96}Mo_{0.02}Ti_{0.02}C$	0.02	0.02	0.01
B60 QL	$Nb_{0.96}Mo_{0.03}Ti_{0.01}C$	0.02	0.02	0.01
T36-1 CL	$Nb_{0.96}Mo_{0.02}Ti_{0.02}C$	0.01	0.01	0.01
T36-2 CL	$Nb_{0.97}Mo_{0.01}Ti_{0.02}C$	0.01	0.01	0.01
T36-3 CL	$Nb_{0.98}Mo_{0.01}Ti_{0.01}C$	0.01	0.01	0.01
D-1 CL	$Nb_{0.99}Ti_{0.01}C$	0.01	-	0.01

*SD: Standard deviation

B-2 STEM/EDX results for fine TiN-rich particles

The following presents the STEM ADF micrographs and EDX spectra and maps of the fine TiN-rich particles extracted with the carbon replica method.

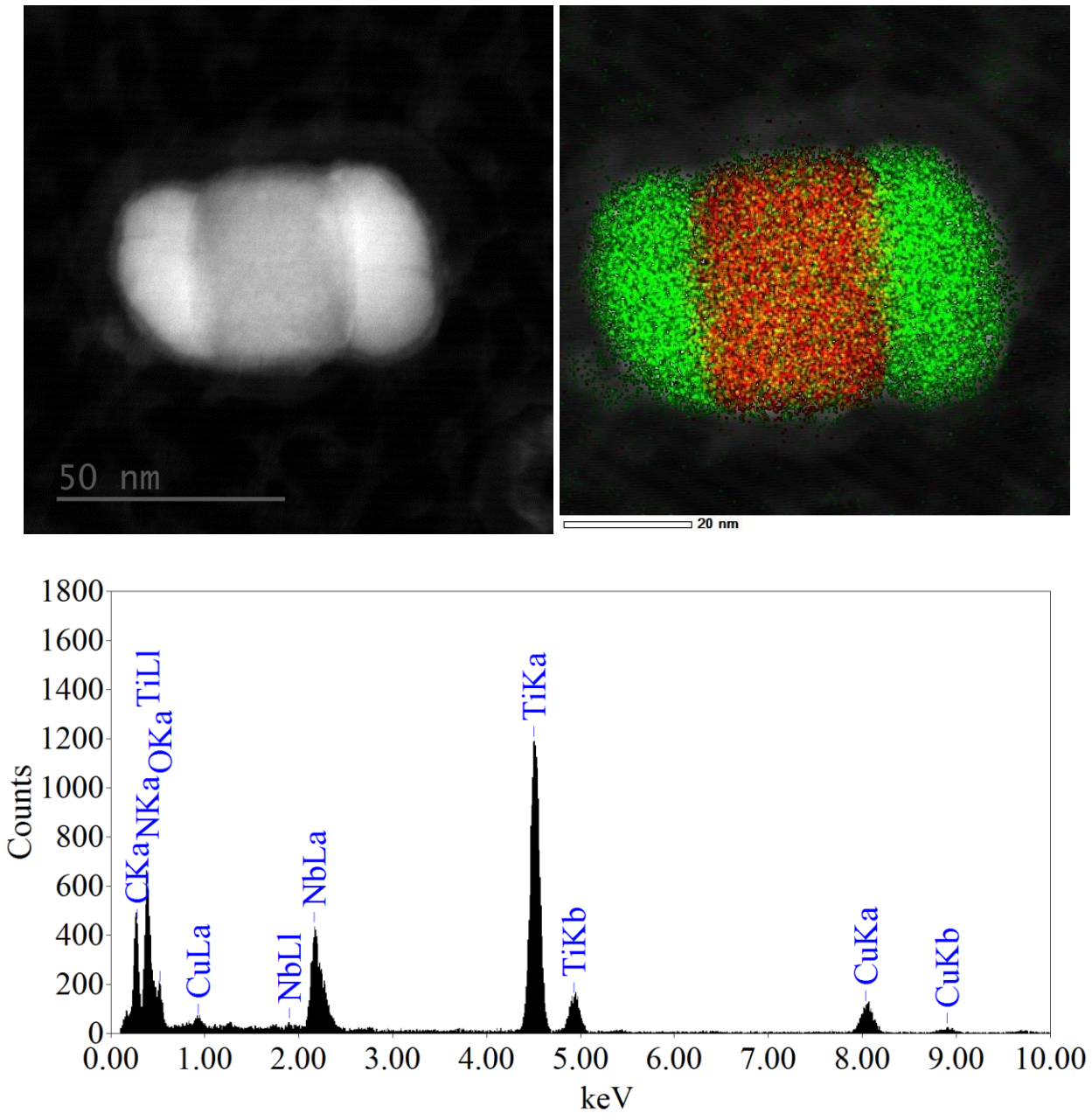

Figure B.1– STEM ADF micrograph and EDX map (Ti: red, Nb: green) of fine TiN-rich and NbC-rich particles along with spectrum of the fine TiN-rich particle extracted using carbon replica from T36-1 QL.

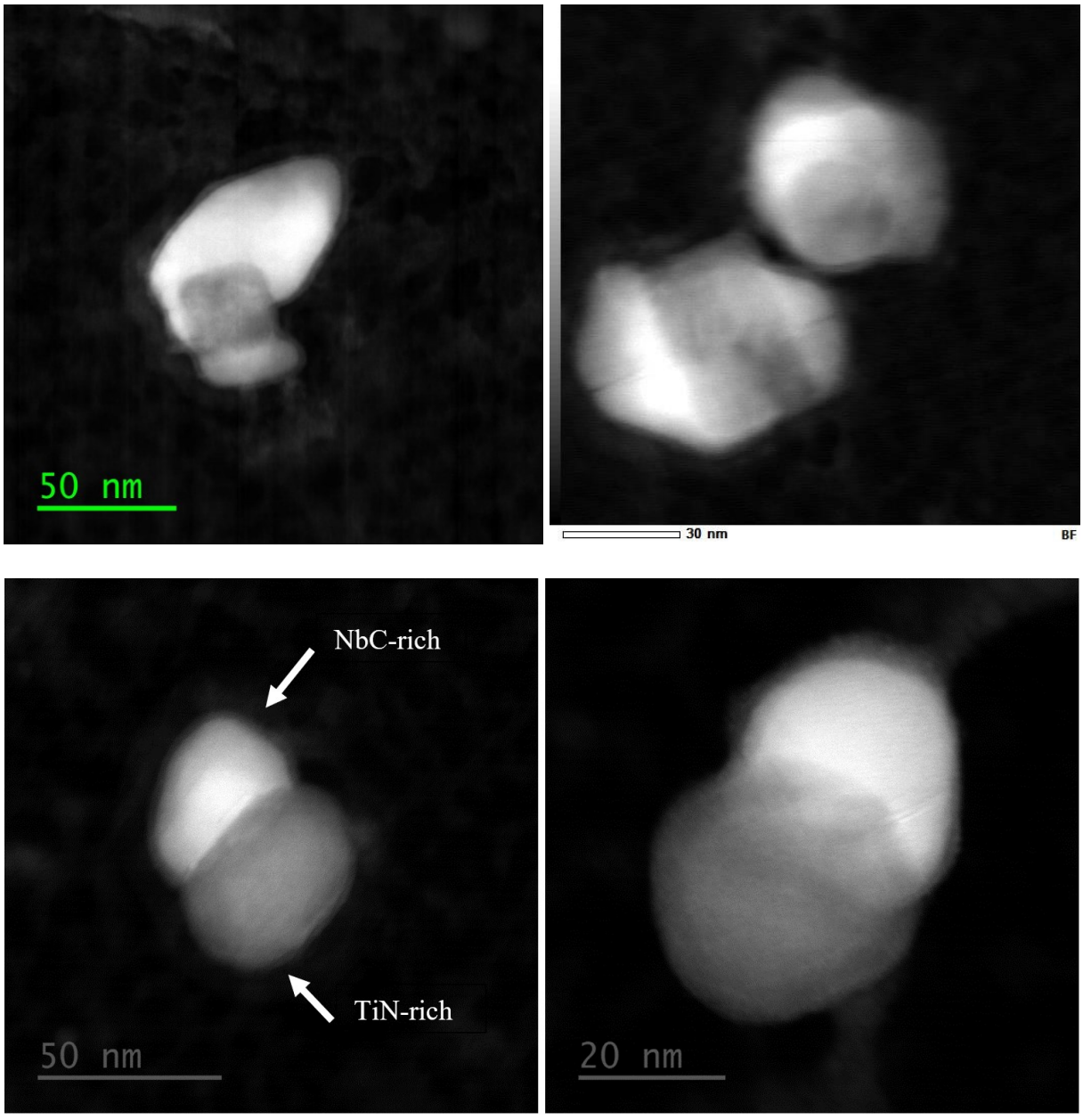

Figure B.2– STEM ADF micrographs of the fine TiN-rich and NbC-rich particles extracted using carbon replica from T36-1 QL.

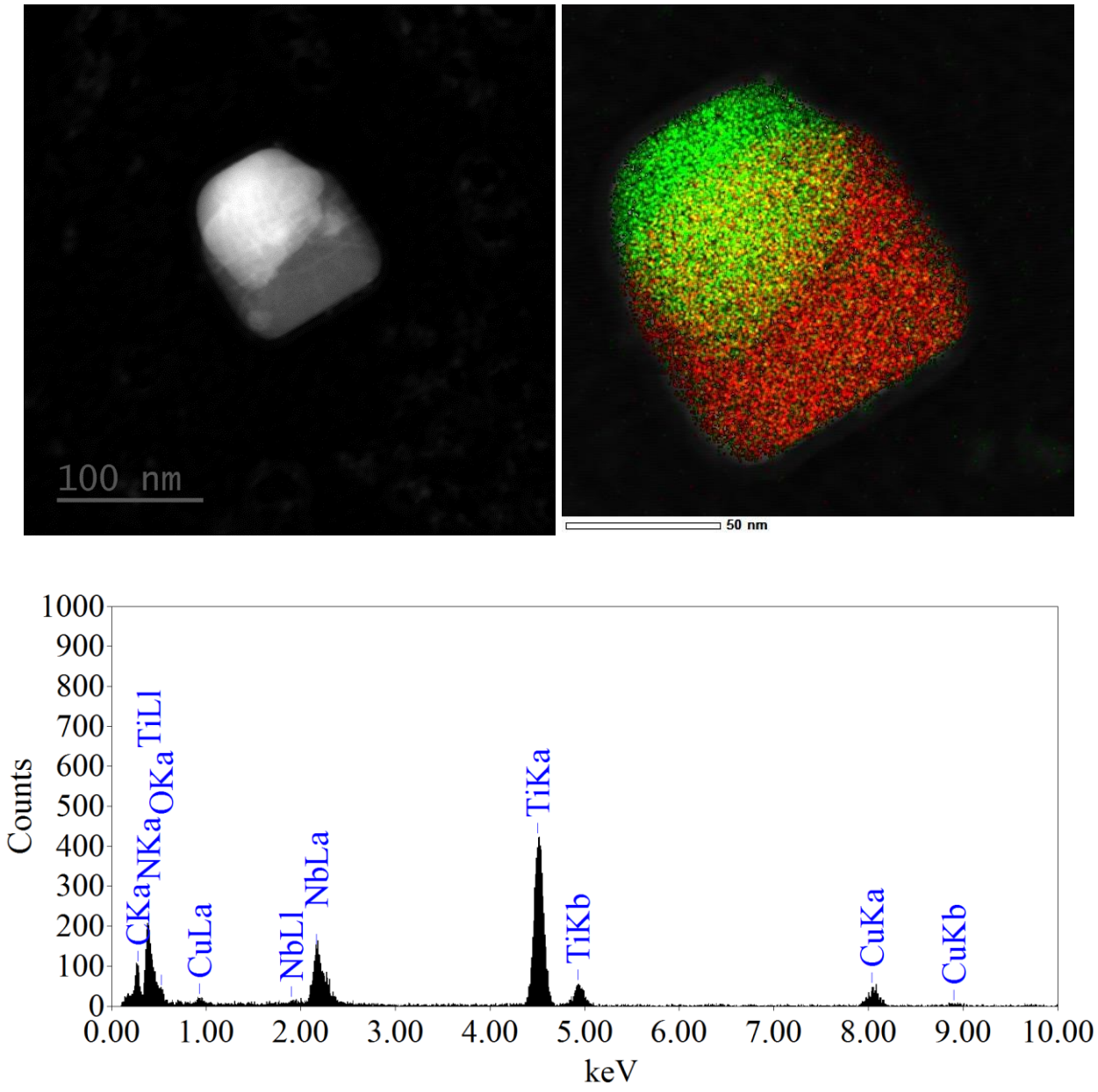

Figure B.3– STEM ADF micrograph and EDX map (Ti: red, Nb: green) of fine TiN-rich and NbC-rich particles along with spectrum of the fine TiN-rich particle extracted using carbon replica from T36-2 QL.

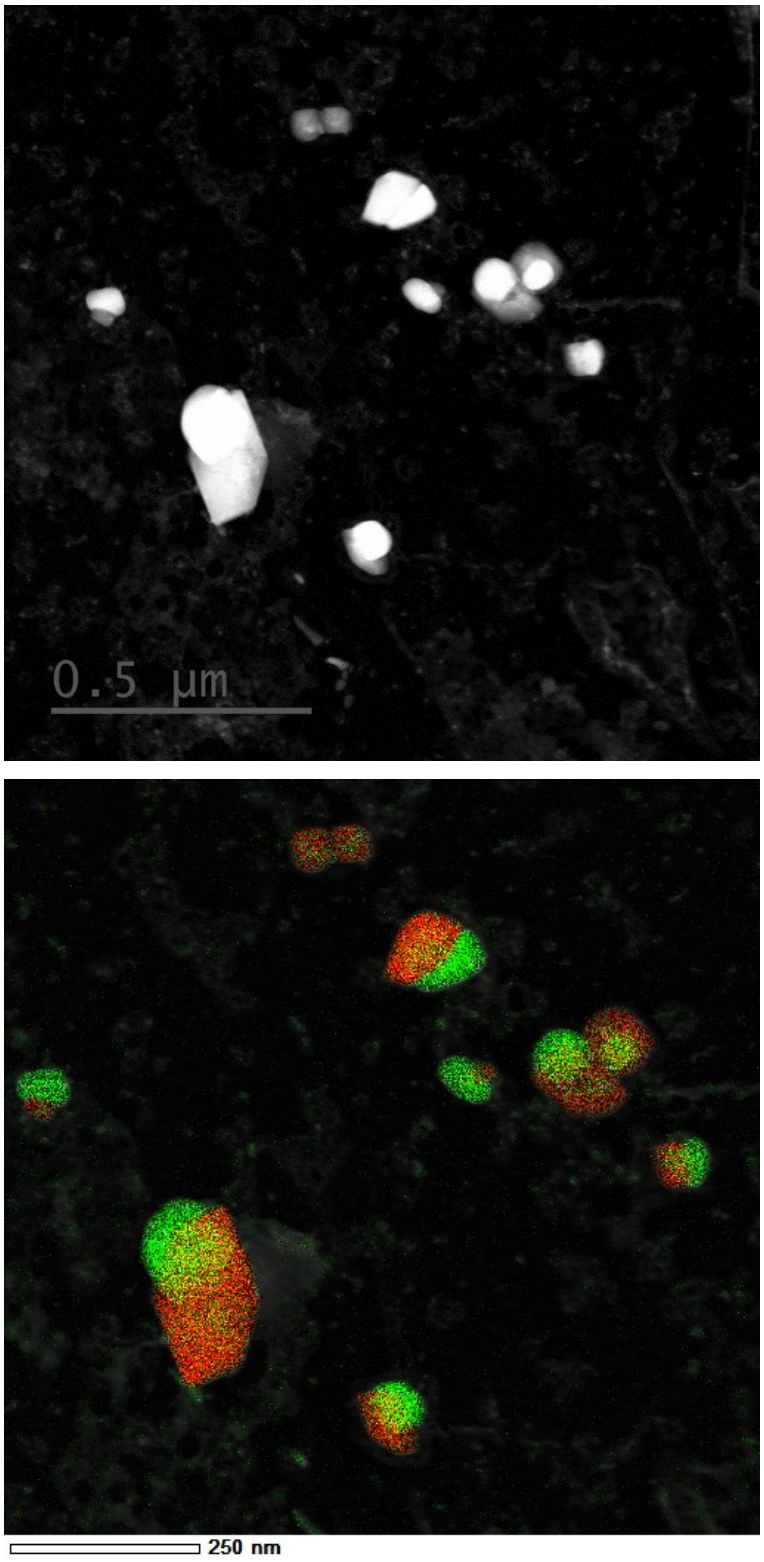

Figure B.4– STEM ADF micrograph and EDX map (Ti: red, Nb: green) of the fine TiN-rich and NbC-rich particles extracted using carbon replica from T36-2 QL.

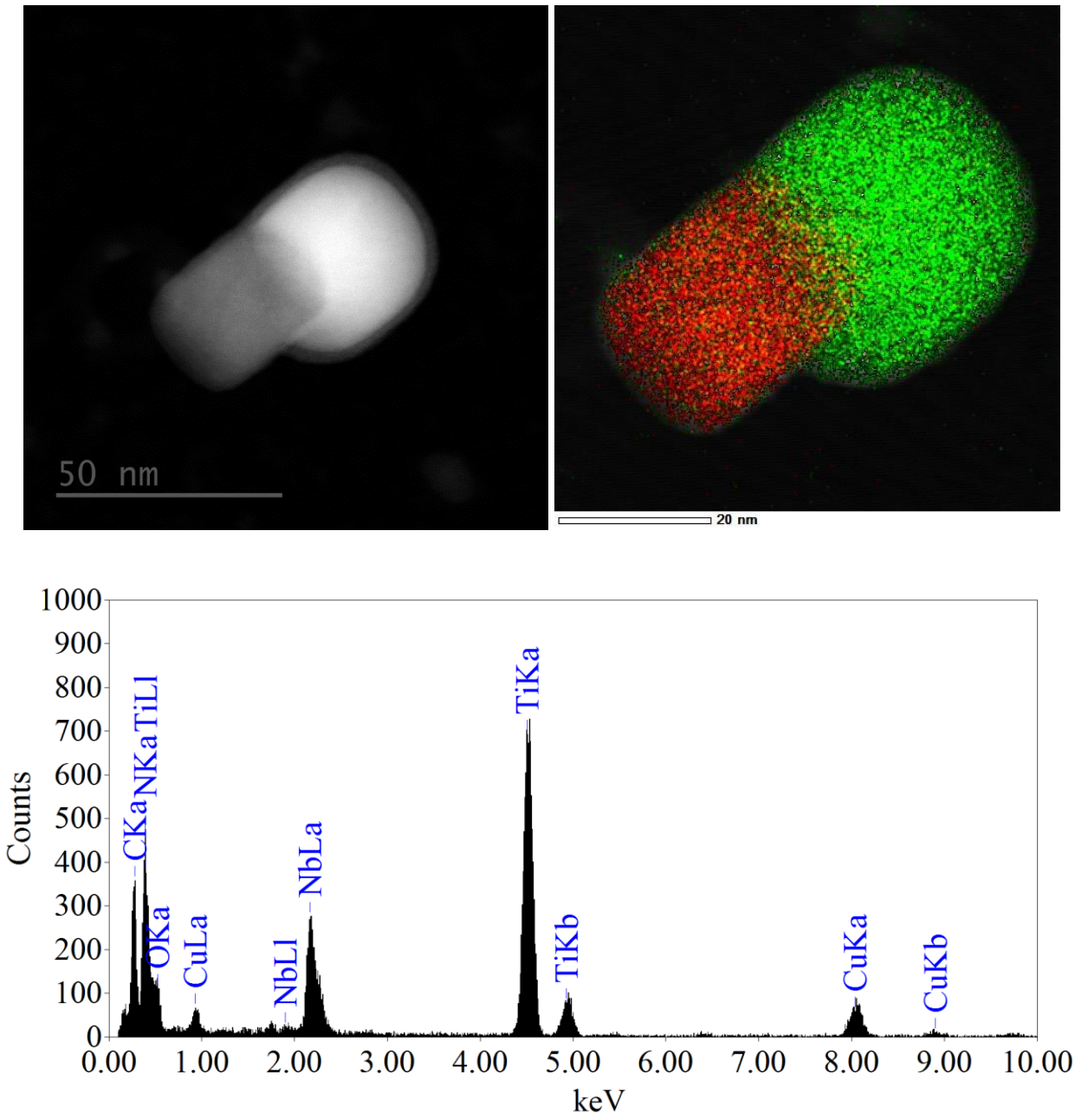

Figure B.5– STEM ADF micrograph and EDX map (Ti: red, Nb: green) of fine TiN-rich and NbC-rich particles along with spectrum of the fine TiN-rich particle extracted using carbon replica from T36-3 QL.

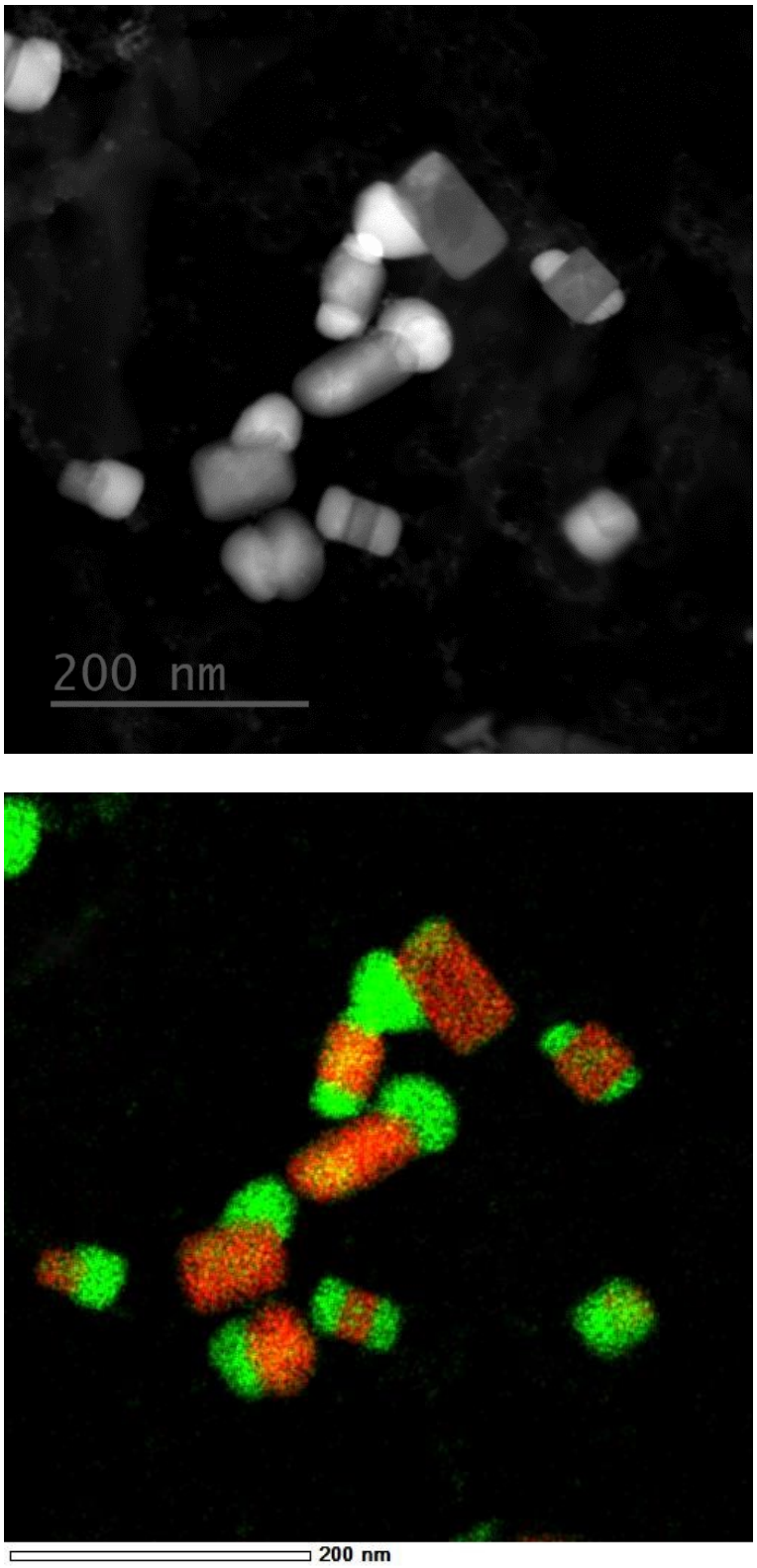

Figure B.6– STEM ADF micrograph and EDX map (Ti: red, Nb: green) of the fine TiN-rich and NbC-rich particles extracted using carbon replica from T36-3 QL.

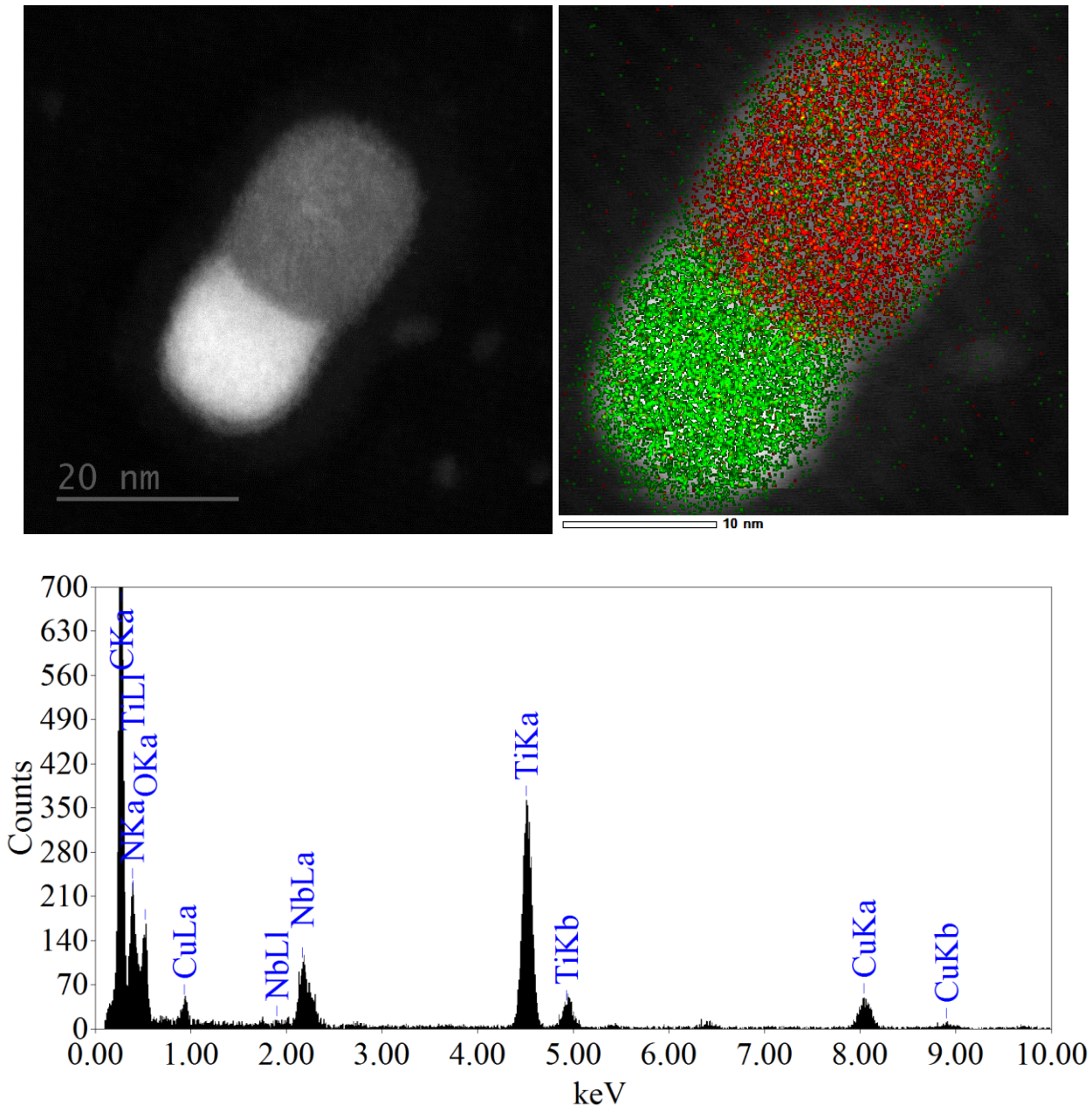

Figure B.7– STEM ADF micrograph and EDX map (Ti: red, Nb: green) of fine TiN-rich and NbC-rich particles along with spectrum of the fine TiN-rich particle extracted using carbon replica from D-1 QL.

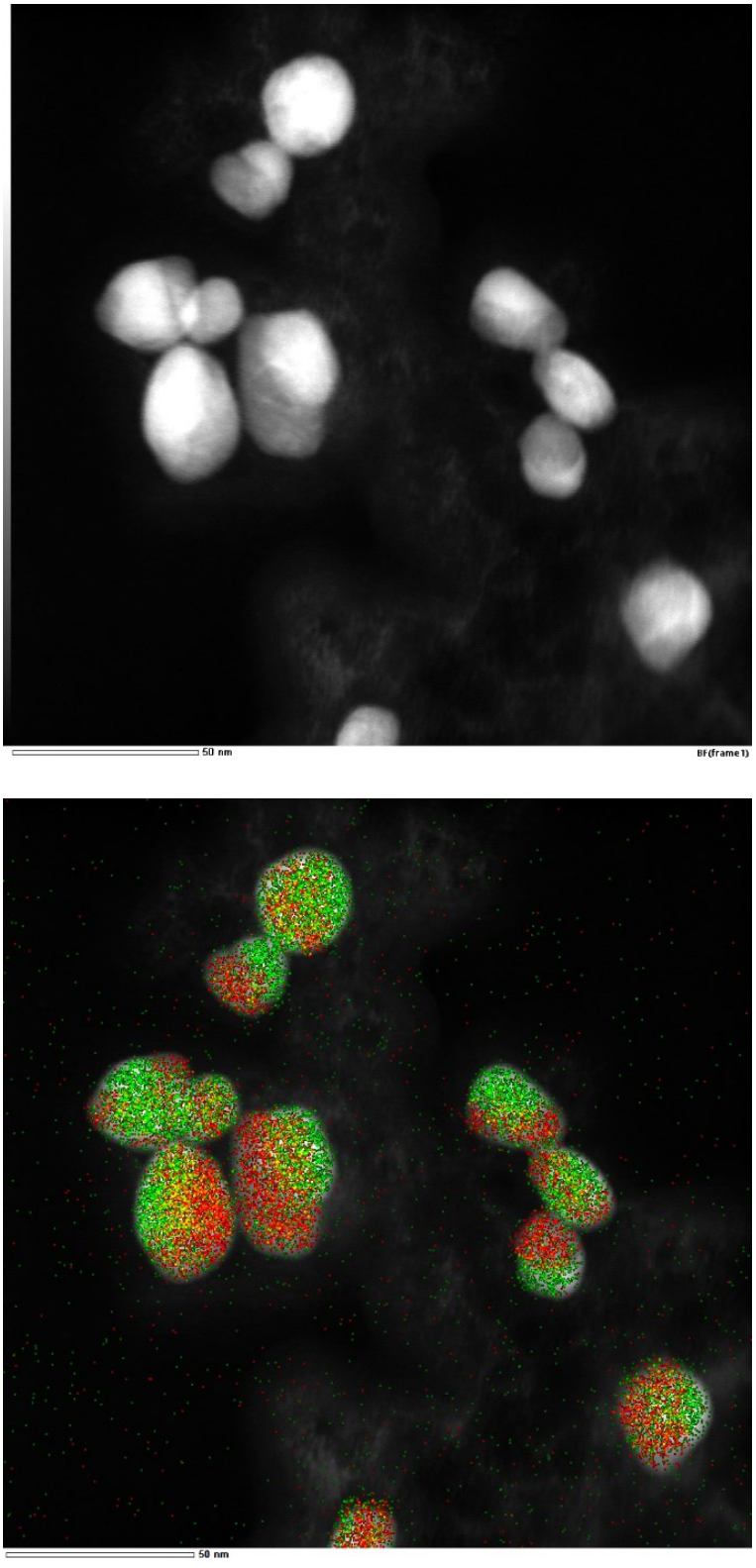

Figure B.8– STEM ADF micrograph and EDX map (Ti: red, Nb: green) of the fine TiN-rich and NbC-rich particles extracted using carbon replica from D-1 QL.

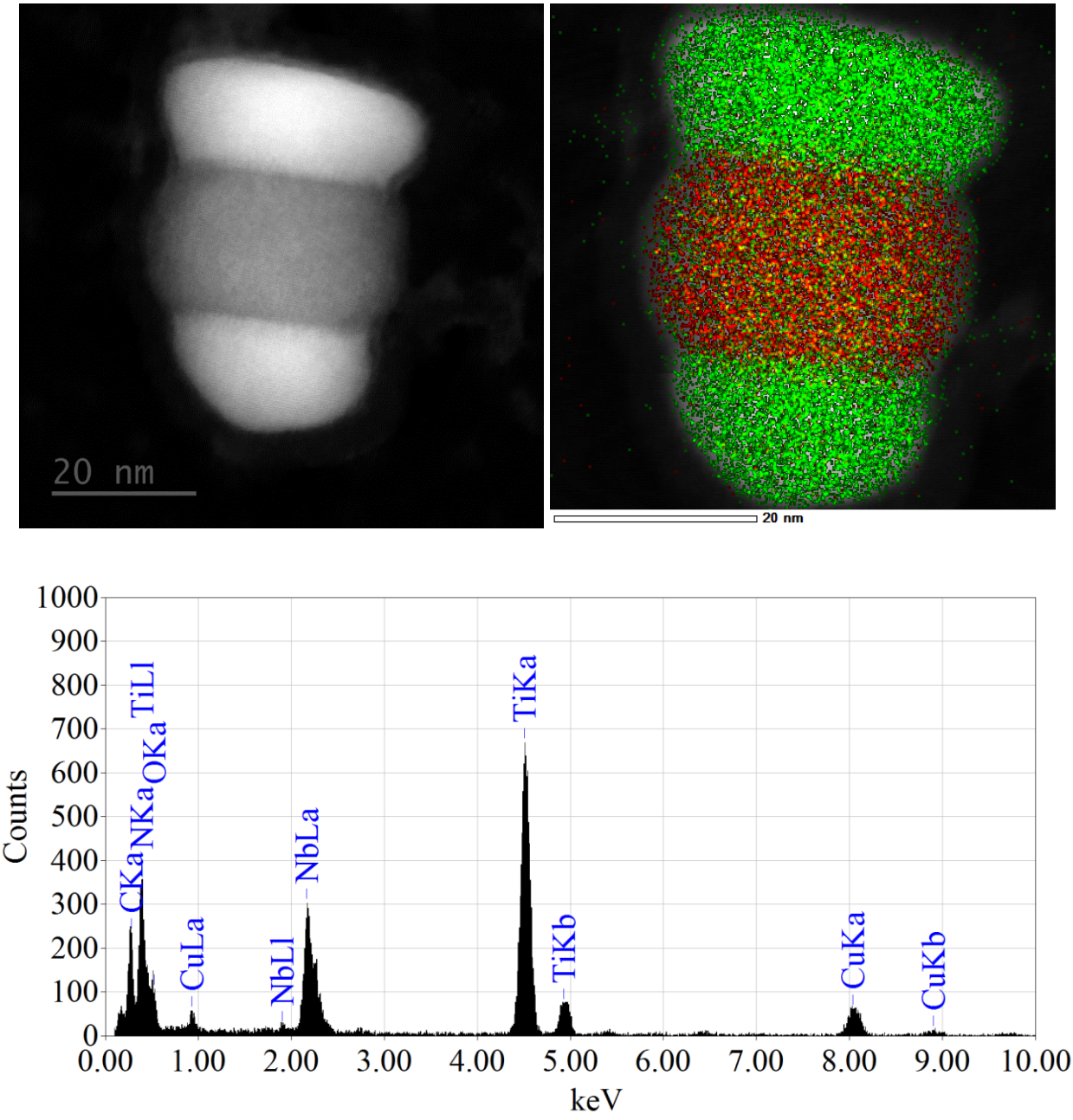

Figure B.9– STEM ADF micrograph and EDX map (Ti: red, Nb: green) of fine TiN-rich and NbC-rich particles along with spectrum of the fine TiN-rich particle extracted using carbon replica from B60 QL.

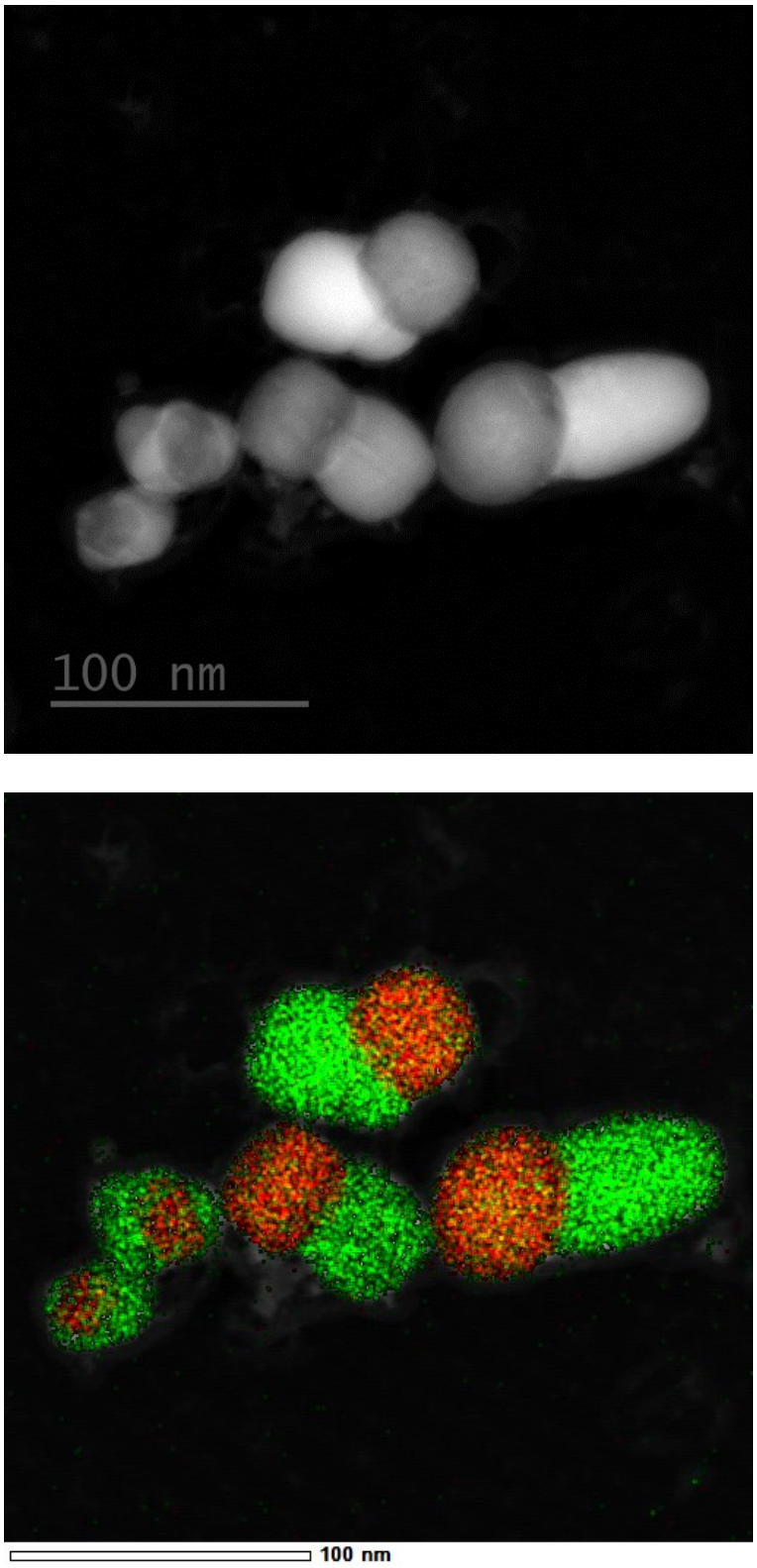

Figure B.10– STEM ADF micrograph and EDX map (Ti: red, Nb: green) of the fine TiN-rich and NbC-rich particles extracted using carbon replica from B60 QL.

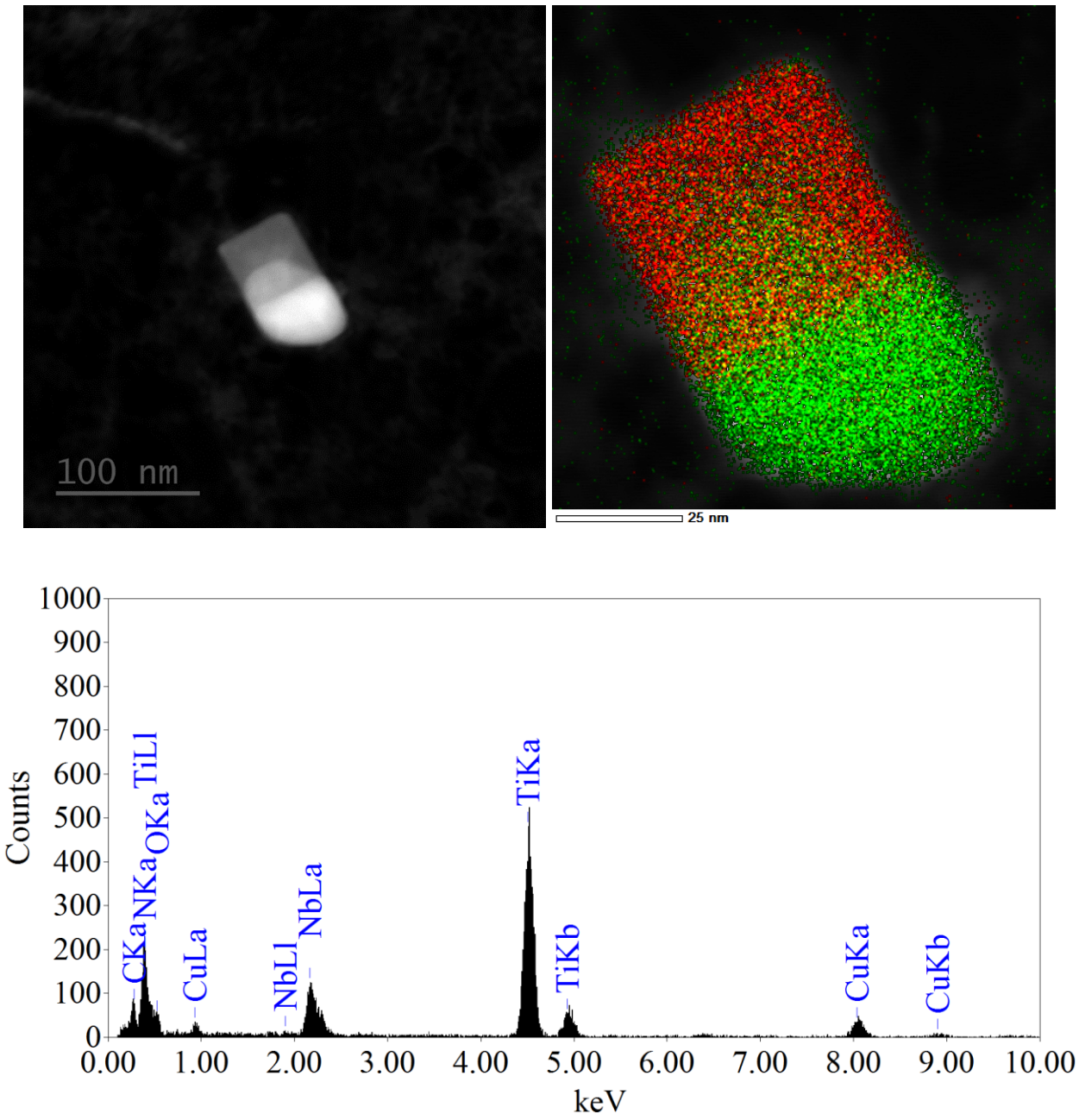

Figure B.11– STEM ADF micrograph and EDX map (Ti: red, Nb: green) of fine TiN-rich and NbC-rich particles along with spectrum of the fine TiN-rich particle extracted using carbon replica from 3F-565 QL.

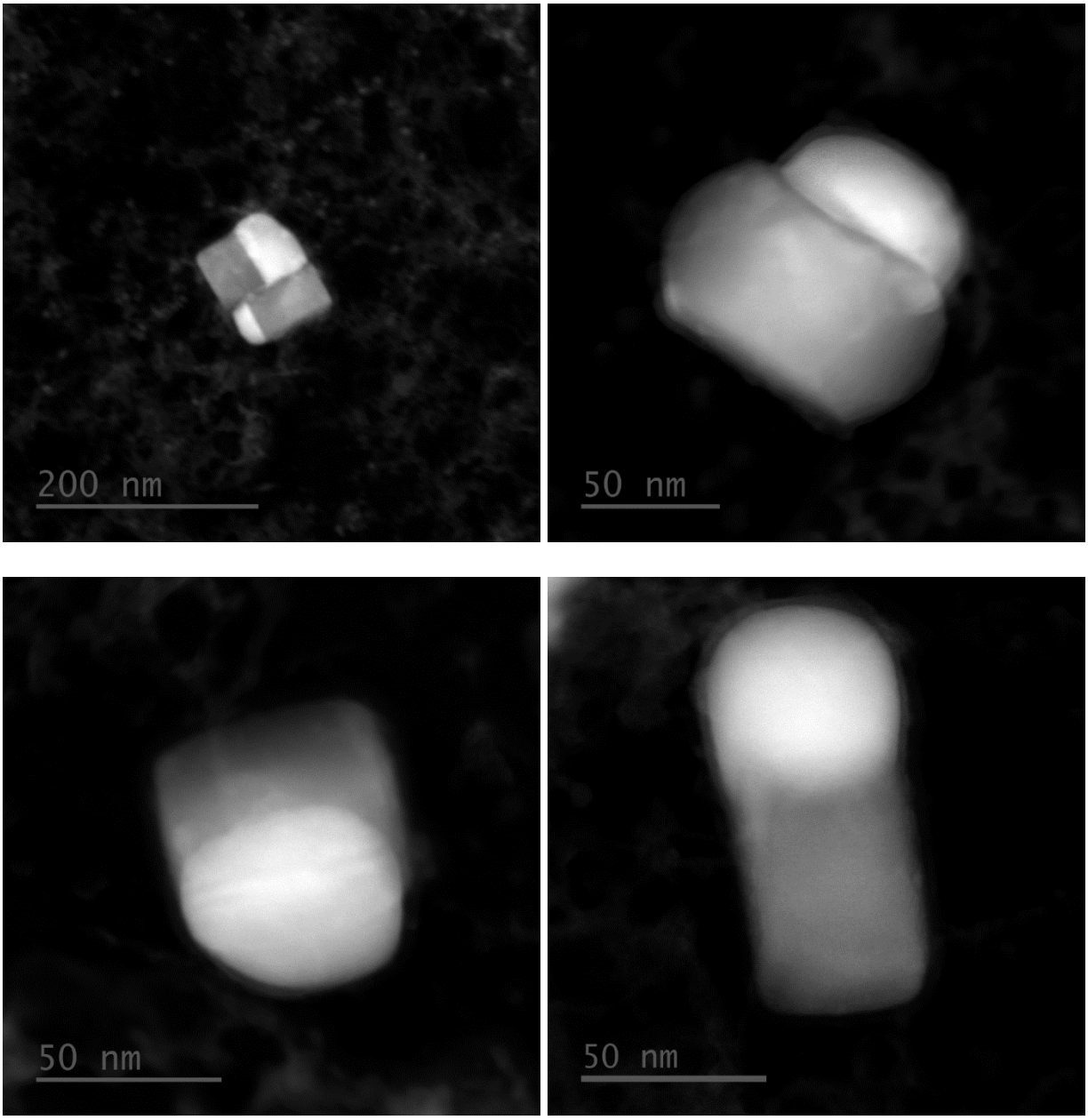

Figure B.12– STEM ADF micrographs of the fine TiN-rich and NbC-rich particles extracted using carbon replica from 3F-565 QL.

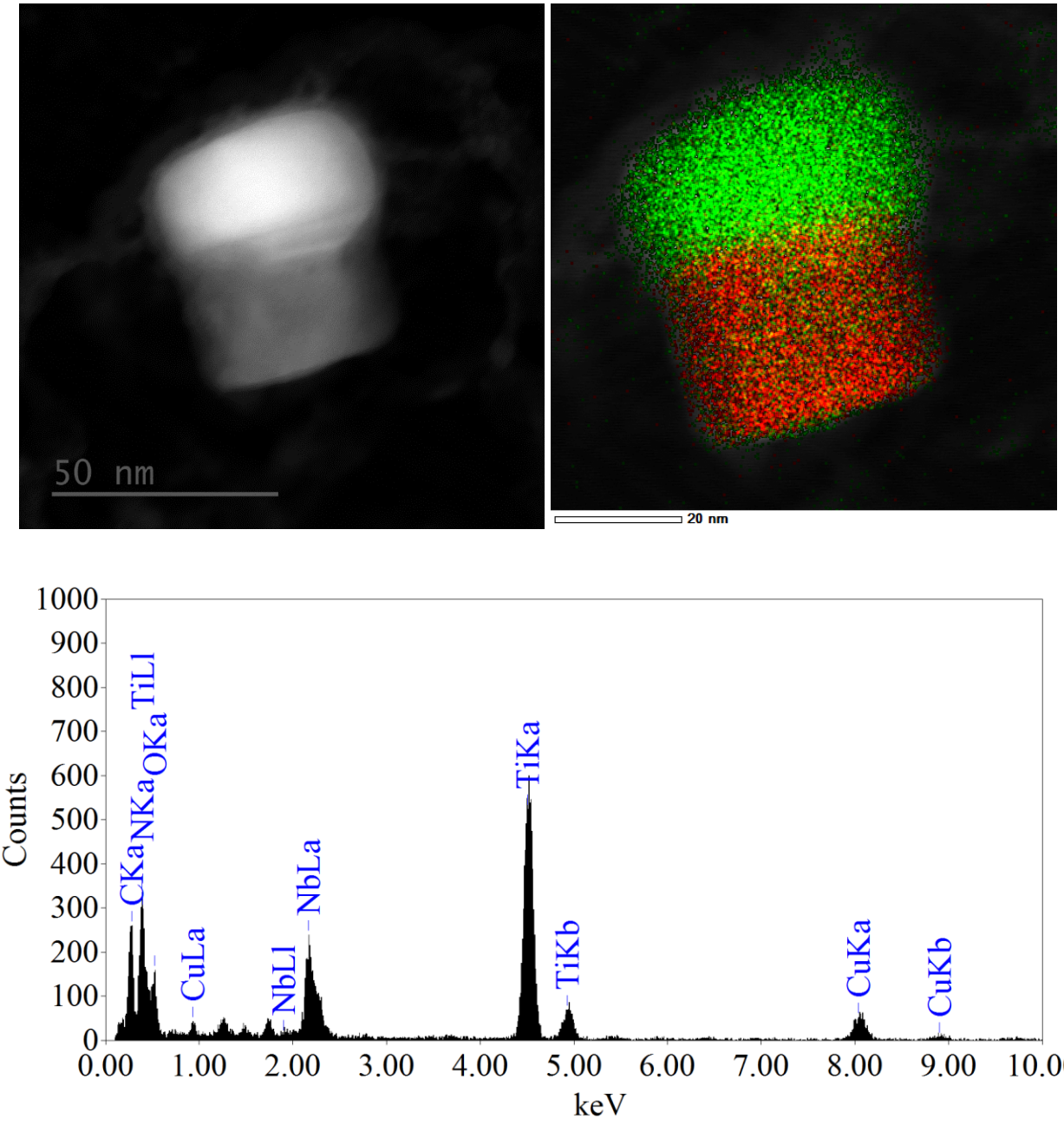

Figure B.13– STEM ADF micrograph and EDX map (Ti: red, Nb: green) of fine TiN-rich and NbC-rich particles along with spectrum of the fine TiN-rich particle extracted using carbon replica from TWX70 QL.

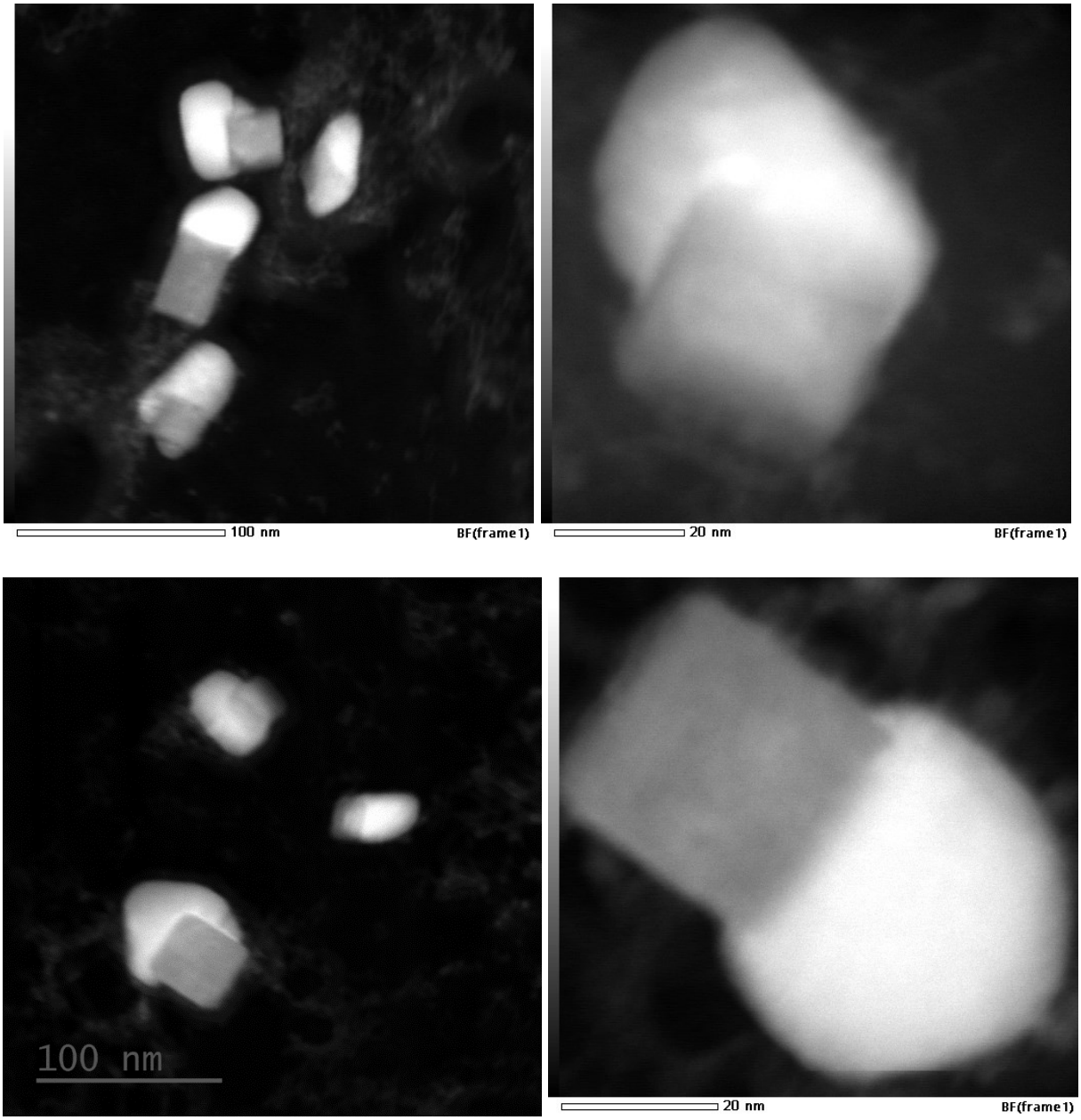

Figure B.14– STEM ADF micrographs of the fine TiN-rich and NbC-rich particles extracted using carbon replica from TWX70 QL.

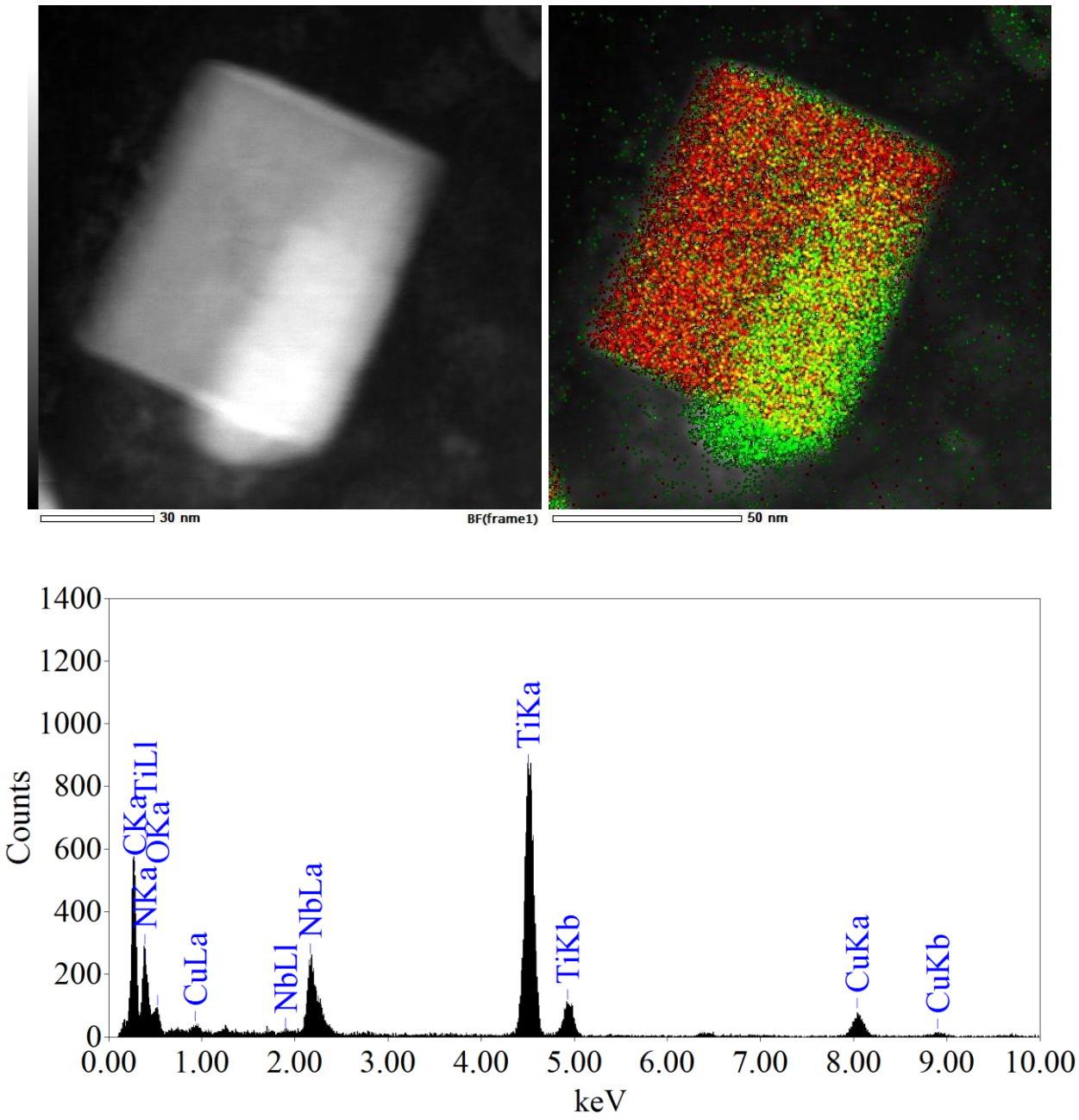

Figure B.15– STEM ADF micrograph and EDX map (Ti: red, Nb: green) of fine TiN-rich and NbC-rich particles along with spectrum of the fine TiN-rich particle extracted using carbon replica from T36-1 CL.

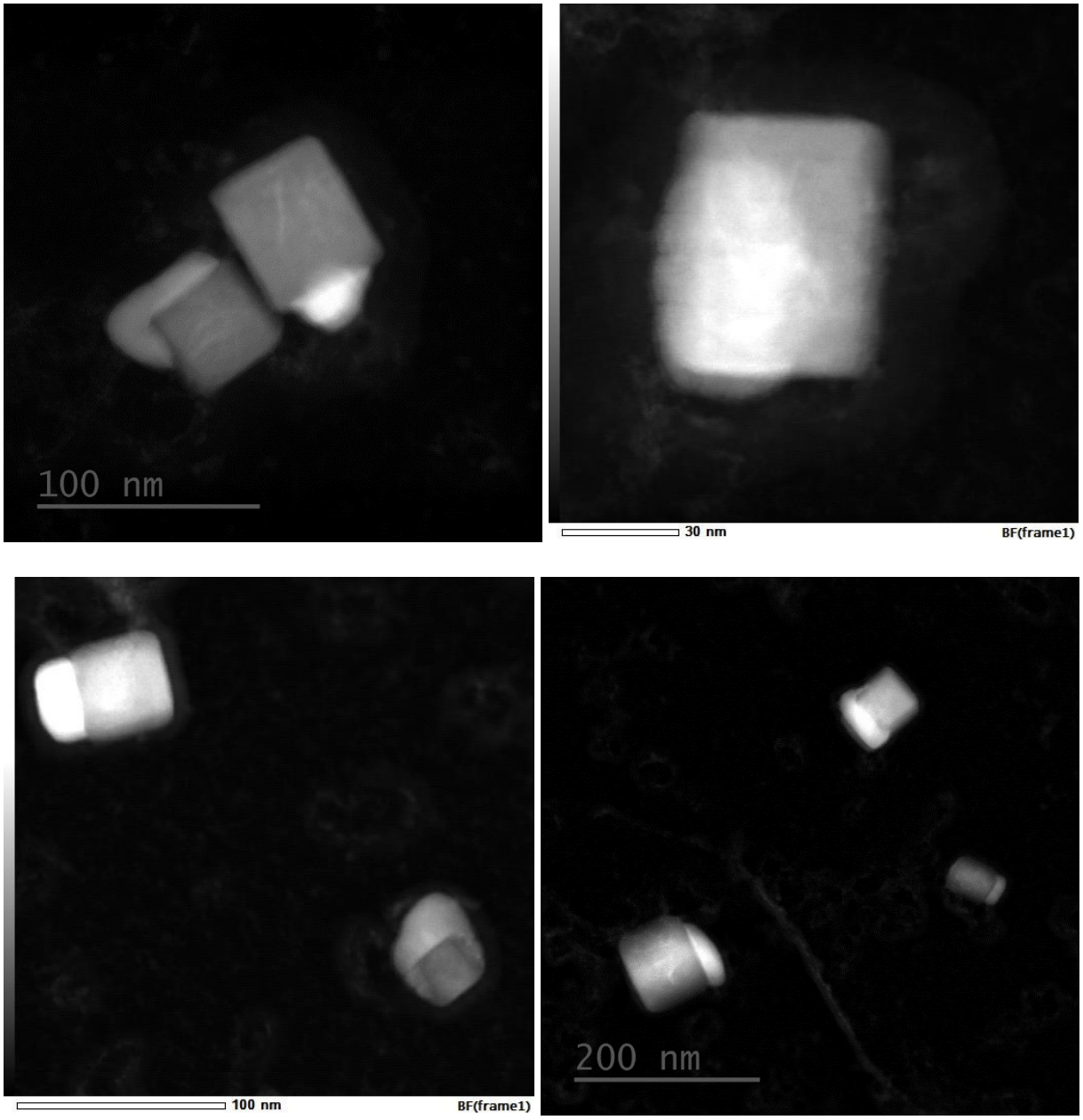

Figure B.16– STEM ADF micrographs of the fine TiN-rich and NbC-rich particles extracted using carbon replica from T36-1 CL.

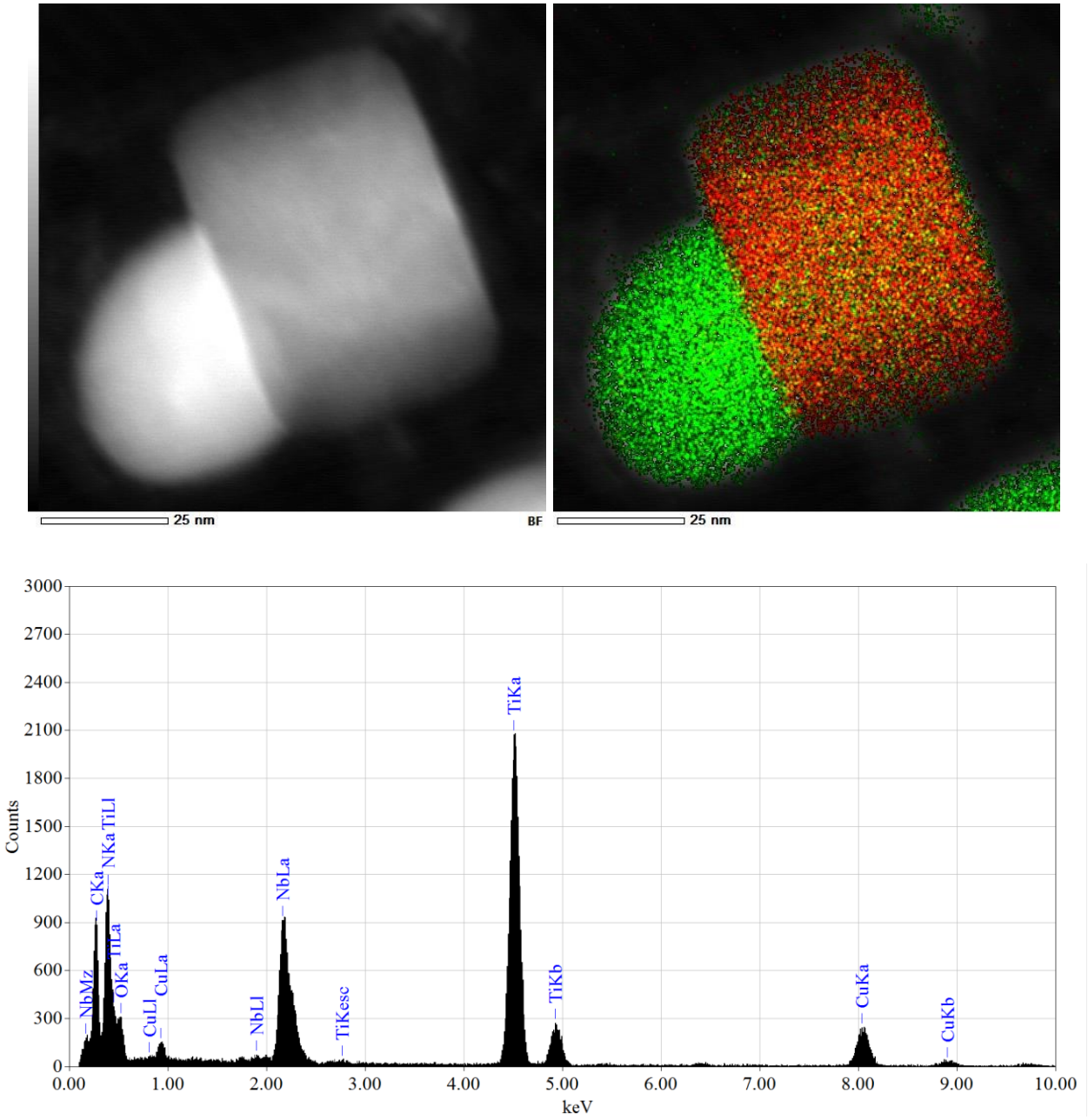

Figure B.17– STEM ADF micrograph and EDX map (Ti: red, Nb: green) of fine TiN-rich and NbC-rich particles along with spectrum of the fine TiN-rich particle extracted using carbon replica from T36-2 CL.

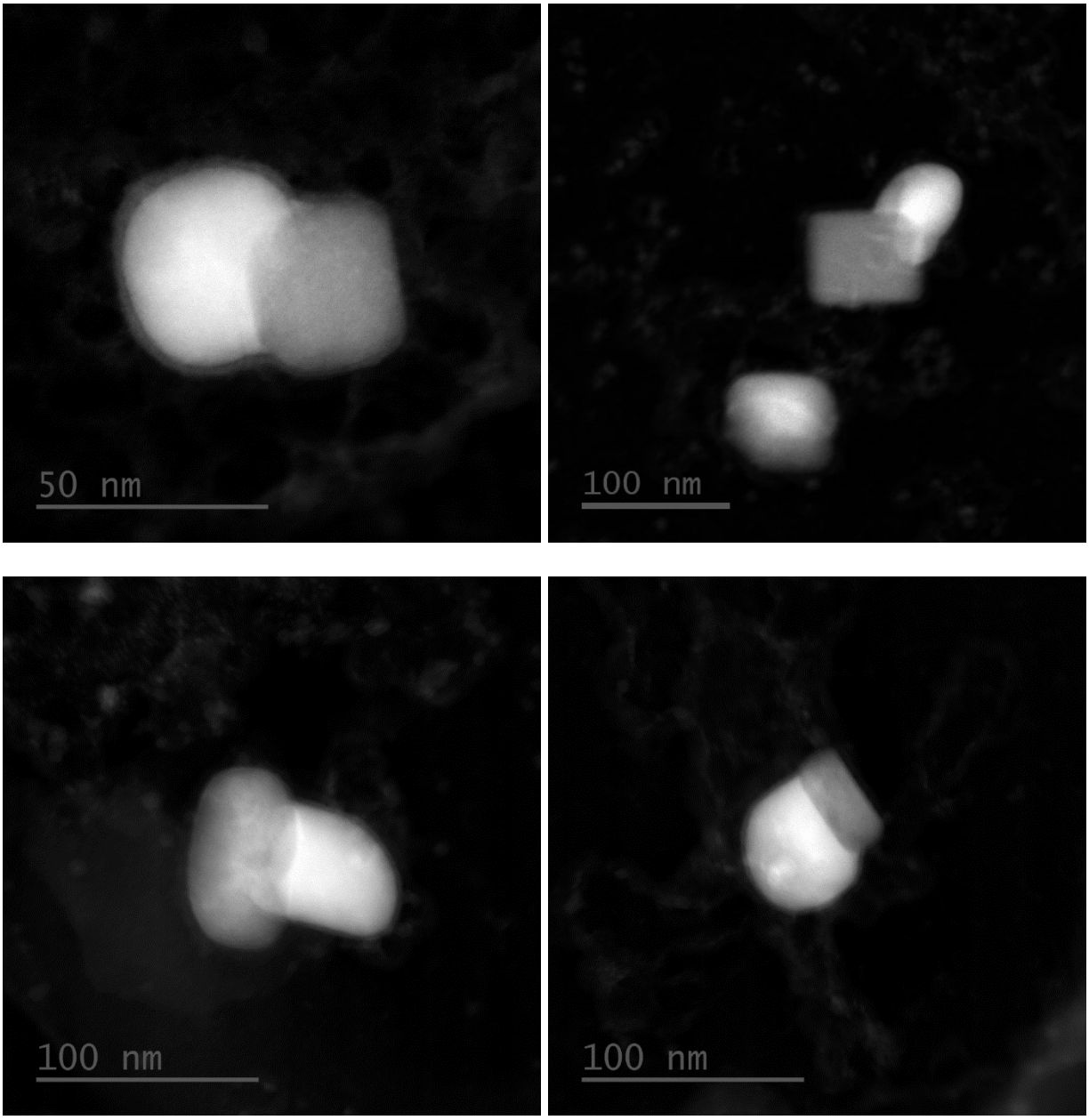

Figure B.18– STEM ADF micrographs of the fine TiN-rich and NbC-rich particles extracted using carbon replica from T36-2 CL.

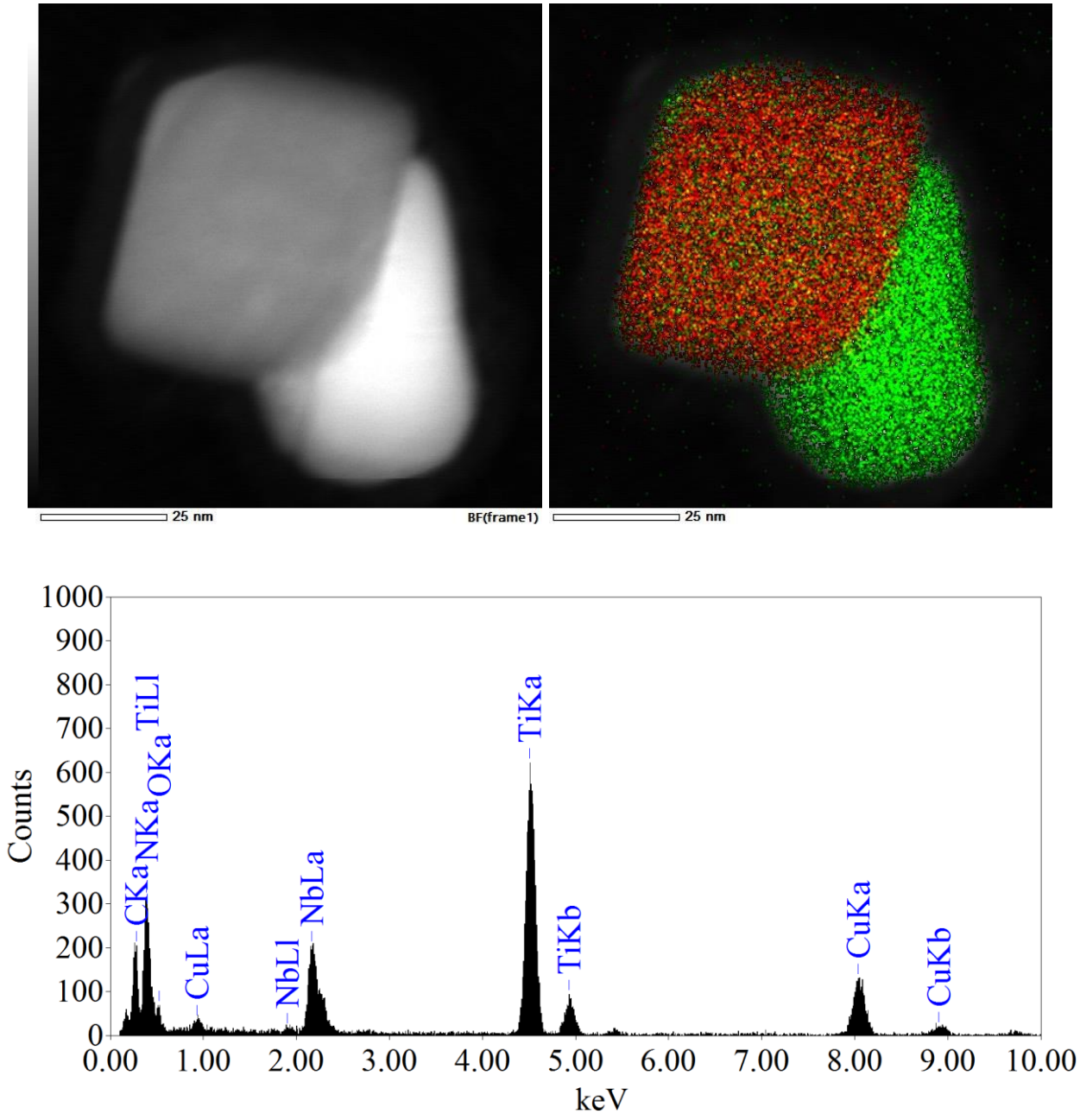

Figure B.19– STEM ADF micrograph and EDX map (Ti: red, Nb: green) of fine TiN-rich and NbC-rich particles along with spectrum of the fine TiN-rich particle extracted using carbon replica from T36-3 CL.

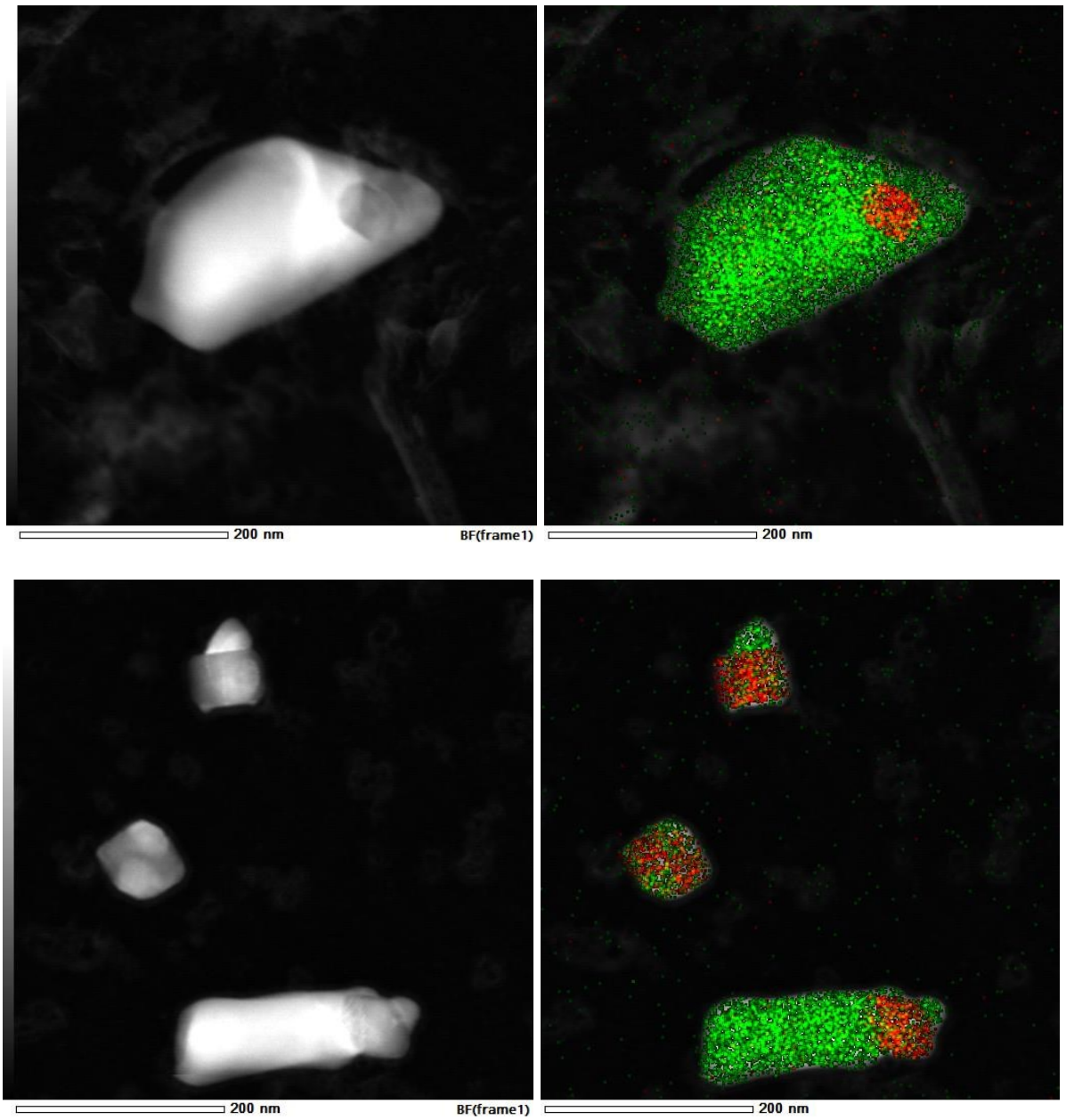

Figure B.20– STEM ADF micrographs and EDX maps (Ti: red, Nb: green) of the fine TiN-rich and NbC-rich particles extracted using carbon replica from T36-3 CL.

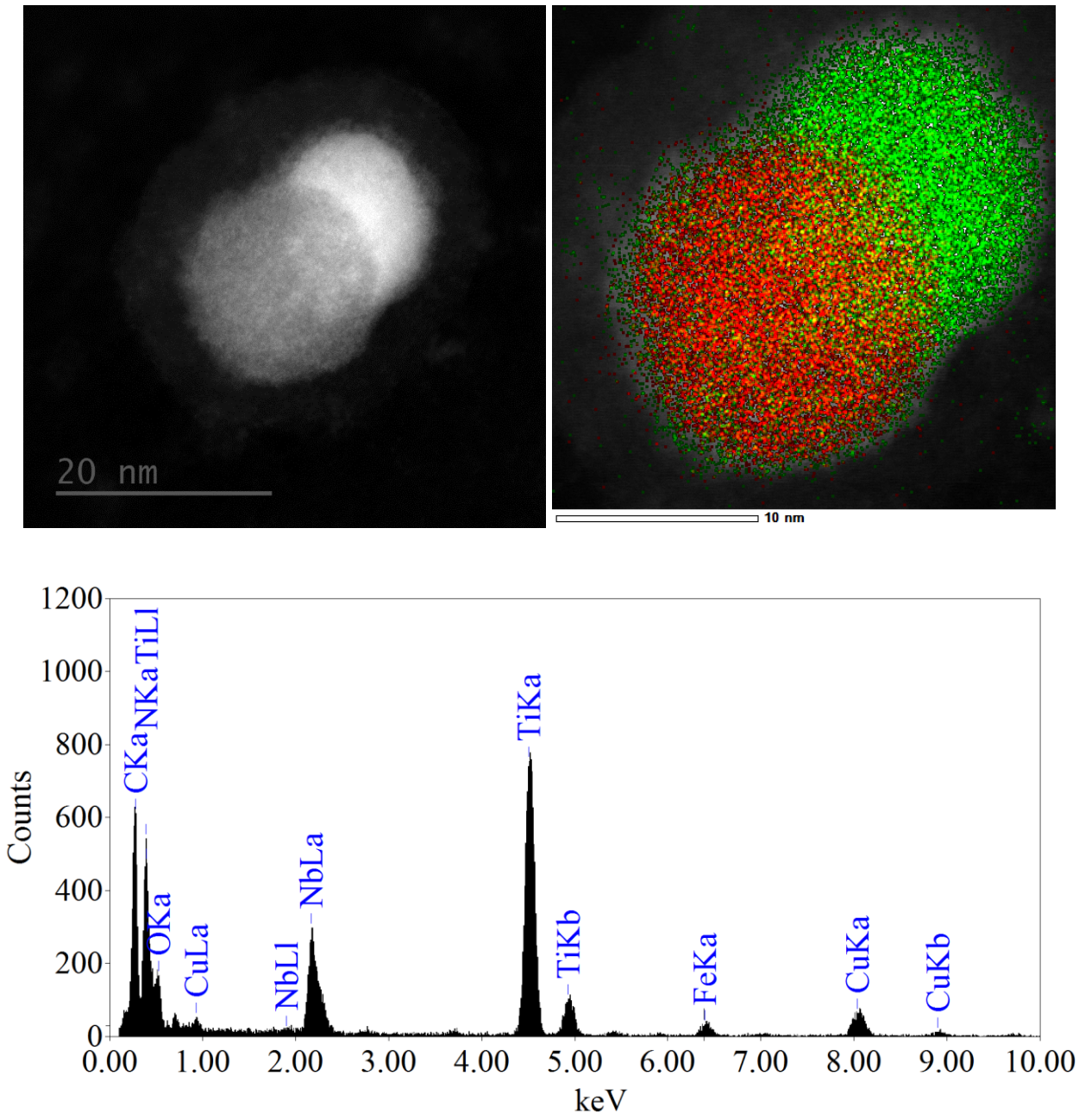

Figure B.21– STEM ADF micrograph and EDX map (Ti: red, Nb: green) of fine TiN-rich and NbC-rich particles along with spectrum of the fine TiN-rich particle extracted using carbon replica from D-1 CL.

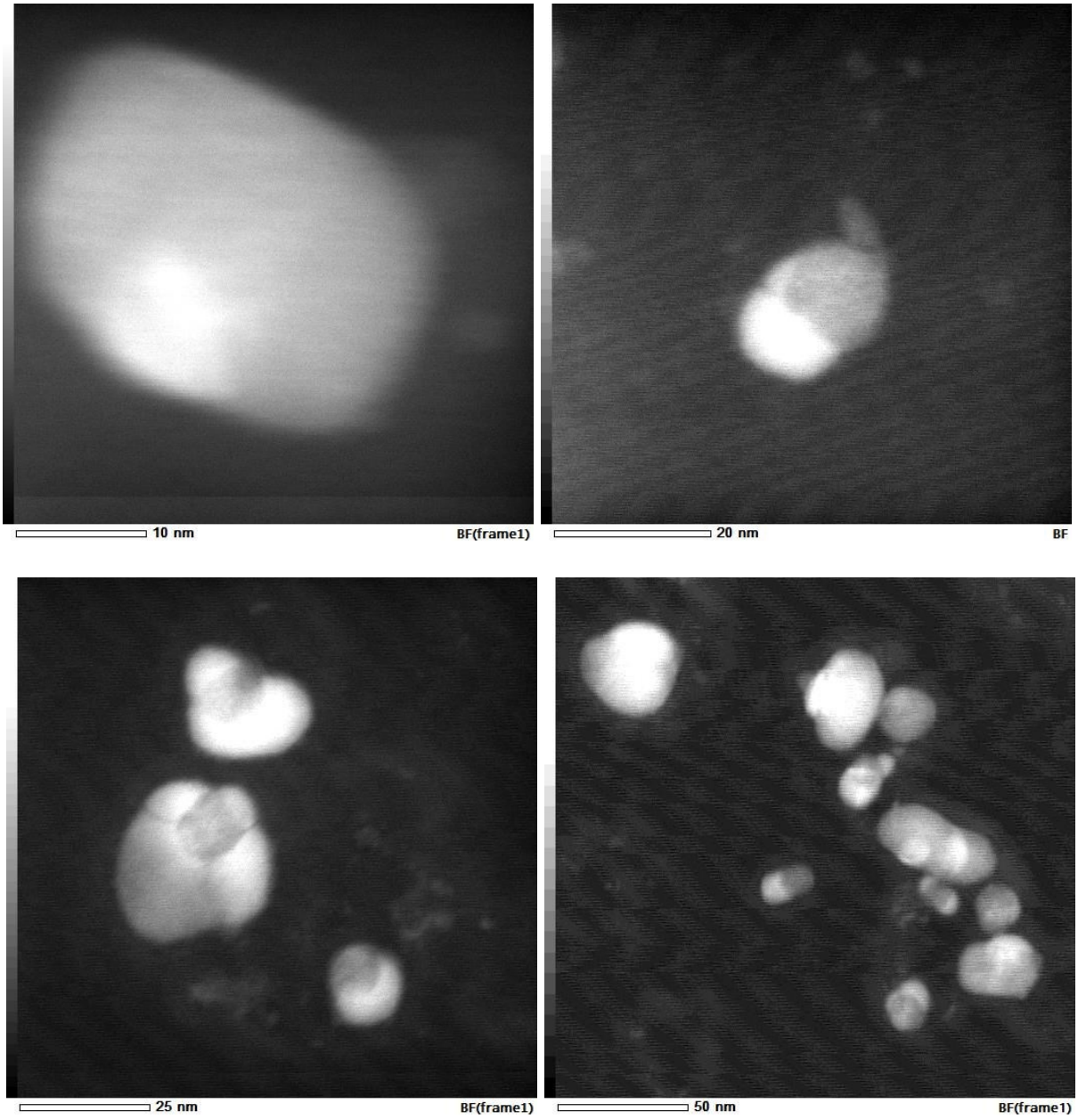

Figure B.22– STEM ADF micrographs of the fine TiN-rich and NbC-rich particles extracted using carbon replica from D-1 CL.

Appendix C TEM/EDX analysis of residues extracted with matrix dissolution

The following presents the electron microscopy analysis conducted by Dr. Douglas Ivey. Figure C.1 shows a TEM bright field (BF) image and the corresponding selected area diffraction (SAD) pattern of the residues extracted from T36-1 CL using the matrix dissolution method. It shows particles of different sizes. The SAD pattern shows a faint crystalline ring indicating an amorphous ring (arrow), which has a d spacing of ~0.390 nm. The EDX map of the region in Figure C.1 is presented in Figure C.2, showing individual EDX maps for Nb, Mo, Ti, and O. Based on the d spacing and the maps, it was suggested that the phase could be Nb_2O_5 or Nb-Mo oxide ($3MoO_2.Nb_2O_5$).

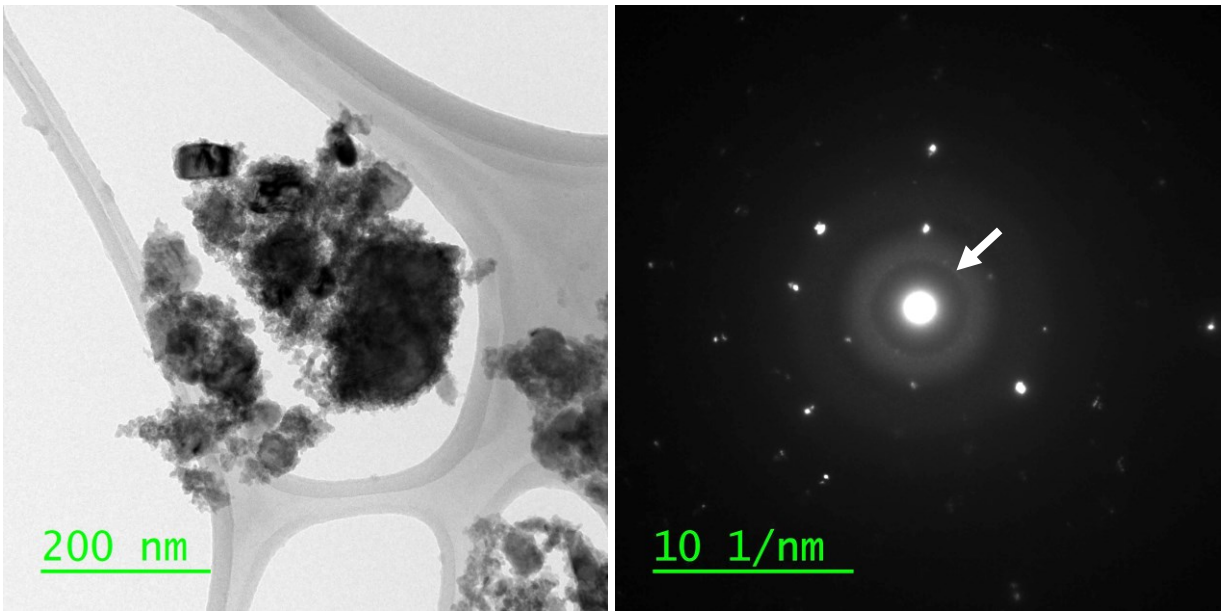

Figure C.1– TEM BF and SAD analysis of the residues extracted from T36-1 CL using matrix dissolution. The arrow indicates a ring with a d spacing of ~0.390 nm.

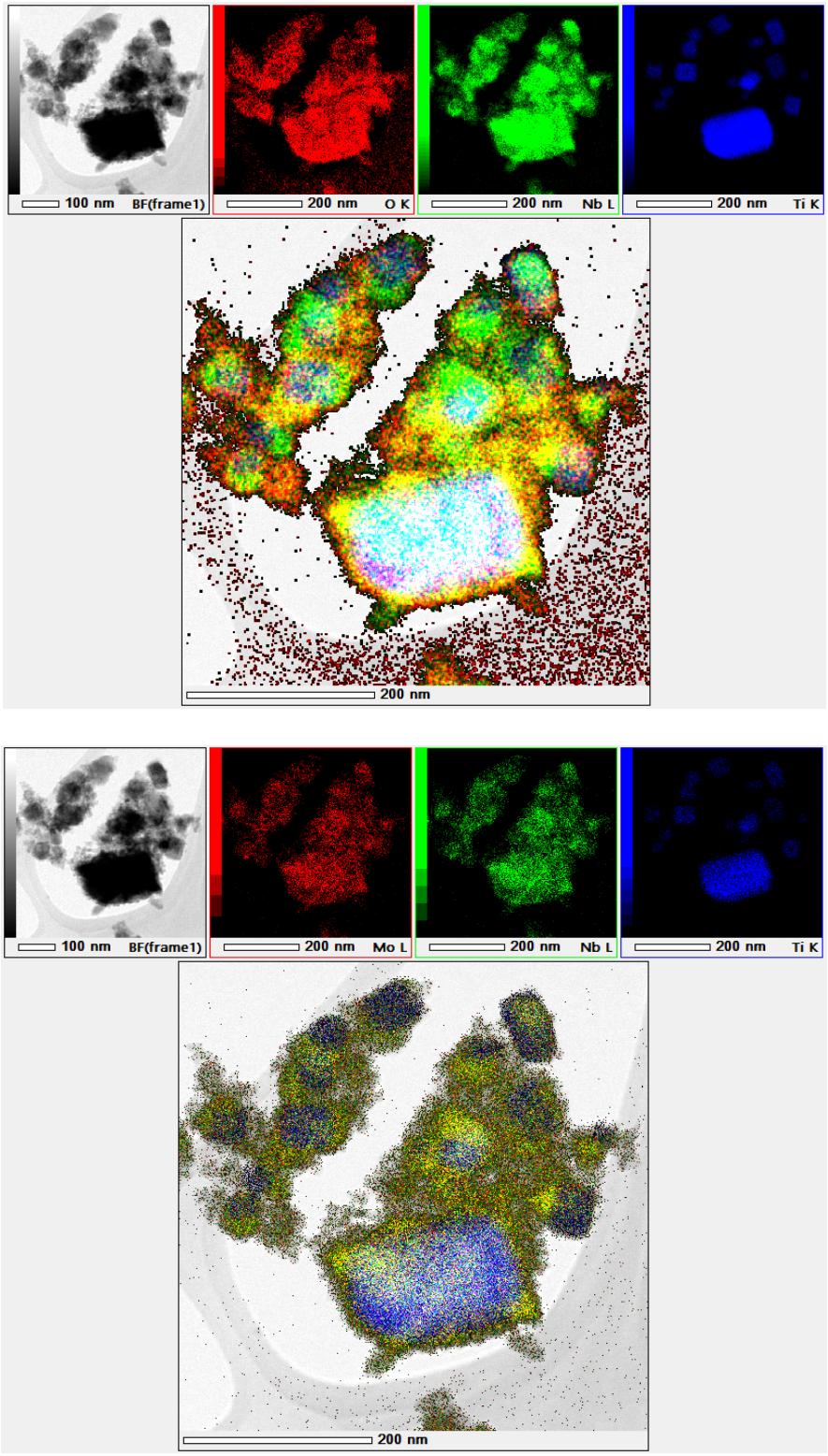

Figure C.2– TEM/EDX maps of the residues in Figure C.1.

Appendix D ThermoCalc analysis of oxidation of NbC

The steel samples contain NbC-rich nano-precipitates and when they are extracted from the steels using the matrix dissolution method, they are exposed to oxygen in the air. Single point equilibrium module of ThermoCalc was employed to study the equilibrium phases under such conditions. Table D.1 shows the equilibrium phases at 25 °C when different concentrations of oxygen are present. NbC does not form under equilibrium conditions indicating the Nb oxide phase is more stable than NbC.

Table D.1– ThermoCalc results for Nb-C-O system

Composition of the system (mole)			Stable phases (mole fraction)			
Nb	C	O	NbO_2	CO_2	O_2	C (graphite)
0.25	0.25	0.5	0.75	-	-	0.25
0.125	0.125	0.75	0.375	0.312	0.312	-
0.05	0.05	0.9	0.15	0.106	0.744	-
0.01	0.01	0.98	0.03	0.02	0.95	-

Appendix E QXRD

E-1 Introduction

In this Appendix, an example of the scripts used in TOPAS academic software is provided. The repeatability of QXRD analysis is evaluated. Then, the observed and calculated XRD patterns for the residues extracted from the studied steels via the matrix dissolution method are presented.

E-2 Examples of scripts used in TOPAS academic

Figure E.1 and Figure E.2 show the script used in the software and the observed XRD pattern (blue line) and calculated XRD pattern (red line) for the standard sample (LaB_6), respectively. Figure E.3 presents an example of the script used in the software to analyze the residues extracted with the matrix dissolution method.

```
r_wp  6.69823765 r_exp  2.24005159 r_p  4.40698836 r_wp_dash  15.127149 r_p_dash  17.3011154

iters 100000
chi2_convergence_criteria 0.001

   xdd X12881.xy
      x_calculation_step = Yobs_dx_at(Xo); convolution_step 4
      bkg @  1705.37144` -946.17671`  526.326928` -235.926933`  80.6045621` -38.4547778`
      LP_Factor(!th2_monochromator, 0)
      CoKa3(0.0001)
      '  Cagliotti parameters
      UVW(@u,-0.04074`, @v, 0.00320`, @w,-0.05899`)
      Zero_Error(@zero, 0.05530`)
      Simple_Axial_Model(@axial, 12.73134`)
      start_X 20
      finish_X 100

   str
      LVol_FWHM_CS_G_L(1, 4489.51014 ,0.89, 5424.90744, !csgcl3, 10000, !cslcl3, 10000)
      e0_from_Strain( 0.00004, !sgcl, 0.0001, !slcl, 0.0001)
      MVW( 203.772, 71.875`, 100.000`)
      phase_name "LaB6"
      space_group "Pm-3m"
      al 90.0
      be 90.0
      ga 90.0
      Cubic (@lpA  4.157760` ) ' 4.157597
      site La     x .0          y .0          z .0        occ La 1
      site B      x .19169      y 0.5         z 0.5       occ B  1
      scale @  0.0191286347`
```

Figure E.1– Screenshot of the script used as the input for TOPAS Academic in Rietveld refinement analysis of the LaB_6 standard XRD pattern.

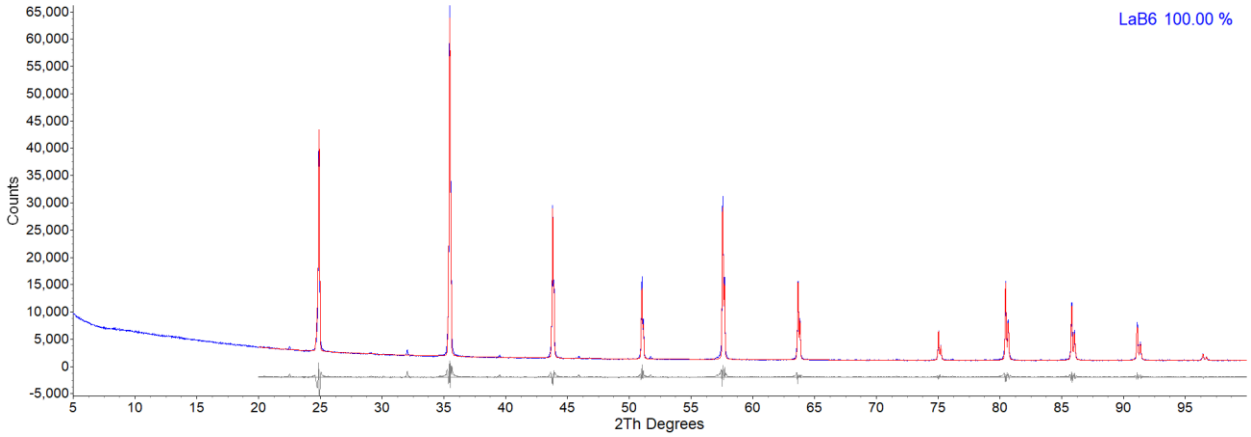

Figure E.2– Observed and calculated XRD patterns of LaB_6 standard sample analyzed along with residues collected via the matrix dissolution experiment.

```
r_wp  3.19963221 r_exp  2.48458923 r_p  2.52077103 r_wp_dash  9.87552457 r_p_dash  12.0768486 r_exp_dash  7.

iters 100000
chi2_convergence_criteria 0.00001


    xdd X12880.xy
        x_calculation_step = Yobs_dx_at(Xo); convolution_step 4
        CoKa3(0.0001)
        LP_Factor(!th2_monochromator, 0)
        '--------------------------------------------------------------
        '  Cagliotti parameters
        UVW(!u,-0.04074, !v, 0.00320, !w,-0.05899)
        '--------------------------------------------------------------
        Zero_Error(!zero, 0.05530)
        Simple_Axial_Model(!axial, 12.73134)
        bkg  @  1349.17768` -583.925672`  196.099519` -102.619723`  114.342038` -53.3698597` -37.6795538`  46.
        Specimen_Displacement(@sd,-0.00052`)
        start_X 35
        finish_X 100

    str
        LVol_FWHM_CS_G_L( 1, 23.80823`, 0.89, 33.26226`, csgcl, 10000.00000`_LIMIT_MIN_0.3, cslcl, 37.35446`)
        e0_from_Strain( 0.02008`, sgcl, 0.00010`_LIMIT_MIN_0.0001, slcl, 0.08034`)
        MVW( 416.308, 88.570`, 40.558`)
        phase_name "NbC-rich"
        space_group "Fm-3m"
        Cubic (lpAl  4.457548`)
        site Til    x 0            y 0            z 0            occ Ti  0.02
        site Nb2    x 0            y 0            z 0            occ Nb 0.96
        site Mo22    x 0            y 0            z 0            occ Mo 0.02
        site N3     x 0.5          y 0.5          z 0.5          occ N  0
        site C4     x 0.5          y 0.5          z 0.5          occ C  1
        scale  @  0.00284266363`
        PO_Spherical_Harmonics(shl, 8 load sh_Cij_prm {
            k00   !shl_c00  1.00000
            k41   shl_c41   0.03163`
            k61   shl_c61  -0.02492`
            k81   shl_c81   0.01182`
            } )
```

Figure E.3– Screenshot of script used as input for Topas Academic in Rietveld refinement analysis of the XRD pattern for residue extracted from T36-1 QL (part 1 of 2)

```
str
   LVol_FWHM_CS_G_L( 1, 4489.51014`, 0.89, 5424.90744`, csgc2, 10000.00000`_LIMIT_MIN_0.3, cslc2, 10000.0
   e0_from_Strain( 0.13212`, sgc2, 0.52842`, slc2, 0.00010`_LIMIT_MIN_0.0001)
   MVW( 263.709, 77.479`, 24.839`)
   phase_name "TiN-rich I"
   space_group "Fm-3m"
   Cubic (lpA2  4.263120`)
   site Ti5    x 0            y 0            z 0            occ Ti 0.91
   site Nb6    x 0            y 0            z 0            occ Nb 0.09
   site N7     x 0.5          y 0.5          z 0.5          occ N  1
   site C8     x 0.5          y 0.5          z 0.5          occ C  0
   scale  @  0.00314179466`
   PO_Spherical_Harmonics(sh2, 8 load sh_Cij_prm {
      k00   !sh2_c00  1.00000
      k41   sh2_c41   0.19388`
      k61   sh2_c61  -0.09925`
      k81   sh2_c81  -0.03808`
      } )

str
   LVol_FWHM_CS_G_L( 1, 33.06853`, 0.89, 46.18956`, csgc3, 9992.11414`_LIMIT_MIN_0.3, cslc3, 51.86298`)
   e0_from_Strain( 0.22295`, sgc3, 0.62989`, slc3, 0.42790`)
   MVW( 299.740, 79.095`, 34.603`)
   phase_name "TiN-rich II"
   space_group "Fm-3m"
   Cubic (lpA3  4.292557`)
   site Ti9    x 0            y 0            z 0            occ Ti  0.71
   site Nb10    x 0            y 0            z 0            occ Nb 0.29
   site N11     x 0.5          y 0.5          z 0.5          occ N  1
   site C12     x 0.5          y 0.5          z 0.5          occ C  0
   scale  @  0.00377202017`
   PO_Spherical_Harmonics(sh3, 8 load sh_Cij_prm {
      k00   !sh3_c00  1.00000
      k41   sh3_c41   0.00596`
      k61   sh3_c61   0.06681`
      k81   sh3_c81   0.12988`
      } )
```

Figure E.3– Screenshot of script used as the input for Topas Academic in Rietveld refinement analysis of the XRD pattern for residue extracted from T36-1 QL (part 2 of 2).

In order to incorporate the aberrations arising from the instrument and the powder samples (extracted residues from the matrix dissolution method), several functions were included in the analysis. The Lorentz-Polarization factor (LP_Factor) was used to account for the effects of Lorentz factor and polarization factor on the intensity of the diffracted beam. In an X-ray powder diffractometer, as the diffraction angle increases ($2\theta < 90^{o}$), the part of the Debye-Scherrer cone that intersects with the detector decreases, leading to a decrease in the intensity of the reading (Lorentz factor) [1], [2]. X-ray diffractometers employ X-ray sources that generate unpolarized beams. When an unpolarized beam is diffracted, it partially becomes polarized and its intensity

decreases. Using a primary or secondary beam monochromator in the X-ray diffractometer also results in the polarization effect [1], [2]. Zero shift (Zero_Error) and sample displacement (Specimen_Displacement) aberrations cause a shift in the angle of diffraction. Zero shift is due to instrument misalignment (the detector arm) [3] and the sample displacement aberration occurs when the surface of the sample is below or above the focusing circle of the instrument (Figure D.4) [2]. Simple_Axial_Model was used to rectify the asymmetry in the peak shapes due to axial divergence of the X-ray in the emitted beam from the source and in the diffracted beam collected by the detector [4].

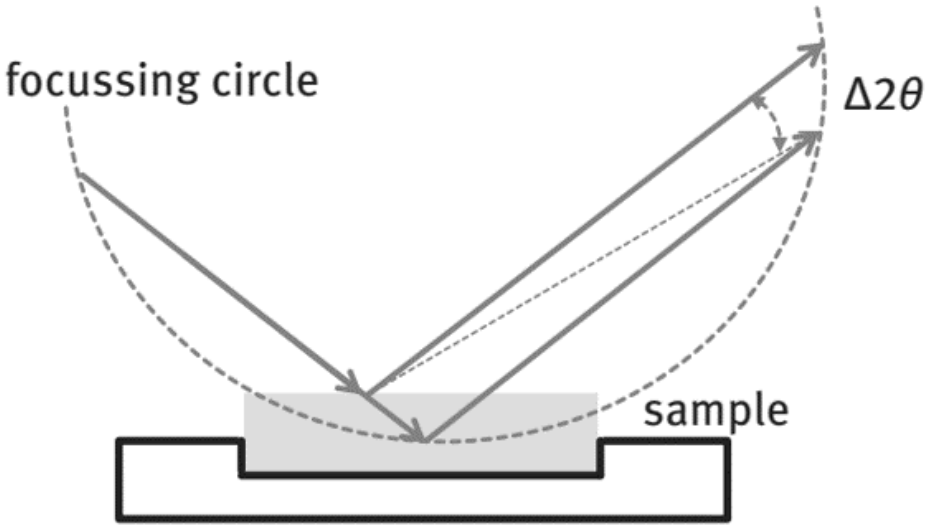

Figure E.4– Shift in 2θ caused by sample displacement [2].

E-3 Repeatability of QXRD analysis

To investigate the repeatability of QXRD analysis, the starting values of the parameters used in the scripts were changed several times and it was observed that the results showed negligible differences. Table E.1 shows two examples of the starting value sets and the obtained results in each analysis for T36-1 QL. The effect of changes in the composition of the phases on their volume fractions has been demonstrated in Section 3-9-2.

Table E.1– Starting values and the results obtained in QXRD analysis for T36-1 QL

Phase	Parameter	First set		Second set	
		Starting value	Result	Starting value	Result
Coarse TiN-rich	Size (nm)	100	4490	50	4490
	Lattice parameter (Å)	4.25	4.263	4.27	4.263
	Volume fraction (%)	-	0.024	-	0.023
Fine TiN-rich	Size (nm)	40	32	500	32
	Lattice parameter (Å)	4.31	4.293	4.28	4.292
	Volume fraction (%)	-	0.029	-	0.030

E-4 The observed and calculated XRD patterns

The following presents the observed XRD patterns and calculated XRD patterns of the residues extracted with the matrix dissolution method.

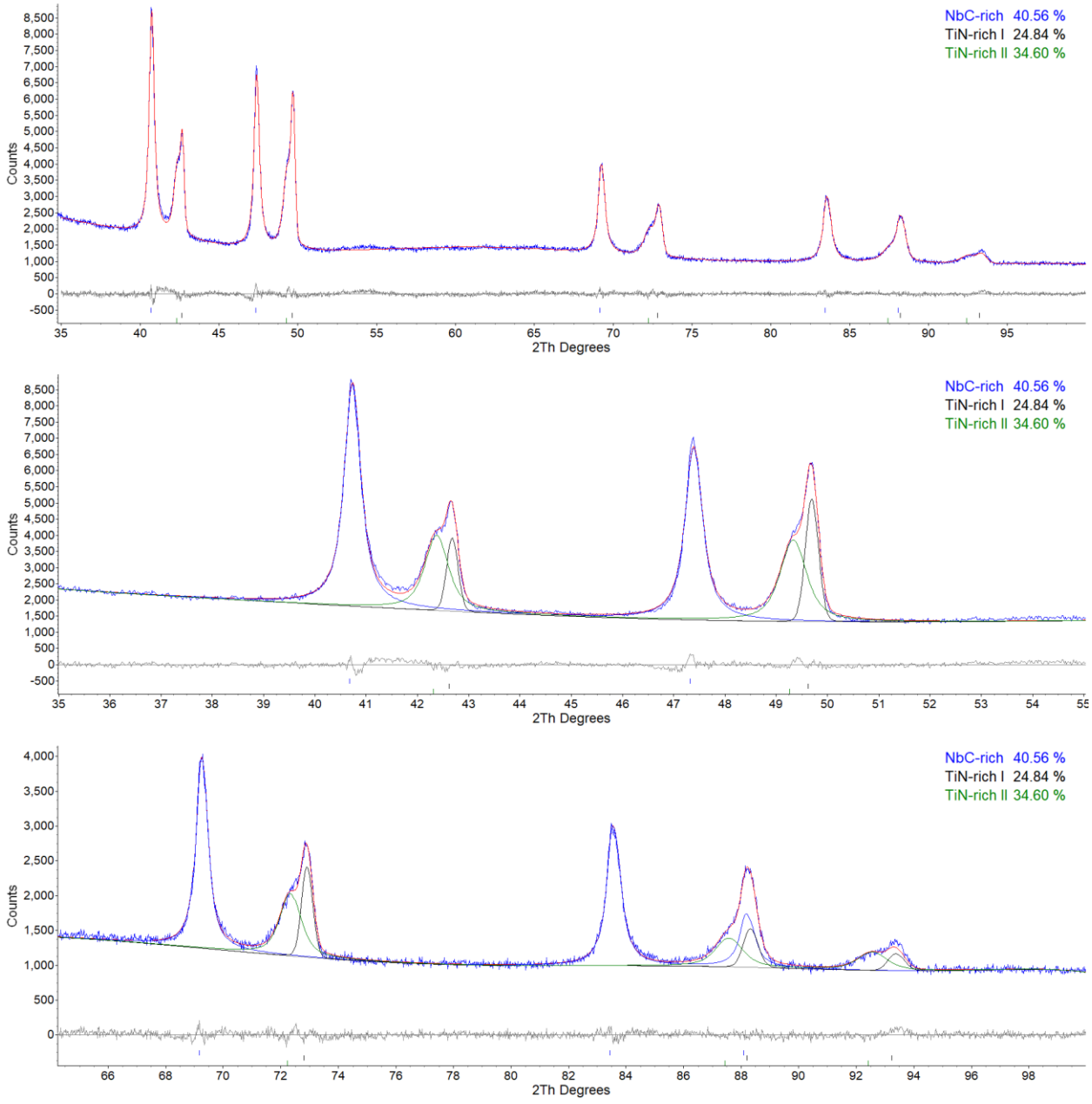

Figure E.5– Observed and calculated XRD patterns for residues extracted from T36-1 QL via the matrix dissolution method.

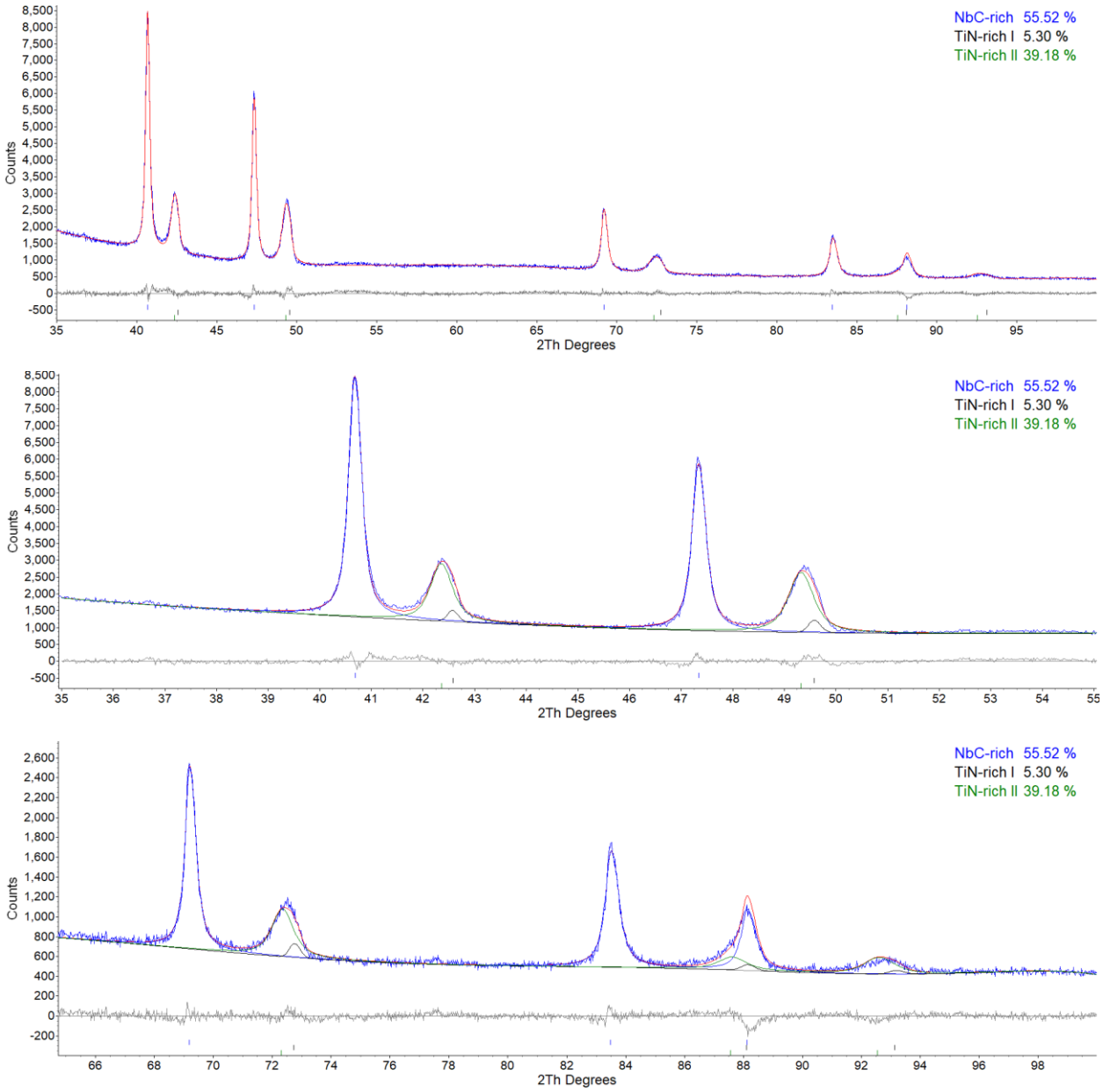

Figure E.6– Observed and calculated XRD patterns for residues extracted from T36-2 QL via the matrix dissolution method.

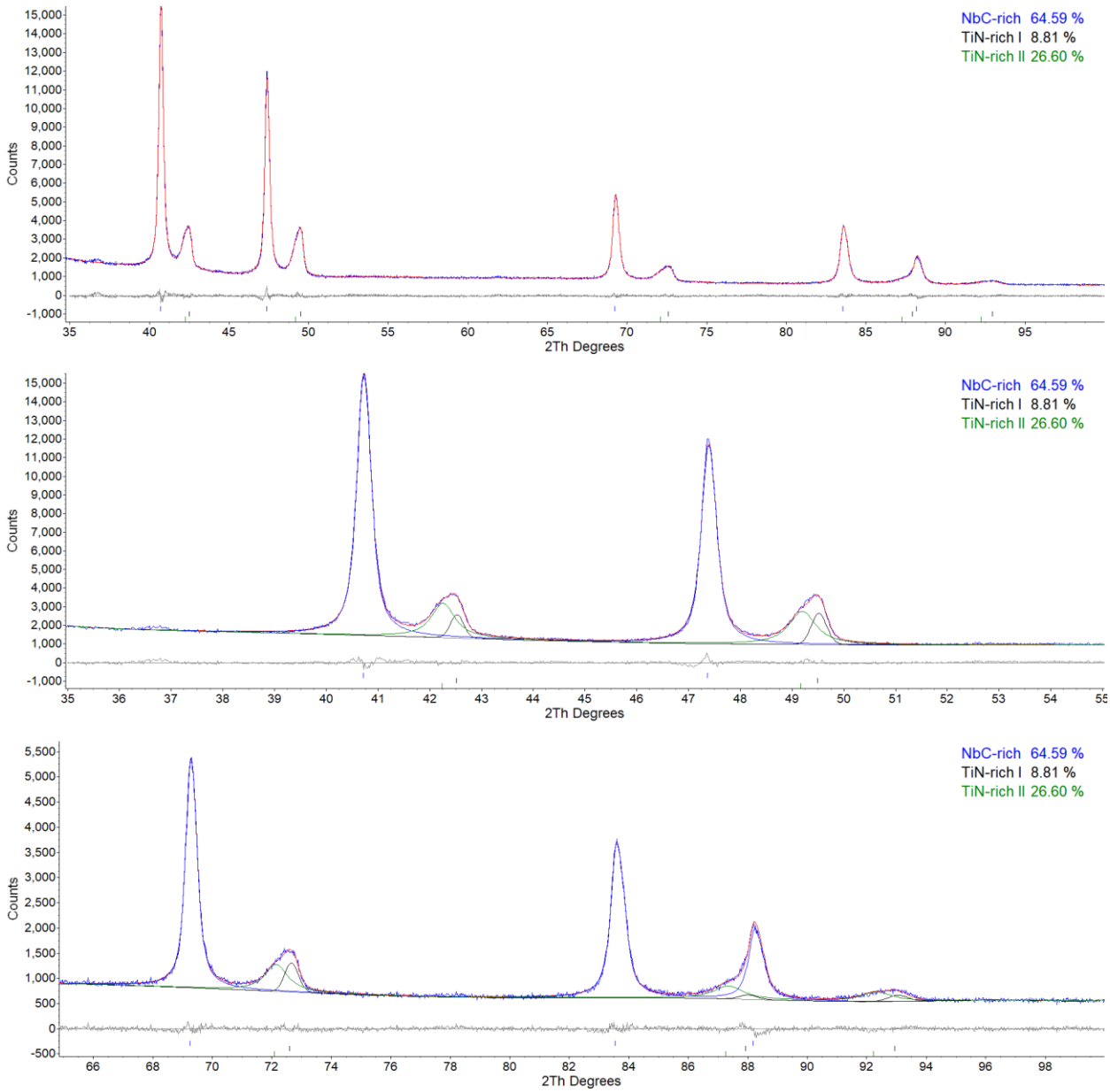

Figure E.7– Observed and calculated XRD patterns for residues extracted from T36-3 QL via the matrix dissolution method.

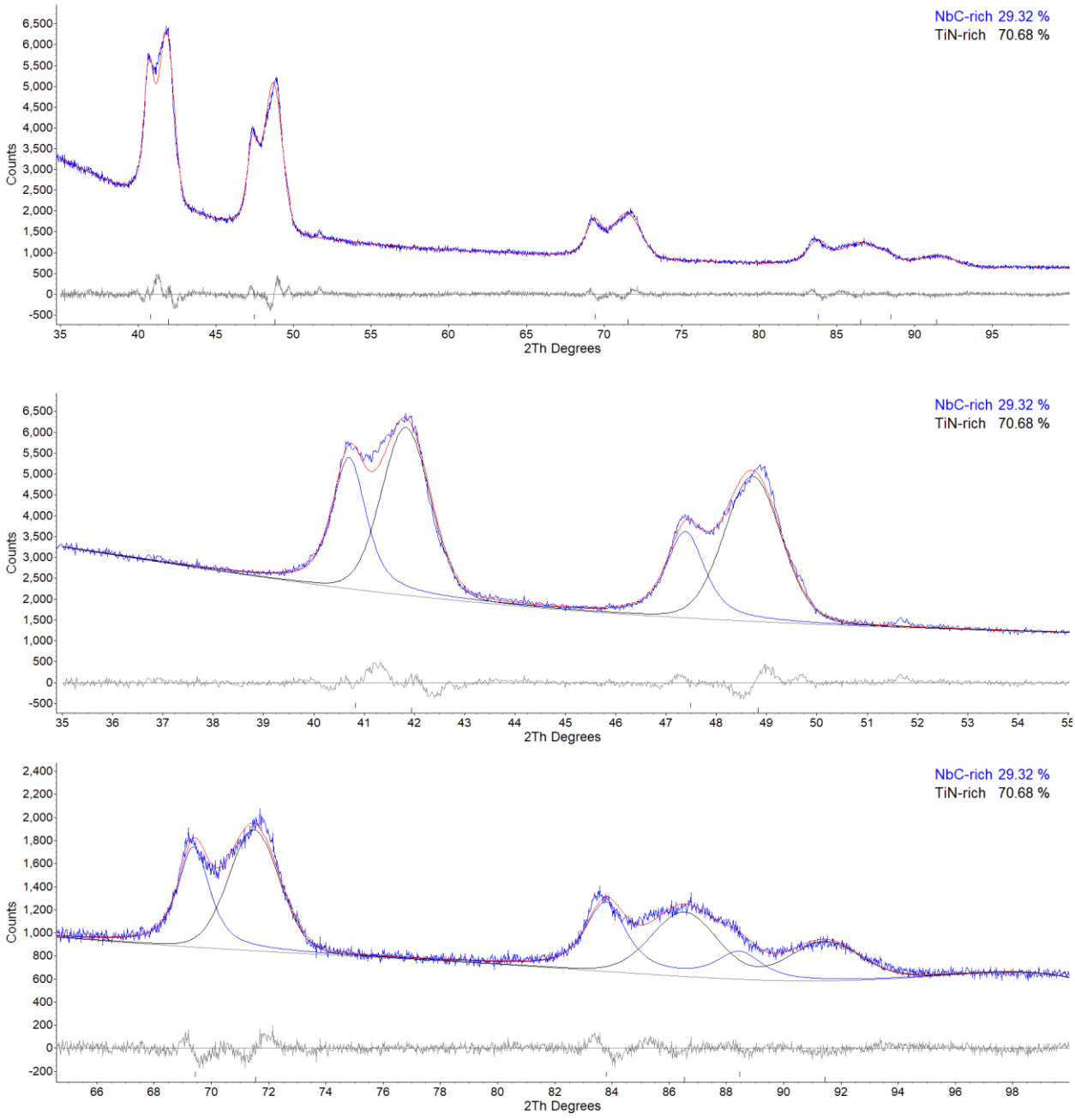

Figure E.8– Observed and calculated XRD patterns for residues extracted from D-1 QL via the matrix dissolution method.

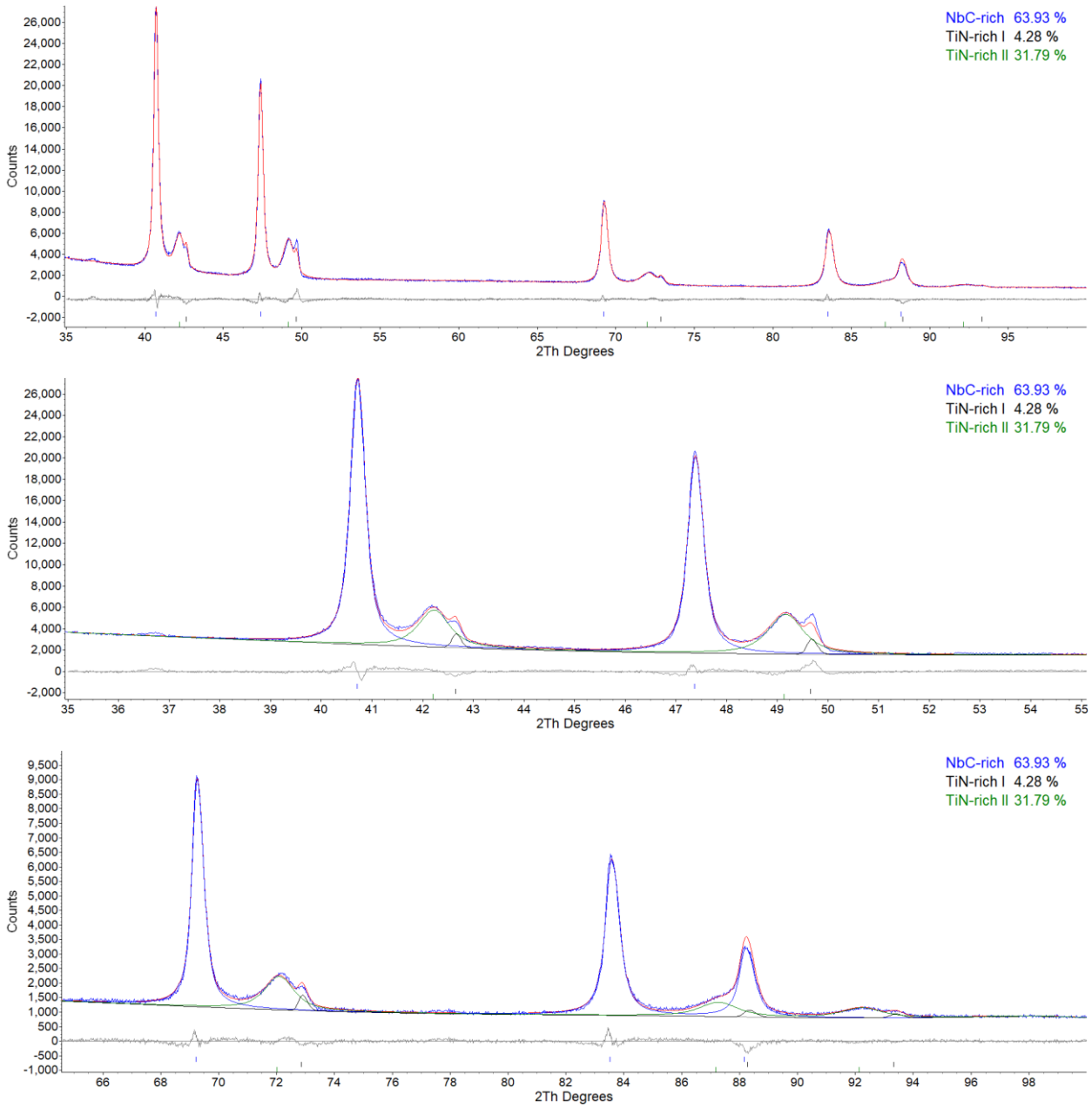

Figure E.9– Observed and calculated XRD patterns for residues extracted from B60 QL via the matrix dissolution method.

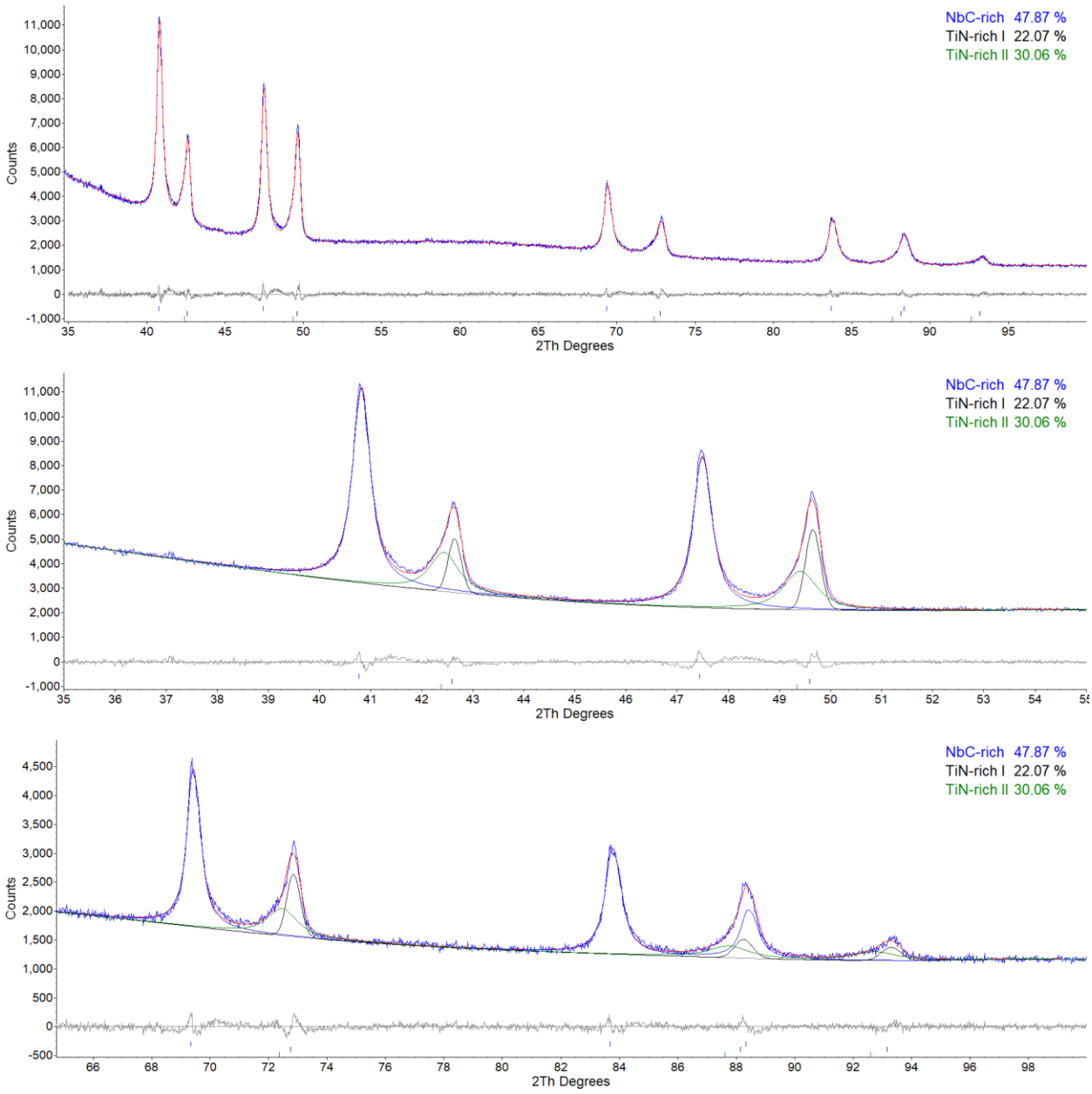

Figure E.10– Observed and calculated XRD patterns for residues extracted from 3F-565 QL via the matrix dissolution method.

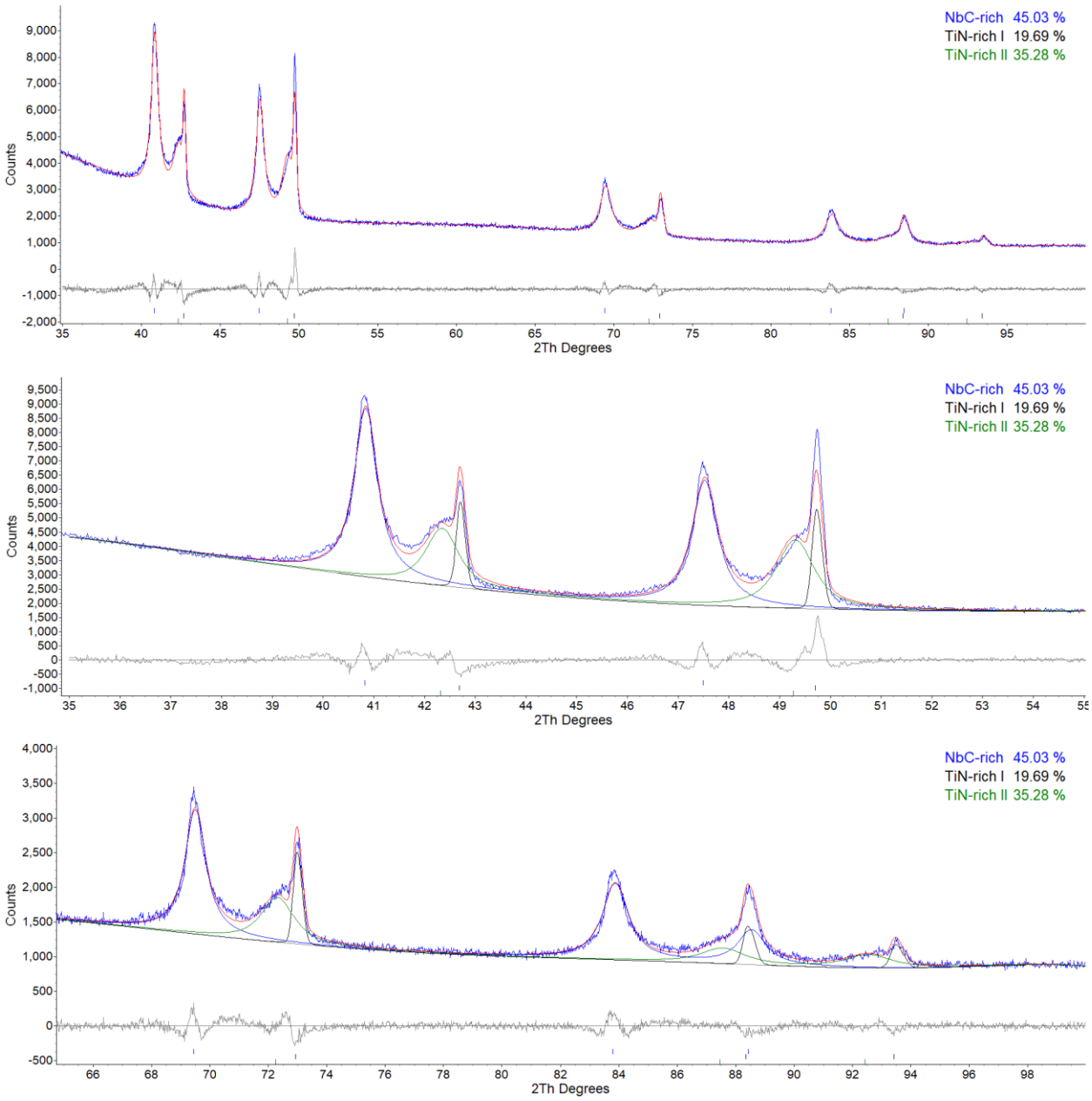

Figure E.11– Observed and calculated XRD patterns for residues extracted from TWX70 QL via the matrix dissolution method.

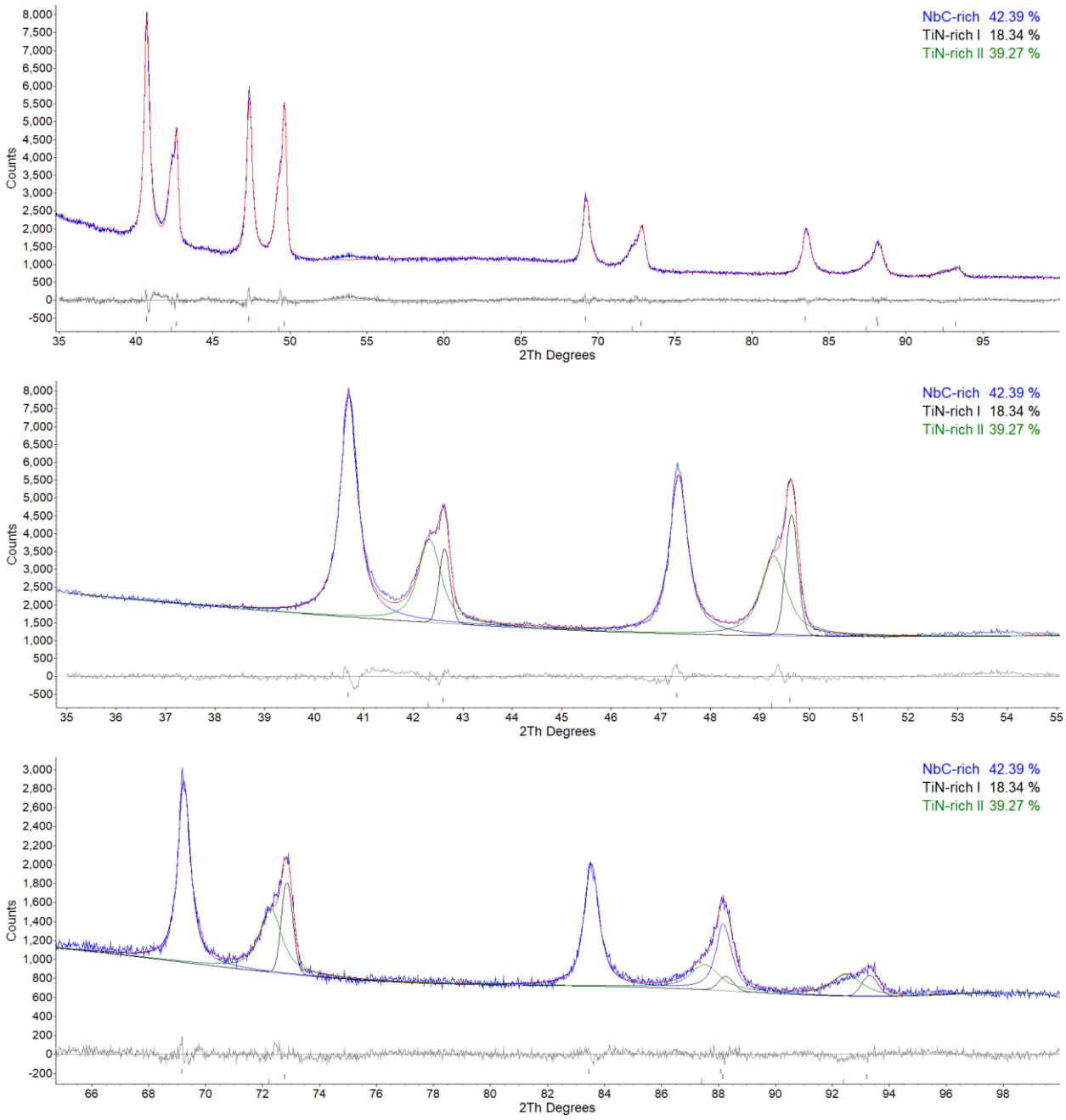

Figure E.12– Observed and calculated XRD patterns for residues extracted from T36-1 CL via the matrix dissolution method.

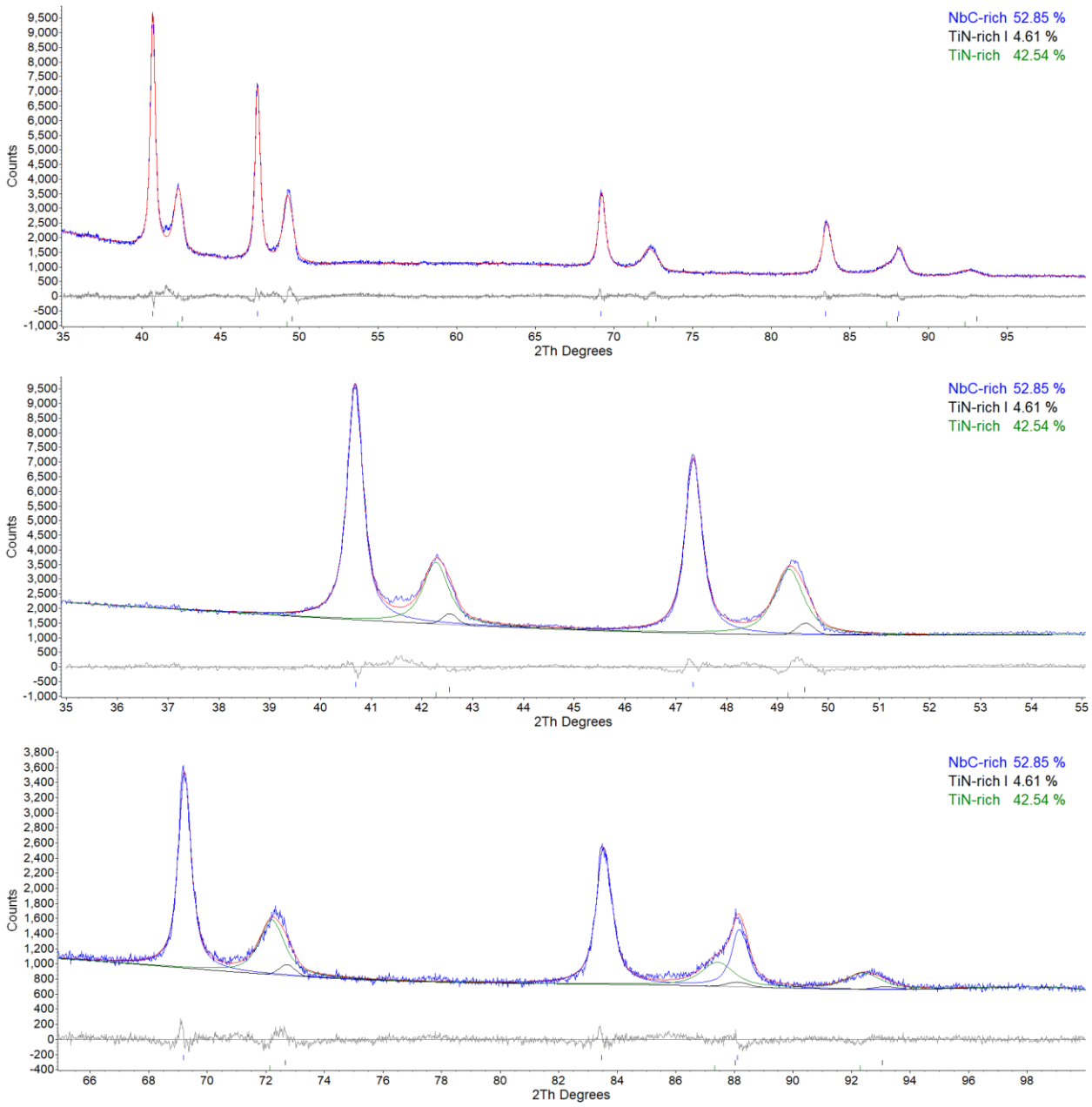

Figure E.13– Observed and calculated XRD patterns for residues extracted from T36-2 CL via the matrix dissolution method.

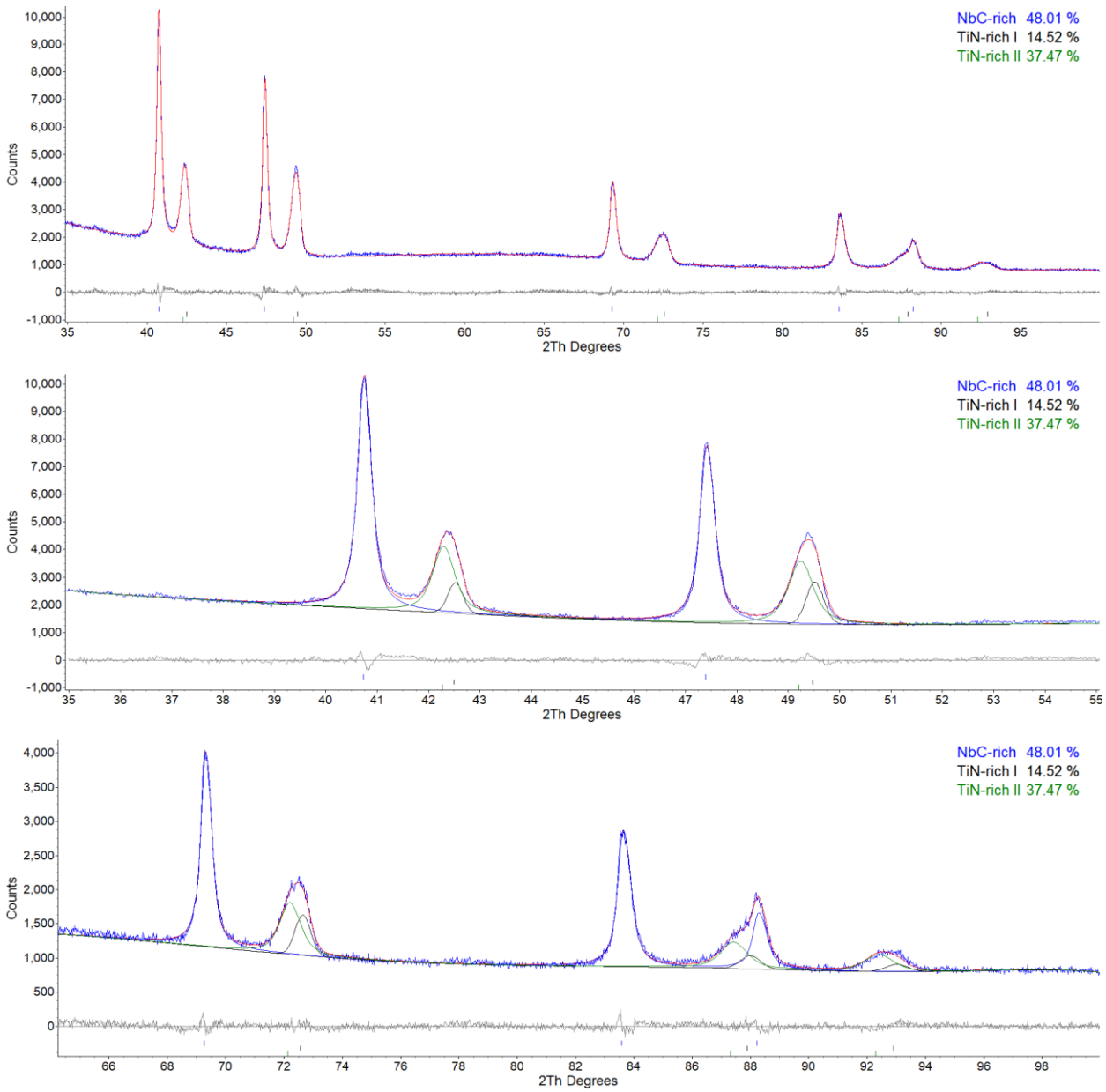

Figure E.14– Observed and calculated XRD patterns for residues extracted from T36-3 CL via the matrix dissolution method.

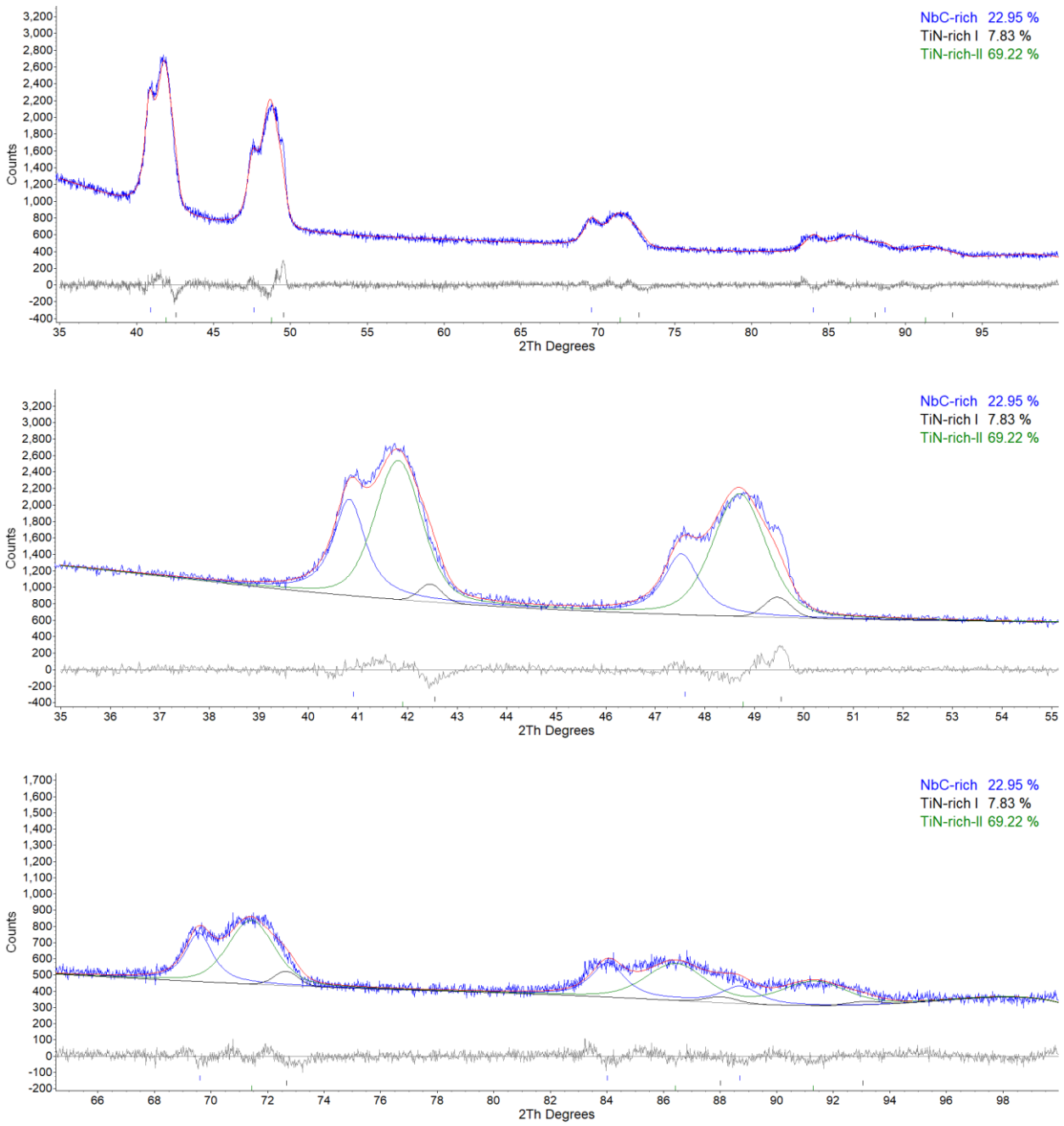

Figure E.15– Observed and calculated XRD patterns for residues extracted from D-1 CL via the matrix dissolution method.

References

[1] P. Barnes, J. K. Cockcroft, S. Jacques and M. Vickers, Advanced Certificate in Powder Diffraction on the Web, School of Crystallography, Birkbeck College, University of London, 1999, Accessed on: May 13, 2021. [Online]. Available: http://pd.chem.ucl.ac.uk/pdnn/pdindex.htm

[2] R. E. Dinnebier, A. Leineweber, and J. S. O. Evans, Rietveld Refinement Practical Powder Diffraction Pattern Analysis using TOPAS. De Gruyter, 2019.

[3] S. A. Speakman, Profile Fitting for Analysis of XRPD Data using HighScore Plus v3, Center for Materials Science and Engineering at MIT, Accessed on: May 13, 2021. [Online]. Available: http://prism.mit.edu/xray/education/downloads.html

[4] R. W. Cheary and A. A. Coelho, "Axial divergence in a conventional X-ray powder diffractometer. I. Theoretical foundations," *Journal of Applied Crystallography*, 1998, vol. 31, pp. 851–861.

Appendix F SEM microstructures

The following presents the microstructure of the steels studied using SEM SE.

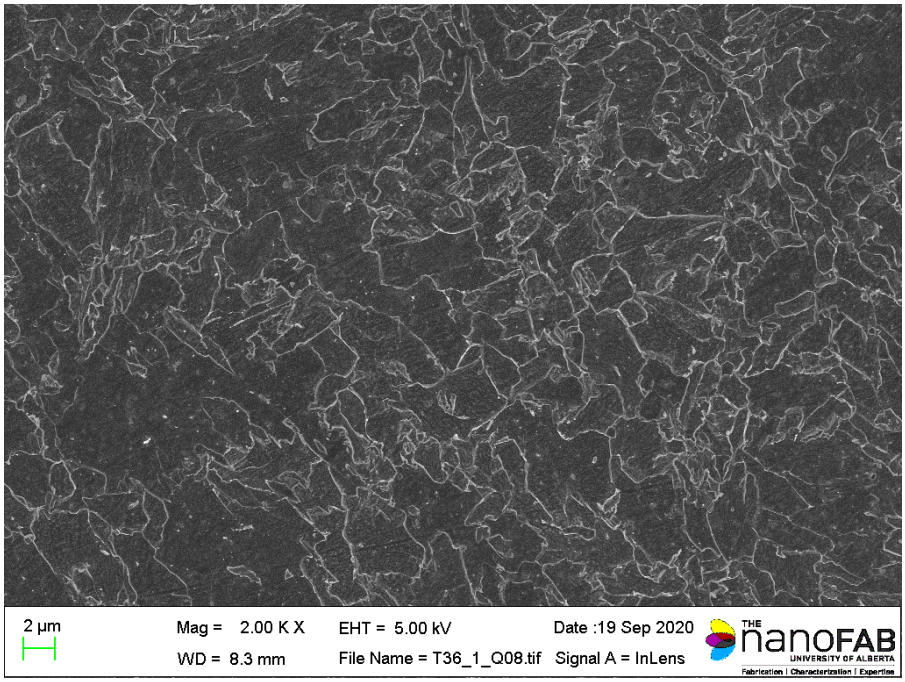

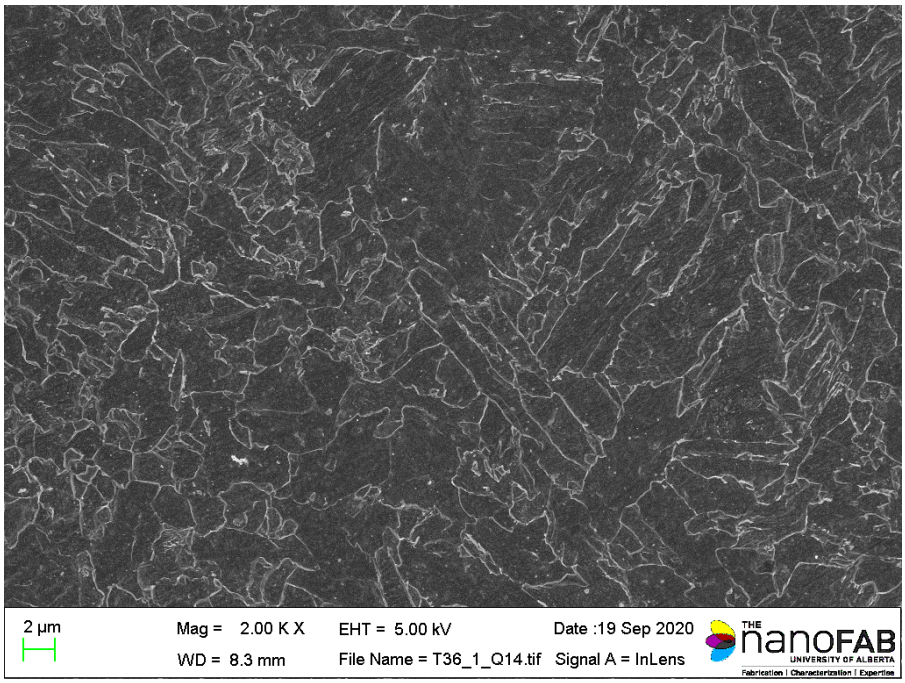

Figure F.1– SEM SE micrographs of T36-1 QL.

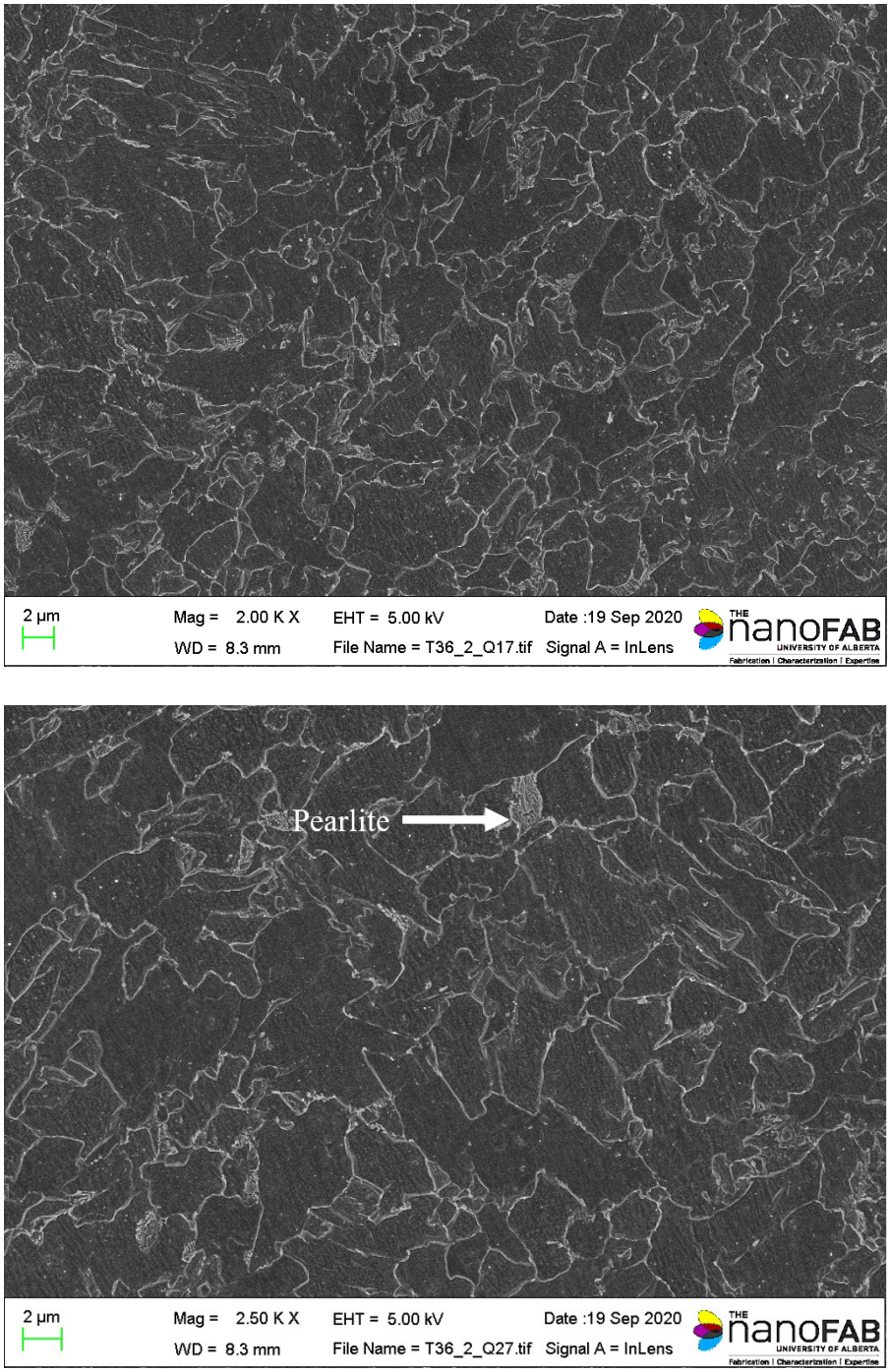

Figure F.2– SEM SE micrographs of T36-2 QL.

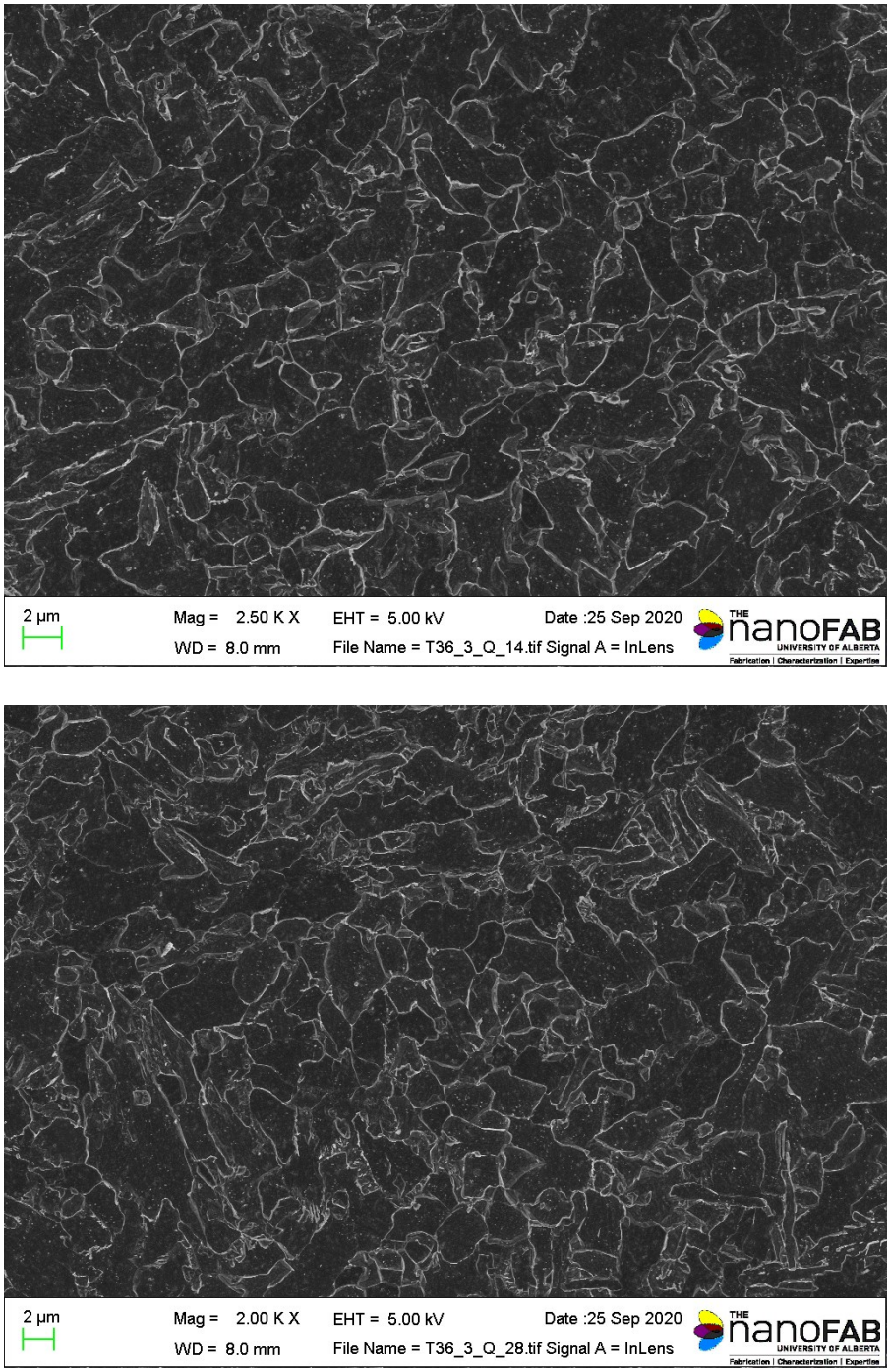

Figure F.3– SEM SE micrographs of T36-3 QL.

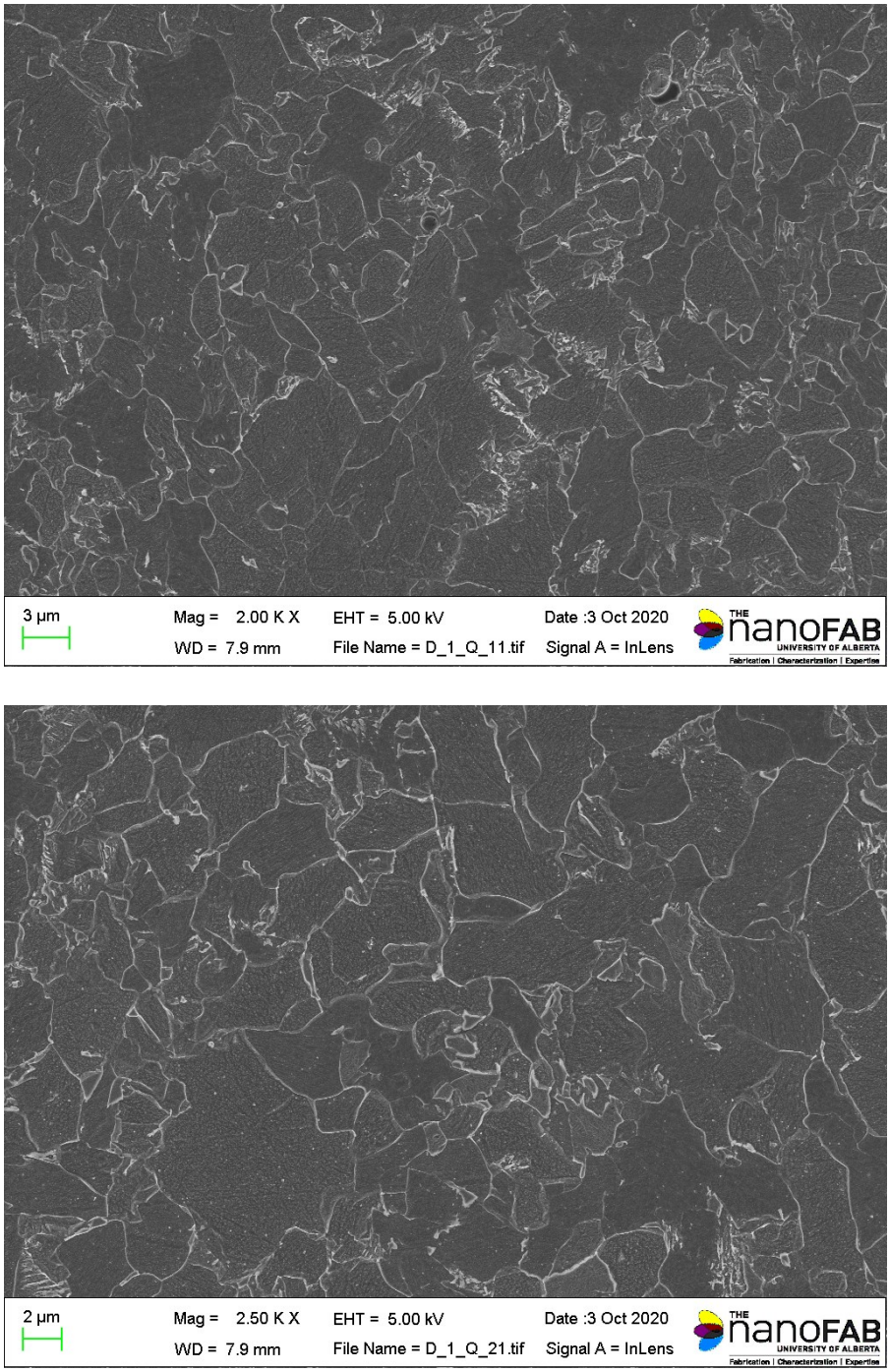

Figure F.4– SEM SE micrographs of D-1 QL.

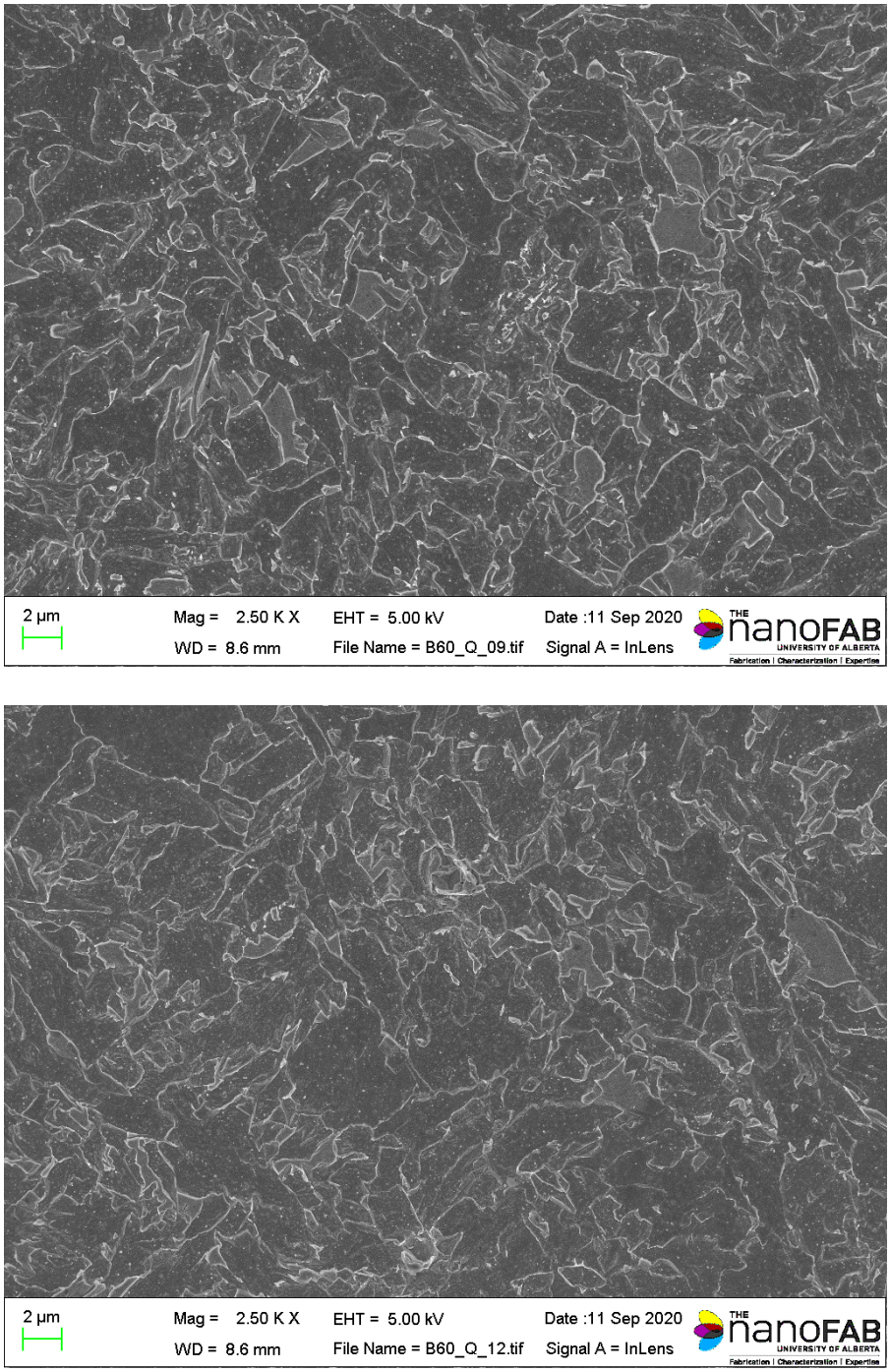

Figure F.5– SEM SE micrographs of B60 QL.

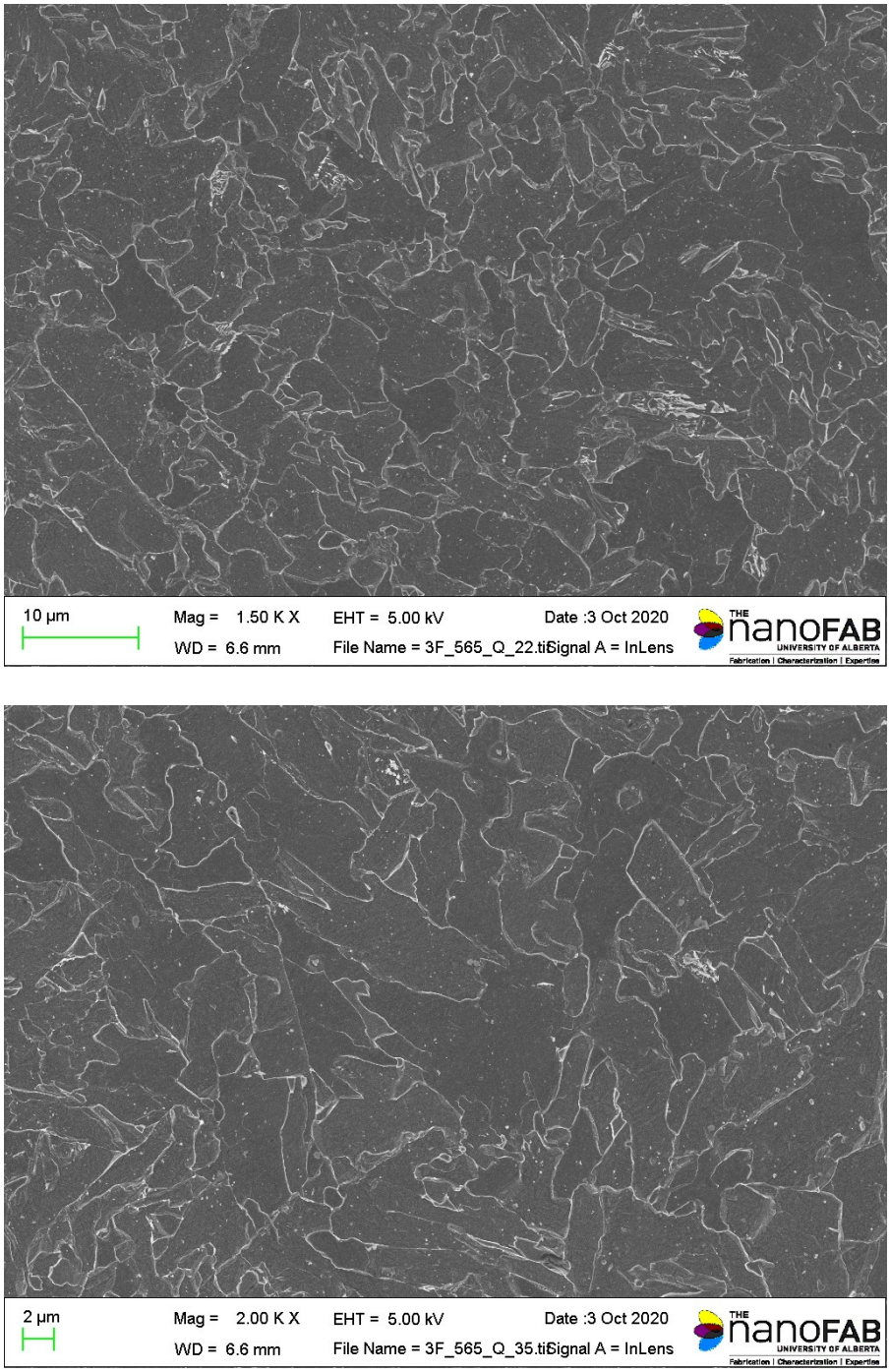

Figure F.6– SEM SE micrographs of 3F-565 QL.

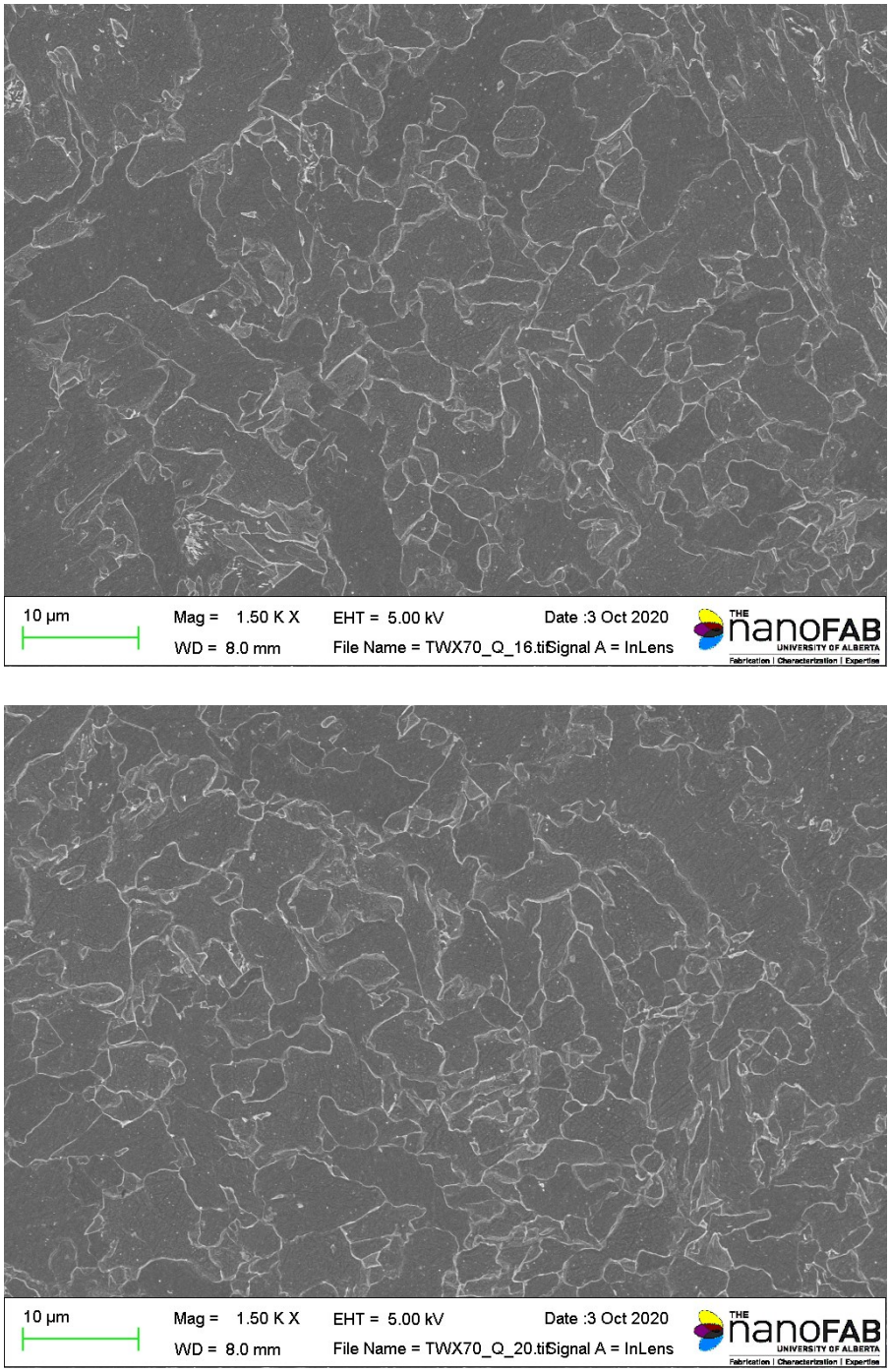

Figure F.7– SEM SE micrographs of TWX70 QL.

Appendix G ICP-MS (QL and CL comparison)

In this Appendix, the concentration of the alloying elements in the supernatant solutions obtained from the matrix dissolution experiments is presented. Three ICP analyses were conducted on the solution obtained from the centerline samples and one ICP analysis was conducted on the solution obtained from the quarterline samples.

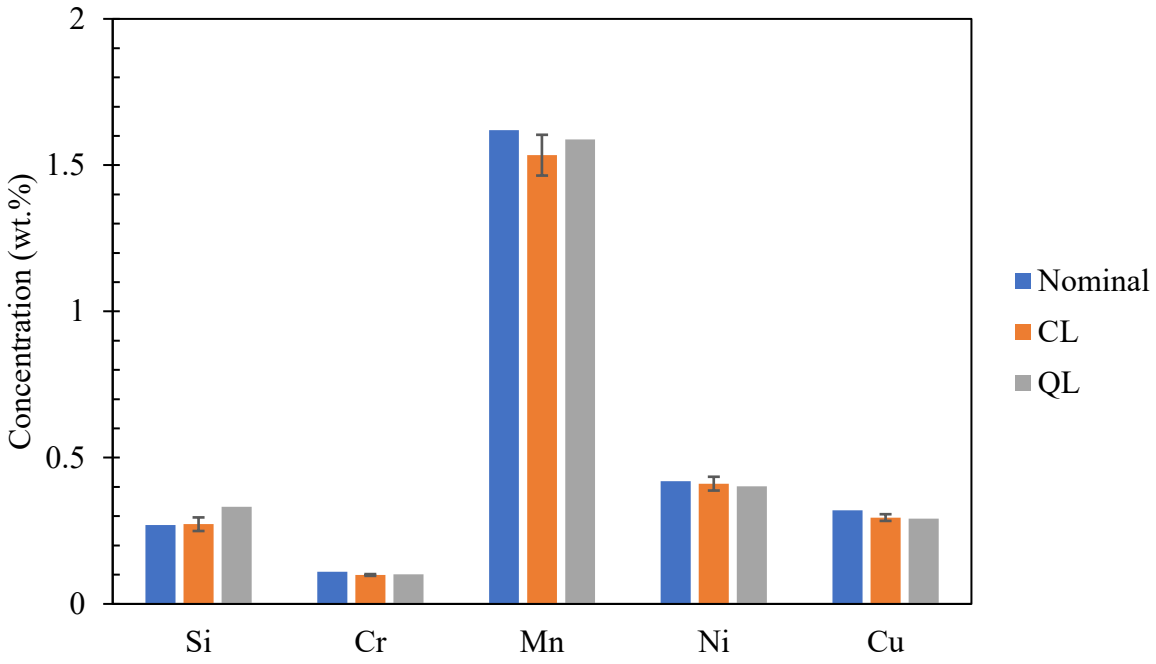

Figure G.1– Concentration of alloying elements in supernatant solutions of T36-2 QL and CL.

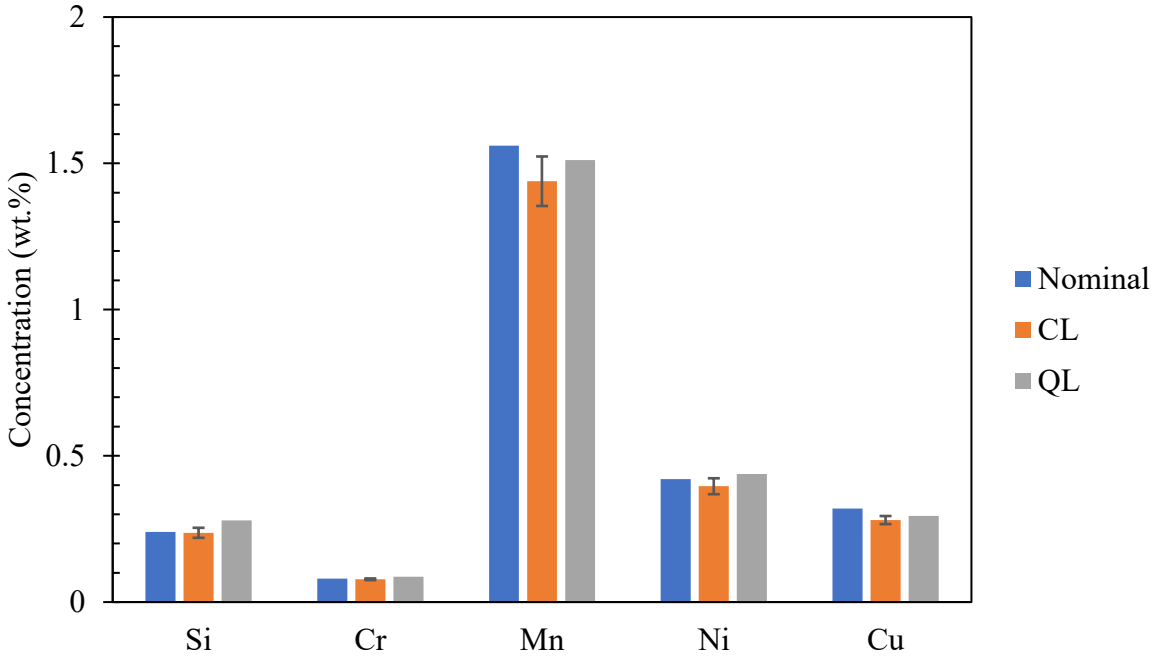

Figure G.2– Concentration of alloying elements in supernatant solutions of T36-3 QL and CL.

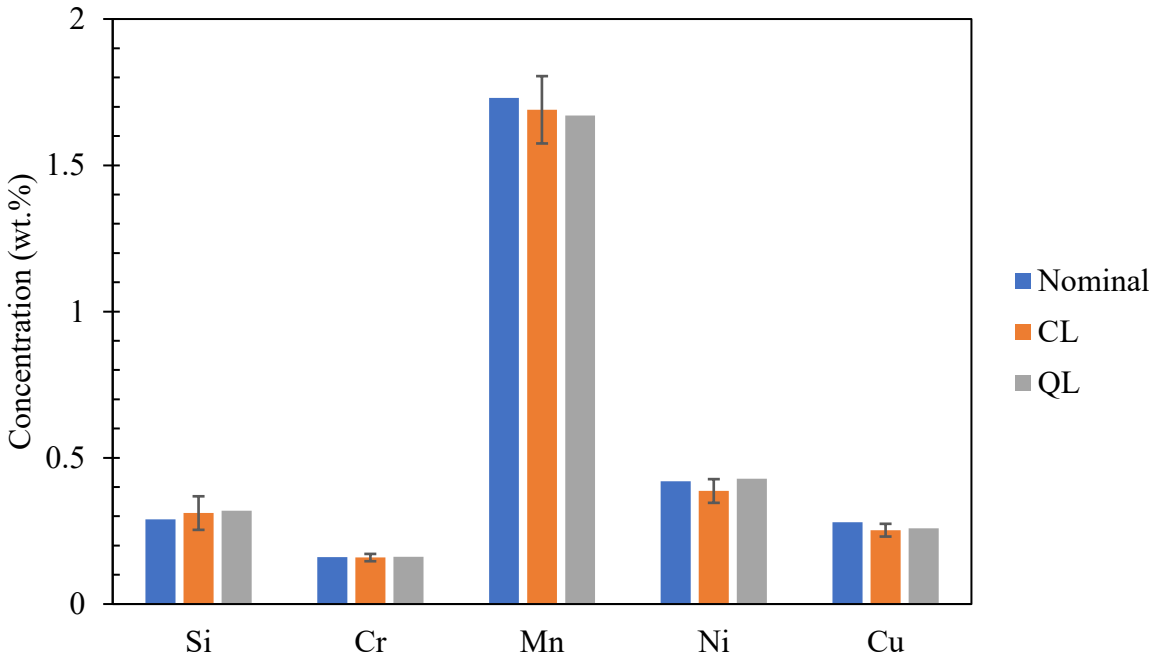

Figure G.3– Concentration of alloying elements in supernatant solutions of D-1 QL and CL.

Appendix H SEM/EDX analysis of 3F-as-cast

This Appendix shows the SEM SE micrographs and EDX spectra and maps of the coarse TiN-rich and Nb-rich particles extracted using carbon replica from 3F-as-cast.

H-1 Coarse TiN-rich particles

Figure H.1 to Figure H.3 show the coarse TiN-rich particles extracted using carbon replica from 3F-as-cast.

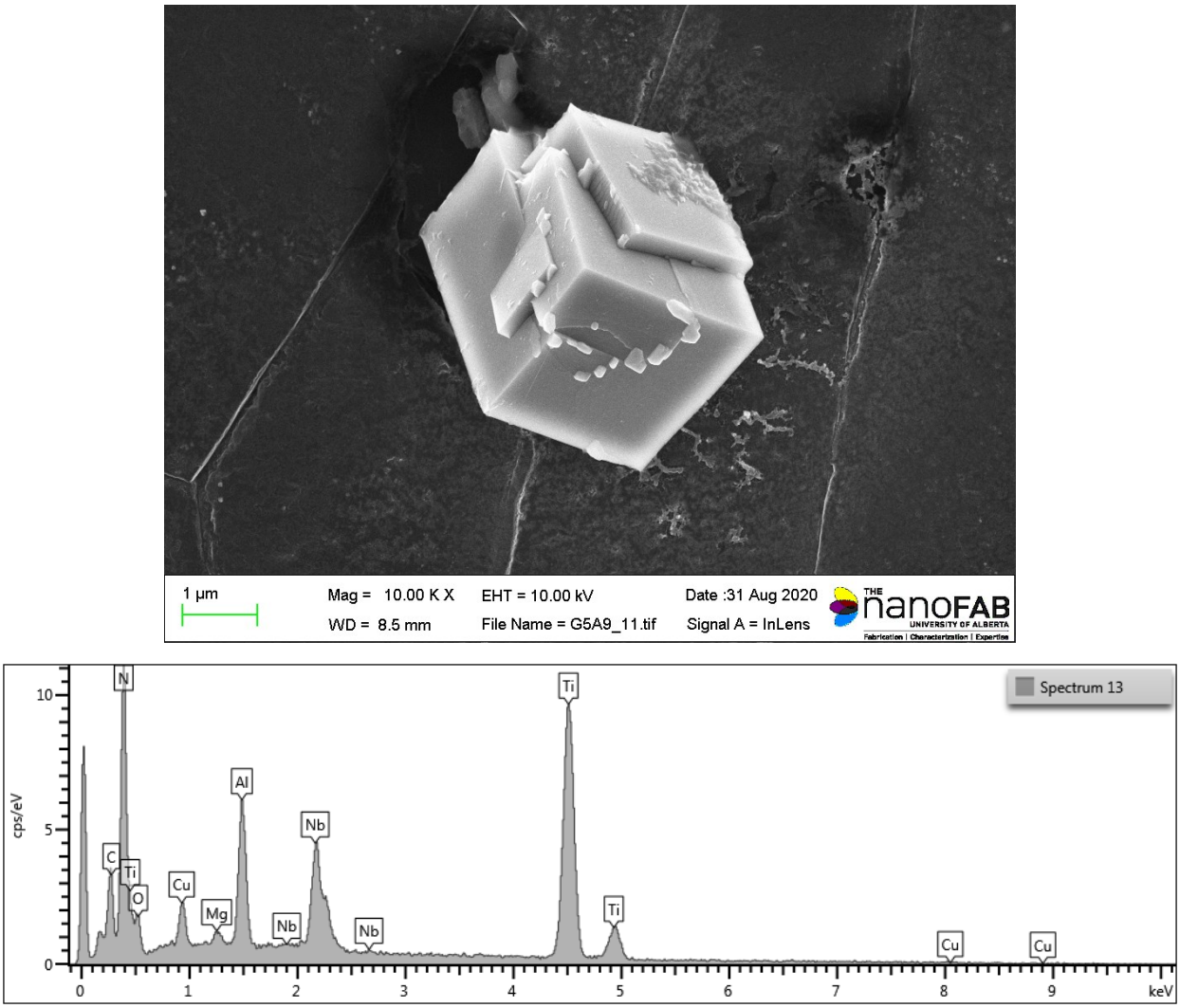

Figure H.1– SEM SE micrograph and EDX spectrum of the coarse TiN-rich particle extracted using carbon replica from 3F-as-cast QL.

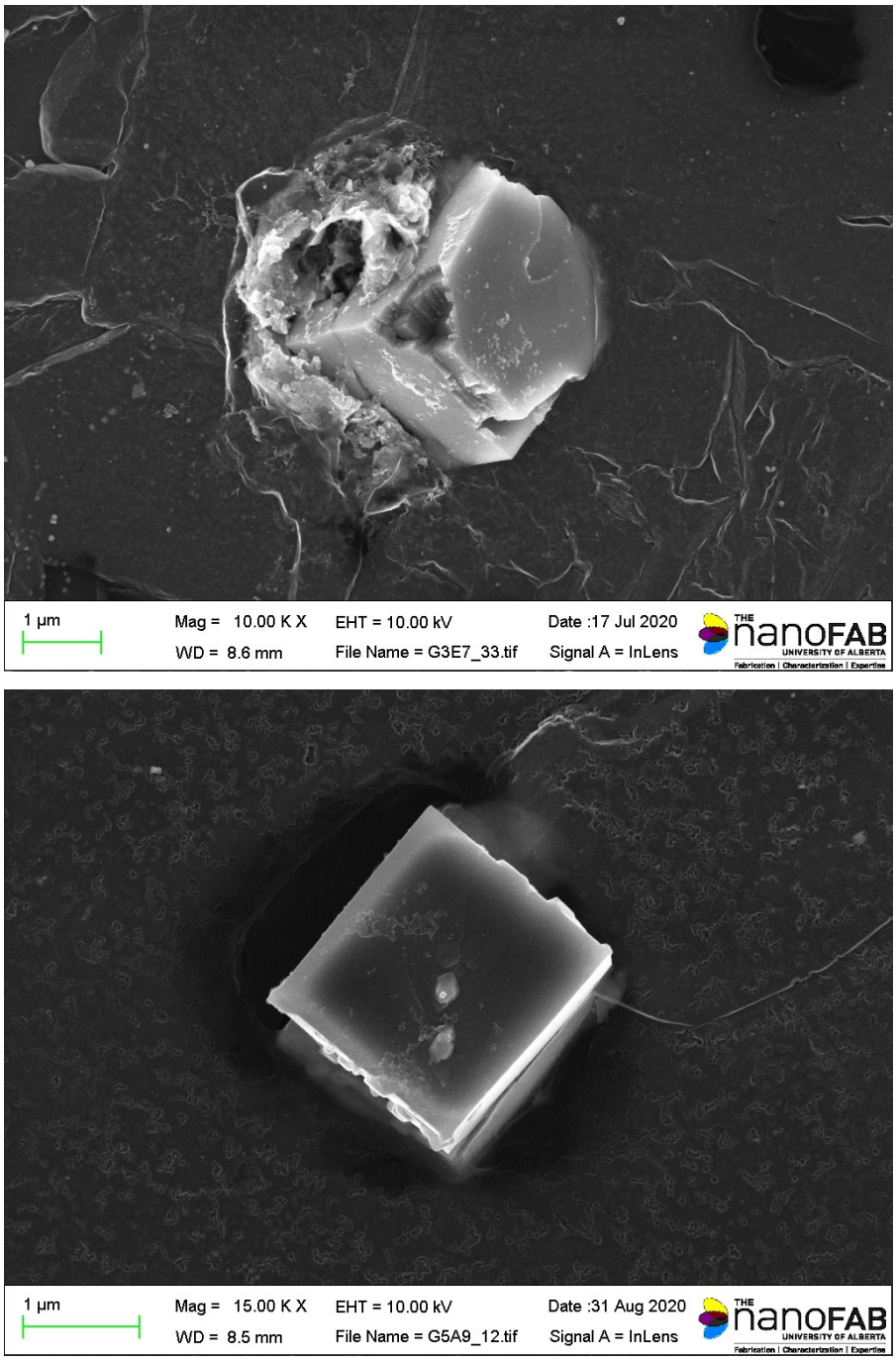

Figure H.2– SEM SE micrograph of the coarse TiN-rich particle extracted using carbon replica from 3F-as-cast QL.

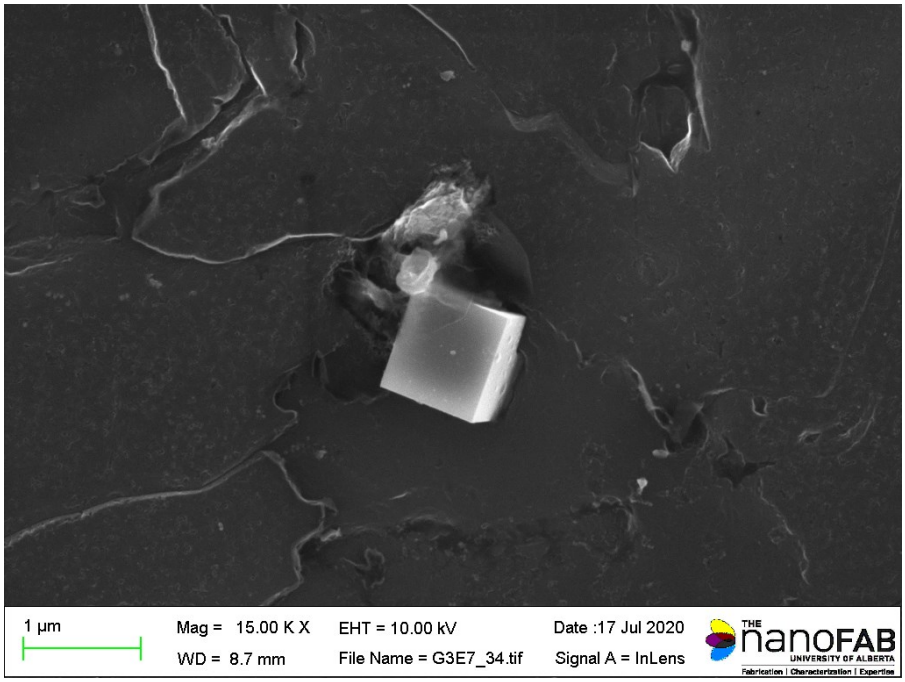

Figure H.3– SEM SE micrograph of the coarse TiN-rich particle extracted using carbon replica from 3F-as-cast QL.

H-2 Coarse Nb-rich particles

Figure H.4 to Figure H.8 show the SEM micrographs and EDX maps of the coarse Nb-rich particles extracted using carbon replica from 3F-as-cast.

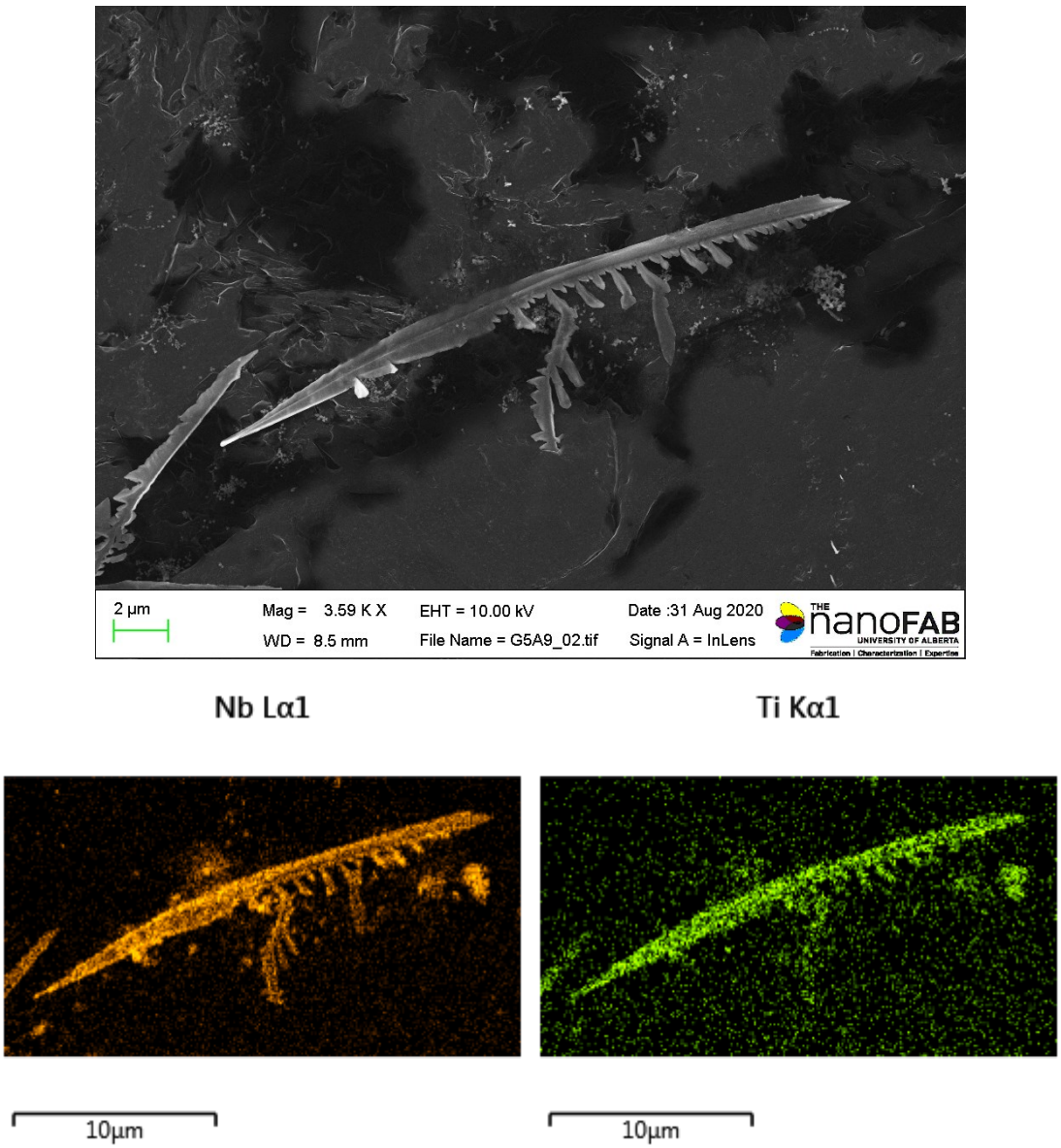

Figure H.4– SEM SE micrograph and Nb and Ti EDX maps of the coarse Nb-rich particle extracted using carbon replica from 3F-as-cast QL.

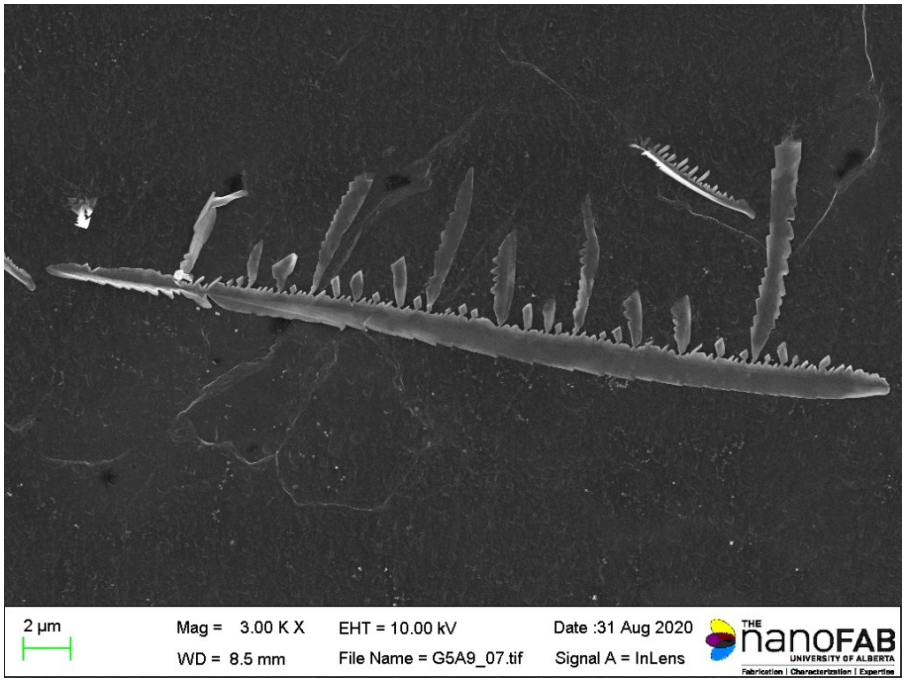

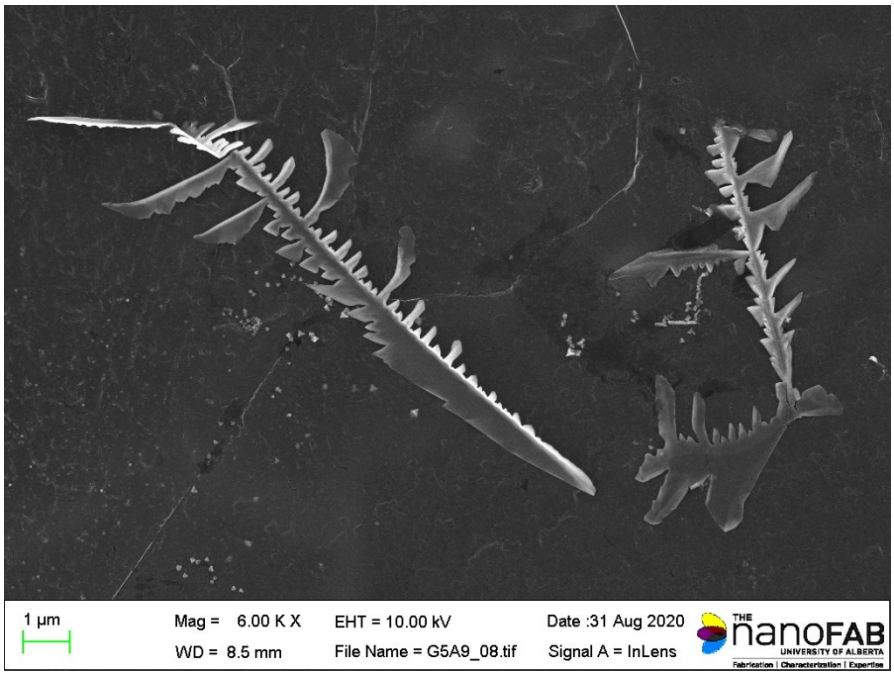

Figure H.5– SEM SE micrographs of the coarse Nb-rich particles extracted using carbon replica from 3F-as-cast QL.

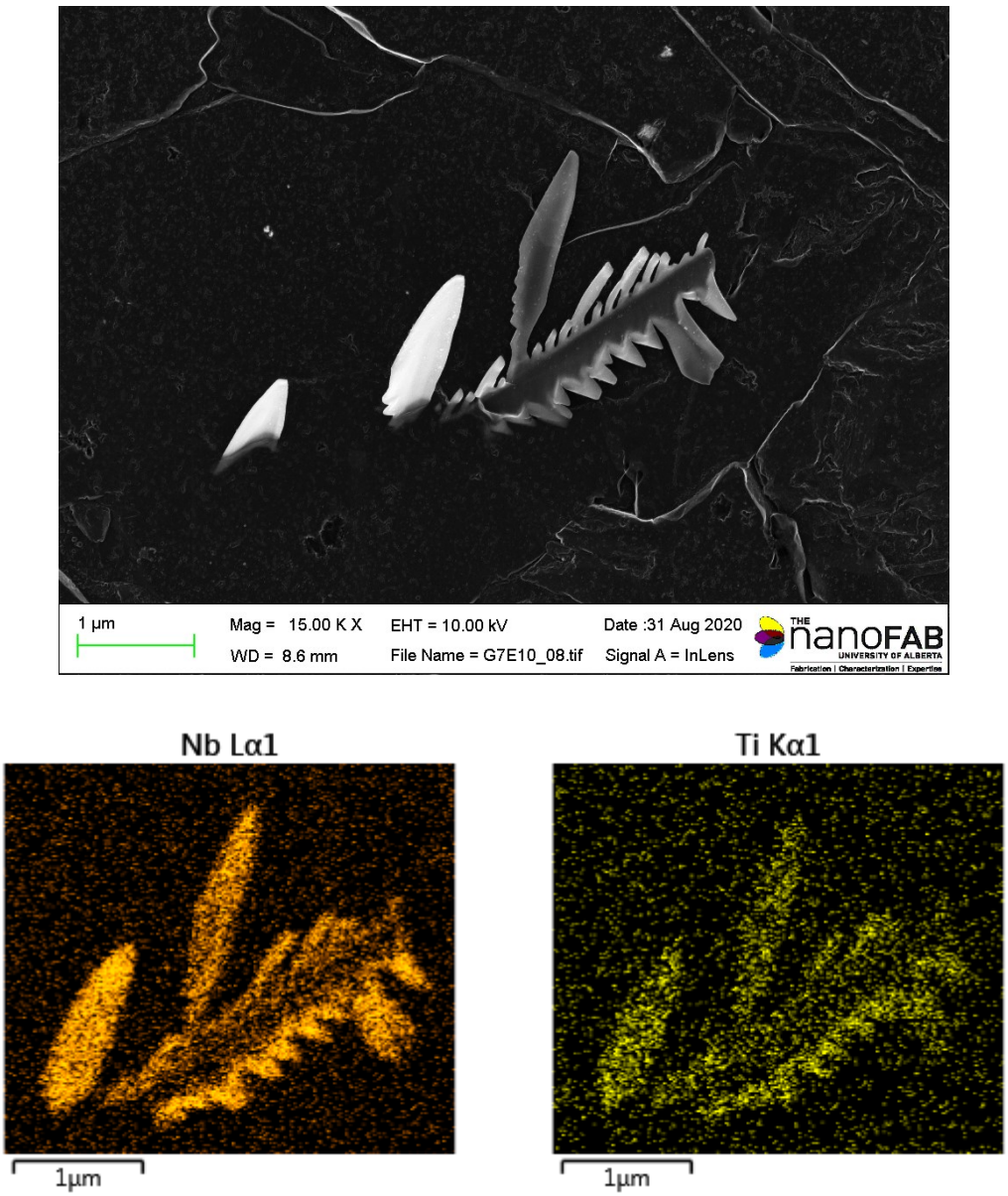

Figure H.6– SEM SE micrograph and Nb and Ti EDX maps of the coarse Nb-rich particle extracted using carbon replica from 3F-as-cast CL.

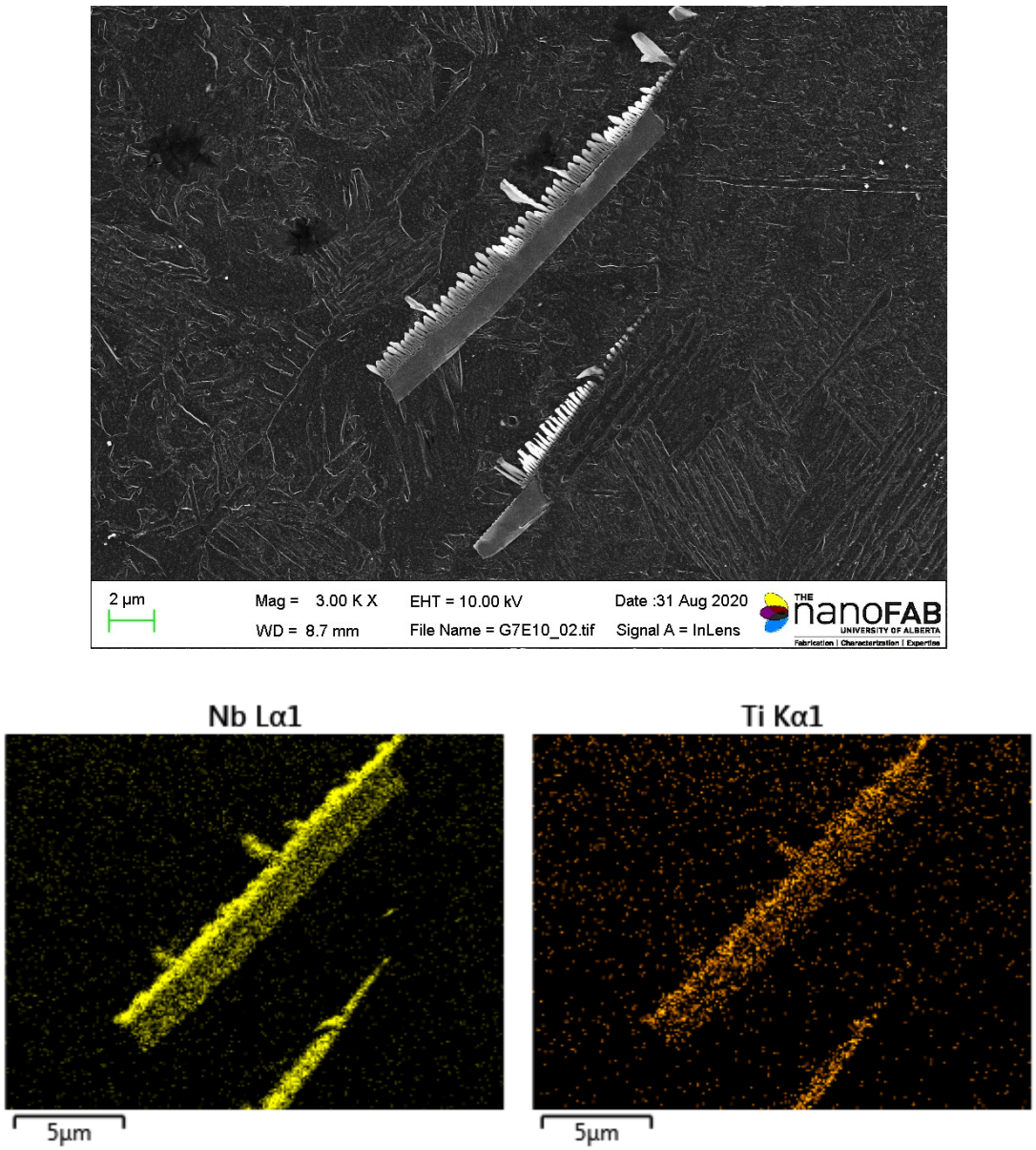

Figure H.7– SEM SE micrograph and Nb and Ti EDX maps of the coarse Nb-rich particle extracted using carbon replica from 3F-as-cast CL.

Figure H.8– SEM SE micrograph of the coarse Nb-rich particles extracted using carbon replica from 3F-as-cast CL.

Appendix I STEM/EDX analysis of 3F-as-cast

The following presents the STEM ADF micrographs and EDX maps of the fine Nb-rich particles extracted with the carbon replica method from 3F-as-cast.

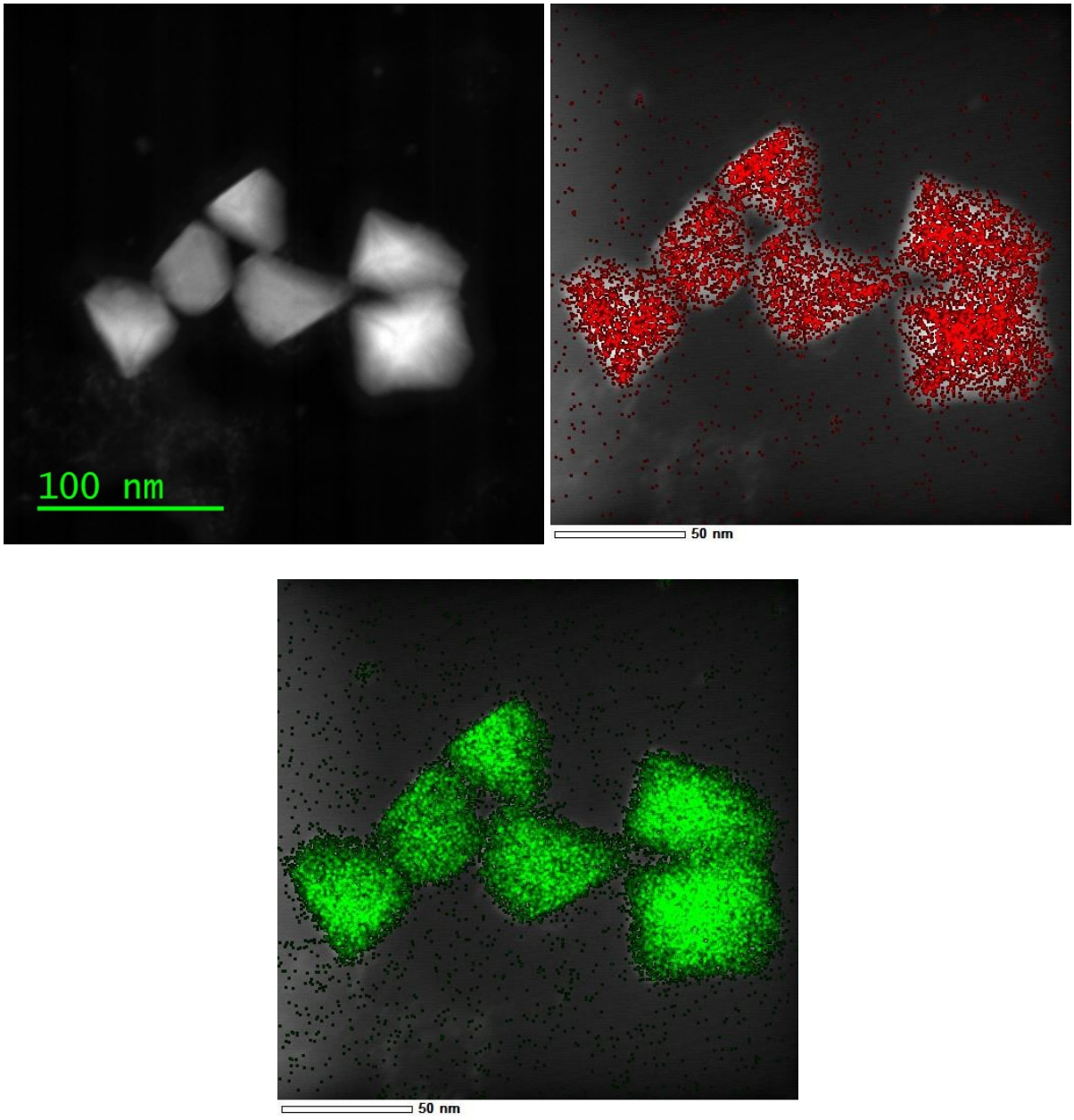

Figure I.1– STEM ADF micrograph and EDX maps (Ti: red, Nb: green) of the fine Nb-rich particle extracted using carbon replica from 3F-as-cast QL.

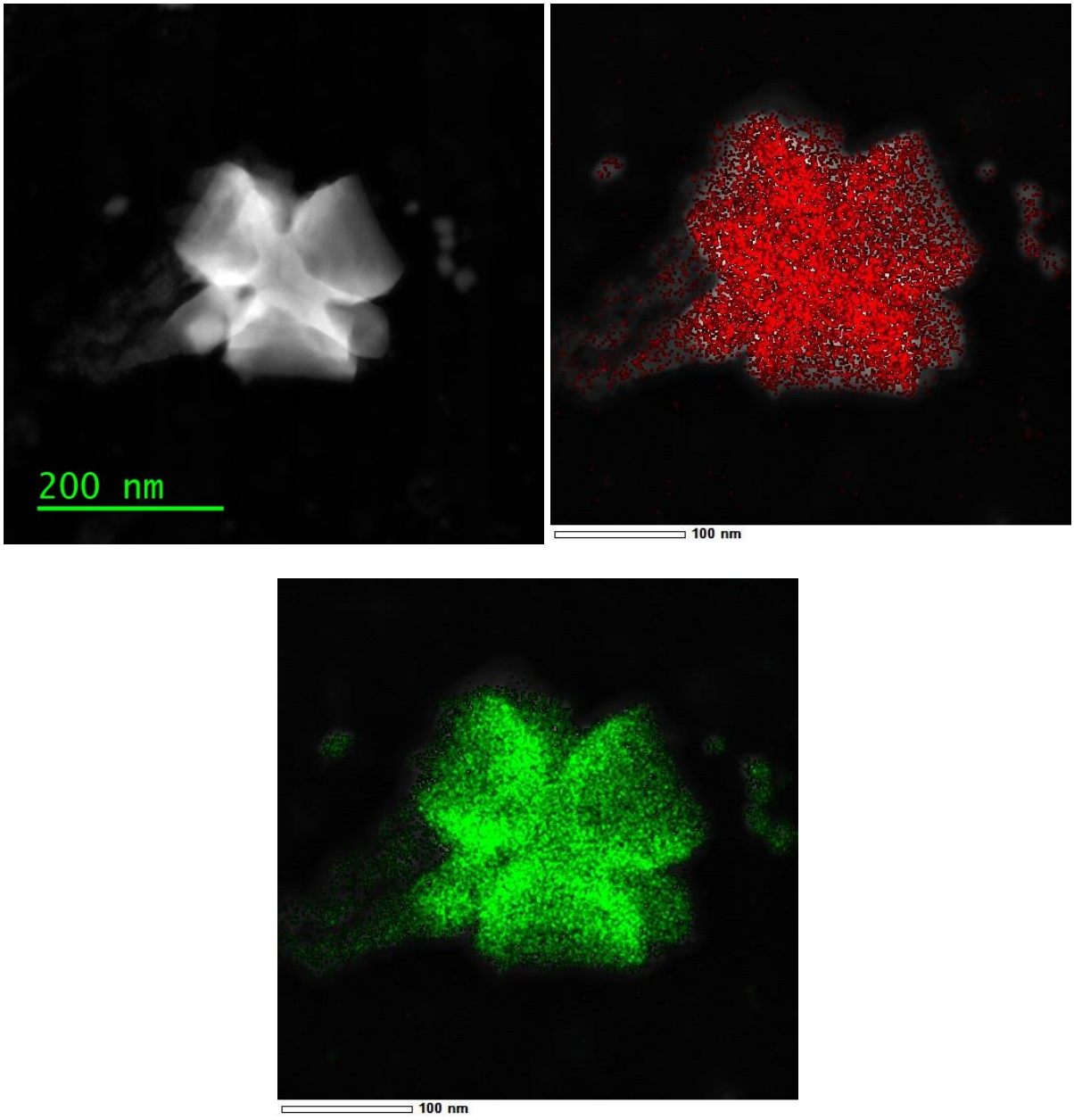

Figure I.2– STEM ADF micrograph and EDX maps (Ti: red, Nb: green) of the Nb-rich particle extracted using carbon replica from 3F-as-cast QL.

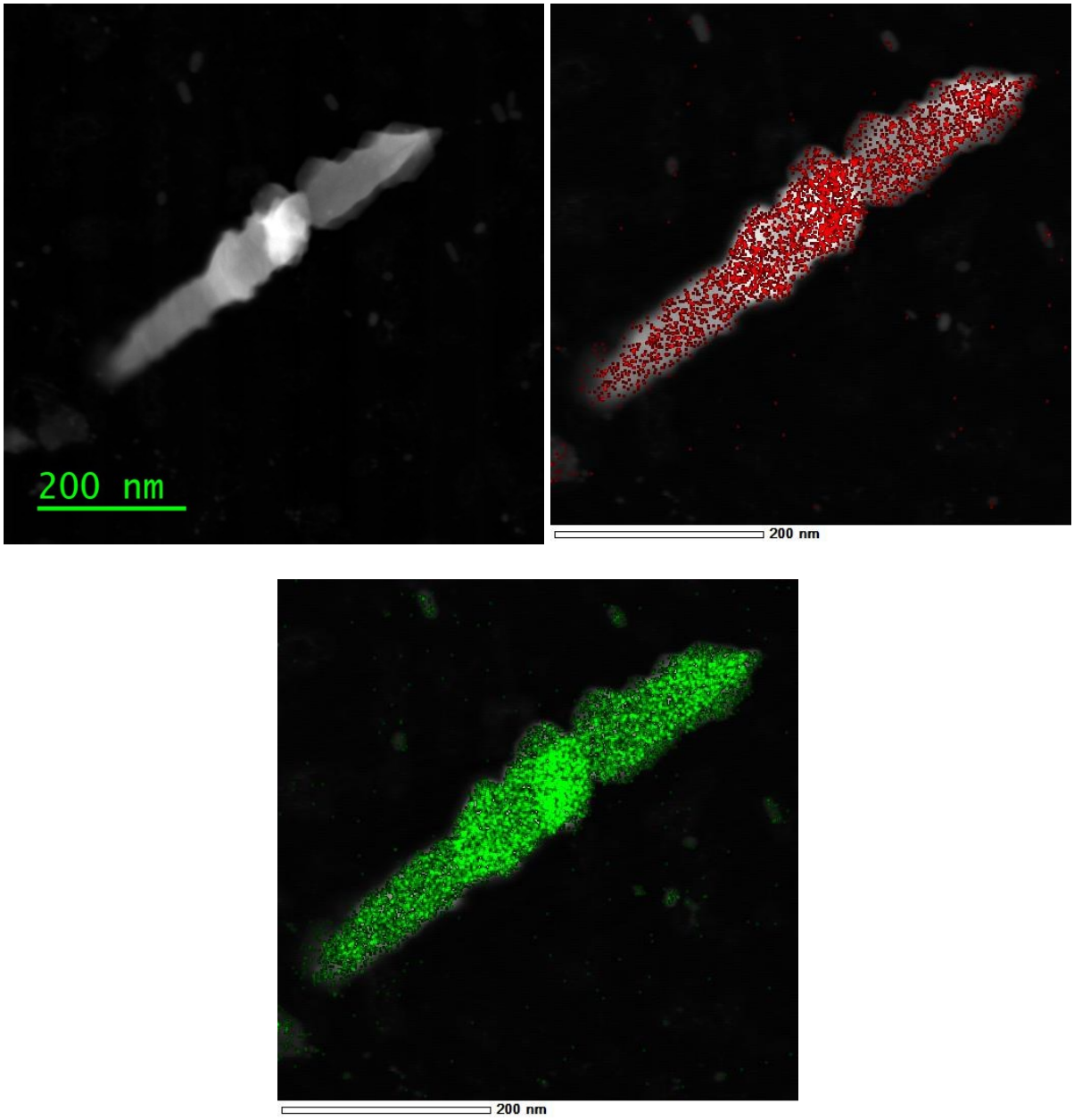

Figure I.3– STEM ADF micrograph and EDX maps (Ti: red, Nb: green) of the Nb-rich particle extracted using carbon replica from 3F-as-cast QL.

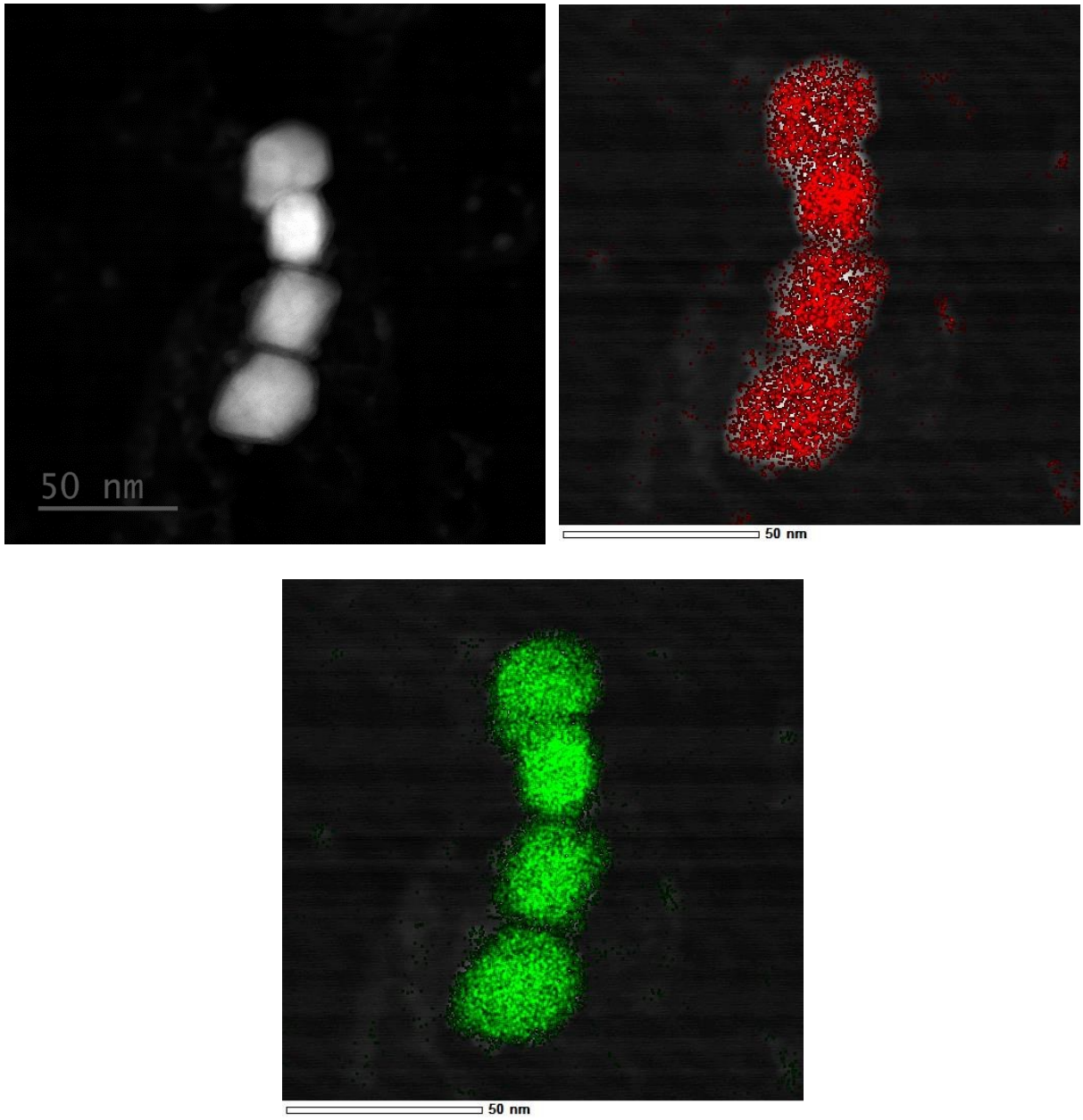

Figure I.4– STEM ADF micrograph and EDX maps (Ti: red, Nb: green) of the fine Nb-rich particle extracted using carbon replica from 3F-as-cast CL.

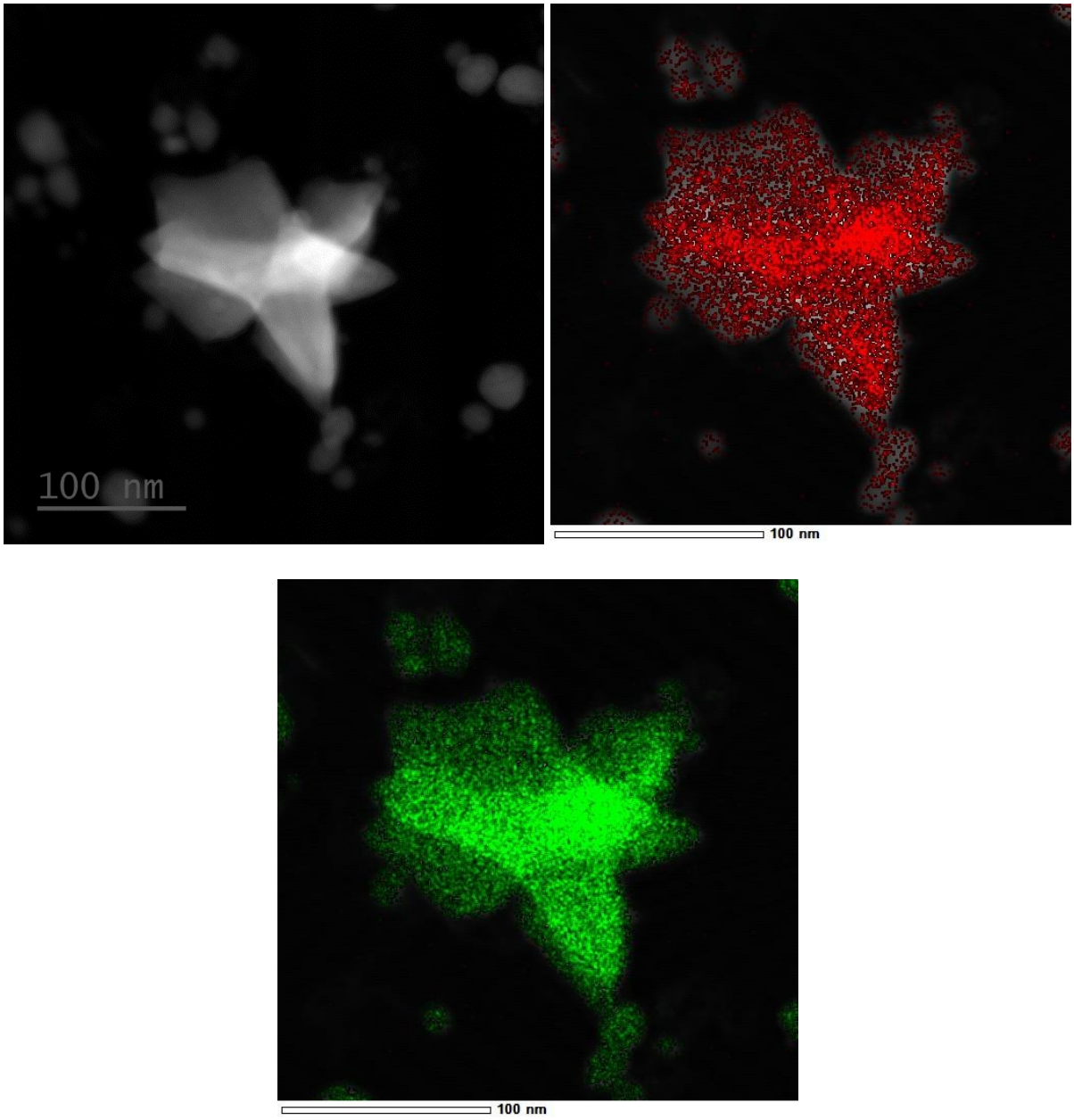

Figure I.5– STEM ADF micrograph and EDX maps (Ti: red, Nb: green) of the Nb-rich particle extracted using carbon replica from 3F-as-cast CL.

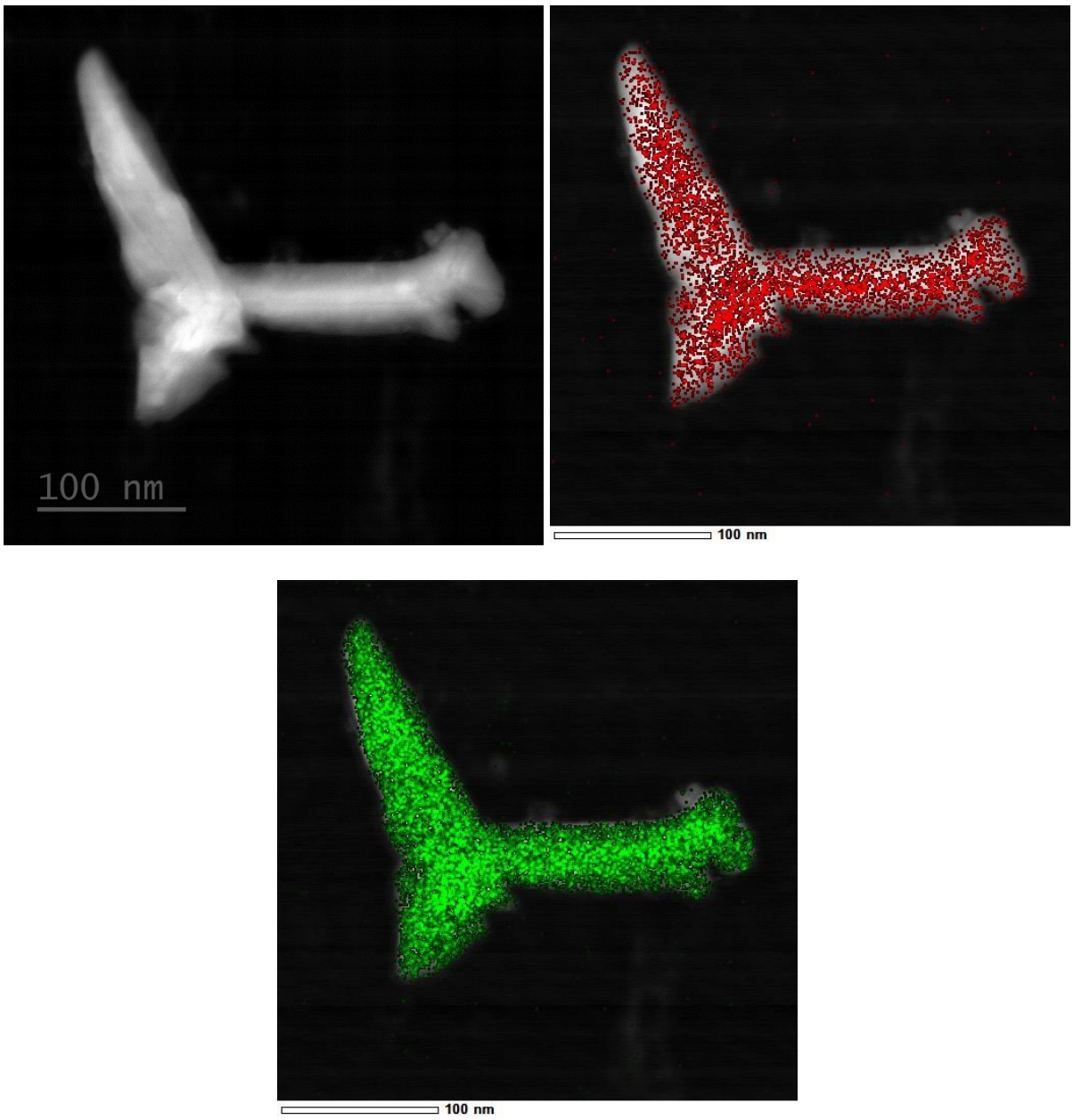

Figure I.6– STEM ADF micrograph and EDX maps (Ti: red, Nb: green) of the Nb-rich particle extracted using carbon replica from 3F-as-cast CL.